Imperial College London

GROUND STATE COOLING OF THE RADIAL MOTION OF A SINGLE ION IN A PENNING TRAP AND COHERENT MANIPULATION OF SMALL NUMBERS OF IONS

Pavel Hrmo

Thesis submitted in partial fulfilment

of the requirements for the degree of Doctor of Philosophy

DEPARTMENT OF PHYSICS

IMPERIAL COLLEGE LONDON

May 2018

COPYRIGHT AND DECLARATION

I also declare that all work presented within this thesis is my own unless explicitly cited or referenced.

ACKNOWLEDGEMENTS

Before I started the PhD I had an image of it that involved blood, sweat and tears, working in a dark lab, thanklessly twiddling things late into the night hoping to serendipitously discover something that works only to have it fail the next time for some unknown reason. While this Sisyphian nature of the last few years indeed came to pass, I never imagined how much fun I would have along the way. For this I have have to thank the wonderful team environment that was fostered by Richard that allowed the unholy trinity of Manny, Vince and me to survive without turning the lab into the Lord of the flies. Richard, you've been a really great supervisor, not only volunteering time out of your busy schedule to entertain our silly physics ideas, but also to just talk and joke around. It wasn't always smooth sailing in the lab, but you were never critical of our failures and always encouraging us to get back up on our feet and try something else. You really made our small group into an tightly knit ion trapping family. I would also love to praise your critical contributions to running the experiment, but all that is springing to mind right now is how we quenched the magnet and the time we were trying to glue the cavity mirror on the new piezo and you dropped it, giving us a guilty "sorry chaps" as I spotted a crack on it.

Next up, Manny. I think you and I could sometimes make for a brilliant bickering couple in a soap opera, but ultimately I think we pushed each other to refine and polish our ideas to achieve better results. I really admired your hard working attitude and drive and it has certainly influenced me positively to try to improve. From the time we worked in the lab side by side without talking to each other to running spectra late into the night, we covered all styles of lab co-operation. You're one of the best people to have around on a night out because somehow mischief always follows you, like when you nicked a Japanese businessman's chips in the casino or almost got into a fight with the "owner" of Troy 22.

The final vertex of our lab triangle is of course Vince. I think our combined constructive pessimism was essential to survive the trials and tribulations of the oft infuriating equipment. Your unparalleled quality of criticising the absurdities of the world was only matched by your finesses in calculation and electronics (and refined dress sense). A special shout out to the long Sporcle sessions that made spectrum taking bearable. The adventures are countless, from the moment you made an impression in the summer school by ejecting a quarrelling pair of weapons from a pub, Les Houches to the nights on the dance floor where your shirt grew progressively sweatier and the button count decreased as you rode the groove.

Rounding out the lab experience is a wonderful cast of characters that appeared throughout the years. Firstly, Joe and Graham, you guys were instrumental in instilling the foundations of rigorous lab work in me. I learned so much invaluable knowledge from you guys without which I would certainly have struggled to achieve all the results in this thesis. You also set the tone for a great lab atmosphere that was always friendly and collaborative, probably best highlighted by our multi-monitor streams of the world cup.

I hope that we've been able to pass on the joys of ion trapping to the Next-Gen boys Ollie and Jake. You guys have the skills and humour to walk in our humble footsteps and really move the lab into the Radio ages. Ollie, don't get spoiled by all your new toys, you have to remember the tradition of the lab of squeezing every penny from these bloody lasers. Jake, I expect you to have automated the whole experiment so in a year I will be able to run a robust two qubit gate from my phone. I have high expectations of two engineers running a quantum lab. Thanks also goes out to Florian for all the theoretical support in the final push (not the Christmas party

kind, off a Twister mat) of our experimental run and for all the fruitful discussions during the write up phase. With your theory support the ion trapping team will be stronger than ever.

Next comes the array of Bsc/MSci etc. students who were always a pleasure to work with. Special mention goes to Jamie and Nicolas who really gave the cursed electronic detection a good shot and were chilled out dudes while doing it. Also, John's brief stint as a summer student far exceeded my expectations of what could be achieved by an undergrad in such a short time! You also convinced me that you can survive a summer in London in flip flops and shorts (even though you had to leave your guns at home).

Finally, I would also like to acknowledge Danny, who passed away during the PhD. Danny was the person who initially inspired me to join the group. His extremely friendly character, and infectious enthusiasm for ion trapping that he transmitted during his CDT lectures had me instantly hooked. I was really looking forward to working with him, but his diagnosis cut this short. Yet despite his condition, Danny still skyped into our group meetings for as long as he could and really showed the passion and character that defined him as a human and scientist.

A big thank you to all the support staff, Miranda, Judith, Sanja, Marcia, Veena, Joe that had to deal with my not always diligent approach to bureaucratic matters. Also thanks to Brian, for his willingness to help with technical things, small and large around the lab and most importantly for keeping us safe.

Next up, the amazing friends and acquaintances that I've met during these years who made my time unforgettable. Special mention go to all the CCM folks for lunch, viva parties and equipment. There are so many of you that I can't start a full list now, but if you have ever been to a karaoke with me its safe to say that I won't be forgetting you any time soon.

Lastly, the biggest thanks goes to my family, mom, dad and aunt, who made this journey possible with their continuous support. Much love to all of you. Ďakujem!

CONTENTS

ABSTRACT

This thesis extends the recently reported ground state sideband cooling of the axial motion of a single ion to a broader frequency range of the axial motion, the radial motion and ion crystals. Once cold, coherent control of these different configurations is demonstrated.

The experimental work in this thesis uses $^{40}Ca^{+}$ ions that can be coherently addressed on a narrow linewidth optical transition at 729 nm. The technique of axialization that resonantly couples the two radial modes of motion is used to enhance laser Doppler cooling leading to mean phonon occupation numbers in the low hundreds for both modes. The sideband cooling technique is then used to simultaneously cool both the motional modes to within one phonon of the ground state for the first time evers. Sideband cooling is then also employed to cool the axial modes of many ion Coulomb crystals in two different configurations. For two ions in a 1D chain, motional occupation numbers of $\bar{n}_{COM} = 0.30(4)$ and $\bar{n}_B = 0.07(3)$ are achieved. For two ions in a planar 2D configuration the result for the two modes are $\bar{n}_T = \bar{n}_{COM} < 0.1$. This technique is scaled up to demonstrate ground state occupation of up to 10 ions in the planar configuration.

The axial mode of motion of a single motion is used to characterise the coherent addressing capabilities in our system through optical and motional Ramsey spectroscopy. We observe optical coherence times of 1.78(4) ms and motional coherence times of 590(12) ms. Dynamical decoupling techniques are shown to extend these coherence times. Furthermore, basic decoherence models are validated in high-lying non-thermal motional states that are prepared by a sideband heating technique. Progress towards entangling gates is demonstrated using a bichromatic laser beam to prepare non-classical states of motion.

LIST OF FIGURES

LIST OF TABLES

CHAPTER 1

INTRODUCTION

1.1 Motivation and Background

The 20^{th} century witnessed the birth of two monumental achievements of theory and technology: the development of quantum mechanics and the digital computer. These two subjects have become intimately intertwined as the computers of today are filled with technologies that are underpinned by quantum mechanics such as transistors, lasers and semiconductor memory, while the computation power of these devices is indispensable when finding solutions to many quantum mechanical problems. The rapid pace of progress in both fields has been staggering, but some problems in these fields remain intractable such as being able to factor large numbers on a classical computer in sub-exponential time or solving the Schrödinger equation for a system with a large number of interacting particles. The next step in the relationship between these fields is a marriage between the two whereby the unique properties of quantum systems can be used for a digital computing approach that fundamentally changes the domain of possible algorithms, making some problems such as the aforementioned factoring problem tractable [1]. Furthermore, instead of using classical computers to simulate quantum systems, a quantum system over which we have complete control can be used to simulate an analogous system where this is not the case [2]. The applications of such simulations can shed light on many difficult problems within quantum chemistry or solid state physics.

The basic principle behind quantum information processing is that a singe quantum bit (qubit) is described by two complex amplitudes α, β:

$$\alpha|0\rangle + \beta|1\rangle \tag{1.1}$$

where the $|0\rangle, |1\rangle$ state vectors represent two distinguishable states of a quantum system. In contrast to a classical binary bit that is always in a state of on or off (0 or 1) the qubit can reside in a superposition of the two quantum states. These qubits can be read out by a projective measurement which collapses them to one or the other state – where the probability of detecting the qubit in the state of $|0\rangle, |1\rangle$ is given by the square magnitude of the complex amplitudes. The quantum computational power is derived from the fact that two qubits in such superposition states can interact in such a way that the complex amplitudes undergo interference and the resulting detection probabilities are modified. In this sense, quantum computing is a completely different paradigm for performing calculations where the laws of quantum mechanics govern the underlying logic operations as opposed to classical mechanics. In the last few lines, we have identified three prerequisites for quantum information processing: the ability to initialise a

qubit to a known state, the ability to interfere with another qubit to perform a logic operation known as a gate and the ability to individually measure each qubit state. Additional criteria, as proposed by DiVincenzo [3], state that the set of gates must be universal, the system must be scalable to large numbers of qubits and that the coherence time is longer than the time necessary to perform an algorithm. The coherence time in this context defines how long it takes for the quantum information in the complex amplitudes to be lost by interaction with the environment. Very similar criteria must also hold for quantum simulation.

There are many different possible realisations that fulfil these criteria to a varying degree. The work in this thesis will focus on one system in particular that has the potential to fulfil all these criteria: trapped atomic ions at ultra high vacuum that can be coherently manipulated by laser beams. Other implentations will be discussed in section 1.2.

The history of ion traps begins with the Nobel prize winning inventions of two methods to confine charged particles, the Radio Frequency (RF) trap by Wolfgang Paul[4, 5] and the the Penning trap by Hans Dehmelt[6, 7]. In the first case, as the name suggests, radio frequency and static electric fields are used for confinement, whereas in the second a strong static magnetic field replaces the radio frequency fields. While both techniques found success as mass spectrometers, [8, 5, 9, 10] (with Penning traps achieving much higher precisions) the difference in trapping mechanism led to their application paths diverging. Penning traps became the tools of choice for high precision measurement where the large magnetic field is necessary achieving the most precise values of the g-factors of the electron [11], the proton [12] and anti-proton [13] and their charge to mass ratios [14] allowing constraints to be placed on fundamental theories such as quantum electrodynamics or CPT invariance. A review of such applications can be found in references [15, 16]. Furthermore, Penning traps with a large cylindrical geometry are also very useful for trapping non-neutral plasmas. The ability to capture, cool and shuttle a large amount of hot anti-protons in a Penning trap was crucial in the trapping of anti-hydrogen in a magnetic trap, allowing for the first direct spectroscopy of the 1S-2S transition [17] and hyperfine splitting [18].

On the other hand RF traps were preferred in applications where laser addressing of ions was required such as quantum information science and optical frequency standards. While the first laser cooling experiments on clouds of ions were demonstrated in both Penning [19] and RF traps [20] in 1978, it soon became obvious that using Penning traps was much more difficult due to reasons including restricted optical access due to the cumbersome magnets required to generate the large magnetic field, large Zeeman shifts that increase the demands on the laser systems and the inherent difficulty in efficiently cooling both radial modes of motion simultaneously.

RF traps thus stole a march on Penning traps and by 1989 demonstrated the laser sideband cooling technique, bringing a single ion to its ground state in one dimension [21], and by 1995 extending this to all three. In that same year, the proposal by Cirac and Zoller established a quantum computation scheme that used laser addressing of a linear chain of cold ions to perform quantum gate operation using their common modes of motion [22], kick-starting the rapid growth in the field of ion quantum information. The first quantum gate between two ions, producing deterministic entanglement on demand, was then realised in 1998 [23]. Soon after, new types of universal gate interactions were proposed by Mølmer and Sørensen [24, 25] and Milburn *et. al.* [25], with experimental realisations on small number of ions following in the early 2000s [26, 27, 28, 29]. The largest entangling gate to date has been implemented on

a string of 14 ions [30]. The best two qubit gate has reached fidelities of 99.9%[31], which is above the threshold required to implement certain error correction schemes that would allow for scalable digital quantum processor. The focus of cutting edge research is now on improving the robustness [32] and speed [33, 34] of the gate operations.

Using these techniques, various quantum algorithms have already been implemented including the Deutsh-Josza algorithm [35, 36], Grover's algorithm for searching unsorted databases [37, 38] and Shor's algorithm for factoring integers [39]. Experiments have also demonstrated error correcting schemes where multiple qubits define one logical qubit [40, 41, 42] that will certainly be necessary in any useful future implementation of these algorithms. The big challenge remaining is to scale the number of qubits in these systems to be able to show the quantum algorithms outperforming a classical system. The approach of a linear string of ions does not meet this demand as it is unlikely to surpass the 10-100 qubit range due to fundamental limitations [43]. The next generation of trapping architectures is exploring chip surface traps with multiple trapping zones for manipulation and memory [44] between which the ions can be shuttled [45, 46] and swapped around [47], quantum network approaches where individual traps are coupled by photonic fibre links [48] or 2D arrays with microwave based gates [49].

With the established track record in the field what is motivation for pursuing work in this field in a Penning trap? It is evident from the presented history that the RF traps benefited from the early demonstrations of sideband cooling and coherent addressing as a platform upon which to build a toolbox for versatile coherent quantum manipulation. It was just three years ago that our ion trapping group at Imperial College first demonstrated sideband cooling of the axial mode of motion to the ground state [50], overcoming many of the thorny issues with optical access and large Zeeman splitting. The challenge for my PhD was to extend this cooling to encompass all the motional modes of a single ion as well as cooling many ion crystals, while expanding the available toolbox of coherent laser operations to approach parity with RF traps and inspire new theoretical approaches. The main attraction of Penning traps is that for certain confinement strengths, the ions form triangular 2D lattices in the plane perpendicular to the magnetic field without any RF micromotion, which can form the basis of a large quantum register with hundreds of qubits. Proposals for performing entangling gates on the axial modes of these crystals have been appearing over recent years [51, 52, 53] including a scheme for encoding an error protected logical qubit in a six ion crystal [54]. The usefulness in digital quantum computing is currently limited by the fact that these 2D crystals are constantly rotating at ~ 100 kHz about the magnetic field and hence single ion addressing is very difficult to achieve without stroboscopic laser pulsing which restricts interaction time.

On the other hand, in analogue quantum simulation experiments where single ion addressing is not required, Penning traps have excelled. In particular, the Bollinger group at NIST were able to use spin-motional entanglement to perform thermometry on the modes of a large radial crystal of ions in a Penning trap [55] and in the the same year used 300 ion quantum simulator to engineer Ising type interactions between the ions [56]. Varying the strength of the optical dipole force applied to the ions allowed them to tune the effective interaction strength between the ion spins and thus establishing a platform for simulating quantum magnetism [57]. By comparison, quantum simulations on 1D chains in RF traps range in size from a few to approximately 30 ions [58, 59, 60, 61]. The fidelity of the Penning trap quantum simulations is affected due to motion induced spin dephasing since they are only Doppler cooled to a thermal state. The

fidelity could be improved by ground state cooling the ions. This is true in general of almost any experiment that seeks to explore coherent quantum behaviour and is a strong motivation for us to ground state cool these 2D planar crystals. Lastly, a new theory proposal suggests that using just a pair of entangled ions, an analogue version of Shor's algorithm can factor digits orders of magnitude larger than currently achievable with its digital counterpart [62]. By demonstrating the coherent manipulation capabilities in our Penning trap, it is our hope that further ingenious theoretical ideas such as this one will spring forth.

A further point of interest to the community is provided by the unusual characteristics of our trap. Because we operate a large trap with relatively low electric fields, we often work in regimes where the trapping frequencies are quite low compared to experiments in RF traps (Few hundreds of kHz compared to a few MHz). This is especially true in any attempts at cooling two or more ions in an axial string for stability reasons. This leads to us work outside what is called the Lamb-Dicke regime, where the coupling to higher order motional sidebands is not negligible. Traditionally, it was thought that to cool an ion to its ground state, the ion should intially be Doppler cooled to within the Lamb-Dicke regime. Consequently, we have worked on devising efficient cooling methods to show that this is not the case. On the other hand, it allows us to explore coherent control of ions in large quantum harmonic oscillator Fock states ($n > 100$) where we can excite transitions that change the internal motional Fock state up to $\Delta n \leq 7$. To populate these high lying Fock states, we reverse the method of sideband cooling and instead add motional quanta. Looking to the future, we expect to use the current Penning trap setup to explore which parameters are most relevant to achieve effective coherent control outside the Lamb-Dicke regime before moving to a new RF trap where we aim to build schemes for efficient ground state cooling and production of entangled states. While working outside the Lamb-Dicke regime can be challenging, it opens up a chance to perform faster operations since the coupling between the adjacent motional states is enhanced whilst also being protected against heating mechanism [63] and off-resonant excitation [64] when using appropriately designed polychromatic pulse sequences

1.2 Other Quantum Information Platforms

There are two major platforms that compete with trapped ions in fulfilling the DiVincenzo criteria: superconducting qubits and photonic qubits. A superconducting qubit is formed by constructing a resonant inductor-capacitor (LC) circuit from a macroscopic metallic superconductor and a Josephson junction to introduce a desired non-linear coupling. The lowest two energy levels of the anharmonic oscillator formed in this circuit can thus act as a qubit. The physical quantity that actually defines the qubit depends on the architecture. Common realisations include the charge qubit [65], flux qubit [66] or the phase qubit [67]. More complex realisations that improve on these basic realisations such as the transmon, a charge qubit with reduced noise sensitivey, have gained prominence [68]. By adding couplings to microwave cavities, effective multiqubit coupling can be engineered. The field of superconducting qubits has matured very quickly and boasts the ability to satisfy all the of the required DiVincenzo criteria [69] with coherence times in the 100 μs range compared to gate times of 10s of ns allowing for thousands of quantum operations with high fidelity [70]. These properties have attracted large tech companies such as Google, IBM and Intel to the field with the companies claiming to have

built prototype systems consisting of 72, 50 and 49 qubits respectively [71, 72, 73]. Given the large number of qubits, it can appear as though superconducting qubits hold an unassailable lead in the race, but there are other potential bottlenecks such as the fact that the connectivity between qubits is limited to nearest neighbour interactions which can yield lower algorithm fidelities compared to a fully connected implementation such as in trapped ions for the same number of qubits [74]. Superconducting qubits have also been used in quantum simulations [75] with the most recent result being the successful simulation of the BeH_2 molecule [76] using 6 qubits.

Compared to trapped ions and superconducting qubits a photon is in many ways an ideal quantum information carrier since it can transmit a quantum state over large distances without interacting with the environment. Many different single photon encodings are possible, such as polarisation, orbital angular momentum, photon number or arrival time. The downside is that two-photon quantum gates require a non-linear process such as a Cross-Kerr interaction that is difficult to realise [77]. An alternative paradigm called linear optical quantum computing was proposed in 2000 [78] where only simple linear optical elements such as beam splitters, phase shifters or mirrors are used to perform computation in a non-deterministic way in conjunction with single photon sources and detectors. With such a non-deterministic approach, scalability can be difficult as the overhead of photons required to represent one physical qubit and perform entangling operations can grow very large. The leading approach in the field is to now use silica waveguides on silicon chips in integrated photonic circuits [79] demonstrating a factoring of the number 21 using Shor's algorithm [80] and of a 15 qubit entangled state with over 80% fidelity [81]. Outside the academic research lab, startups are also pursuing integrated photonic quantum computing [82, 83]. Photonic quantum information also goes beyond digital computation, especially in quantum communication, which involves quantum cryptography and key distribution. For a recent review of these applications see reference [84].

Besides these two platforms there is a myriad of quantum information processing platforms with varying degrees of maturity. These include, but are not limited to: nuclear-electron spins in doped silicon [85] which have the allure of using well established manufacturing techniques to achieve scalable designs as well as long qubit life times of 30 seconds [86] with work on two qubit gates still in progress [87]; nuclear-electron spins in nitrogen-vacancy or silicon-vacancy centres in diamond, which have been used to perform Grover's search algorithm using two qubits [88] and could be used in modular hybrid architecture with photons mediating interactions in a fibre-connected network of spins [89, 90]; other approaches with neutral atoms include Rydberg atoms in optical lattices [91, 92], but gate fidelities in these systems remain an order of magnitude lower than in the leading technologies.

1.3 Thesis Outline and Context

During the course of the PhD I worked extensively alongside two fellow PhD candidates Manoj Joshi and Vincent Jarlaud, who both started at the same time and were given the same remit to operate the Penning trap experiment. Since we only had a single working Penning trap that was mostly already fully assembled before our arrival and no scope to develop a new system, we worked together on all aspects of day to day running and data acquisition. Given the particularly stringent demands of the experiment on constant monitoring of all equipment,

extended daily maintenance and limited acquisition time, we decided to fully share all our raw experimental data. While each one of us would have overseen different sections of the result depending on their availability at the time and responsibility with other lab related tasks, we were all involved in the design and implementation of experimental protocols and hence we felt that dividing data would be an unfair reflection on the total contribution of each of us. All subsequent analysis was then performed independently by each one of us unless referenced otherwise. With this working structure in place, each one of us took the leading initiative in developing different aspects of the research program. In particular my leading contributions were the development of the analysis models for motional decoherence experiments in chapter 6, the numerical fitting and analysis of experimental results of two ion crystals in chapter 7 and the simulation and experimental implementation of radial Doppler cooling that paved the way for the sideband cooling experiments in chapter 8.

The thesis is structured as follows. Chapter 2 describes the classical and quantum treatment of the motion of ions in a Penning trap. The normal modes of Coulomb crystals are derived from classical principles. Chapter 3 is a brief summary of the particular atomic features of a $^{40}Ca^{+}$ in a Penning trap, including energy level diagrams, Zeeman shifts and geometric factors concerning emission and polarisation.

Chapter 4 begins with the theoretical treatment of a free two level atom in space interacting with a laser beam, which is then extended to include the harmonic trapping potential to obtain the spin-motion coupling Hamiltonian essential for understanding the behaviour of trapped ions interacting with lasers. The next part of the chapter focuses on the Doppler cooling theory with particular detail dedicated to the cooling limits of the radial modes and also contains a brief description of the axialization technique for improving these limits. The final part contains theoretical and numerical results for the limits of the sideband cooling technique which is instrumental in driving the ion to the ground state of motion.

Chapter 5 describes the experimental setup. It begins with a broad overview of the whole system, followed by the descriptions of the trap, the magnet, the lasers, the optical setup, experimental hardware/software control and fluorescence detection. Particular attention is given to the last two sections as they detail the new upgrades to the system which I worked on.

Chapter 6 contains all the experimental results pertaining to cooling and coherent manipulation of a single ion. The chapter begins with sideband cooling and adiabatic cooling results, demonstrating our ability to cool outside the Lamb-Dicke regime. The performance of the optical qubit is then assessed through Rabi oscillations and Ramsey spectroscopy followed by a demonstration of dynamical decoupling to extend the coherence time. The last section is concerned with preparing different motional states and measuring the motional coherence both by characterising the heating rate and the trap frequency stability. The preparation of highly non thermal motional mixed states that exhibit coherence is demonstrated. Finally, the bichromatic laser interaction is used to demonstrate the preparation of non classical coherent and squeezed states.

Chapter 7 presents the experimental results of our efforts to sideband cool ion Coulomb crystals to the ground state. Two different configurations are considered: 2 ions in a 1D chain and up to 15 ions in a 2D planar crystal. Coherent driving and heatings rates are also presented.

Chapter 8 is concerned with cooling the radial motion of a single ion. The first section focuses on a numerical simulation of cooling dynamics and cooling limits for Doppler cooling in the

presence of coupling between two motional modes using the axialization technique. The second section then presents the experimental data of Doppler and sideband cooling demonstrating the first ever simultaneous cooling of both modes to the ground state of motion. Chapter 9 provides a concluding summary of the presented results and discusses their context and implications for future experiments.

CHAPTER 2

ION DYNAMICS IN A PENNING TRAP

The dynamics of trapped charged particles is a well established area of physics and can be found in many reference texts. Included here is a focussed account of the dynamics that give rise to the particular types of motion in a Penning trap. The treatment first begins with classical dynamics and then translates the results to a quantum mechanical picture.

2.1 Limitation of Static Fields

The simplest static electric potential that gives rise to trapping in three dimensions is given by:

$$\phi = (az^2 + bx^2 + cy^2) \tag{2.1}$$

To see why this ideal scenario is not achieved in practice we can invoke Gauss' law, which states that within any volume of space free of any charges the divergence of the field must be zero. Hence the potential must satisfy Laplace's equation:

$$\bigtriangledown^2 \phi = 0 \tag{2.2}$$

It is easy to see that the only way the equation is satisfied upon the substitution of the harmonic potential is that at least one of the coefficients must be negative. Consequently, a trapped particle will always feel a repulsive force in at least one dimension. This fact was originally reported by Earnshaw in 1842 [93]. To overcome this limitation, two approaches exist:

- Introduce time varying radio-frequency potentials, which lead to a time averaged confining force, the approach pioneered by Wolfgang Paul [4] and commonly referred to as the Radio Frequency (RF) or Paul trap.
- Use a static quadrupolar field where a magnetic field is introduced parallel to the static trapping axis. This forms the Penning trap developed by Dehmelt [6].

This thesis will exclusively focus on describing the physics of the Penning trap. For a thorough text covering the principles of RF traps one can consult ref. [94]

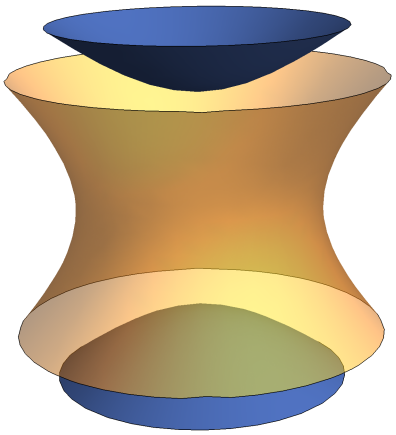

(a) 3D Electrodes

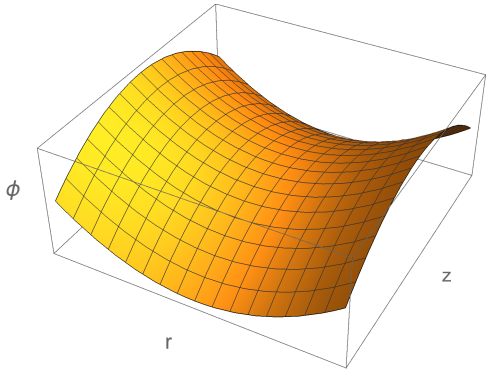

(b) Electric Potential

Figure 2.1: Figure (a) shows the 3D shape of the hyperboloid surfaces giving rise to the saddle potential in two dimensions as seen in figure (b). The r coordinate represents the degenerate x and y coordinates. The two endcaps define the z axis.

2.2 Single Ion in a Penning Trap

The ideal electrode structure[1] of a Penning trap consists of hyperboloid surfaces (eq. 2.1) that create a harmonic potential well in the axial z direction and a potential hill in the radial x and y directions giving rise to a total potential:

$$\phi = \frac{V_0}{R_0^2}(2z^2 - x^2 - y^2) \tag{2.3}$$

$R_0^2 = 2z_0^2 + r_0^2$ is a term encompassing the axial and radial dimension of the trap and V_0 gives the applied voltage. A charged particle in such a potential would quickly exit the trap along the radial plane. Now consider introducing a magnetic field $\underline{B} = [0, 0, B]$ parallel to the z axis. An ionized particle with charge q and moving with velocity $\underline{v}$ is subject to a force given by:

$$\underline{F} = q\underline{B} \times \underline{v} - q \bigtriangledown \phi \tag{2.4}$$

Since $\underline{B} \times \underline{v} = 0$ for motion in the z direction, the equation of motion for a particle of mass M can be simply obtained by substituting 2.3 into 2.4:

$$\ddot{z} + \omega_z^2 z = 0 \tag{2.5}$$

with $\omega_z = \sqrt{4qV_0/MR_0^2}$. Hence the motion is simple harmonic with solution:

$$z(t) = r_z \cos(\omega_z t + \phi_z) \tag{2.6}$$

where ϕ_z is a phase that depends on the initial condition and r_z is the amplitude of motion.

In the radial plane, the motion emerges from the interplay between the electric and magnetic field. An unbounded charged particle moving in a perpendicular magnetic field follows a circular

[1] In practice these ideal hyperboloid surfaces are almost never used due to the difficulty in machining them and the heavily restricted optical access to the trapping region. Instead other geometries that preserve the cylindrical symmetry of the system can be used. This will inevitably introduce some degree of anharmonicity.

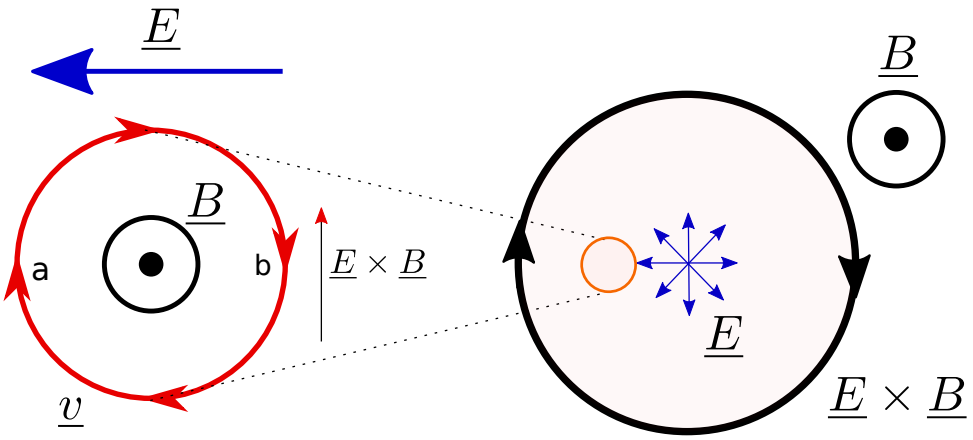

Figure 2.2: On the left, a positively charged particle undergoes cyclotron loops with velocity $\underline{v}$ in the presence of a magnetic field $\underline{B}$ coming out of the page. An electric field $\underline{E}$ (blue) produces an $\underline{E} \times \underline{B}$ precession (black), which acts to oppose the motion at point b while at point a there is an additional force in the direction of its motion. This leads to the cyclotron motion not closing in on itself. The new modified cyclotron motion precesses around the trap centre following the $\underline{E} \times \underline{B}$ drift. The E field is shown to be radially outward from the trap centre.

cyclotron trajectory. In a Penning trap, the presence of the electric field constantly pushes the particle radially outwards. Thus the cyclotron motion no longer forms closed loops, but instead precesses around the trap in the $\underline{E} \times \underline{B}$ direction. This can be seen by calculating this term and observing that it always acts perpendicular to any position vector in the radial orbit (eq. 2.2). The motion arising from this interaction is called the magnetron motion. The frequencies and trajectories can be solved by writing the equation of motion in terms of a single complex variable $u = x + iy$ and once again performing the substitution of 2.3 into 2.4:

$$\ddot{u} + i\dot{u}\omega_c - \frac{\omega_z^2}{2}u = 0 \tag{2.7}$$

where we have introduced the cyclotron frequency $\omega_c = qB/M$. Expecting the resulting motion to be circular, we make the ansatz $u = u_0 e^{i\omega t}$ and find the characteristic equation for ω:

$$\omega^2 - \omega_c\omega + \frac{1}{2}\omega_z^2 = 0 \tag{2.8}$$

This quadratic can be solved to obtain the frequencies

$$\omega_+ = \frac{1}{2}\left(\omega_c + \sqrt{\omega_c^2 - 2\omega_z^2}\right) = \frac{\omega_c}{2} + \omega_1 \tag{2.9}$$

$$\omega_- = \frac{1}{2}\left(\omega_c - \sqrt{\omega_c^2 - 2\omega_z^2}\right) = \frac{\omega_c}{2} - \omega_1 \tag{2.10}$$

ω_+ corresponds to a higher frequency modified cyclotron motion, whereas ω_- corresponds to a lower frequency magnetron motion. The two modes are linked by the cyclotron frequency and the frequency $\omega_1 = \sqrt{\omega_c^2 - 2\omega_z^2}/2$. We can use the fact that the discriminant of ω_1 in the above terms must always stay positive to set a stability limit:

$$2\omega_z^2 \leq \omega_c^2 \tag{2.11}$$

which can define a limit on the trapping parameters:

$$V_0 \leq \frac{qR_0^2B^2}{8M} \tag{2.12}$$

Effectively, this means that for a given magnetic field strength, trap dimension and ion species, there is an upper limit for the applied potential. At this limit the magnetron and modified cyclotron frequencies become degenerate. The axial frequency can be higher or lower than the modified cyclotron frequency, but always remains higher than the magnetron frequency.

Another useful relation is found by summing equations 2.9 and 2.10:

$$\omega_c = \omega_+ + \omega_- \tag{2.13}$$

Thus by careful measurement of these frequencies the true cyclotron frequency can be reconstructed. However, in the presence of a misalignment between the magnetic field vector and the z axis the potential is modified by higher order anharmonic terms resulting in a shift of all the mode frequencies. Despite this, the true cyclotron frequency can still be extracted using the invariance relation:

$$\omega_c^2 = \omega_z^2 + \omega_+^2 + \omega_-^2 \tag{2.14}$$

which is robust against these misalignments to first order [95]. This result is of particular importance for g-factor measurements that require ω_c to be measured to the highest possible precision.

Equation 2.7 can be solved in terms of the magnetron and modified cyclotron amplitudes r_- and r_+ respectively:

$$x(t) + iy(t) = r_-e^{-i(\omega_-t+\phi_-)} + r_+e^{-i(\omega_+t+\phi_+)} \tag{2.15}$$

where the phases ϕ_- and ϕ_+ are included to account for the initial position and velocity of the ion. Now by taking the real and imaginary parts of the above equation and including the axial motion from 2.6 we obtain the Cartesian coordinate trajectories:

$$\begin{aligned} x(t) &= r_- \cos(\omega_-t + \phi_-) + r_+ \cos(\omega_+t + \phi_+) \\ y(t) &= -r_- \sin(\omega_-t + \phi_-) - r_+ \sin(\omega_+t + \phi_+) \\ z(t) &= r_z \cos(\omega_z t + \phi_z) \end{aligned} \tag{2.16}$$

Typical trajectories of this sort are shown in figure 2.3.

It would appear that these solutions give a neat and stable, if not always immediately intuitive, motion that can be easily manipulated. To uncover why this is not quite so, we must look at one further subtlety that complicates the practical research in a Penning trap. Of interest to us is the total energy of the system given by the sum of the average kinetic $E_k = \frac{1}{2}M\underline{v}^2$ and potential $E_p = q\phi(\underline{r})$ energy. Differentiating equations 2.16 to obtain $\underline{v}$ and substituting gives:

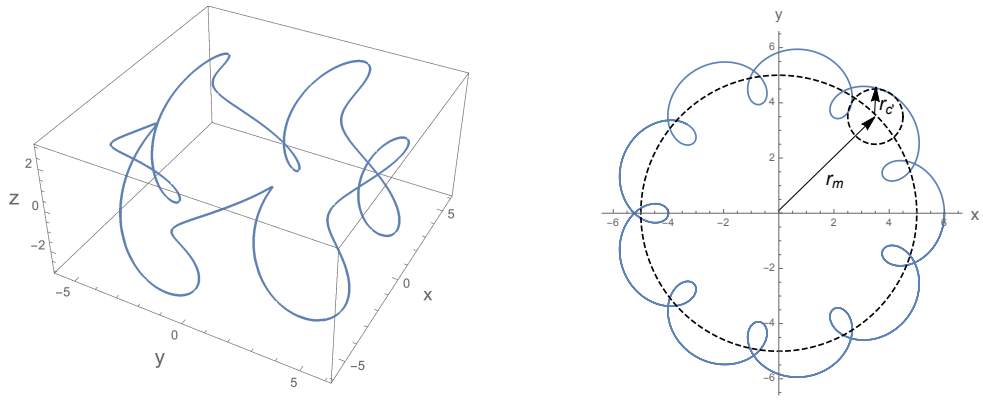

(a) 3D Trajectory **(b)** 2D trajectory at $z = 0$

Figure 2.3: The trajectories of an ion in a Penning trap with parameters $\omega_+ = 10\omega_-$, $\omega_z = 5\omega_-$, $r_z = 3r_+$ and $r_m = 5r_+$

$$\langle E_K \rangle_t = \langle \frac{1}{2} M \underline{v}^2 e \rangle = \frac{1}{2} M \left(\frac{1}{2} r_z^2 \omega_z^2 + r_+^2 \omega_+^2 + r_-^2 \omega_-^2 \right) \tag{2.17}$$

$$\langle E_V \rangle_t = \langle q\phi \rangle = \frac{1}{4} M \left(r_z^2 \omega_z^2 - r_+^2 \omega_z^2 - r_-^2 \omega_z^2 \right) \tag{2.18}$$

Summing the above results, substituting from equations 2.9 and 2.10 and re-expressing in terms of ω_1 the following form for the total energy is obtained:

$$E_T = \langle E_K \rangle_t + \langle E_V \rangle_t = \frac{1}{2} M \left(r_z^2 \omega_z^2 + 2 r_+^2 \omega_+ \omega_1 - 2 r_-^2 \omega_- \omega_1 \right) \tag{2.19}$$

The interesting fact to notice is that the term with magnetron frequency contributes negatively to the total energy. This implies that the magnetron motion is actually unstable. The first consequence of this is that in the presence of any damping, we would expect the orbit to decay in time as the ion loses energy and hence leave the trap. However, the time scale for this process in ultra high vacuum is on the order of weeks to months and thus for all intents and purposes is considered stable. The second consequence is that to reduce the orbital radius (commonly defined as cooling the ion), energy must be added to the magnetron mode. This greatly complicates the standard Doppler cooling techniques that employ a frequency selective cooling force only, since they instead act to increase the magnetron motion radius. Taming this motion was one of the main experimental challenges in this thesis.

Another way to think of this is to remind ourselves that the electric potential in the radial plane is a hill and the magnetic field merely makes the ion perform orbits around it. Thus reducing the orbital radius is akin to pushing a ball all the way to the top of a hill. Methods to deal with this problem will be discussed in sections 4.3.1 and 8.1.2.

2.3 Many ions in a Penning trap

Upon loading or creating charged particles in a Penning trap we may ask what is the general structure that will emerge? The key factor in determining this is the degree to which the ions interact with each other. This property can be parametrised by the Coulomb coupling

parameter Γ:

$$\Gamma = \frac{e^2}{4\pi\epsilon_0 a_{WS} k_B T} \tag{2.20}$$

where the Wigner-Seitz radius $a_{WS}^3 = 3/(4\pi n_0)$ is defined in terms of the particle number density n_0, T is temeperature, e is the unit of fundamental charge and k_B is the Boltzmann constant. This correlation parameter is effectively a ratio of the Coulomb energy to kinetic energy per particle. When $\Gamma \ll 1$ and in the limit that particles are far enough apart to not feel each other's presence, they execute largely independent motion as described in the previous section. Still in the regime $\Gamma \ll 1$, but allowing for weak coupling the ions form a non-neutral plasma. These plasmas, in particular their transport and equilibrium properties, were extensively studied in theory, predicting the formation of spheroids that have near constant density up to a sharp cutoff near the edges. [96, 97]. This was experimentally confirmed with pure electron plasmas [98]. By cooling the surrounding environment with liquid helium to 4K the pure electron plasmas underwent a transition from gaseous to liquid phase where $\Gamma \simeq 2$ [99]. The same transition could be observed with laser cooled trapped ions [100].

By further decreasing the temperature through better laser cooling, a liquid-solid transition occurs for $\Gamma > 170$ [101], forming structures called Coulomb (or Wigner) crystals. Initially, these were studied in the context of large ion crystals ($N > 10^4$), forming a rotating body-centered crystal lattice [102]. Subsequently, large 2D structures forming varied lattice shapes were produced [103]. When the confining axial potential and the number of ions ($N \sim 10^2$) is sufficiently low, 1D chains can form along the magnetic field axis [104] just like chains typically observed in linear RF traps [105]. It is the last two regimes that are of particular relevance to the experimental work in this thesis. The next two sections describe the modes of motion for small 1D chains and 2D planar crystals in a Penning trap.

Before proceeding, we first describe the general approach to finding the modes of any crystal. We begin by writing down the Lagrangian for N ions of mass M:

$$L = \sum_{n=1}^{N} \left[\frac{1}{2} M |\dot{\mathbf{r}}_n|^2 - q\phi_n + q\mathbf{A}_n \cdot \dot{\mathbf{r}}_n \right] \tag{2.21}$$

where $\mathbf{r}_n$ is the n^{th} ion position in Cartesian coordinates, ϕ_n is the total scalar potential including ion-ion Coulomb terms and $\mathbf{A}_n = \frac{1}{2}(\mathbf{B} \times \mathbf{r}_n)$ is the vector potential in the symmetric gauge. Using this Lagrangian one needs to first find the equilibrium separation (position) between all the ions. For special cases such as two ions this can be done analytically, but typically requires either numerically solving coupled equations or finding the minimum energy configuration by numerical optimisation methods [53]. In the next step, a Taylor expansion of the electromagnetic potential is performed around the equilibrium positions $\mathbf{r}_n^{(0)}$ of the ions assuming a small displacement $\mathbf{q}_n(t)$ such that $\mathbf{r}_n(t) \approx \mathbf{r}_n^{(0)} + \mathbf{q}_n(t)$, leading to the motional Lagrangian:

$$L = \sum_{n=1}^{N} \frac{1}{2} M \dot{\mathbf{q}}_n^2 - \frac{1}{2} \sum_{n,m=1}^{N} \mathbf{q}_n \mathbf{q}_m \left[\frac{\partial U}{\partial \mathbf{r}_n \partial \mathbf{r}_m} \right]_{\mathbf{q}_n, \mathbf{q}_m = 0} \tag{2.22}$$

The double partial derivatives can then be explicitly calculated, neglecting any anharmonic terms as they are sufficiently small to induce little error [51]. The derivatives can then be written down as a matrix that can be diagonalised by standard methods to obtain the eigenvalues and

eigenvectors of the motional modes.

2.3.1 1D Ion Chains

The formation of 1D ion chains requires strong confinement in the radial plane and very weak axial confinement. In macroscopic RF traps, typical electrode structures consist of equally spaced parallel linear rods or blades [106] arranged in a square that naturally provide the required geometry. Penning traps, however, tend to have weak radial confinement due to the requirements placed on the strength of the magnetic field. Thus, ion chains can only form at very low axial electric potential and consequently have much lower axial oscillation frequencies (< 200 kHz). In practice this means that they are less stable and more difficult to cool (see section 7.2.1). This restricted our experimental exploration to the axial modes of two ions and hence we limit our discussion to $N = 2$. A general treatment for N ions can be found in reference [107].

From equation 2.21 we can write down the potential energy for two ions:

$$U = \frac{1}{2}M\omega_z^2(z_1(t)^2 + z_2(t)^2) + \frac{e^2}{4\pi\epsilon_0}\cdot\frac{1}{z_1(t) - z_2(t)} \tag{2.23}$$

We also define an appropriate length scale l to clean up the constants and make the rest of the problem dimensionless:

$$l^3 = \frac{e^2}{4\pi\epsilon_0 M\omega_z^2} \tag{2.24}$$

This allows us to define a rescaled position $k_{1,2} = z_{1,2}/l$. Then for small displacements $q(t)$ around the equilibrium position $k_{1,2}^{(0)}$ we have:

$$k_{1,2}(t) = k_{1,2}^{(0)} + q(t) \tag{2.25}$$

Performing the minimisation:

$$\left[\frac{\partial U}{\partial k_{1,2}}\right]_{k_{1,2}=k_{1,2}^{(0)}} = 0 \tag{2.26}$$

yields two coupled equations:

$$\begin{aligned} k_1 - \frac{1}{|k_1 - k_2|^2} &= 0 \\ k_2 + \frac{1}{|k_1 - k_2|^2} &= 0 \end{aligned} \tag{2.27}$$

These equations can be solved to give the equilibrium positions:

$$z_1 = -\left(\frac{1}{2}\right)^{2/3} l \quad , \quad z_2 = \left(\frac{1}{2}\right)^{2/3} l \tag{2.28}$$

The next step is to describe the motion for small displacements from equilibrium. To do this, we perform a Taylor expansion around the equilibrium points leading to the Lagrangian:

$$L = \frac{M}{2}(\dot{q}_1^2 + \dot{q}_2^2) - \frac{\omega_z^2}{2}\sum_{n,m=1}^{2} q_n q_m \left[\frac{\partial U}{\partial k_n \partial k_m}\right]_{q_n,q_m=0} \tag{2.29}$$

Calculating the derivatives explicitly yields a matrix:

$$A = \omega_z^2 \begin{bmatrix} q_1^2\left(1+\frac{2}{|k_1-k_2|}\right) & \frac{-2q_1q_2}{|k_1-k_2|} \\ \frac{-2q_2q_1}{|k_1-k_2|} & q_2^2\left(1+\frac{2}{|k_1-k_2|}\right) \end{bmatrix} \tag{2.30}$$

Now we can simply solve the eigenvalue problem $\det(A-\omega^2 I)=0$ and combining with the results of equation 2.28 we obtain the normal mode frequencies:

$$\omega_1 = \omega_z \quad , \quad \omega_2 = \sqrt{3}\omega_z \tag{2.31}$$

The ω_1 mode corresponds to a centre of mass (COM) motion where the two ions move rigidly together in phase. The higher ω_2 mode corresponds to an out of phase motion where the two ions move apart and then back towards each other; we label this motion the breathing mode. These modes are illustrated in figure 2.4. In this treatment we haven neglected any transverse

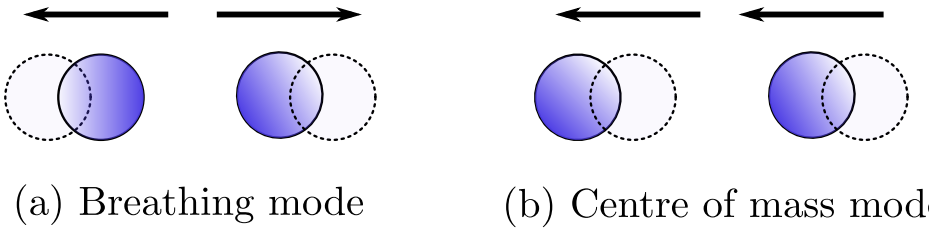

Figure 2.4: (a) The breathing mode at $\omega_B = \sqrt{3}\omega_z$ with the motions of the ions out of phase. (b) Centre of mass mode at $\omega_{COM} = \omega_z$ with the motions in phase

modes because we have experimentally only performed axial spectroscopy of the chain. If we were to repeat the same derivation for the radial modes there would again be an in-phase radial centre of mass motion and an out-of-phase rocking motion in both degrees of freedom.

2.3.2 2D Planar Crystals

The treatment of the planar crystals is complicated by the fact that the crystal rotates as a rigid body around the magnetic field z axis. Thus the natural way to express the potential for these crystals is to transform into a frame of reference that rotates at the same angular velocity ω_r as the crystal. To do this, we introduce a new position vector in the rotating frame $\mathbf{r}'$ defined by:

$$\mathbf{r} = R_z(\theta(t))\mathbf{r}' \tag{2.32}$$

where $R_z(\theta(t))$ is the rotational transformation operator with angle $\theta(t)$. We can then write the operator in terms of the crystal rotation frequency, ω_r:

$$R_z(-\omega_r t) = \begin{bmatrix} \cos(\omega_r t) & \sin(\omega_r t) & 0 \\ -\sin(\omega_r t) & \cos(\omega_r t) & 0 \\ 0 & 0 & 1 \end{bmatrix} \tag{2.33}$$

Under this transformation the crystal Lagrangian 2.21 becomes:

$$L' = \sum_{m=1}^{N}\left[\frac{M}{2}|\dot{\mathbf{r}}'_m|^2 - \frac{eB^{eff}[\omega_r]}{2}(\dot{x}'_m y'_m - \dot{y}'_m x'_m) - e\phi'_m\right] \tag{2.34}$$

where the Lorentz force term appears with an effective axial magnetic field $B^{eff} = B_z - 2\omega_r M/e$ and a new effective potential given by:

$$\phi'_m = V_0(z'_m)^2 + \frac{1}{2}(B_z\omega_r - M\omega_r^2 - V_0)(x'^2 + y'^2) + \frac{e}{8\pi\epsilon_0}\sum_{n\neq m}\frac{1}{|\mathbf{r}'_n - \mathbf{r}'_m|} \tag{2.35}$$

The physical origin of the effective magnetic field is the Coriolis force. While the ions are at equilibrium in the rotating frame, the Coriolis force is absent, however it must be taken into account when calculating the normal modes of the radial motion. A further consequence of the transformation is the appearance of the potential term $M\omega_r^2(x'^2 + y'^2)/2$ that leads to a centrifugal force. It is also helpful to recast the effective potential in terms of the natural frequencies ω_z and ω_c of the trap, giving:

$$\phi'_m = \frac{M}{2e}\omega_z^2 z'^2_m + \frac{M}{2e}(\omega_c\omega_r - \omega_r^2 - \frac{1}{2}\omega_z^2)(x'^2 + y'^2) + \frac{e}{8\pi\epsilon_0}\sum_{n\neq m}\frac{1}{|\mathbf{r}'_n - \mathbf{r}'_m|} \tag{2.36}$$

Now we can clearly identify the second term as an effective trapping frequency in the radial plane $\omega_{eff} = (\omega_c\omega_r - \omega_r^2 - \frac{1}{2}\omega_z^2)^{1/2}$.

To obtain the equilibrium positions in the rotating frame, the effective potential energy must be minimised. Where possible, direct minimisation of the potential:

$$\left[\frac{\partial\phi'}{\partial\mathbf{r}'_m}\right]_{\mathbf{r}_n=\mathbf{r}_n^{(0)}} \tag{2.37}$$

is the simplest method. As for the case of a chain, we can define a dimensionless length scale, but this time with the effective radial frequency:

$$l'^3 = \frac{e^2}{4\pi\epsilon_0 M\omega_{eff}^2} \tag{2.38}$$

Then for a dimensionless position $\mathbf{u}_m = \mathbf{r}_m^{(0)}/l$, the potential minimisation yields 3N equations:

$$\begin{aligned} u_m^x - \sum_{n=1,n\neq m}^{N}\frac{u_m^x - u_n^x}{l_{mn}^3} &= 0 \\ u_m^y - \sum_{n=1,n\neq m}^{N}\frac{u_m^y - u_n^y}{l_{mn}^3} &= 0 \\ u_m^z - \left(\frac{\omega_{eff}}{\omega_z}\right)^2\sum_{n=1,n\neq m}^{N}\frac{u_m^z - u_n^z}{l_{mn}^3} &= 0 \end{aligned} \tag{2.39}$$

where $l_{mn} = \sqrt{(u_n^x - u_m^x)^2 + (u_n^y - u_m^y)^2 + (u_n^z - u_m^z)^2}$ is the dimensionless ion distance. When dealing with 2D crystals, we can assume that $\omega_z \gg \omega_{eff}$ hence the u_m^z terms are zero. The $2N$ coupled equations can be solved numerically, though their solutions are not unique. Different solutions usually correspond to unstable equilibrium points. For example, $N = 4$ ions can be arranged in a square or in a triangle with one ion at its centre. The latter configuration, however, is unstable and only represents a saddle point or local minimum in the potential. Thus the strategy employed in this thesis is to numerically find a set of stable positions based on a randomised initial guess for the positions, calculate the potential energy and iterate the process

until the lowest energy solution is found.

To find the normal modes, we must analyse the behaviour of the ions displaced from equilibrium. We define a small displacement $\mathbf{q}_m(t)$ in the coordinates of the rotating frame where $\mathbf{r}'_m(t) = \mathbf{r}'^{(0)}_m + \mathbf{q}_m(t)$. This allows us to Taylor expand the potential to second order in $\mathbf{q}_m(t)$:

$$L = L_0 + \frac{M}{2}\sum_{m=1}^{N}\dot{\mathbf{q}}_m^2 - \frac{1}{2}\sum_{m,n=1}^{N}\mathbf{q}_m \cdot \mathbf{q}_n \left[\frac{\partial \phi'}{\partial \mathbf{r}'_m \partial \mathbf{r}'_n}\right]_{\mathbf{q}_m=\mathbf{q}_n=0} \tag{2.40}$$

By inspecting this equation we can see that there is no coupling between the axial and radial modes in this harmonic expansion, which will allow us to treat these degrees of freedom as separable. This follows from the cylindrical symmetry of the trapping potential and the fact that the Lorentz force due to the B field acts only in the radial plane. Coupling could occur in the presence of significant anharmonicity, but this contribution will be very small. Since we are interested in the axial phonon modes only, the motional Lagrangian simplifies to:

$$L^z = \frac{M}{2}\sum_{m=1}^{N}(\dot{\mathbf{q}}_m^z)^2 - \frac{M\omega_{eff}^2}{2}\sum_{m,n=1}^{N}K_{mn}q_m^z q_n^z \tag{2.41}$$

where the stiffness matrix $\mathbf{K}$ is a real, symmetric, Hermitian matrix with elements:

$$K_{mn} = \begin{cases} \left(\frac{\omega_z}{\omega_{eff}}\right)^2 - \sum_{p=1,p\neq m}^{N}\frac{1}{\left[(u_n^x-u_p^x)^2+(u_n^y-u_p^y)^2\right]^{3/2}} & (m=n), \\ \frac{1}{\left[(u_m^x-u_n^x)^2+(u_m^y-u_n^y)^2\right]^{3/2}} & (m\neq n). \end{cases} \tag{2.42}$$

The axial normal mode frequencies come out from the solutions of the eigenvalue problem:

$$\sum_{k=1}\left[\omega_{z\nu}^2\delta_{jk} - K_{mn}\right]b_k^{z\nu} = 0, \quad j\nu = 1,2...,N \tag{2.43}$$

with eigenvectors $b_k^{z\nu}$. Thus the frequencies can be calculated using the scaled equilibrium coordinates found from solving 2.39, giving $\omega_{z\nu} = \sqrt{\mu_z}\omega_{eff}$, where μ_z are the eigenvalues of the stiffness matrix. The largest eigenvalue is always one corresponding to the centre of mass motion and successive eigenvalues lead to lower frequency modes. It is important to note that all the calculated frequencies should be real. If this is not the case, the crystal configuration is an unstable equilibrium [108] . This provides a useful check on the result of the equilibrium position calculations. The realness of the eigenvalues can also be used to check if this particular combination is stable at a given rotation frequency and used to find the onset of a a transition to a 3D crystal [109]. In general, it is easiest to solve the eigenvalue problem numerically, but there is a special case of the tilt mode that has a simple analytical expression given by:

$$\omega_{z2} = \sqrt{\omega_z^2 - \omega_{eff}^2} \tag{2.44}$$

2.4 Quantum dynamics

2.4.1 Single Ion

We first begin by writing down the classical Hamiltonian of a singly ionised particle of mass M in a Penning trap:

$$H = \frac{(\mathbf{p} - e\mathbf{A})^2}{2M} + e\phi \tag{2.45}$$

$$= \frac{\mathbf{p}^2}{2M} - \frac{\omega_c}{2}(p_y x - p_x y) + \frac{M}{2}\omega_1^2(x^2 + y^2) + \frac{M\omega_z^2 z^2}{2} \tag{2.46}$$

where we have chosen the symmetric gauge $\mathbf{A} = (\mathbf{B} \times \mathbf{r})/2$. To further simplify the expression and remove the cross-coupling terms. the following coordinate transformation is useful:

$$q_\pm = \frac{1}{\sqrt{2}}\left[(M\omega_1)^{1/2}x \mp (M\omega_1)^{-1/2}p_y\right], \quad p_\pm = \frac{1}{\sqrt{2}}\left[\pm(M\omega_1)^{1/2}y + (M\omega_1)^{-1/2}p_x\right] \tag{2.47}$$

The axial motion can also be written in the scaled coordinates using the transformation:

$$q_z = \sqrt{M\omega_z}z, \quad p_z' = \frac{p_z}{\sqrt{M\omega_z}} \tag{2.48}$$

The new Hamiltonian now takes the form

$$H = \frac{\omega_-}{2}(q_+^2 + p_+^2) - \frac{\omega_+}{2}(q_-^2 + p_-^2) + \frac{\omega_z}{2}(q_z^2 + p_z'^2) \tag{2.49}$$

Once again we are reminded of the fact that the magnetron term is negative just as in the total energy contribution in equation 2.19. The other important observation is that the Hamiltonian consists of three decoupled harmonic oscillators for which we can construct solutions by standard quantum mechanical methods following [94]. The generalised coordinates satisfy the Poisson bracket $\{q_i, p_j\} = \delta_{ij}$ for $i, j = (+, -, z)$ and thus can be converted to quantum mechanical operators by satisfying the commutation relation $[\hat{q}_i, \hat{p}_j] = i\hbar\delta_{ij}$. Hence we can use this commutator to define ladder operators of the form:

$$\hat{a}_i = \frac{\hat{q}_i}{\sqrt{2\hbar}} + \frac{i\hat{p}_i}{\sqrt{2\hbar}} \tag{2.50}$$

$$\hat{a}_i^\dagger = \frac{\hat{q}_i}{\sqrt{2\hbar}} - \frac{i\hat{p}_i}{\sqrt{2\hbar}} \tag{2.51}$$

where $\hat{a}_i^\dagger$ and $\hat{a}_i$ are the raising and lowering operators respectively. We can now write the quantum mechanical Hamiltonian in terms of these operators:

$$\hat{H} = \hbar\omega_+\left(\hat{a}_+^\dagger\hat{a}_+ + \frac{1}{2}\right) - \hbar\omega_-\left(\hat{a}_-^\dagger\hat{a}_- + \frac{1}{2}\right) + \hbar\omega_z\left(\hat{a}_z^\dagger\hat{a}_z + \frac{1}{2}\right) \tag{2.52}$$

The Hilbert space of the system is given by $\mathcal{H} = \mathcal{H}_+ \otimes \mathcal{H}_- \otimes \mathcal{H}_z$ hence we can write the energy eigenstate vector in the number (Fock) basis as $|n_+\rangle \otimes |n_-\rangle \otimes |n_z\rangle = |n_+, n_-, n_z\rangle$. This leads to the Schrödinger equation

$$\hat{H}|n_+, n_-, n_z\rangle = (E_+ - E_- + E_z)|n_+, n_-, n_z\rangle \tag{2.53}$$

with the energies given by:

$$E_+ = \hbar\omega_+\left(n_+ + \frac{1}{2}\right), \quad E_- = -\hbar\omega_-\left(n_- + \frac{1}{2}\right), \quad E_z = \hbar\omega_z\left(n_z + \frac{1}{2}\right) \tag{2.54}$$

The raising and lowering operators behave accordingly to standard rules, for example

$$\hat{a}_+^\dagger|n_+, n_-, n_z\rangle = \sqrt{n_+ + 1}|n_+ + 1, n_-, n_z\rangle \tag{2.55}$$

$$\tag{2.56}$$

$$\hat{a}_+|n_+, n_-, n_z\rangle = \sqrt{n_+}|n_+ - 1, n_-, n_z\rangle \tag{2.57}$$

and likewise for the other modes. For completeness we also include the full wavefunction solution. This can be done following the method in [110] by promoting all the position and momentum variables in 2.46 to operators and solving the Schrödinger equation in cylindrical coordinates (r, θ, z) where $x = r\cos(\theta)$ and $y = r\sin(\theta)$ to obtain:

$$\psi(r,z)_{k,j,m_j} = \frac{1}{\pi^{3/4} r_0 z_0^{1/2}}\left(\frac{j!}{2^k k!(j+|m_j|)!}\right)^{1/2}\left(\frac{r}{r_0}\right)^{|m_j|} L_j^{|m_j|}\left(\frac{r^2}{r_0^2}\right) H_k\left(\frac{z}{z_0}\right) e^{-\left(\frac{z^2}{2z_0^2}\right)-\left(\frac{r^2}{2r_0^2}\right)+im_j\theta} \tag{2.58}$$

where k, j, m_j are integers related to the radial quantum numbers by $n_+ = j + \frac{1}{2}(|m_j| - m_j)$, $n_- = j + \frac{1}{2}(|m_j| + m_j)$, $k = n_z$, H_k are Hermite polynomials and $L_j^{|m_j|}$ are generalised Laguerre polynomials. The constants $r_0 = \sqrt{\frac{\hbar}{m\omega_1}}$ and $z_0 = \sqrt{\frac{\hbar}{m\omega_z}}$ give the ground state wavefunction length scale for the radial and axial axes respectively.

We can also write the position operators in terms of the ladder operators:

$$\hat{x} = \frac{r_0}{2}\left(\hat{a}_+ + \hat{a}_+^\dagger + \hat{a}_- + \hat{a}_-^\dagger\right) \tag{2.59}$$

$$\hat{y} = \frac{r_0}{2i}\left(\hat{a}_+ - \hat{a}_+^\dagger - \hat{a}_- + \hat{a}_-^\dagger\right) \tag{2.60}$$

$$\hat{z} = \frac{z_0}{\sqrt{2}}\left(\hat{a}_z + \hat{a}_z^\dagger\right) \tag{2.61}$$

Using these expressions we can calculate the expectation value of the coordinate variance:

$$\langle\hat{z}^2\rangle = z_0^2\left(n_z + \frac{1}{2}\right) \tag{2.62}$$

$$\langle\hat{y}^2\rangle + \langle\hat{x}^2\rangle = r_0^2\left[\left(n_+ + \frac{1}{2}\right) + \left(n_- + \frac{1}{2}\right)\right] \tag{2.63}$$

Finally, by comparison with the classical kinetic energy equation 2.17 we can relate the classical amplitudes to the quantum numbers by:

$$r_z^2 = 2z_0^2\left(n_z + \frac{1}{2}\right) \tag{2.64}$$

$$r_+^2 = r_0^2\left(n_+ + \frac{1}{2}\right) \tag{2.65}$$

$$r_-^2 = r_0^2\left(n_- + \frac{1}{2}\right) \tag{2.66}$$

2.4.2 Coulomb Crystals

The analysis of the previous section extends naturally to the case of larger Coulomb crystals. Since we only consider the axial modes in the absence of anharmonicity for linear chains and planar crystals, the modes are completely uncoupled. This is not true for arbitrary 3D crystals. As before, we must define the canonically conjugate variables. We first set the small displacement coordinate from 2.40 to $q_j(t) = \sum_\nu \chi_\nu(t) b_j^{z\nu}$ where χ_ν are real generalised coordinates. This allows the axial mode Lagrangian from 2.41 to be recast as:

$$L_\nu^A = \frac{M}{2} \sum_\nu^N \left[\dot{\chi}^2 - \omega_{z\nu}^2 \chi^2\right] \tag{2.67}$$

The generalised momentum for the ν phonon mode can now be written as

$$P_\nu^A = \frac{\partial L^A}{\partial \chi_\nu} = M\dot{\chi}_\nu \tag{2.68}$$

The Hamiltonian for the axial modes can now be written down as a simple summation of N uncoupled harmonic oscillators

$$H^A = \sum_{\nu=1}^N \left[\frac{P_\nu^{A2}}{2m} + \frac{1}{2} M\omega_{z\nu}^2 \chi_\nu^2\right] \tag{2.69}$$

Using the same quantisation principle as in the previous section for a single ion, the generalised coordinates are promoted to operators obeying $[\chi_\nu, P_\nu^A] = i\hbar\delta_{\nu\nu}$ and raising and lowering operators are defined as

$$\hat{a}_{z\nu} = \sqrt{\frac{M\omega_{z\nu}}{2\hbar}} \left(\chi_\nu + \frac{i}{m\omega_{z\nu}} P_\nu^A\right) \tag{2.70}$$

$$\hat{a}_{z\nu}^\dagger = \sqrt{\frac{M\omega_{z\nu}}{2\hbar}} \left(\chi_\nu - \frac{i}{m\omega_{z\nu}} P_\nu^A\right) \tag{2.71}$$

Thus the final Hamiltonian takes the very simple form

$$\hat{H}^A = \sum_{\nu=1}^N \hbar\omega_{z\nu} \left(\hat{n}_{z\nu} + \frac{1}{2}\right) \tag{2.72}$$

where $\hat{n}_{z\nu} = \hat{a}_{z\nu}^\dagger \hat{a}_{z\nu}$ is the number operator of the ν^{th} phonon mode. Thus each mode comes with its own ladder of equally spaced energy levels where the separation in energy is only governed by the mode frequency.

CHAPTER 3

THE CALCIUM ION

This chapter will briefly introduce the ion species used in the experimental work presented in this thesis. In particular, the energy level structure in the presence of a strong magnetic field required to operate the trap, branching ratios, emission and absorption patterns will be described. These components are essential to quantitatively treat the processes of laser cooling and coherent manipulation of ions in a Penning trap.

3.1 Choosing an ion. Why Calcium?

The primary consideration when selecting an ion for coherent manipulation and quantum information/simulation purposes is that it is amenable to the well established techniques of Doppler and sideband cooling, thus implying it has a suitable set of transitions that can form (with the possible aid of repump lasers) a closed cooling cycle that scatters photons at a sufficient rate. The typical ions of choice are usually the Alkali-Earth metals since, when singly ionized, they retain one valence electron in their outer shell and thus have 'hydrogen-like' level structure. There are also alternatives elsewhere in the periodic table such as cadmium, ytterbium or mercury. Selecting a suitable element and corresponding isotope from amongst these candidates depends on the needs and means of the experiment. We can separate these into categories:

- The laser cooling transitions are addressable with a set of lasers. Consideration here has to be given to the commercial availability of such laser systems, their price, output power, as well as to the availability of optical components and detectors at the required wavelengths
- There is a pair of accessible energy levels that can be used as a two level qubit to store quantum information. The upper state needs to have a long lifetime and coherent population transfer between the two states should be possible.
- Charge to mass ratio e/m limits the size of the stability region at a fixed magnetic field (equation 2.11). Increasing this ratio allows for higher axial trapping frequencies, which can be beneficial for improving the ease with which the ions can be cooled.

The choice $^{40}Ca^{+}$ was historically made by the group in the previous decade mainly on the grounds of satisfying the first two points, namely having all the necessary transitions for Doppler cooling and repumping accessible with relatively cheap solid state diode lasers. $^{40}Ca^{+}$ also has a narrow linewdith $\Gamma = 2\pi \times 0.136$ Hz dipole forbidden transition at 729 nm, which can be used as an optical qubit that can be addressed with a suitably narrow linewidth solid state laser. The e/m ratio is moderate, but still requires the use of a few tesla magnetic field to reach useful

axial trapping frequencies in the $\sim$ 100s of kHz range. An alternative species used in other Penning trap experiments, $^9Be^+$, improves on the ratio by a factor of three, but does not have a quadrupole transition that can be used as an optical qubit. Instead, one would need to use pairs of Raman laser beams to drive transitions between hyperfine levels of the ground state to have appreciable motion-spin coupling necessary for sideband cooling. The wavelength of 313 nm required the use of dye lasers in the past, but more recently solid state alternatives have been developed [111].

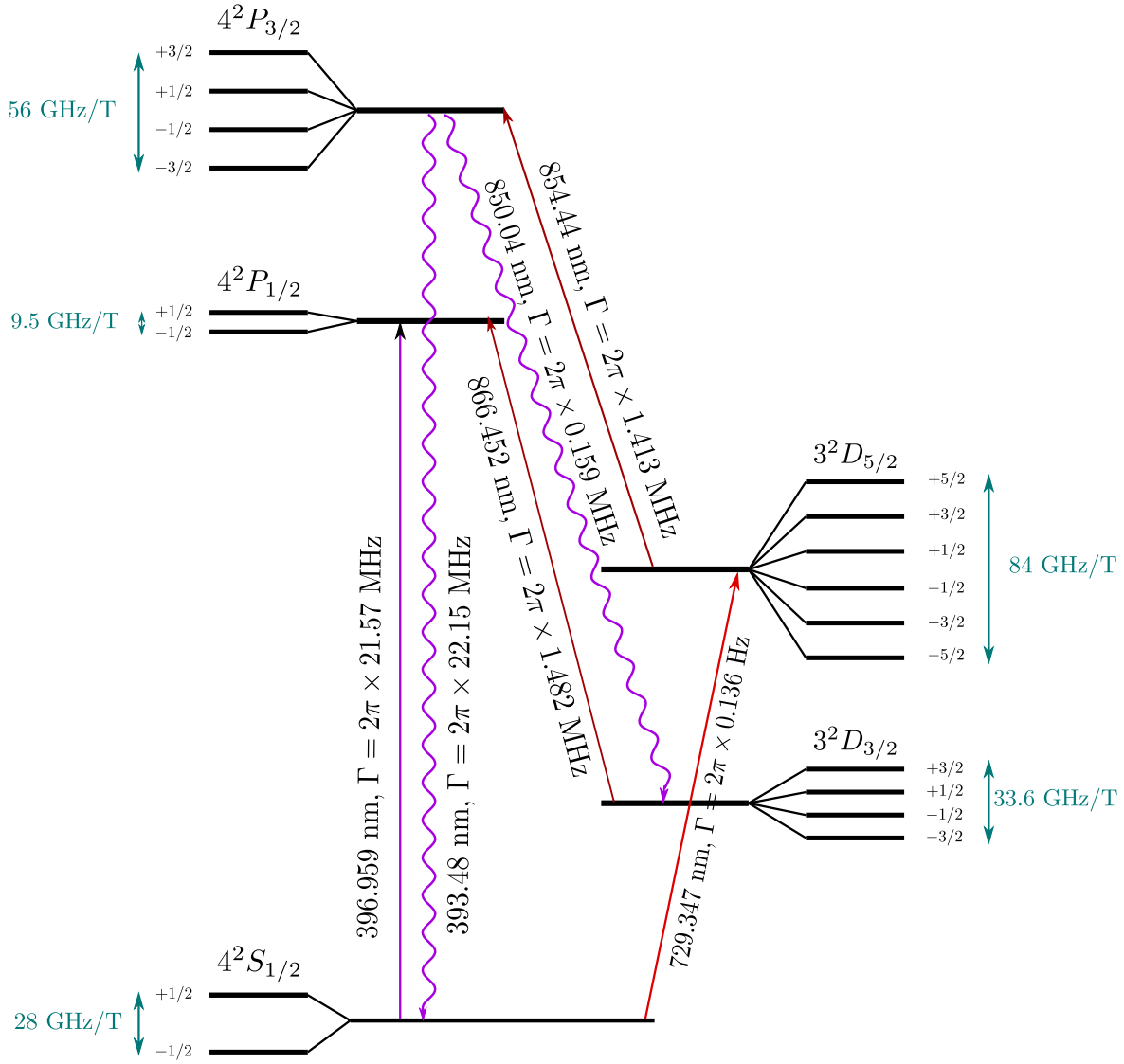

Figure 3.1: Energy levels and relevant transitions of $^{40}Ca^+$ with Zeeman splittings included to scale. The transitions that are addressed by lasers in our experiment are shown with straight lines, whereas the squiggly transitions are not. Where possible, the latest experimental values were taken for the wavelengths and linewidths. [1]

Figure 3.1 shows the energy levels and transitions relevant to our experiment. Ignoring the Zeeman splitting for one moment, we can summarize the role of each of the states and transitions in our experiment. First, the $S_{1/2} \leftrightarrow P_{1/2}$ dipole allowed transition at 397 nm is suitable for Doppler cooling and fluorescence detection of the internal ion states. Decay on the $P_{1/2} \leftrightarrow D_{3/2}$ transition at 866 nm occurs 6.43% of the time, hence a constant repumping laser

[1] Exp: λ_{729}, Γ_{729} [112],λ_{397} [113],λ_{866} [114], $\Gamma_{397}, \Gamma_{393}, \Gamma_{397}$ [115]. Th: $\lambda_{393}, \lambda_{854}, \lambda_{850}, \Gamma_{854}, \Gamma_{850}$ [116]

is required to close the cooling cycle. The aforementioned quadrupole transition $S_{1/2} \leftrightarrow D_{5/2}$ at 729 nm forms the optical qubit and its narrow linewidth of $2\pi \times 0.136$ Hz makes it suitable to resolve motional sidebands, a requirement for performing sideband cooling to the motional ground state. To accelerate this cooling process a quench laser at 854 nm on the $D_{5/2} \leftrightarrow P_{3/2}$ transition followed by fast decays on the 393 nm or 850 nm transitions brings the ion back into the cooling cycle.

3.2 Magnetic field effects

3.2.1 Zeeman Shifts

Returning to the large Zeeman splittings that are induced by the ~ 1.9 T field used in our experiment, the picture gets more complicated. The splitting between the subleveles $S_{1/2,-1/2}$ and $S_{1/2,+1/2}$ of 53.2 GHz means we now require two separate lasers for Doppler cooling out of these Zeeman sublevels. If we now consider the same scenario for the $D_{3/2}$ manifold we might naively think that we would require a further 4 laser frequencies. Furthermore, the large magnetic field mixes states of the same j quantum number meaning that forbidden transitions between $P_{1/2} \rightarrow D_{5/2}$ become weakly allowed, potentially requiring 6 further frequencies of repumping. In fact, in our experiment we manage to synthesize all the required frequencies by passing both 854 and 866 nm beams through the same Electro-optical modulator (EOM) to create sideband frequencies that pump out all levels. In the following calculations we will show how this is possible by defining all the first and second order Zeeman shifts as well as explaining the consequences of j-mixing.

To find the Zeeman shifts, we employ the framework of perturbation theory. We have a perturbing Hamiltonian describing the magnetic field B_z interacting with the spin S_z and angular momenta L_z:

$$H_Z = \frac{\mu_B}{\hbar}\left(g_l L_z + g_s S_z\right) \tag{3.1}$$

where μ_B is the Bohr magnetorn and the g-factors for the angular momentum and spin are $g_l = 1$ and $g_s \approx 2$. For the first order shift, we simply need to consider the matrix element of the perturbation acting on the unshifted electronic energy states $n^{(0)}$ giving:

$$E_n^{(1)} = \frac{\mu_B B_z}{\hbar}\langle n^{(0)}|\left(L_z + 2S_z\right)|n^{(0)}\rangle = \mu_B g_j B_z m_j \tag{3.2}$$

with the answer in terms of the Lande g-factor $g_j = \frac{j(j+1)-s(s+1)+l(l+1)}{2j(j+1)} + 2\frac{j(j+1)+s(s+1)-l(l+1)}{2j(j+1)}$. The result shows a linear dependence on the magnetic field, with the m_j sublevels split equally. The total width of the manifolds per tesla is shown in figure 3.1. We are also interested in the effect of the second order Zeeman shift given by:

$$E_n^{(0)} = \sum_{m \neq n} \frac{\mu_B^2 B_z^2 |\langle m^{(0)}|(L_z + 2S_z)|n^{(0)}\rangle|^2}{\hbar^2\left(E_n^{(0)} - E_m^{(0)}\right)} \tag{3.3}$$

In this case there is a sum over all the other unperturbed states. A direct evaluation of the matrix elements is not practical, but can instead be performed through an expansion in terms of the Clebsch-Gordan coefficients. This allows us to re-express states of the form $|j, m_j\rangle$ in

Manifold	m_j	1 st order (GHz/T)	2 nd order (MHz/T^2)
$S_{1/2}$	$\pm\frac{1}{2}$	± 14.00	0
$P_{1/2}$	$\pm\frac{1}{2}$	± 4.67	-6.52
$P_{3/2}$	$\pm\frac{1}{2}$	± 9.33	$+6.52$
	$\pm\frac{3}{2}$	± 27.99	0
$D_{3/2}$	$\pm\frac{1}{2}$	± 5.60	-25.9
	$\pm\frac{3}{2}$	± 16.80	-17.3
$D_{5/2}$	$\pm\frac{1}{2}$	± 8.40	$+25.9$
	$\pm\frac{3}{2}$	± 25.19	$+17.3$
	$\pm\frac{5}{2}$	± 41.99	0

Table 3.1: Table of first and second order Zeeman shifts for $^{40}Ca^+$

the basis $|l, m_l, s, m_s\rangle$. The full set of Clebsch-Gordan coefficients is given in reference [117][2]. Looking at the states in the expanded basis, we see that the overlap can only be non-zero for the case where states have the same l and m_j quantum numbers, but different j i.e. $D_{5/2,+3/2}$ and $D_{3/2,+3/2}$ or $P_{1/2,-1/2}$ and $P_{3/2,-1/2}$. This leaves all the sublevels in the S manifold unshifted as well as the outermost ones of the $P_{3/2}$ and $D_{5/2}$ manifolds. The shifts are now quadratically proportional to B, but are no longer directly proportional to m_j hence the sublevels will no longer be equally spaced. Table 3.1 summarizes the first order and second order Zeeman shifts. We can see that the pairs of states with the same l and m_j get pushed symmetrically apart. The implication of the asymmetric shift and non-linear shift of sublevels within the D manifolds means that it is not possible to address all the states resonantly with a comb of equally spaced frequencies. What we do, however, see is that the magnitude of the differential shifts between the repumping transitions from $D_{3/2} \rightarrow P_{1/2}$ and $D_{5/2} \rightarrow P_{3/2}$ at 1.89 T is only around 20-30 MHz, meaning that with sufficient power in the repumping lasers, we can still address these states off-resonantly and achieve the required repumping rates. The specific method and setting of the EOM frequencies will be discussed in section 5.3.2.

3.2.2 j-Mixing

A further effect of the second-order perturbation theory result is that the eigenstates are modified by:

$$|n^{(1)}\rangle = \sum_{m \neq n} \frac{\mu_B B_z \langle m^{(0)}| \left(L_z + 2S_z\right) |n^{(0)}\rangle}{\hbar \left(E_n^{(0)} - E_m^{(0)}\right)} |m^{(0)}\rangle \tag{3.4}$$

This equation has the same matrix elements as 3.3 and hence we know that the states that share the same l and m_j, but different j get mixed, hence the designation 'j-mixing '. The presence of an admixture of a different state affects the transition probability in a striking way. Under no magnetic field, the transition $P_{1/2} \leftrightarrow D_{5/2}$ is strongly dipole forbidden, but since the new $P_{1/2}$ eigenstates will have a small admixture of their $P_{3/2}$ counterparts and likewise for $D_{5/2}$

[2]There is a typographical error: the $S_{1/2,-1/2} \rightarrow D_{5/2,-3/2}$ coefficient should be $-\sqrt{\frac{4}{15}}$

and $D_{1/2}$ the transition becomes weakly allowed. To find the magnitude of this effect, we find the transition element matrix:

$$|\langle D^{(1)}_{5/2}|\hat{\mathbf{d}}\cdot\mathbf{E}|P^{(1)}_{1/2}\rangle|^2 \approx |\epsilon_D\langle D^{(0)}_{3/2}|\hat{\mathbf{d}}\cdot\mathbf{E}|P^{(0)}_{1/2}\rangle + \epsilon_P\langle D^{(0)}_{5/2}|\hat{\mathbf{d}}\cdot\mathbf{E}|P^{(0)}_{3/2}\rangle|^2 \tag{3.5}$$

where $\hat{\mathbf{d}}\cdot\mathbf{E}$ is the atomic dipole moment operator, ϵ_P, ϵ_D are the prefactors from 3.3 and we have ignored the term of order $\epsilon_P \times \epsilon_D$. Using these matrix elements, calculations have been performed [118] to find the branching ratio:

$$\frac{\Gamma(P_{1/2} \to D_{5/2})}{\Gamma(P_{1/2} \to S_{1/2})} = 4.2 \times 10^{-7} B^2 \tag{3.6}$$

For the field strength of $B = 1.89$ T we thus expect an average of 0.67×10^6 photons scattered on the cooling transition before decaying to the dark $D_{5/2}$ state. For any period of continuous illumination it is evident that the $D_{5/2}$ state will have to be repumped. Even for a modest scattering rate $\Gamma_{397}/10$ the ion will decay to the dark state in a mean time of 50 ms. For typical cooling times of 10 ms used in our experimental sequence we would expect the decay $\approx 20\%$ of the time. Hence for any cooling process the repumping is also inevitable. We also note that even though j-mixing decay from $S_{1/2}$ only occurs to the central four states of the $D_{5/2}$ manifold, after repumping to the $P_{3/2}$ decays to the $\pm 5/2$ Zeeman sublevels can occur, hence all 6 states must be addressed by the laser.

A more serious problem is when we are not free to use the repump laser. We often use one of the $D_{5/2}$ Zeeman sublevels as an upper state of an optical qubit. After conducting some form of coherent operation we perform a projective measurement by driving the $S_{1/2} \leftrightarrow P_{1/2}$ transition and observing fluorescence. The absence of the fluorescence distinguishes the population in the 'dark' $D_{5/2}$ state from that in the the 'bright' $S_{1/2}$ state. However, if a j-mixing induced decay from the cooling cycle to the $D_{5/2}$ occurs early within the detection period, the collected fluorescence data will appear as a false positive for the dark state. Thus at a given scattering rate, the j-mixing rate provides a limit to the length of fluorescence collection and affects the quality of state discrimination.

3.3 Emission, polarisation and geometry

An important part of addressing and observing the ion is to familiarise ourselves with the spontaneous emission distributions, the absorption probabilities and the required polarisation to drive different transitions. There are two disadvantages particular to our Penning trap setup: limited optical access due to the positioning of the trap inside the superconducting magnet and the presence of the axial magnetic field defining a quantization axis parallel to the trapping axis. In RF trap experiments, laser beams can often be pointed at various angles and a weak magnetic field can be used to define a quantization axis that is suitable for stimulating any desired transition whereas we do not have this freedom. Later in this section we will see the consequences on our ability to address certain transitions.

From standard time dependent perturbation theory, following the method of ref [107] we can write down excitation rates for electric dipole and quadrupole transitions between $|g\rangle \to |e\rangle$

respectively:

$$\Omega^{E1} = \left| \frac{eE}{\hbar} \langle g|\hat{r}_i|e\rangle \epsilon_i \right| \tag{3.7}$$

$$\Omega^{E2} = \left| \frac{eE\omega_g e}{2\hbar c} \langle g|\hat{r}_i\hat{r}_j|e\rangle \epsilon_i n_k \right| \tag{3.8}$$

$$\tag{3.9}$$

defined in terms of the atomic electron position operator r_i interacting with a laser of electric field E, propagation vector n_k and polarisation vector ϵ_i where the indices are summed over the Cartesian coordinates. The matrix elements can be rewritten in terms of irreducible spherical tensors $C_q^{(k)}$ in the spherical harmonic basis $c_i^{(q)}$ (defined in appendix of reference [107]):

$$\langle g|\hat{r}_i|e\rangle \epsilon_i = \sum_{q=-1}^{1} \langle g|rC_q^{(1)}|e\rangle c_i^{(q)} \epsilon_i \tag{3.10}$$

$$\langle g|\hat{r}_i\hat{r}_k|e\rangle \epsilon_i n_k = \sum_{q=-2}^{2} \langle g|r^2 C_q^{(2)}|e\rangle c_{ik}^{(q)} \epsilon_i n_k \tag{3.11}$$

In the $L-S$ coupled basis, the states $|g\rangle = |j, m_j\rangle$ where j is the total angular momentum and m_j is the magnetic quantum number of the lower state, and the primed terms are the corresponding quantum numbers for the excited state. Using the Wigner-Eckhart theorem, the matrix elements can be expressed in terms of reduced matrix elements and Wigner $3-j$ symbols:

$$\langle j, m_j|\hat{r}_i|j', m_j'\rangle \epsilon_i = \langle j, m_j||rC^{(1)}||j', m_j'\rangle \sum_{q=-1}^{1} \begin{pmatrix} j & 1 & j' \\ -m_j & q & m_j' \end{pmatrix} c_i^{(q)} \epsilon_i \tag{3.12}$$

$$\langle j, m_j|\hat{r}_i\hat{r}_k|j', m_j'\rangle \epsilon_i = \langle j, m_j||r^2C^{(2)}||j', m_j'\rangle \sum_{q=-2}^{2} \begin{pmatrix} j & 2 & j' \\ -m_j & q & m_j' \end{pmatrix} c_{ik}^{(q)} \epsilon_i n_k \tag{3.13}$$

The $3-j$ symbols are connected to the Clebsch-Gordan coefficients by the relation:

$$\begin{pmatrix} j_1 & j_2 & j \\ m_1 & m_2 & m \end{pmatrix} = \frac{(-1)^{j_1 - j_2 - m}}{\sqrt{2j+1}} \langle j_1, m_1; j_2, m_2|j_1, j_2; j, m\rangle \tag{3.14}$$

Using the Clebsch-Gordan coefficients, the relative probabilities of exciting to any particular Zeeman sublevel can be determined. The geometric dependence is contained in the dot product of the spherical tensors and the beam polarisation vector $c_i^{(q)}\epsilon_i$ for the dipole and the Frobenius product between the spherical tensors and a matrix formed from the outer product of the wavevector and the polarisation vector $c_{ik}^{(q)}\epsilon_i n_k$ for the quadrupole. Thus to maximise a transition's strength we must address the ion with a particular angle and polarisation depending on whether $q = \Delta m_j = 0, \pm 1, \pm 2$ (π, σ, δ transitions respectively). Conversely, the same information tells us the angular distribution of the emission and its polarisation since the exact same geometrical factors govern the decay rate. To parametrise these geometric coefficients, we can define an angle θ as the angle between the laser wavevector and the magnetic field, ϕ as the angle of the polarisation vector in the plane normal to the laser wavevector and the magnetic field vector and a phase angle γ to parametrise the ellipticity of the polarisation vector. In the

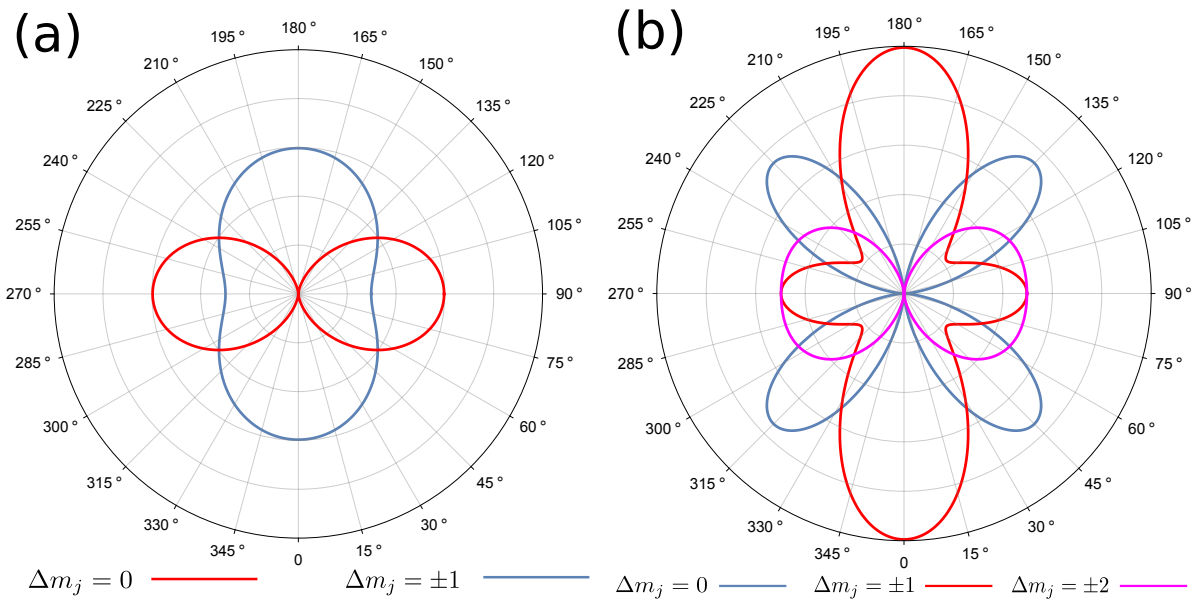

Figure 3.2: Polar plots of the emission distribution as a function of θ, the angle between laser wave vector and the magnetic field axis for (a) dipole transitions and (b) quadrupole transitions.

$\lvert\Delta m_j\rvert$	0 (π)	1 (σ)	2 (δ)
Dipole	$\frac{3}{8\pi}\sin^2\theta$	$\frac{3}{16\pi}(1+\cos^2\theta)$	
Quadrupole	$\frac{15}{8\pi}\sin^2\theta\cos^2\theta$	$\frac{5}{16\pi}(1-3\cos^2\theta+4\cos^4\theta)$	$\frac{5}{16\pi}(1-\cos^4\theta)$

Table 3.2: Angular distribution of the emission patterns of dipole and quadrupole transitions.

coordinate system where the magnetic field is along the z axis, we then have:

$$\mathbf{n} = \begin{pmatrix} -\sin(\theta) \\ 0 \\ \cos(\theta) \end{pmatrix} \tag{3.15}$$

$$\epsilon = \begin{pmatrix} \cos(\theta)\cos(\phi) \\ e^{i\gamma}\sin(\phi) \\ \sin(\theta)\cos(\phi) \end{pmatrix} \tag{3.16}$$

where we can set the y component to zero without loss of generality due to cylindrical symmetry. Using this parametrisation, we first calculate the emission as a function of θ for all the dipole and quadrupole transitions. Since we are interested only in the angular dependence, we integrate out the polarisation dependence ϕ and γ in the geometric factors $c_i^{(q)}\epsilon_i, c_{ik}^{(q)}\epsilon_i n_k$ and use the fact that each distribution must be normalised to unity to find the amplitude. The resulting distributions are given in table 3.2 and they are plotted in figure 3.2.[3]

Armed with this information we will now asses the requirements for the various tasks we wish to perform in our Penning trap. For Doppler cooling, we wish to drive the dipole transitions

[3]We have derived these distributions by what appears like a quantum mechanical result involving matrix elements that yield spherical tensors, but in fact these emission patters are simply the square of the vector spherical harmonics which appear in a classical electrodynamics context as shown in reference [119]

m_j	m'_j	Δm	$\Delta\nu$ (GHz/T)	$\mathbf{n} \parallel \mathbf{B}$	$\mathbf{n} \perp \mathbf{B}$
–1/2	– 5/2	δ^-	–27.99	0	0.56
–1/2	– 3/2	σ^-	–11.19	1	0.5
–1/2	– 1/2	π	5.60	0	0
–1/2	+ 1/2	σ^+	22.9	0.71	0.35
–1/2	+ 3/2	δ^+	39.19	0	0.25
1/2	– 3/2	δ^-	39.19	0	0.25
1/2	– 1/2	σ^-	22.9	0.71	0.35
1/2	+ 1/2	π	5.60	0	0
1/2	+ 3/2	σ^+	–11.19	1	0.5
1/2	+ 5/2	δ^+	–27.99	0	0.56

Table 3.3: Differential Zeeman shifts and normalised relative coupling strengths for various quadrupole transitions between $S_{1/2} \rightarrow D_{5/2}$ assuming ideal polarisation for each transition.

$S_{1/2} \rightarrow P_{1/2}$ for cooling both the radial and axial motion simultaneously. Due to the optical access of the trap being restricted to beams only along or perpendicular to the magnetic field, we must use the σ transitions since the π has no amplitude along the magnetic field axis. For the quadrupole transitions coupling the $S_{1/2} \rightarrow D_{5/2}$ states and used for both sideband cooling and coherent manipulation, we rule out using the π on the same grounds as for the dipole. Since we only have one laser at this frequency, we don't need to address both directions simultaneously and thus can treat them individually. For excitations parallel to the field clearly only the σ transitions are suitable, however, for the perpendicular case there is a choice between σ and δ. The angular amplitude is the same for both transitions exactly at 90° with the δ less sensitive to beam misalignment. We can then take into consideration the differential first order Zeeman shifts between the addressed states and include the coupling strength factor from the Clebsch-Gordan part of equations 3.12 and 3.13. The results are summarized in table 3.3. For coherent operations, any drift in the magnetic field will diminish the fidelity, hence choosing the transition with the least magnetic field sensitivity is preferable. Increased coupling strength effectively allows more of the laser power to interact with the ion and can contribute to faster sideband cooling or faster coherent operations. By these criteria we would preferentially like to work on the σ^+/σ^- transitions between $\pm 1/2 \leftrightarrow \pm 3/2$.

Finally we turn to the issues of polarisation. In the discussion above we have concluded that both the dipole and quadrupole transitions best suited for our experiment are σ transitions. To investigate the polarisation dependence we give the full form of the geometric factors:

$$|c_i^{(\pm 1)}\epsilon_i|^2 = \frac{3}{32\pi^3}\left(\cos^2\theta\cos^2\phi + \sin^2\phi \pm \cos\theta\sin\gamma\sin 2\phi\right) \tag{3.17}$$

$$|c_{ik}^{(\pm 1)}\epsilon_i n_k|^2 = \frac{5}{32\pi^3}\left(\cos^2\theta\sin^2\phi + \cos^2 2\theta\cos^2\phi \pm \cos\theta\cos 2\theta\sin\gamma\sin 2\phi\right) \tag{3.18}$$

For Doppler cooling, we know we have to simultaneously drive $\sigma^{\pm}$ transitions at both axial and

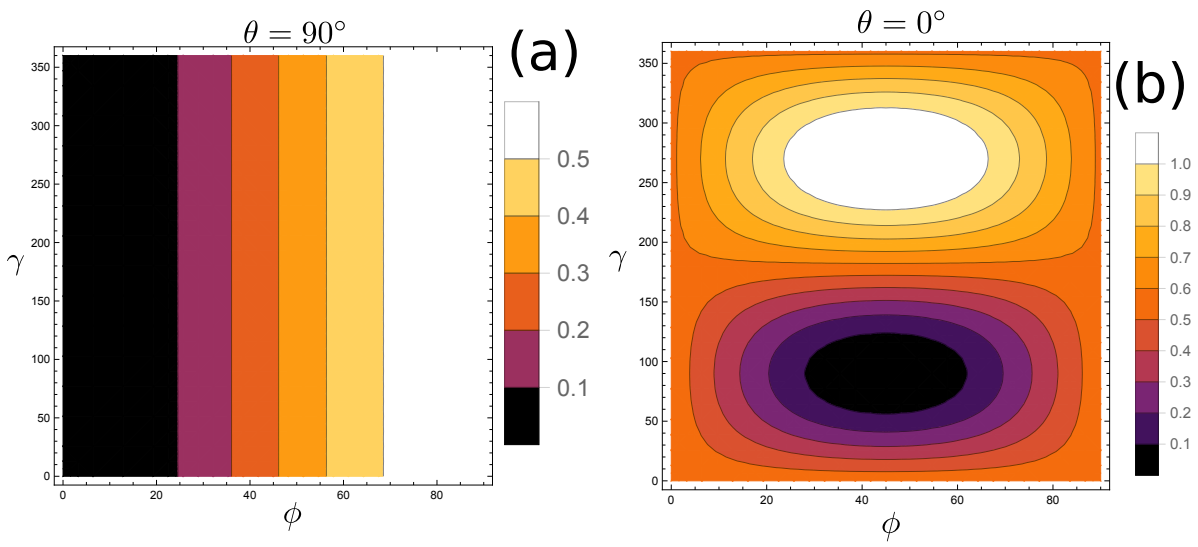

Figure 3.3: Excitation strength of a σ^- transition for (a) radial (b) axial excitation as a function of the polarisation vector parameters ϕ and γ. The amplitude is normalised to a maximum of one.

radial angles $\theta = 0°, 90°$. Plotting the results of equation 3.17 at these angles shows us that for axial addressing the ion requires left or right circularly polarized light for σ^-, σ^+ respectively, while radial addressing requires linear polarisation at $\phi = 90°$ for both transitions such that the polarisation vector is perpendicular to the magnetic field. In our experimental setup, for both radial and axial directions, we have a further geometrical restriction in that we must send both beams through the same polarisation maintaining fibre that requires linear polarisation and subsequently the beams follow the same optical path such that there is no opportunity to independently change their polarisation. This means that for axial addressing, we must use linear polarisation to simultaneously address the $\sigma^\pm$ transitions and hence are always losing half the potential excitation strength. Furthermore, we are very sensitive to any ellipticity acquired by imperfect extinction of the orthogonal polarisation mode through the fibre, which is dependent on environmental factors such as stresses and temperature fluctuations. This is evident by the fact that we reside on the maximum slope of equation 3.17. In the radial case, we observe a greater tolerance to polarisation noise since we are at the minimum of the slope i.e. at the peak of a $\sin^2$ function. For the quadrupole excitation, we can verify by substituting $\theta = 0°, 90°$ that 3.17 is equal to 3.18 hence the exact same considerations apply. The 729 nm beam and the repump lasers also emerge from a PM fibre with linear polarisation, which is necessary to repump all the Zeeman sublevels of the $D_{3/2}$ and $D_{5/2}$ manifolds on $\sigma^\pm$ transitions.

CHAPTER 4

LASER-ION INTERACTION AND LASER COOLING THEORY

The three major features that make trapped ions such a powerful resource with which to study quantum mechanics are:

- A nearly perfectly isolated harmonic oscillator system with well defined motional quanta
- A two-level atom that allows for well defined qubits that can be read out with high fidelity.
- The means to use laser radiation to both cool the ions and to couple the motional and internal states

Chapter 2 focused on describing the first point, while in this chapter the other two will be discussed. First, the standard quantum treatment of a two level atom in free space interacting with a laser is derived as this will serve as the basic description of the qubit introduced in chapter 1. Thereafter, the effect of the trapping potential is added to the description, giving us the fundamental toolbox that underlies techniques such as sideband cooling, coherent state generation and entanglement. Finally, the unique challenges of ground state cooling ions in a Penning trap are described and methods to overcome them are presented.

4.1 Laser interaction with a free two level atom

4.1.1 Propagator derivation

In this section we begin by assuming we have an atom that consists of just a ground state $|g\rangle$ and an excited state $|e\rangle$, which can be coupled by a monochromatic laser with electric field $E_L(t)$. For this to be true, we have to assume that the laser is tuned close to the relevant transition defining these states and has no off-resonant coupling to other transitions. The free Hamiltonian $\hat{H}_f$ can then be written as the sum of the two level atomic Hamiltonian $\hat{H}_e$ and the interaction Hamiltonian $\hat{H}_i$

$$\hat{H} = \hat{H}_e + \hat{H}_i \tag{4.1}$$

To make the derivations more compact we will use Pauli matrices which are commonly used to describe spin-1/2 systems with the mappings:

$$|g\rangle\langle g| + |e\rangle\langle e| \mapsto \hat{I}, \quad |g\rangle\langle e| + |e\rangle\langle g| \mapsto \hat{\sigma}_x, \quad i(|g\rangle\langle e| - |e\rangle\langle g|) \mapsto \hat{\sigma}_y, \quad |e\rangle\langle e| - |g\rangle\langle g| \mapsto \hat{\sigma}_z \tag{4.2}$$

The atomic Hamiltonian can now be written as:

$$\hat{H}_e = \hbar(\omega_g|g\rangle\langle g| + \omega_e|e\rangle\langle e|) = \hbar\frac{\omega_0}{2}(|e\rangle\langle e| - |g\rangle\langle g|) = \frac{\hbar\hat{\sigma}_z}{2} \tag{4.3}$$

where we have defined the transition frequency between the two levels $\omega_0 = \omega_e - \omega_g$ and assumed $\omega_e = -\omega_g$ to remove the state-independent energy contribution by having the levels symmetric spaced around zero. To represent the monochromatic plane laser with frequency ω_L, wavevector $\mathbf{k}_L$ and unit polarisation $\boldsymbol{\epsilon}_L$ we write down its electric field as:

$$\mathbf{E}_L(t) = \frac{\boldsymbol{\epsilon}_L E_0}{2}\left(e^{i(\mathbf{k}_L\cdot\hat{\mathbf{r}}-\omega_L t+\phi)} + e^{-i(\mathbf{k}_L\cdot\hat{\mathbf{r}}-\omega_L t+\phi)}\right) \tag{4.4}$$

The interaction Hamiltonian thus takes the form:

$$\hat{H}_I = -\frac{q}{m\omega_L}\mathbf{E}\cdot\hat{\mathbf{p}} = -\frac{E_0}{2\omega_L}\boldsymbol{\epsilon}_L\cdot\hat{\mathbf{p}}\left(e^{i(\mathbf{k}_L\cdot\hat{\mathbf{r}}-\omega_L t+\phi)} + e^{-i(\mathbf{k}_L\cdot\hat{\mathbf{r}}-\omega_L t+\phi)}\right) \tag{4.5}$$

where $\hat{\mathbf{p}}$ is the atom's momentum operator and the position operator $\hat{\mathbf{r}}$ in the exponent of the travelling wave expression is the position of the atom's electron relative to the atom's centre of mass. To perform useful calculations, this term is usually Taylor expanded as $e^{i\mathbf{k}_L\cdot\hat{\mathbf{r}}} = 1 + i\mathbf{k}_L\cdot\hat{\mathbf{r}} + ...$ to the required order. For dipole allowed transitions the zeroth order is taken, making the assumption that the wavelength of the laser light is much larger than the spatial extent of the atom. Using the fact that $\hat{\mathbf{p}} = \frac{m}{i\hbar}[\hat{\mathbf{r}}, \hat{H}_e]$, we can compute the transition matrix elements $\langle e|[\hat{\mathbf{r}}, \hat{H}_e]|g\rangle = \hbar\omega_0\langle e|\hat{\mathbf{r}}|g\rangle/e$ of the atomic dipole operator. This allows us to define a resonant ($\omega_0 = \omega_L$) coupling strength given by the Rabi frequency:

$$\Omega_0 = \langle e|\hat{\mathbf{r}}|g\rangle\cdot\boldsymbol{\epsilon}_L E_0/\hbar \tag{4.6}$$

If the dipole matrix element is zero, the next leading order term of the expansion is kept as is the case of the quadrupole allowed transitions. We can proceed without loss of generality since the different expansion order matrix elements can be absorbed into the definition of the Rabi frequency The interaction Hamiltonian can then be rewritten as

$$H_i = \frac{\hbar\Omega_0}{2}(\hat{\sigma}_+ + \hat{\sigma}_-)\left(e^{-i(\omega_L t-\phi)} + e^{i(\omega_L t-\phi)}\right) \tag{4.7}$$

where $\hat{\sigma}_\pm = \frac{1}{2}(\hat{\sigma}_x \pm i\hat{\sigma}_y)$.

To proceed with solving the Schrödinger equation, we use the time evolution operator $\hat{U}_0 = e^{-i\hat{H}_e t/\hbar}$ to transform into the interaction picture:

$$\begin{aligned}\hat{H}_{int} = \hat{U}_0^\dagger\hat{H}_i\hat{U}_0 &= \frac{\hbar\Omega_0}{2}e^{i\hat{H}_e t/\hbar}(\hat{\sigma}_+ + \hat{\sigma}_-)e^{-i\hat{H}_e t/\hbar}\left(e^{-i(\omega_L t-\phi)} + e^{i(\omega_L t-\phi)}\right)\\ &= \frac{\hbar\Omega_0}{2}\left[\hat{\sigma}_+\left(e^{i(\omega_0-\omega_L+\phi)t} + e^{i(\omega_0+\omega_L-\phi)t}\right) + \hat{\sigma}_-\left(e^{-i(\omega_0+\omega_L-\phi)t} + e^{-i(\omega_0-\omega_L+\phi)t}\right)\right]\\ &= \frac{\hbar\Omega_0}{2}\left[\hat{\sigma}_+e^{-i(\Delta t-\phi)} + \hat{\sigma}_-e^{i(\Delta t-\phi)}\right]\end{aligned} \tag{4.8}$$

where in the final step we have made the rotating wave approximation and removed the fast oscillating terms containing $\omega_0+\omega_L$ and defined the detuning $\Delta = \omega_L - \omega_0$. This approximation should be valid in the regime of small detuning where $\omega_L \approx \omega_0$, in which case the sum terms can

be assumed to average to zero over the course of the slow interaction. An arbitrary quantum state in the transformed basis can be written as:

$$|\psi(t)_{int}\rangle = c_g(t)|\tilde{g}\rangle + c_e(t)|\tilde{e}\rangle \tag{4.9}$$

where the interaction picture states have now subsumed the time evolution $e^{\pm i\omega_0 t/2}$ from the Schrödinger picture. The Schrödinger equation now simply becomes:

$$i\hbar\frac{\partial}{\partial t}|\psi(t)_{int}\rangle = \hat{H}_{int}|\psi(t)_{int}\rangle \tag{4.10}$$

Substituting in the Hamiltonian and states leads to two coupled equations for the coefficients:

$$\dot{c}_g(t) = -\frac{i\Omega_0}{2}e^{i(\Delta t-\phi)}c_e \tag{4.11}$$

$$\dot{c}_e(t) = -\frac{i\Omega_0}{2}e^{-i(\Delta t-\phi)}c_g \tag{4.12}$$

This system of equations can be recast in terms of the initial state populations $c_g(0), c_e(0)$ as

$$c(t)_g|g\rangle + c(t)_e|e\rangle = U_{int}(t)(c_g(0)|g\rangle + c_e(0)|e\rangle) \tag{4.13}$$

where $U_{int}(t)$ is the time evolution propagator. The solution of this system is obtained by means of a Laplace transform [120]

$$U_{int}(t) = \begin{bmatrix} e^{-\frac{it\Delta}{2}}\left(\cos\left(\frac{t\Omega}{2}\right) + \frac{i\Delta\sin\left(\frac{t\Omega}{2}\right)}{\Omega}\right) & -\frac{\Omega_0}{\Omega}ie^{i\left(\phi-\frac{t\Delta}{2}\right)}\sin\left(\frac{t\Omega}{2}\right) \\ -\frac{\Omega_0}{\Omega}ie^{i\left(\frac{t\Delta}{2}-\phi\right)}\sin\left(\frac{t\Omega}{2}\right) & e^{\frac{it\Delta}{2}}\left(\cos\left(\frac{t\Omega}{2}\right) - \frac{i\Delta\sin\left(\frac{t\Omega}{2}\right)}{\Omega}\right) \end{bmatrix} \tag{4.14}$$

where $\Omega = \sqrt{\Omega_0^2 + \Delta^2}$ gives the generalised Rabi frequency. This propagator is very useful since it allows one to calculate the state populations at any later time t, even in sequences with composite pulses with different detunings, pulse times or phases.

4.1.2 Bloch Sphere Representation

We will also use the Bloch sphere (fig 4.1) as a useful visual resource to describe the action of the propagator $U_{int} = U(\Omega_0, \phi, \Delta, t)$ (eq. 4.14) on a two level qubit defined by:

$$\psi = \cos\left(\frac{\theta}{2}\right)|g\rangle + \sin\left(\frac{\theta}{2}\right)e^{i\phi}|e\rangle \tag{4.15}$$

The action of the unitary operator on the state $|g\rangle$ in the absence of detuning can be visualised as a rotation of the state vector around the y-axis by an angle Ω_0. The state vector traces out a circle and returns to the $|g\rangle$ state after a period of $2\pi/\Omega_0$. In the presence of detuning the state vector also acquires a phase $\phi = \Delta t$ defined by the angle between the projection of the state vector in the equatorial plane and the x-axis. In this case, the state vector traces out a more complicated trajectory as seen in figure 4.2. We can find the excited state population by applying the propagator and projecting on the excited state and taking the square modulus:

$$|\langle e|U(\Omega_0, \phi, \Delta, t)|g\rangle|^2 = \frac{\Omega_0^2}{\Omega^2}\sin^2\left(\frac{\Omega t}{2}\right) \tag{4.16}$$

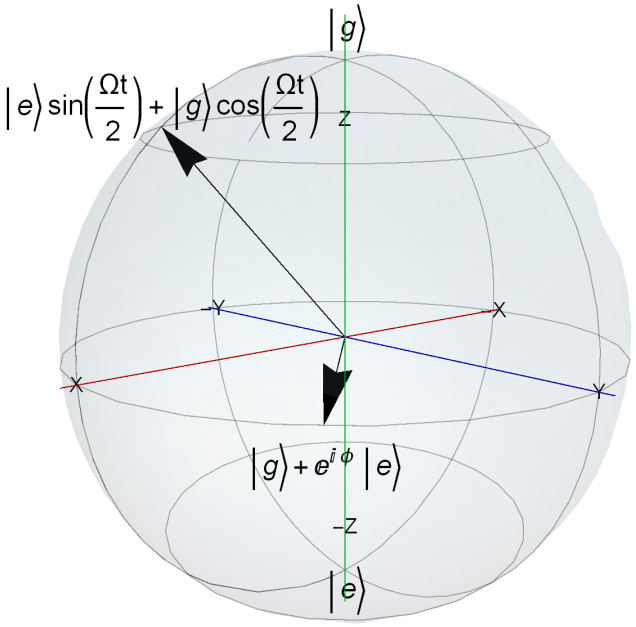

Figure 4.1: Bloch sphere representation of two state vectors. The first corresponding to a pure rotation along the z-x plane by angle $\Omega_0 t$. The second shows a state that is a superposition of the two states with an acquired phase ϕ due to rotation in the x-y plane.

This result is the familiar Rabi oscillation. On resonance, the population evolves with a frequency Ω_0 with full contrast oscillations between the eigenstates. As the detuning gets larger, the oscillation frequency increases and the amplitude reduces.

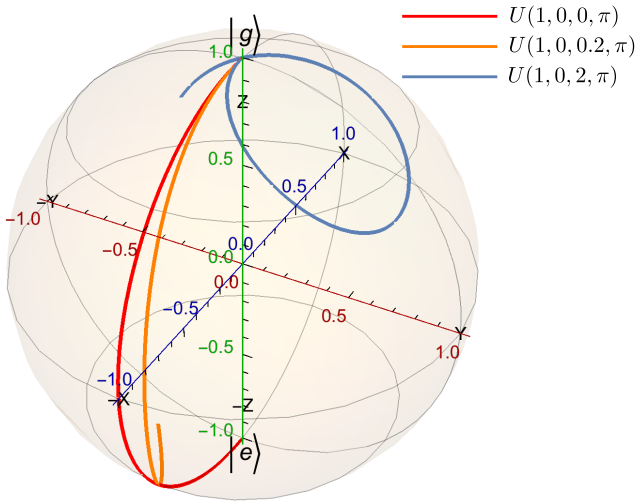

Figure 4.2: Bloch sphere representation of a Rabi π pulse: on resonance in red, with a small detuning in orange and with a large detuning in blue. We clearly see that the larger the detuning the further the distance from $|e\rangle$ and the faster the state returns back to $|g\rangle$

Another important result is when the pulse time is set to $t = \pi/(2\Omega_0)$. In this case we

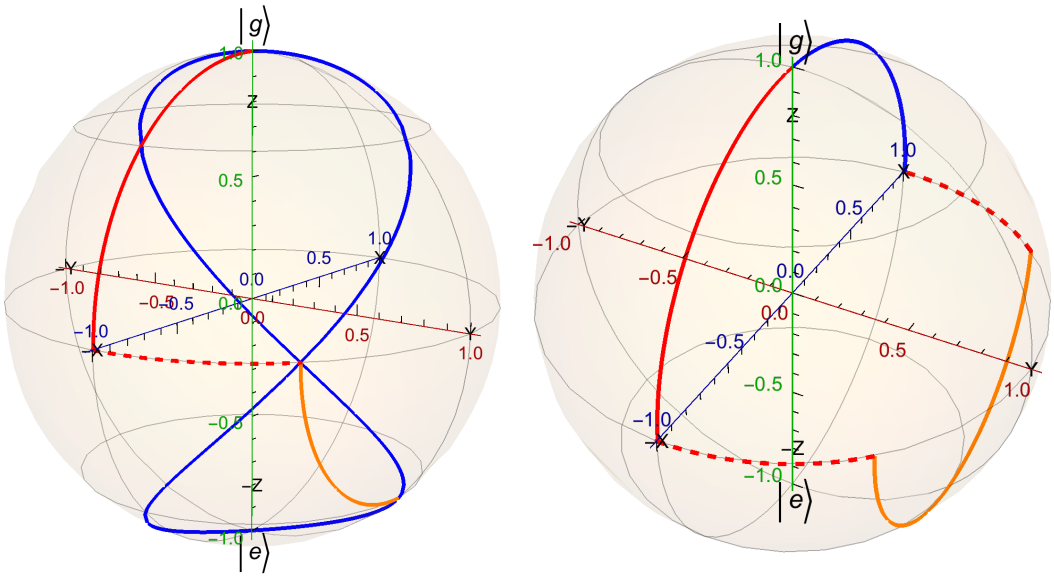

Figure 4.3: (a) A Ramsey type sequence. First, the red curve shows a $U(1, 0, \Delta, \pi/(2\Omega_0))$ pulse to create the $(|g\rangle + |e\rangle)/\sqrt{2}$. The red dotted line then shows a phase acquisition $\phi = \Delta T$. The orange pulse $U(1, 0, \Delta, \pi/(2\Omega_0))$ makes an incomplete transfer towards $|e\rangle$. The blue curve shows all the attainable states if the orange pulse phase were scanned over 2π. (b) A Spin Echo type sequence. The first two steps are as in (a) but the orange pulse is now $U(1, 0, \Delta, \pi/(\Omega_0))$. A second period of free evolution follows, after which the blue pulse $U(1, 0, \Delta, \pi/(2\Omega_0))$ returns the state to $|g\rangle$

obtain a superposition:

$$U(\Omega_0, \phi, 0, \pi/(2\Omega_0))|g\rangle = (|g\rangle + |e\rangle)/\sqrt{2} \tag{4.17}$$

Now if we wait for a certain time T and apply a second pulse of the same form, the population should be fully transferred to $|e\rangle$. However, if there is a mismatch between the phase of the second laser pulse to the phase of the ion the population transfer will be incomplete. In figure 4.1 we see an example of a superposition state that has acquired a phase, which will not be fully transferred to $|e\rangle$ by a laser with $\phi = 0$ as seen in figure 4.3a. Thus by applying two laser pulses of length $t = \pi/(2\Omega_0)$ separated by a wait time T we can create a very sensitive probe of the dephasing of the quantum state. This method is known as Ramsey spectroscopy. Any of the three variables T, ϕ or Δ can be scanned to produce an interferometric signal. By averaging over many experimental realisations of this operation, the presence of random phase evolution will reduce the contrast of this signal. In section 6.2.3 we will develop these results in a quantitative way to describe data obtained from experiment.

We can also ask if there is a simple way to correct for the dephasing without knowing its magnitude. As long as the dephasing rate is constant in time, an addition of a single $t = \pi/(\Omega_0)$ pulse in the middle of the wait time rotates the state about the y axis back to the equator and the continued phase evolution brings the state back into the x-z plane after time T. A final $t = \pi/(2\Omega_0)$ pulse then returns the state back to $|g\rangle$ (or $|e\rangle$ with $\phi = \pi$). This sequence is show on the Bloch sphere in figure 4.3b and forms the basis of the Spin Echo technique – a form of dynamical decoupling that will be discussed in depth in section 6.2.4.

4.2 Laser interaction with a trapped two level atom

Up to now, only interaction with a free atom in space was considered. Since the ion is now bound in the trap, it oscillates periodically towards and away from any incoming laser. This means in the ion's rest frame, classically it sees the incoming light modulated at its oscillation frequency, producing sidebands analogous to radio frequency modulation. A quantum description including the trapping potential H_t is necessary to fully quantify this phenomenon. To simplify the discussion we will isolate two cases. First we shall treat only the axial motion along the z direction in the presence of an axial beam with wavevector k_z. Second, we will treat the case of both radial modes interacting with a single beam along k_x. This is a valid treatment given that our experimental setup only has one spectroscopy beam which, to within small misalignments, always points in one of these directions.

4.2.1 Axial motion

We begin by writing the new form of the atomic Hamiltonian:

$$\hat{H}_0 = \hat{H}_e + \hat{H}_m = \frac{\hbar\omega_0}{2}\hat{\sigma}_z + \hbar\omega_z\left(\hat{a}^\dagger\hat{a} + \frac{1}{2}\right) \tag{4.18}$$

The interaction Hamiltonian from 4.7 has to be modified to include the motion of the ion in the trap. We can add this effect as a phase modulation term dependent on the ion position operator $\hat{z}$ giving[1]

$$H_i = \frac{\hbar\Omega_0}{2}(\hat{\sigma}_+ + \hat{\sigma}_-)\left(e^{-i(\omega_L t - k_z\hat{z} - \phi)} + e^{i(\omega_L t - k_z\hat{z} - \phi)}\right) \tag{4.19}$$

Next, we can substitute the position operator in terms of the raising and lowering operators from 2.61 and define the Lamb-Dicke parameter:

$$\eta_z = \sqrt{\frac{\hbar k_L^2}{2M\omega_z}} \tag{4.20}$$

The Lamb-Dicke parameter is a product of the spatial extent of the ground state wavefunction and the laser wavevector. It gives an indication of the amount of modulation of the incoming light the laser will see, hence we can think of it analogously to the classical modulation index that parametrises the strength of spectral sidebands. Once again, to move forward we move to the interaction picture

$$\begin{aligned}
\hat{H}_{int} &= \hat{U}_0^\dagger \hat{H}_i \hat{U}_0 \\
&= \frac{\hbar\Omega_0}{2} e^{i\hat{H}_e t/\hbar}(\hat{\sigma}_+ + \hat{\sigma}_-)e^{-i\hat{H}_e t/\hbar}e^{i\hat{H}_m t/\hbar}\left(e^{-i(\omega_L t - \eta_z(\hat{a}+\hat{a}^\dagger)\phi)} + e^{i(\omega_L t - \eta_z(\hat{a}+\hat{a}^\dagger) - \phi)}\right)e^{-i\hat{H}_m t/\hbar} \\
&= \frac{\hbar\Omega_0}{2}\left[\hat{\sigma}_+ e^{-i(\Delta t - \eta_z(\tilde{a}+\tilde{a}^\dagger) - \phi)} + \hat{\sigma}_- e^{i(\Delta t - \eta_z(\tilde{a}+\tilde{a}^\dagger) - \phi)}\right]
\end{aligned} \tag{4.21}$$

where we have once more taken the rotating wave approximation and raising and lowering operators were transformed as $\tilde{a} = e^{-i\omega_z t}\hat{a}$ to include the time dependence due to $\hat{H}_m$. We can

[1] It is important to pause and remind ourselves that this is a different phase than the $\mathbf{k}\cdot\hat{\mathbf{r}}$ in 4.5, which was due to the position of the electron relative to the atom's centre of mass.

then write a general quantum state as:

$$|\psi\rangle = \sum_{n'=0}^{\infty} c_{g,n'}|g,n'\rangle + c_{e,n'}|e,n'\rangle \tag{4.22}$$

Using the interaction picture Schrödinger equation, multiplying by $\langle g,n|$ and $\langle e,n|$ respectively and expanding the exponential in a Taylor series, we obtain the following coupled set of equations:

$$\dot{c}_{g,n} = \frac{-i\Omega_0}{2}e^{i(\Delta t-\phi)}\sum_{n'=0}^{\infty} c_{e,n'}\langle n|\sum_{k=0}^{\infty}\frac{(-i\eta)^k}{k!}(a_z^\dagger e^{-i\omega_z t}+a_z e^{i\omega_z t})^k|n'\rangle \tag{4.23}$$

$$\dot{c}_{e,n} = \frac{-i\Omega_0}{2}e^{-i(\Delta t-\phi)}\sum_{n'=0}^{\infty} c_{g,n'}\langle n|\sum_{k=0}^{\infty}\frac{(i\eta)^k}{k!}(a_z^\dagger e^{i\omega_z t}+a_z e^{-i\omega_z t})^k|n'\rangle \tag{4.24}$$

Due to the orthogonality of the harmonic oscillator states, only terms that lower or raise the state n' to n are preserved, oscillating at $-l\omega_z$, where $l = n - n'$ is an integer indicating the change in motional state. The total time dependent oscillation is then $e^{i(\Delta - l\omega_z)t}$. If the laser is assumed to be narrow in linewidth $\Delta_{\omega_l} \ll \omega_z$ and not power broadened $\Omega_0 \ll \omega_z$ then by setting $\Delta \approx l\omega_z$, the l^{th} term dominates the sum effectively picking out a sideband with which the laser interacts. This allows us to drop the sum over all n, leading to a very similar functional form to equations 4.11 & 4.12:

$$\dot{c}_{n,g}(t) = -\,i\frac{\Omega_{n,n+l}}{2}e^{i(\Delta' t-\phi)}c_{n+l,e} \tag{4.25}$$

$$\dot{c}_{n+l,e}(t) = -\,i\frac{\Omega^*_{n,n+l}}{2}e^{-i(\Delta' t-\phi)}c_{n,g} \tag{4.26}$$

where we define a detuning from the sideband $\Delta' = \Delta - l\omega_z$ and a new Rabi frequency:

$$\Omega_{n,n+l} = \langle n|e^{i\eta_z(\hat{a}+\hat{a}^\dagger)}|n+l\rangle = \Omega_0 e^{-\eta_z^2/2}(i\eta_z)^{|l|}L_m^{|l|}(\eta_z^2)\left[\frac{n!}{(n+l)!}\right]^{\text{sgn}\,(l)/2} \tag{4.27}$$

where $L_m^{|l|}$ are associated Laguerre polynomials [121] and $m = \text{Min}(n, n+l)$. The only change from the free atom equations is the addition of the complex phase that depends on the sideband l within the definition of the Rabi frequency. For $l = 0$ the equations are identical to 4.11 & 4.12. This coupling strength is crucial in understanding the response of an ion in a particular phonon Fock state to a laser field. It is important to note that coupling for all sidebands including the carrier drops very close zero at some phonon number, but never at the same point. The minima increase in n for higher order sidebands at a fixed η_z while increasing η_z lowers the whole comb of sideband minima in n. Knowing where they are located in relation to the Doppler cooled Fock state distribution is crucial with regards to the applicability of the simplest sideband cooling technique as will be discussed later in section 4.4.1.

After Doppler cooling, the ion population is in a thermal state described by a Boltzmann distribution of mean $\bar{n}$ with a occupation probability given by [122]

$$P(n) = \frac{\bar{n}^n}{(\bar{n}+1)^{n+1}} \tag{4.28}$$

To obtain the excitation spectrum an incoherent sum over the evolution of the individual Fock

states weighted by their occupation probability is required.

An important special case to consider is when the ion is said to be in the Lamb-Dicke regime. This occurs when the ion wavefunction spread is much smaller than the wavelength of the interacting laser, leading to the condition

$$\eta_z\sqrt{2\bar{n}+1} \ll 1 \tag{4.29}$$

The Rabi frequency calculation in 4.27 can then be simplified through expanding the operator to second order in η_z:

$$\Omega_{n,n+l} = \langle n|e^{i\eta_z(\hat{a}+\hat{a}^\dagger)}|n+l\rangle = \langle n|1 + i\eta_z(\hat{a}+\hat{a}^\dagger) - \frac{1}{2}\eta_z^2(\hat{a}+\hat{a}^\dagger)^2|n+l\rangle \tag{4.30}$$

Then simply by applying the rules of the raising and lowering operators, we obtain the approximate Rabi frequencies for the 0^{th}-2^{nd} order sidebands:

$$\Omega_{n,n-2} = \Omega_0\eta_z^2\frac{\sqrt{n(n-1)}}{2} \tag{4.31}$$

$$\Omega_{n,n-1} = \Omega_0\eta_z\sqrt{n} \tag{4.32}$$

$$\Omega_{n,n} = \Omega_0\left(1 - \frac{1}{2}\eta_z^2(2n+1)\right) \tag{4.33}$$

$$\Omega_{n,n+1} = \Omega_0\eta_z\sqrt{n+1} \tag{4.34}$$

$$\Omega_{n,n+2} = \Omega_0\eta_z^2\frac{\sqrt{(n+1)(n+2)}}{2} \tag{4.35}$$

4.2.2 Radial Motion

In the radial case, the problem is slightly more complicated since a planar laser along the x direction necessarily couples to both the magnetron and cyclotron modes since the ion 'sees' the laser modulated at both frequencies. The Hamiltonian of 4.18 will now have the cyclotron and magnetron harmonic oscillator Hamiltonians and 2.61 will replace the $k_z\hat{z}$ term wih a $k_z\hat{x}$. The subsequent interaction picture transformation is largely the same as for the z case yielding the interaction Hamiltonian

$$\hat{H}^x_{int} = \frac{\hbar\Omega_0}{2}\hat{\sigma}_+ \exp\left[-i(\Delta t - \eta_r(a_+e^{-i\omega_+t} + a_+^\dagger e^{i\omega_+t} + a_-^{-i\omega_-t} + a_-^\dagger e^{i\omega_-t}) - \phi)\right] + \text{h.c.} \tag{4.36}$$

where the time dependence is written explicitly to highlight that there are now two relevant frequencies and a new radial Lamb-Dicke parameter $\eta_r = \sqrt{\hbar k_x^2/2m\omega_1}$ is defined.[2] Carrying through the same analysis as in 4.24 by expanding the exponential and computing $\langle n_+, n_-|\hat{H}^x_{int}|n_+ + l, n_- + j\rangle$ reveals that simultaneous transitions of both modes can now be excited when a narrow linewidth laser is tuned to $\Delta = l\omega_+ + j\omega_-$ for integers j, l. This will inevitably lead to a more dense sideband structure as each high frequency cyclotron resonance and the carrier will be surrounded by low frequency magnetron sidebands. The Rabi frequency

[2]It is interesting to note that both modes have the same Lamb-Dicke parameter defined by ω_1 rather than $\omega_\pm$. This is consistent with the ground state radial spread calculated in 2.63.

is given by:

$$\Omega_{n_+,n_-}^{n_++l,n_-+j} = \Omega_0\langle n_+,n_-|e^{i\eta_r(a_++a_+^\dagger)}|n_++l,n_-+j\rangle\langle n_+,n_-|e^{i\eta_r(+a_-+a_-^\dagger)}|n_++l,n_-+j\rangle \tag{4.37}$$

4.2.3 Multiple Ions

In general, a 3D N ion Coulomb crystal will always have a total of $3N$ motional modes even though some may be degenerate in frequency. Restricting our description to just the N axial modes of a chain or planar 2D crystal, the Hamiltonian then consists of the sum of the individual harmonic oscillator Hamiltonians over the mode frequencies as shown in equation 2.72. We thus obtain a form of the interaction picture Hamiltonian:

$$H_I = \frac{\hbar}{2}\sum_{j=1}^{N}\Omega_0(\sigma_j^+ + \sigma_j^-)e^{-i\sum_k \eta_k^{(j)}(a_k^\dagger + a_k)}e^{i\omega_L t} + \text{h.c.} \tag{4.38}$$

where $a_k^\dagger$ and a_k are the raising and lowering operators of the k-th mode with a corresponding Lamb-Dicke parameter $\eta_k^{(j)}$. As with the radial motion, a sufficiently narrow linewidth laser will now be able to pick out not only the n-th sideband of the k-th mode, but also all the sum and difference terms between all the modes where the motional state of multiple modes is changed simultaneously.

For the special case of two ions we obtain the coupling matrix elements for ion l between two modes n and m:

$$\Omega_{n,m,n',m'} = \Omega_0\langle n|e^{i\eta_n^l(a_ne^{i\omega_n t}+a_n^\dagger e^{-i\omega_n t})}|n'\rangle\langle m|e^{(-1)^l i\eta_n^l(a_me^{i\omega_m t}+a_m^\dagger e^{-i\omega_m t})}|n'\rangle \tag{4.39}$$

Equation 4.39 tells us that sidebands described by the $\Omega_{n,m,n',m'}$ coupling depend on the initial and final states of both modes just as for the radial single ion case (eq. 4.37) with the major difference being the fact that the two motional modes have different Lamb-Dicke parameters.

4.3 Laser Cooling in a Penning trap

Due to the achievable well depth of many electron volts, the ion traps can very easily be loaded with clouds of ions with kinetic energies that are well beyond those given by a room temperature distribution. These ions can occupy large orbits in the trap. For any type of spectroscopic measurement it is generally beneficial to reduce the temperature of the ions in order to minimize the Doppler broadening due the velocity distributions as well as to localise the ions at the trap centre. Before the advent of laser cooling techniques, ion trapping experiments were limited to various classical means of temperature reduction such as coupling the ion motion to an external circuit to dissipate energy or using a cold buffer gas [123]. Resistive cooling works by coupling a resistive load between the axial electrodes in a Penning trap [124, 125] leading to the ions thermalising to the temperature of the load resistor. However, as the magnetron motion has negative total energy, when this coupling is used between segments of a ring electrode to cool the cyloctron motion, the ion is quickly forced out of the trap by heating of the magnetron motion [126]. Buffer gas cooling, where a small amount of low pressure gas such as helium thermalised to a cryogenically cooled trap, suffers from the same exact problem as the repeated collisions

act as a random walk driving the ions to larger magnetron radii. In a proposal by Dehmelt and Wineland [127] the idea was raised that if a resonant coupling was established between the axial and magnetron motion, the two modes would continuously exchange energy, and hence if the cooling of the axial motion was faster than the heating of the magnetron the two modes could be cooled simultaneously. This technique proved crucial in the high precision experiment of Dehmelt *et. al.* to determine the anomalous magnetic moment of the electron in a Penning trap [128], whist performing the most precise frequency ratio measurement at the time. Similarly, it was proposed that for an azimuthal quadrupolar field as produced with a radial electrode ring split into four segments [129], a coupling between the cyclotron and magnetron modes could be realized. This technique allowed even heavy ions to be cooled to 4K in the presence of a cold buffer gas [130]. While the remainder of this thesis will deal with laser cooling as the exclusive means of removing energy from the system, the above history emphasizes the important role the resonant coupling technique, henceforth referred to as axialization (sometimes called sideband-cooling in earlier literature), played in the field of Penning trap physics. As we will see later, it will once again be crucial in the first demonstration of ground state cooled magnetron motion.

To really push beyond the 4K barrier and ultimately to cool ions to their motional ground state, laser cooling is required. First proposed in 1975 for ions [131] and atoms [132] independently, experimental demonstration on clouds of ions in Penning [19] and Paul [20] traps followed soon after. In 1980 a single ion was cooled to tens of mK [133], orders of magnitude lower than achieved with any other technique. The principle behind laser cooling follows from the fact that a laser tuned to the red side of a Doppler broadened transition profile will preferentially absorb photons when the ion's motion towards the laser Doppler shifts the light on to resonance, whereas the re-emission is isotropic, leading to an effective frictional force. The criteria for the effective application of this technique include a suitable closed transition cycle (often with the aid of re-pump lasers), which returns the ion to the initial optical ground state and a suitably broad transition of linewidth Γ so that the cycle can be repeated many times per second. Typically, this means dipole allowed transitions with $\Gamma/(2\pi) \sim 20$ MHz [123] much bigger than the typical trapping frequencies ω_T.[3] The condition $\Gamma \gg \omega_T$ is generally called the 'weak-binding' regime and implies that the optical sidebands around the carrier due to the trap frequency modulation are not resolved using these transitions. Ultimately, the cooling in the weak binding regime is limited by diffusive heating processes to what is often termed the Doppler limit. A naive application of Doppler cooling in a Penning trap still suffers from the same problem as any of the aforementioned methods in that simply removing energy from all modes heats the magnetron mode. However, the position of the laser beam offers another degree of freedom. By offsetting the laser beam from the trap centre in the radial plane, energy can be added to the magnetron mode, hence reducing its orbital radius. The next section will describe the laser cooling in depth.

To push past the Doppler limit we can consider what happens in the 'strong binding' regime $\Gamma \ll \omega_T$. In this case a laser with a suitably narrow linewidth can resolve the discrete spectrum of motional sidebands as described in section 4.2.1 and target one in particular. By picking out

[3]There is an exception where one can use a quadrupole transition [134] where the upper state lifetime is quenched by a repump laser to a fast decaying state to increase the cycle rate. This is akin to our sideband cooling scheme described in section 4.4, but with the difference that the quadrupole excitation laser has a linewidth of 200 kHz to span a wide range of the Doppler velocity profile – at least 3 orders of magnitude too large for coherent addressing.

sidebands on the red side of the carrier frequency, motional quanta can be iteratively removed until the ground state is reached. The frequency selectivity means that this technique can cool particular modes of the radial motion of an ion or the vibrational modes of many ions. Other techniques that can achieve ground state occupation include using a pair of Raman beams to drive the resolved sidebands [135, 136] or Electromagnetically Induced Transparency (EIT), where the dressing laser is used to tune the interference between the matrix dipoles of another probe laser with the dressed states to coincide with the carrier, while maximising absorption over the red sidebands [137]. This technique might hold promise for the future, especially for a larger number of ions [138, 139], but could be more complicated to implement in a Penning trap due to the more complex Zeeman level structure for the $^{40}Ca^{+}$ ion used in our experiment.

4.3.1 Doppler Coooling

We can now focus on the specifics of Doppler cooling in a Penning trap, following the treatment of reference [140]. Before moving on note that 'cooling' in terms of reducing the total energy only makes sense for the axial and cyclotron motions since the magnetron contribution is negative. If we consider the aim of any cooling experiment to be the localization of the ions at the trap centre, we can take a pragmatic definition of cooling as reducing the motional radius, hence kinetic energy, irrespective of the total energy. Thus the quantities that we wish to find are the square amplitudes of the radii of all the motions following a single photon scattering event. The photon scattering is assumed to result in an instantaneous velocity change $\Delta\mathbf{v} \equiv \mathbf{v} - \mathbf{v}' = \frac{\hbar}{m}(\mathbf{k} - \mathbf{k}')/m$ where an atom of mass m and initially moving with velocity $\mathbf{v}$ absorbs a photon with a wave vector $\mathbf{k}$ and then emits a photon with wave vector $\mathbf{k}'$ changing its velocity to $\mathbf{v}'$. We can differentiate the position vector $\mathbf{r}(t, r_i, \phi_i)$ defined by equations (2.14) to obtain the ion velocities $\mathbf{v}(t, r_i, \phi_i)$ where $i = z, +, -$ identifies each mode. After the scattering event $t > t_0$ the amplitudes and phases are modified to r_i' ϕ_i' respectively. Then, using the assumption that the scattering event instantaneously changes the velocity but not the position allows us to write a set of equations:

$$\mathbf{r}(t_0, r_i, \phi_i) = \mathbf{r}(t, r_i', \phi_i') \tag{4.40}$$

$$\mathbf{v}(t_0, r_i, \phi_i) + \Delta\mathbf{v} = \mathbf{v}'(t, r_i', \phi_i') \tag{4.41}$$

By multiplying the z coordinate equation in 4.40 with ω_z and then taking the square sum with the z equation of 4.41 we obtain:

$$\Delta r_z^2 \equiv r'^2 - r^2 = \left(\frac{\Delta v_z}{\omega_z}\right)^2 - \frac{2 r_z \Delta v_z}{\omega_z} \sin(\omega_z t_0 + \phi_z) \tag{4.42}$$

It is evident that to achieve cooling, the second term must be negative, which is the case when the Δv_z is opposing the direction of the z motion. This can be achieved quite simply with a single red detuned laser beam in the z direction. For the radial amplitudes the algebra is slightly more involved. The x, y equations of 4.40 need to be multiplied by ω_+ and ω_- in turn, yielding 4 equations which are combined with the x, y terms of the velocity equations to yield

equations where the amplitudes are uncoupled:

$$-2\omega_1 r_+ \cos(\omega_+ t + \phi_+) + \Delta v_y = -2\omega_1 r'_+ \cos(\omega_+ t' + \phi'_+) \tag{4.43a}$$

$$2\omega_1 r_- \cos(\omega_- t + \phi_-) + \Delta v_y = 2\omega_1 r'_- \cos(\omega_- t' + \phi'_-) \tag{4.43b}$$

$$-2\omega_1 r_+ \sin(\omega_+ t + \phi_+) + \Delta v_x = -2\omega_1 r'_+ \sin(\omega_+ t' + \phi'_+) \tag{4.43c}$$

$$2\omega_1 r_- \sin(\omega_- t + \phi_-) + \Delta v_x = 2\omega_1 r'_- \sin(\omega_- t' + \phi'_-) \tag{4.43d}$$

To obtain the square amplitude differences we then combine 4.43a^2+4.43c^2 and 4.43b^2+4.43d^2:

$$\Delta r_-^2 \equiv r_-'^2 - r_-^2 = \frac{\Delta v_x^2 + \Delta v_y^2}{4\omega_1^2} + \frac{r_-}{\omega_1}\left[\Delta v_x \sin(\omega_- t_0 + \phi_-) + \Delta v_y \cos(\omega_- t_0 + \phi_-)\right] \tag{4.44}$$

$$\Delta r_+^2 \equiv r_+'^2 - r_+^2 = \frac{\Delta v_x^2 + \Delta v_y^2}{4\omega_1^2} - \frac{r_+}{\omega_1}\left[\Delta v_x \sin(\omega_+ t_0 + \phi_+) + \Delta v_y \cos(\omega_+ t_0 + \phi_+)\right] \tag{4.45}$$

From the sign of second term in both equations we can immediately deduce the impact of collisions from laser scattering. As in 4.42 the sign in front of the second term for 4.45 implies that the cyclotron is cooled when the change of velocity opposes the initial velocity. On the other hand, for the magnetron motion in 4.44 the sign is reversed implying that the change in velocity should be in the same direction as the initial velocity. It is from this apparent contradiction between the cooling requirements where the difficulty in using frequency selective Doppler cooling techniques arises. If the interacting laser is detuned below resonance such that the photons are preferentially absorbed when the ion is travelling towards the beam, the cyclotron motion can be cooled, while the magnetron motion is heated.

To overcome this limitation and cool both modes simultaneously, the scattering must be engineered such that there is an appreciable net scattering when the ion is moving away from the laser beam during the magnetron orbit compared to when it is moving towards it. One method to solve this problem is to offset the laser beam from the trap centre and use its spatial intensity profile to create a scattering gradient across the centre of the trap so that this condition can be fulfilled. The combination of this gradient and the red detuning of the laser beam allows for simultaneous cooling of both motions within a region of the parameter space as will be shown below. Figure 4.4 illustrates the idea behind using the offset beam and its Gaussian intensity profile to engineer the magnetron cooling.

To find the final steady state radii of the motion and hence the associated energies & temperature requires a full quantitative treatment including the scattering rates. For this derivation we shall work with two laser beams, an axial beam with uniform intensity I_z, wave vector $\mathbf{k}_z = k\hat{\mathbf{z}}$ and scattering cross-section $\sigma_z(\omega_L, \mathbf{v})$, and a radial beam with intensity $I_r(y)$, wave vector $\mathbf{k}_x = k\hat{\mathbf{x}}$ and scattering cross-section $\sigma_r(\omega_L, \mathbf{v})$, with a common laser frequency ω_L. We shall assume that while the true intensity profile of the laser is Gaussian, it can be approximated by a linear function $I_r = I_{r0}(1 + y/y_0)$ provided that the ion orbit amplitudes are small compared to the beam size ($y \ll y_0$), where y_0 parametrises the intensity gradient. This will generally be true once the ions are already somewhat cooled and is valid for deriving the

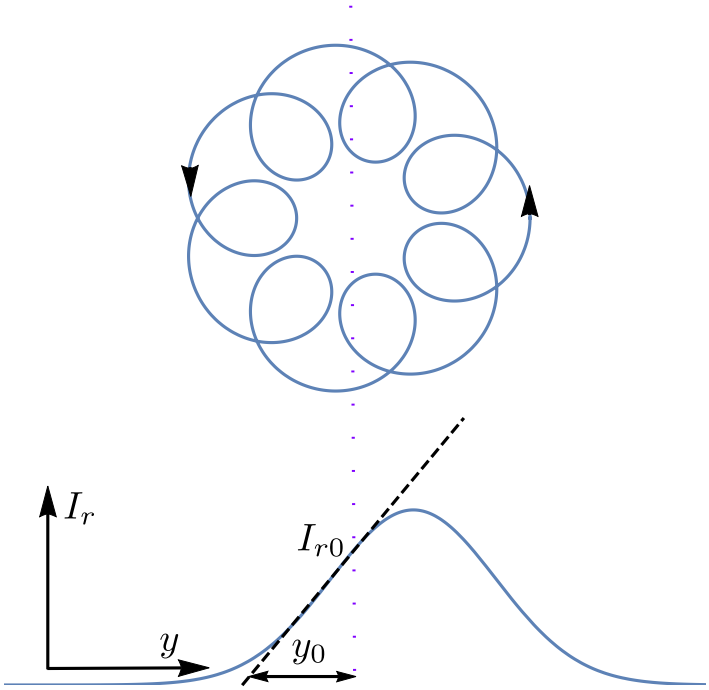

Figure 4.4: A schematic of the Doppler cooling laser in the radial plane with a Gaussian intensity profile offset from the trap centre. The linear approximation considers the intensity at the trap centre as I_{r0} giving a slope of I_{r0}/y_0. The trajectory of the ion, shown at the top, is greatly exaggerated.

cooling limit.[4]We can now write the rate equations for the mean-squared amplitudes as

$$\frac{d\langle r_i^2\rangle}{dt} = \frac{I_z}{\hbar\omega_L}\langle\sigma_z(\omega_L,\mathbf{v})\Delta r_i^2\rangle + \frac{I_{r0}}{\hbar\omega_L}\langle\left(1+\frac{y}{y_0}\right)\sigma_r(\omega_L,\mathbf{v})\Delta r_i^2\rangle \tag{4.46}$$

where $i = z,+,-$. The scattering cross section is defined from the standard solutions of the optical Bloch equations for a two level atom and is given by:

$$\sigma(\omega,\mathbf{v}) = \frac{\sigma_0(\Gamma/2)^2}{(\omega_0-\omega+\mathbf{k}\cdot\mathbf{v})^2+(\Gamma/2)^2} \approx \frac{\sigma_0(\Gamma/2)^2}{(\omega_0-\omega)^2+(\Gamma/2)^2}\left[1-\frac{2(\omega_0-\omega)\mathbf{k}\cdot\mathbf{v}}{(\omega_0-\omega)^2+(\Gamma/2)^2}\right] \tag{4.47}$$

where Γ is the resonance linewidth. The approximate expression is given by a Taylor expansion under the assumption that $\mathbf{k}\cdot\mathbf{v} \ll \Gamma$. Before proceeding we make a few useful definitions. The average scattering rates far below saturation are defined as:

$$\gamma_l = \frac{I_l\sigma_{l0}}{\hbar\omega_L}\frac{(\Gamma/2)^2}{(\Gamma/2)^2+\delta^2} \tag{4.48}$$

where $l = z,r$ and $\delta = \omega_0 - \omega_L$; here we have the same detuning for the radial and axial laser since we do not have independent control of them in our experiment. Next we define geometric

[4]One may ask what happens when ions are loaded at high temperatures or are knocked into a large orbit by a collision with a background gas molecule. Indeed it is experimentally seen that in this scenario the cooling beam, left at a small offset suitable for low final temperatures, is not ideal to cool ions in a large magnetron orbit and the ion can appear dark for minutes at a time. In this case we move the laser offset further away from the trap centre to retrieve the ions by allowing a stronger interaction with the large magnetron orbit.

factors corresponding to absorption and emission respectively:

$$f_l = \left(\hat{k}_l/k\right)^2 \tag{4.49}$$

$$f_{ls} = \sum_{\Delta m_j} p_{\Delta m_j} \int P_{\Delta m_j}(\hat{k}_s)\hat{k}_{sl}^2 d\Omega \tag{4.50}$$

where the emission is over a $d\Omega$ solid angle, $P_{\Delta m_j}$ is the distribution corresponding to a particular Δm_j transition as given in table 3.2 and $p_{\Delta m_j}$ is the probability of the decay on this transition. The rate equations now become:

$$\frac{d\langle r_i^2\rangle}{dt} = \gamma_z \left\langle \Delta r_i^2 \left[1 - \frac{2\delta k_z v_z}{(\Gamma/2)^2 + \delta^2}\right]\right\rangle + \gamma_r \left\langle \Delta r_i^2 \left(1 + \frac{y}{y_0}\right)\left[1 - \frac{2\delta k_x v_x}{(\Gamma/2)^2 + \delta^2}\right]\right\rangle \tag{4.51}$$

To perform the averaging, equations 4.42, 4.45 and 4.44 are substituted in as well as the position coordinates from 2.16 and their derivatives. What follows is a lot of algebra that is underpinned by a few key results.

- Any terms that have a combination of periodic functions that are not of the form $\sin(\omega_i t + \phi_i)^2, \cos(\omega_i t + \phi_i)^2$ average to zero.
- Terms of the form $\langle(\Delta v_{x,y,z})^2\rangle$ always contribute $\frac{\hbar^2 k^2}{\omega_i^2 m^2}(f_l + f_{ls})$
- Terms of the form $\langle \Delta v_{x,y,z}\rangle$ evaluate to $-\frac{\hbar}{km}$.

The derived rates are the following:

$$\frac{d\langle r_z^2\rangle}{dt} = \frac{\gamma_z \hbar k^2}{m}\left(\frac{\hbar}{m\omega_z^2}\left[1 + \left(1 + \frac{\gamma_r}{\gamma_z}\right) f_{sz}\right] - \frac{2\delta\langle r_z^2\rangle}{(\Gamma/2)^2 + \delta^2}\right) \tag{4.52a}$$

$$\frac{d\langle r_+^2\rangle}{dt} = \frac{\gamma_r \hbar k^2}{m}\left(\frac{\hbar}{4m\omega_1^2}\left[1 + \left(1 + \frac{\gamma_z}{\gamma_r}\right)(f_{sx} + f_{sy})\right] - \frac{\delta\omega_+\langle r_+^2\rangle}{\omega_1((\Gamma/2)^2 + \delta^2)} + \frac{\langle r_+^2\rangle}{2y_0\omega_1 k}\right) \tag{4.52b}$$

$$\frac{d\langle r_-^2\rangle}{dt} = \frac{\gamma_r \hbar k^2}{m}\left(\frac{\hbar}{4m\omega_1^2}\left[1 + \left(1 + \frac{\gamma_z}{\gamma_r}\right)(f_{sx} + f_{sy})\right] + \frac{\delta\omega_-\langle r_-^2\rangle}{\omega_1((\Gamma/2)^2 + \delta^2)} - \frac{\langle r_-^2\rangle}{2y_0\omega_1 k}\right) \tag{4.52c}$$

From 4.52a we can see that the axial motion can be cooled as long as δ is positive, corresponding to a red detuning from the transition. Based on the second terms of 4.52b and 4.52c a red detuning cools the modified cyclotron and heats the magnetron motion. Conversely, a positive offset, $y_0 > 0$ cools the magnetron, but heats the cyclotron. To achieve simultaneous cooling of both modes, the detuning and offset must obey:

$$\omega_- < \frac{(\Gamma/2)^2 + \delta^2}{2ky_0\delta} < \omega_+ \tag{4.53}$$

The cooling rates also depend on the recoil, which is given by the first term in all 4.52 equations. By solving for the steady state of these equations we can obtain expressions for the mean square amplitudes, which we can use to define temperature using 2.17 to find the energy in each mode and converting with $T = 2E_k/k_B$ and likewise using equations 2.64-2.66 to find the mean phonon

number. Using $f_{sz} = f_{sx} = f_{sy} = \frac{1}{3}$ corresponding to isotropic emission[5]

$$T_z = \frac{\hbar((\Gamma/2)^2 + \delta^2)}{4\delta k_B}\left[1 + \frac{1}{3}\left(1 + \frac{\gamma_r}{\gamma_z}\right)\right] \tag{4.54}$$

$$n_z \approx \frac{(\Gamma/2)^2 + \delta^2}{4\omega_z \delta}\left[1 + \frac{1}{3}\left(1 + \frac{\gamma_r}{\gamma_z}\right)\right] \tag{4.55}$$

$$T_+ = \frac{y_0 k \omega_+^2 \hbar((\Gamma/2)^2 + \delta^2)}{2\omega_1 k_B[2\delta\omega_+ y_0 k - ((\Gamma/2)^2 + \delta^2)]}\left[1 + \frac{2}{3}\left(1 + \frac{\gamma_z}{\gamma_r}\right)\right] \tag{4.56}$$

$$n_+ \approx \frac{y_0 k((\Gamma/2)^2 + \delta^2)}{2(2\delta\omega_+ y_0 k - ((\Gamma/2)^2 + \delta^2)}\left[1 + \frac{2}{3}\left(1 + \frac{\gamma_z}{\gamma_r}\right)\right] \tag{4.57}$$

$$T_- = \frac{y_0 k \omega_-^2 \hbar((\Gamma/2)^2 + \delta^2)}{2\omega_1 k_B[((\Gamma/2)^2 + \delta^2) - 2\delta\omega_- y_0 k]}\left[1 + \frac{2}{3}\left(1 + \frac{\gamma_z}{\gamma_r}\right)\right] \tag{4.58}$$

$$n_- \approx \frac{y_0 k((\Gamma/2)^2 + \delta^2)}{2((\Gamma/2)^2 + \delta^2) - 2\delta\omega_- y_0 k)}\left[1 + \frac{2}{3}\left(1 + \frac{\gamma_z}{\gamma_r}\right)\right] \tag{4.59}$$

We will now take these results and consider their implications for our experimental parameters. The first observation from these equations is that the ultimate temperature for the radial and axial modes depends on the relative power of the respective cooling beams γ_z and γ_r. Thus if one motion is to be preferentially cooled to near its minimum, the intensity of the laser cooling the other motion should be minimized. Furthermore, for the axial motion it is easy to minimize equations 4.54 and 4.55 giving the $\delta = \Gamma/2$ as the optimal detuning. For the radial motion, there is no simple minimisation since the radial modes are coupled. As for the axial motion, the cyclotron motion seeks a detuning $\delta = \Gamma/2$ and a large gradient parameter y_0, approaching a uniform beam, both of which heat the magnetron. Thus it is always necessary to compromise within the allowed parameter space of 4.53. Figure 4.5 shows the final average phonon numbers after cooling for a fixed y_0 as a function of red detuning from the transition. It is clear to see that the two motions have minima corresponding to the cyclotron motion and maxima corresponding to the magnetron motion at $\delta = \Gamma/2$. Looking at the 30 kHz curves in the vicinity of $\delta \approx 1.6\Gamma$, the mean phonon number of the magnetron motion has roughly fallen by 50% while for the modified cyclotron it has doubled, but in absolute terms, the total number of phonons in both modes is still almost 50% lower owing to the large initial magnetron phonon number. These results suggest that it would be best to red-detune the radial cooling laser to around $1.5-2\times\Delta$. This is, however, impractical in our experiment since we do not have independent control of the frequency of the radial and axial cooling beams and hence detuning far red will significantly reduce the fluorescence that is necessary to detect the state of the ion using the electronic shelving technique.

We also note that the cooling limit for the magnetron motion is sensitive to the trapping voltage and hence magnetron mode frequency, increasing quickly. Figure 4.6 shows how for various realistic values of y_0 the cooling limit scales with the magnetron mode frequency. The magnetron mean phonon cooling limit begins an order of magnitude hotter than the cyclotron and increases rapidly with applied voltage for larger y_0. A smaller y_0, and consequently a very steep gradient that requires a tight beam focus, leads to a shallower rate of change allowing a greater range of accessible frequencies. Note that for the green and red curves corresponding

[5]This corresponds to equal likelihood of emission for $\pi, \sigma^{\pm}$ transitions, which can be easily obtained by looking at the Clebsch-Gordan coefficients in [117]. There are two π transitions with a probability 1/6 and one $\sigma^{\pm}$ transition with 1/3 probability each. We neglect any effects due to repumping.

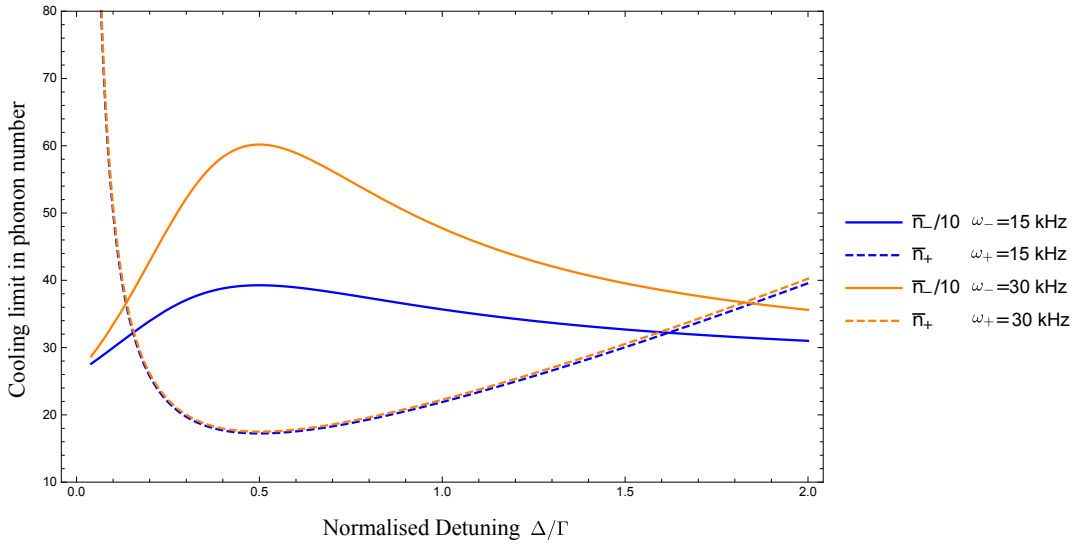

Figure 4.5: The mean phonon number as a function of red-detuned laser frequency normalised to the transition linewidth for a beam offset parameter $y_0 = 15\mu$m and $\gamma_z/\gamma_r = 0$. Curves for the cyclotron and magnetron mean phonon numbers are shown as dashed and solid lines, respectively. Note that the magnetron phonon numbers are reduced by a factor of 10.

to $y_0 = 40\mu$m and $y_0 = 20\mu$m the magnetron phonon mean goes negative, implying cooling is no longer possible in this model. This is a limitation of the model and such behaviour is not reproduced experimentally. This can interpreted as a breakdown of the $y \ll y_0$ condition as can be seen in figure 4.7 where this ratio sharply increases for various detunings making this description inadequate for larger y_0 values.

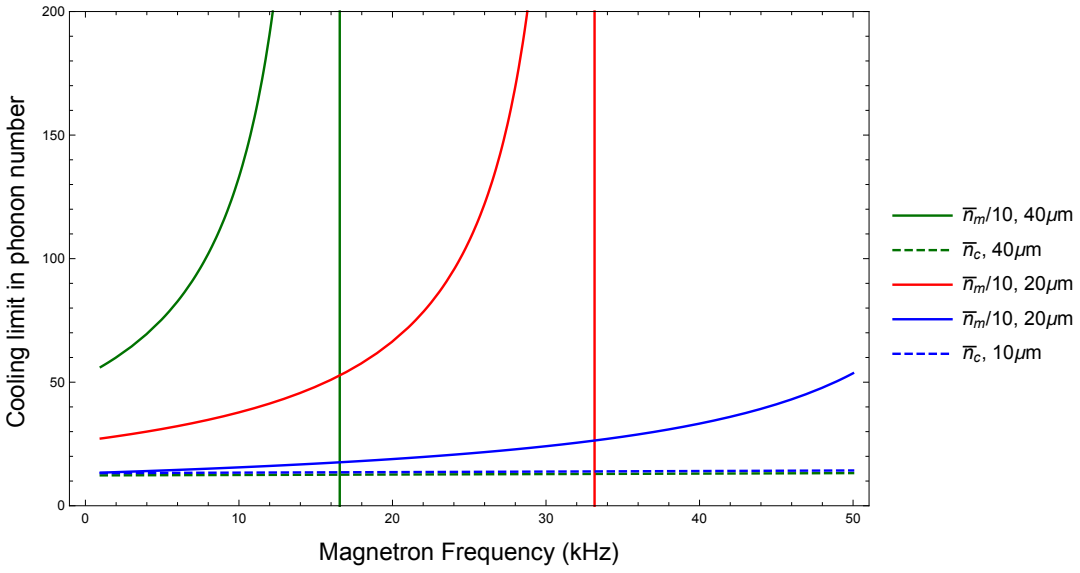

Figure 4.6: The mean phonon number as a function of magnetron frequency at various beam offset parameters and $\gamma_z/\gamma_r = 0$. Curves for the cyclotron and magnetron mean phonon numbers are shown as dashed and solid lines, respectively. The vertical lines for the red and green curves intersecting zero show the limit of cooling stability. Note that the magnetron phonon numbers are scaled down by a factor of 10.

Since the final aim is for the Doppler cooling to prepare the ion for sideband cooling where each of the sidebands has to be effectively resolved, larger magnetron frequencies are desirable.

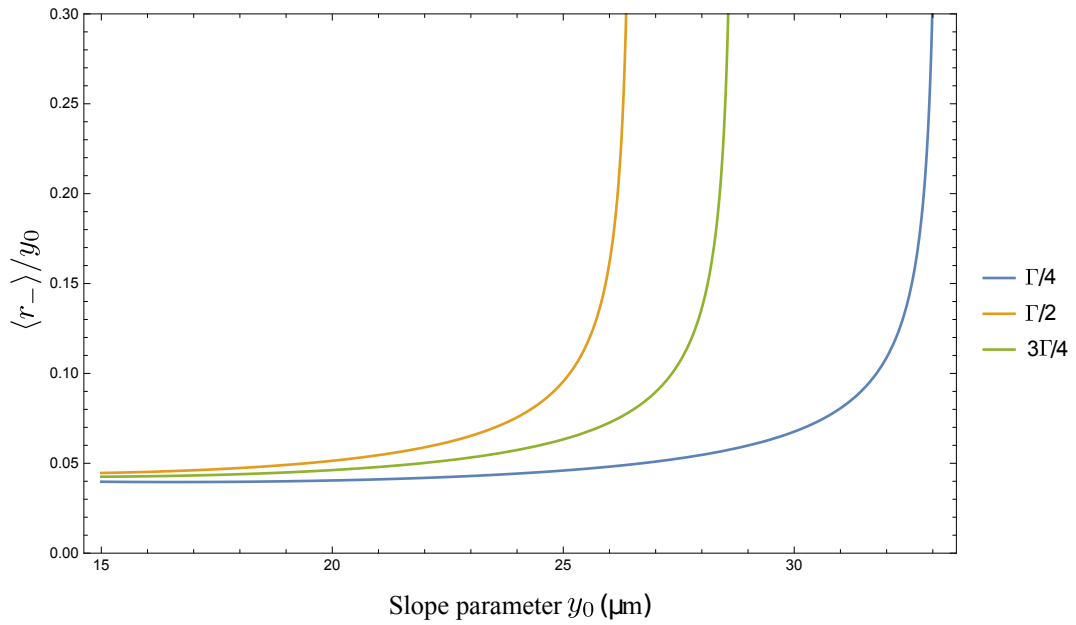

Figure 4.7: The magnetron amplitude to y_0 ratio as a function of y_0 shows a sharp increase for various red laser detunings as a fraction of the linewidth Γ. $\gamma_z/\gamma_r = 0$

Ultimately, the use of a very tight beam necessary to achieve a small y_0 is limited by other practical considerations. Cooling freshly loaded ions that have large magnetron amplitudes becomes difficult as the beam only weakly interacts with them. Similarly, if during the cooling sequence there is any larger perturbation such a collision with a background gas or an unlocking of the lasers that leads to the magnetron amplitude increasing, recooling becomes difficult. This makes running the experiment in a stable configuration for hours at a time necessary to obtain quality spectra very difficult.

4.3.2 Axialization

The results of the previous section demonstrate that to achieve mean phonon numbers of the magnetron mode after Doppler cooling that are amenable to sideband cooling to the ground state, use of the offset beam technique is often not sufficient. A different method that exploits the efficient cooling of the modified cyclotron motion by coupling it to the magnetron motion promises a more reliable method of achieving this goal. To achieve this effect, we generate a quadrupolar potential of the form:

$$\phi_{ax} = \frac{V_a}{2r_0^2}(x^2 - y^2)\sin(\omega_c t + \phi_0) \tag{4.60}$$

by applying a voltage V_a oscillating at the cyclotron frequency ω_c, which is the sum of the magnetron and modified cyclotron frequencies, to the 4 segments of the ring electrodes of radius r_0 with a π phase shift between adjacent electrodes. Including this potential in the equations of radial motion 2.7 gives:

$$\ddot{u} + i\dot{u}\omega_c - \left(\frac{\omega_z^2}{2} - i\frac{eV_{ax}}{Mr_0^2}\sin(\omega_c t + \phi_0)\right)u = 0 \tag{4.61}$$

While we can't solve this equation analytically in the lab frame, we will consider a more intuitive approach of reference [141] that assumes an instantaneous power absorption $P(t)$ where the coupling of the driving field is sufficiently weak so that the motional amplitudes remain approximately constant over the course of a period of the relevant motion. The instantaneous power is then given by:

$$P(t) = q\nabla\phi_{ax} \cdot \mathbf{v} = \frac{qV_a}{r_0^2} \sin(\omega_c t + \phi_0) \left[r_+^2 \omega_+ \sin(2\omega_+ t) + r_-^2 \omega_- \sin(2\omega_- t) + r_+ r_- \omega_c \sin(\omega_c t)\right] \tag{4.62}$$

where we have used equations 2.16 and their derivatives. Now we can see that a resonant excitation with $\phi_0 = 0$ averaged over one period of ω_c gives an average change of total power:

$$\frac{dE_{tot}}{dt} = \frac{qV_a r_+ r_- \omega_c}{2r_0^2} \tag{4.63}$$

where the first two terms average to zero. Now the total power must also equal the sum of the individual mode powers:

$$\frac{dE_{tot}}{dt} = \frac{dE_+}{dt} + \frac{dE_-}{dt} \tag{4.64}$$

which are related by:

$$\omega_+ \frac{dE_+}{dt} = \omega_- \frac{dE_-}{dt} \tag{4.65}$$

when excited by RF at ω_c. The derivatives can be obtained by differentiating the total energy equation 2.19 and then substituted along with equation 4.65 into the total power equation 4.63 to obtain coupled equations:

$$\dot{r}_+ = \frac{qV_a}{4M\omega_1} r_- \tag{4.66}$$

$$\dot{r}_- = \frac{qV_a}{4M\omega_1} r_+ \tag{4.67}$$

The solutions of these equations are simple sinusoidal oscillations of the amplitudes with frequency:

$$\omega_a = \frac{eV_a}{4Mr_0^2\omega_1} \tag{4.68}$$

An example of the ion trajectory under the influence of axialization is show in figure 4.8 where the amplitude of the two motions exchange magnitude in time.

Since the two motions continuously exchange energy, then in a time averaged measurements the amplitudes should be in equilibrium $\langle r_+ \rangle = \langle r_- \rangle$. However, if we introduce a laser that can efficiently cool the cyclotron motion faster than the magnetron, we will approach a new equilibrium of amplitudes that can significantly reduce the mean number of phonons in the system. Published work with analytical models used a coordinate transformation of the equations of motion to a frame rotating at $\omega_c/2$ to demonstrate that axialization is a resonant process that can significantly increase the damping rate of the magnetron motion in the presence of laser cooling [142], but does not provide cooling limits. Since we cannot analytically solve this equation, we cannot repeat the analysis of the previous section to find the limits. Instead, in section 8.1 we will take a Monte-Carlo approach to integrating equation 4.61 under the presence of a laser beam

In the mean time, we can think about the cooling under the effect of axialization as an

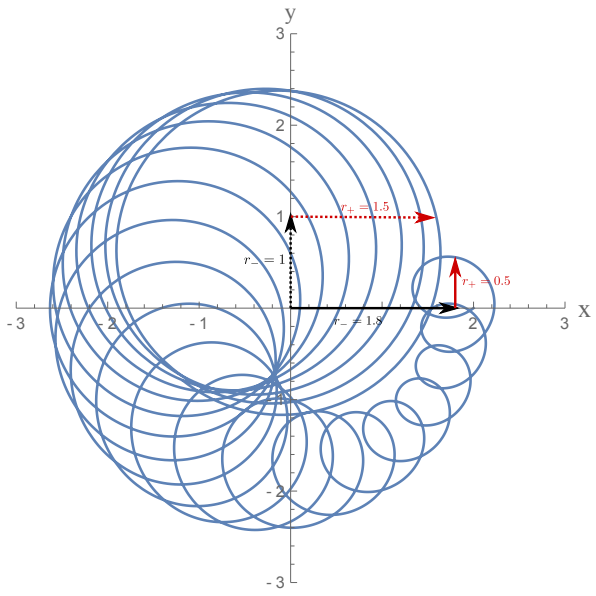

Figure 4.8: Radial trajectory of an ion under the influence of a weak axialization field. The ion is initialised to have a $r_- > r_+$ at $t = 0$ and $x = 0$. The axialization drive coherently exchanges the amplitudes of the motion so that later on $r_- > r_+$. The solid arrows represent the initial amplitudes, while the dashed arrows represent the final amplitudes. Axes in arbitrary units of position.

RF field driving the transition $\phi_{ax}|n_+, n_-\rangle \rightarrow |n_+ + 1, n_- - 1\rangle$ followed by frequency selective Doppler cooling removing phonons from the modified cyclotron mode at a rate faster than the magnetron is heated. Under these conditions, the net effect of the axialization drive and laser cooling is for a removal of phonons from both modes. A diagram of the process is shown in figure: 4.9.

4.4 Sideband Cooling

Sideband cooling is an effective technique that targets motional sidebands of a particular mode to remove phonons from it. Unlike Doppler cooling, sideband cooling is typically performed in the strong binding regime where $\Gamma \ll \omega_T$ (either an electric quadrupole transition or Raman process), hence when using a narrow linewidth laser $\Delta_{\omega_L} \ll \omega_T$ the motional sidebands can be resolved and addressed with very little off-resonant excitation of other modes or the carrier transition. Targeting red motional sidebands removes a number of phonons corresponding to the sideband order. After excitation, the decay on average preserves the motional state since the Rabi coupling strengths from equation 4.27 are almost symmetric for $\Omega_{n,n+l} \approx \Omega_{n,n-l}$. Furthermore, as the quantum number is reduced to within the Lamb-Dicke regime, the sideband decays are suppressed compared to the carrier as seen in equations 4.31 – 4.35. This means that after many iterations of absorption and decay, the targeted mode can be driven all the way to the ground state after which there is no further lower motional level. A diagram of the process is seen in figure 4.10.

To describe the principle in more detail, it is instructive to just focus on the axial motion of a single $^{40}Ca^+$ ion first. We use the narrow linewidth ($1.1/2\pi$ Hz) $S_{1/2} \rightarrow D_{5/2}$ transition detuned by ω_z to the red of the carrier to drive the transition $|g, n\rangle \rightarrow |e, n-1\rangle$ transition. Due to the very long lifetime of the $D_{5/2}$ state any cooling cycle relying on the spontaneous

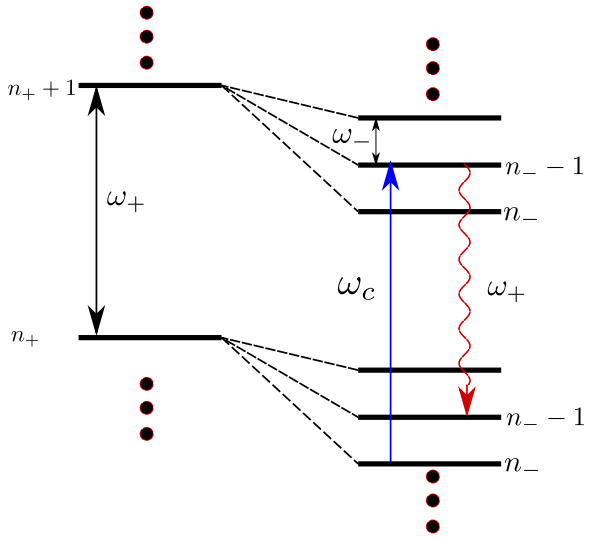

Figure 4.9: A schematic diagram showing the modified cyclotron and magnetron phonon state ladder with the axialization drive and Doppler cooling transitions. The Doppler cooling is shown as a wavy line to indicate it is a stochastic process via intermediate excite electronic states, whereas the axialization is a coherent drive.

decay of this state would be unreasonably slow, in fact much slower than the heating rate of the trap, hence a quench laser is used to drive the dipole allowed transition $D_{5/2} \rightarrow P_{3/2}$, which can then decays back to the $S_{1/2}$ state in a few nanoseconds. This kind of broadening scheme is called the cascade scheme and has been studied in detail for RF traps [143]. Figure 4.11 shows a diagram of the relevant energy levels and transitions. Provided that the quench laser Rabi frequency Ω_{854} isn't too high to saturate the transition, this scheme adiabatically eliminates the $P_{3/2}$ state to give an effective two level system with the excited state effective linewidth given by

$$\tilde{\Gamma} = \frac{\Omega_{854}^2}{(\Gamma_{854} + \Gamma_{393})^2 + 4\delta_{854}^2}\Gamma_{393} \tag{4.69}$$

tunable by the quench laser detuning δ_{854} and Rabi frequency Ω_{854}. This flexibility allows the parameters to be set to either maximize the cooling rate or alternatively minimize the final mean phonon number.

The quench beam also produces an ac Stark shift

$$\delta_{ac} = \frac{\Omega_{854}^2}{(\Gamma_{854} + \Gamma_{393})^2 + 4\delta_{854}^2}\delta_{854} \tag{4.70}$$

which is often larger than the Rabi frequency on the red sidebands $\eta_z\Omega_{729}$ so that in the experimental realisation of this scheme care must be taken to measure and compensate for this shift by adjusting the 729 nm laser frequency. Similarly, the 729 nm laser will also create a further Stark shift of magnitude $\Omega_{729}^2/2\omega_z$.

4.4.1 Sideband Cooling Outside the Lamb-Dicke Regime

The previous section described the simplest method of sideband cooling where the laser only excites on the first red sideband and even in the presence of weak diffusion upon decay the population is eventually driven to the ground state of motion. This method, however, fails to successfully cool ions outside of the Lamb-Dicke regime. An implicit consequence of the Lamb-

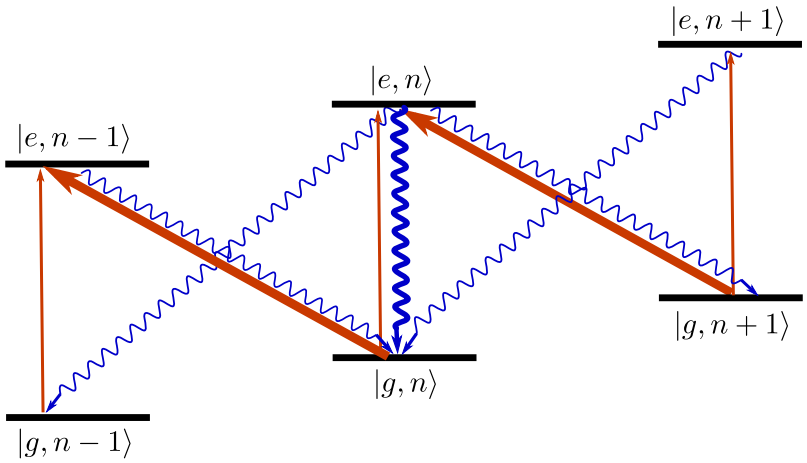

Figure 4.10: Two level atom schematic of the sideband cooling process showing all the first order couplings to the n state when the narrow linewidth cooling laser is resonant with the first red sideband. Off resonant excitation of the carrier is included. The thickness of the curves indicates the strength of the coupling.

Dicke regime is that for all the phonon states in the thermal distribution prepared by Doppler cooling, there is an appreciable coupling strength on the first red sideband. However, equation 4.27 tells us that the coupling strength depends on Laguerre polynomials that have minima very close to zero at particular phonon states. Thus if the Doppler cooled population distribution has an appreciable population above this minimum phonon state of the first red sideband, this population will accumulate in this state rather than reaching the ground state. We refer to this phenomenon as population trapping. The position of these minima is solely determined by the Lamb-Dicke parameter, getting further away from zero as the parameter is decreased. Since the Lamb-Dicke parameter scales with the inverse of the trap oscillation frequency, increasing the frequency mitigates this problem. Furthermore, the mean phonon number also depends inversely on the trap frequency (eq. 4.55), exacerbating the trapping at low frequencies. Figure 4.12 shows the coupling strengths of various sidebands at different axial trap frequencies with the thermal phonon distribution after Doppler cooling overlaid. In the 400 kHz example, the population above the first red sideband minimum is negligible, whereas for 160 kHz it is 32%. These plots also immediately suggest a solution to the problem, which is to incorporate higher order sidebands into the cooling sequence since the minima of their respective couplings never occur at the same phonon number.

We can consider what happens with two modes as is the case in either a two-ion crystal or the radial motion of a single ion. Extending the simple method of cooling one mode, the laser can be tuned to the red sideband of one mode followed by the other, cooling them independently. The total coupling strength is now the product of the couplings of each mode as in equation 4.37. This means that if we target the first red sideband of one mode, we are also in effect performing a carrier transition in the other mode. Thus not only does the problem become one of the red sideband couplings of each mode approaching zero, but also the coupling to the red sideband of one mode can be strongly suppressed by being in a phonon state near the minimum of the carrier coupling of the other mode. The challenge is then to find a path that can most effectively navigate from large phonon states of both modes of motion, avoiding trapping in both dimension on the red sidebands as well as the carrier. It can be seen that, unlike for the

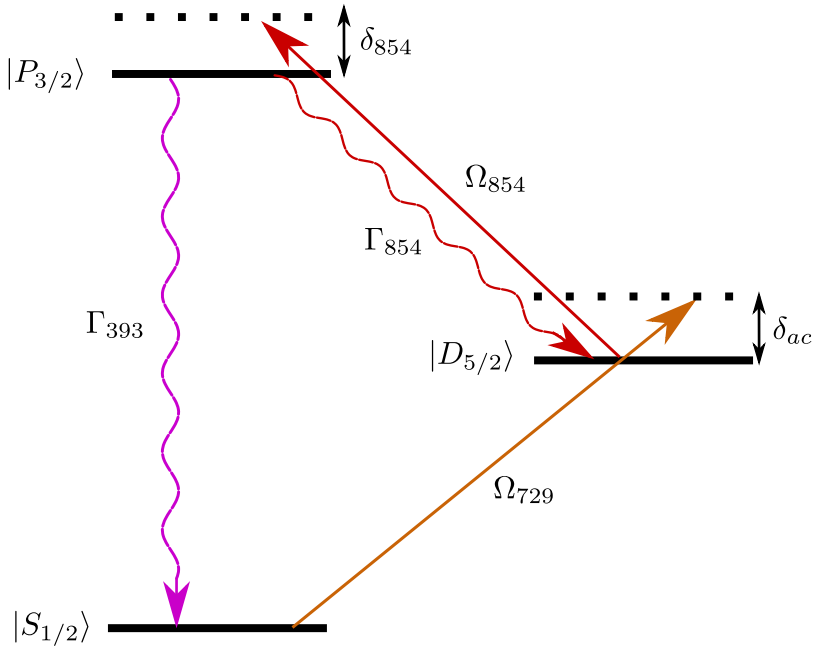

Figure 4.11: Cascade broadening scheme in a simplified $^{40}Ca^{+}$ energy level diagram.

red sidebands, no process directly drives population into the carrier minima, but population can still drift into these minima through diffusion upon decay, which is prominent at high phonon numbers outside the Lamb-Dicke regime. Thus when one mode is cooled, it can cause the phonon state of the other mode to drift into a carrier minimum. To construct a robust pulse sequence to protect from all these minima thus requires not only higher order sidebands of each mode, but also at least one sideband that changes both phonon modes simultaneously. This is evident from the contour plots of the coupling strength in figure 4.13 for a two-ion chain with $\omega_{COM}/2\pi = 162$ kHz. Plots (a) and (b) show that for each individual mode respectively, averaging over the coupling strengths of higher order sidebands is sufficient to drive the phonon number down, provided the carrier coupling of the other mode is not weak, which is the case at $n_B \approx 80$ and $n_{COM} \approx 50$ for (a) and (b) respectively. If we average these two plots, we obtain the contour plot in (c), which clearly shows a coupling minimum where the above mentioned carrier coupling minima of the modes overlap. To overcome this, we can use a pulse such as in (d) that changes $\Delta n_{COM} = -1, \Delta n_B = -2$. Now when we average (a), (b) and (d), we see that in plot (e) the minimum coupling grows stronger. For different frequencies and Lamb-Dicke parameter values, we can use this approach of averaging over sideband coupling strengths to design pulse sequences that will prevent population trapping. This is also applicable for the cooling of the magnetron and cyclotron modes of the radial motion of a single. Since these two motions have the same Lamb-Dicke parameter, the contour plots of each sideband would appear symmetric.

4.4.2 Sideband Cooling Limit

We will now perform a new analysis to find the final ground state occupation after sideband cooling in a Penning trap. To do so we must consider the probability of the individual steps of the cooling cycle to alter the phonon number, as well as the probability of unwanted off resonant exciation. The final mean phonon number is not only limited by off resonant absorption on the

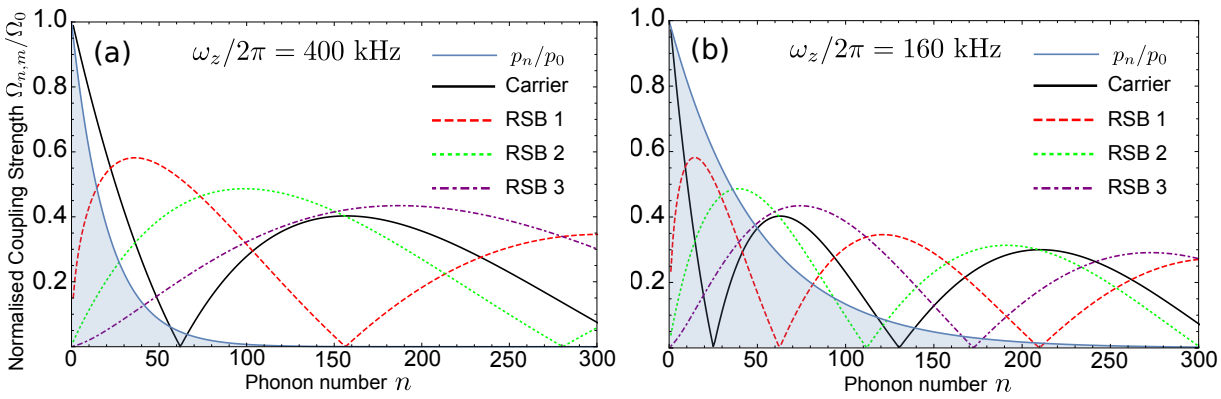

Figure 4.12: Plots of the normalised coupling strengths of the carrier and first three red sidebands. (a) 400 kHz and (b) 160 kHz axial trapping frequency. The scaled occupation probability per phonon state based on the Doppler limit thermal distribution is overlaid in the solid fill. In (a) only 0.4% of the population resides above the zero of the first red sideband, whereas in (b) it is 32%

blue sidebands, but also absorption on the carrier followed by the absorption and emission of photons during the process to return the ion to the correct Zeeman sublevel of the $S_{1/2}$ state involving decay and absorption at 854 nm, 393 nm and 397 nm. We shall assume that these processes are instantaneous on the timescale of the 729 nm absorption. To find the final population distribution, we have to construct a set of rate equations between all the relevant couplings and solve for the steady state condition. We can write down the full set of rate equations for a laser detuned by δ from the first red sideband:

$$\begin{aligned}\frac{dp_n}{dt} = &- \sum_{m=n-\Delta n}^{m=n+\Delta n} \sum_{\substack{r=m-\Delta n \\ r\neq n}}^{r=m+\Delta n} p_n \frac{\tilde{\Gamma}\Omega_{n,m}^2 D_{m,r}}{2\Omega_{n,m}^2 + \tilde{\Gamma}^2 + 4((1+m+k)\omega_z)^2} \\ &+ \sum_{\substack{k=n-\Delta n \\ k\neq n}}^{n+\Delta n} \sum_{m=k-\Delta n}^{m=k+\Delta n} p_k \frac{\tilde{\Gamma}\Omega_{k,m}^2 D_{m,n}}{2\Omega_{k,m}^2 + \tilde{\Gamma}^2 + 4((1+m+k)\omega_z)^2}\end{aligned} \tag{4.71}$$

where we have summed over laser excitation to the nearest $\pm\Delta N$ phonon states next to a given state p_n, with a Rabi coupling Ω corresponding to absorption at 729 nm and a diffusion coefficient D corresponding to normalised sum of the decay and absorption probabilities at the aforementioned cooling cycle frequencies (we shall define this term more precisely shortly). From here we can proceed in two ways:

- Assume that only the p_1 state retains any significant population outside the ground state and hence consider only first order couplings. After making the further approximation of well resolved sidebands and small effective linewidth ($\Omega_0^2 \ll \omega_z$ and $\tilde{\Gamma}^2 \ll \omega_z$) this system of rate equations can be solved analytically.

- Numerically solve the rate equations 4.71 including states up to p_N and higher order couplings Δn. This approach will be important as ω_z gets small, resulting in large Lamb-Dicke parameters and stronger off-resonant coupling.

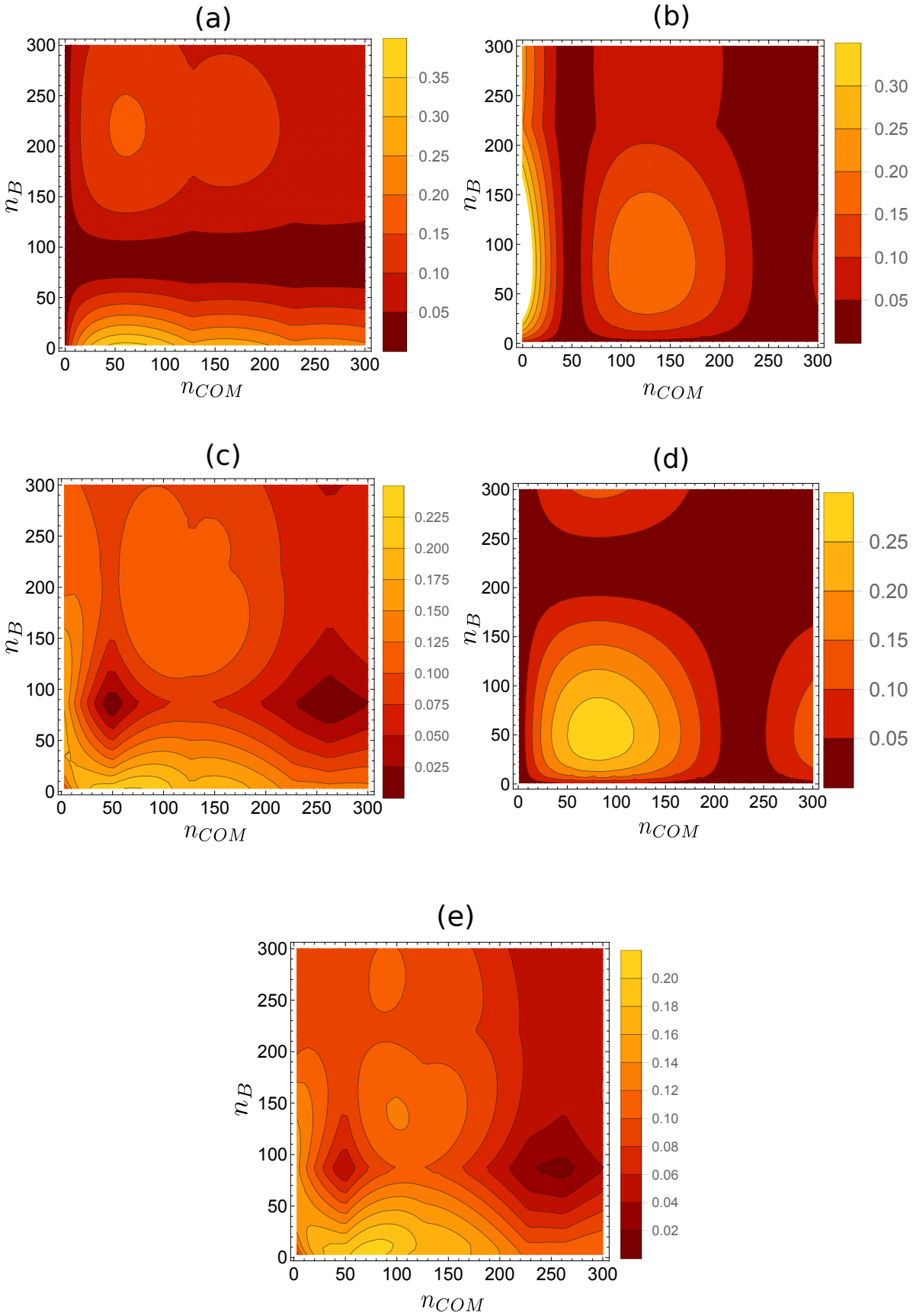

Figure 4.13: Plots of the normalised coupling strengths at $\omega_{COM}/2\pi = 162$ kHz kHz as a function of phonon number of (a) the average of the first three red sidebands of the COM mode, (b) the average of the first two red sidebands of the breathing mode, (c) the average of (a) and (b), (d) the $\Delta n_{COM} = -1$ $\Delta n_B = -2$ sideband and (e) the average of (a), (b) and (d).

We begin by first deriving the analytical solution. From 4.71 we can write:

$$\frac{dp_0}{dt} = -\sum_{m=0}^{m=1} p_0 \frac{\Omega_{0,m}^2 D_{m,1}}{4((1+m)\omega_z)^2} + p_1 \frac{\Omega_{1,0}^2 D_{0,0}}{\tilde{\Gamma}}$$
$$\frac{dp_1}{dt} = -\frac{dp_0}{dt}$$

The solution of these equation at equilibrium for p_0 is:

$$\bar{n} \approx \left(\frac{\tilde{\Gamma}}{2\omega_z}\right)^2 \left(\frac{1}{4} + \frac{\Omega_{0,0} D_{0,1}}{\Omega_{1,0} D_{0,0}}\right) \tag{4.72}$$

We now need to carefully define what the diffusion parameter is. In principle, any transition that takes place after the ion gets excited by a 729 nm photon to the $m_j = -3/2$ of the $D_{5/2}$ manifold and before returning to the correct $m_j = -1/2$ Zeeman sublevel of the $S_{1/2}$ can change the motional state. The first approximation we make is that we neglect any decays into the $D_{3/2}$ and $D_{5/2}$ states since their branching ratios are over ten times smaller than to the $S_{1/2}$ states. Thus the limiting steps will only involve the 854 nm quench absorption, emission at 393 nm and potential steps of repumping at 397 nm and subsequent decay at 397 nm. These transitions and their associated probabilities are show in figure 4.14. To construct the diffusion

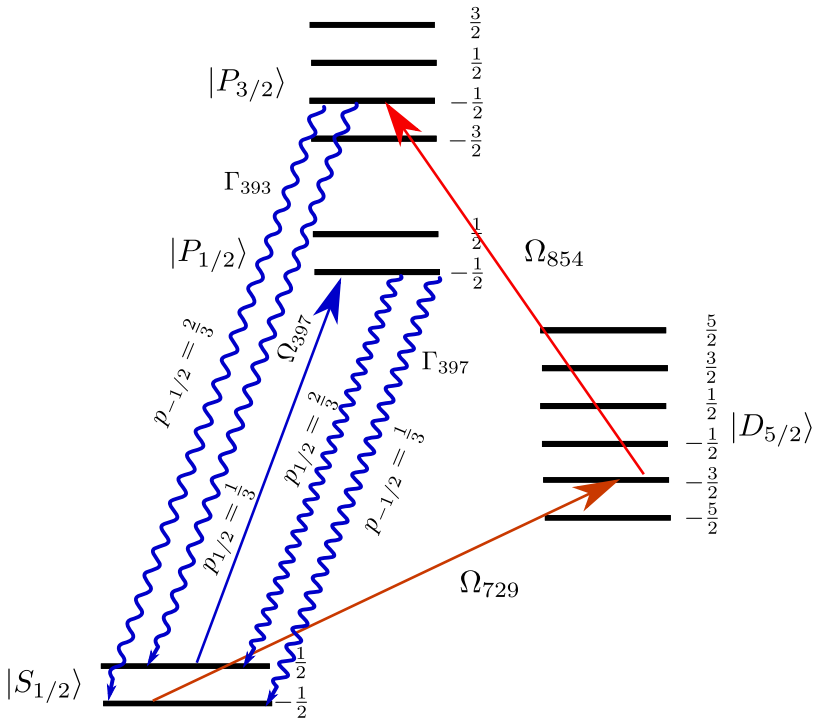

Figure 4.14: Transitions in the sideband cooling sequence that limit the final mean phonon number for $^{40}Ca^+$. Zeeman splitting not drawn to scale and 866 repumping omitted.

parameter requires a probability tree sum over normalized transitions probabilities which we will denote $\Omega_{n,m}(\eta)'$ with $\tilde{\eta}$ indicating decay. The sum over all branches is given by:

$$P = \Omega_{n,m}(\eta_{854})^2 \Omega_{n,m}(\tilde{\eta}_{393})^2 \left[\frac{2}{3} + \frac{1}{9}\sum_{k=0}^{\infty}\left(\frac{2}{3}\right)^k \left(\Omega_{n,m}(\eta_{397})^2 \Omega_{n,m}(\tilde{\eta}_{397})^2\right)^{k+1}\right] \tag{4.73}$$

To obtain the diffusion parameter from this term would in principle require a sum over all the possible combinations of the transitions that lead to the desired Δn. While this full form of the diffusion coefficient is useful when considering a Monte-Carlo type simulation, it is unwieldy in a rate equation approach. To make this problem tractable we instead use an ordered sum over of all transitions that change the phonon state by up to $|\Delta n|$, keeping those combinations that give the desired final phonon number. Care must be taken to order so that any preceding transition modifies the initial phonon state of the next transition. As an example, for a total phonon number change $\Delta n = 1$ the first term of equation 4.73 would become $\Omega_{m,m+1}(\eta_{854})^2\Omega_{m+1,m+1}(\tilde{\eta}_{393})^2 + \Omega_{m,m}(\eta_{854})^2\Omega_{m,m+1}(\tilde{\eta}_{393})^2$. Additional terms get exponentially smaller, but can still contribute and are not negligible for $\Delta n > 1$. To simplify the problem further and remove the sum to infinity, we can consider the fact that it takes on average three cycles of repumping on the 397 nm transition to return to the correct $S_{1/2}$ Zeeman sublevel, which cancels out with the one third probability of beginning in the wrong sublevel, so on average each possible transition takes place once. The approximate sum over all branches is then given by:

$$P \approx \Omega_{n,m}(\eta_{854})^2\Omega_{n,m}(\tilde{\eta}_{393})^2\Omega_{n,m}(\eta_{397})^2\Omega_{n,m}(\tilde{\eta}_{397})^2 \tag{4.74}$$

This approximation has the effect of removing some of the possible higher order combinations in 4.73 for $k > 1$, but these terms get small exponentially with k. The diffusion coefficient can thus be defined as:

$$D(n,m) = \sum_{\substack{i,j,k=-\Delta n \\ -\Delta n<i+j+k+n-m<\Delta n}}^{\Delta n} \Omega_{n,n+i}(\eta_{854})^2\Omega_{n+i,n+i+j}(\tilde{\eta}_{393})^2\Omega_{n+i+j,n+i+j+k}(\eta_{397})^2\Omega_{n+i+j+k,m}(\tilde{\eta}_{397})^2 \tag{4.75}$$

Returning to the the analytical solution 4.72, we can make the further assumption that we are in the Lamb-Dicke regime, and thus $D(0,0) = \Omega_0$ while $D(0,1) = \eta_{854}^2 + \tilde{\eta}_{393}^2 + \eta_{397}^2 + \tilde{\eta}_{397}^2$ giving the final result:

$$\bar{n} \approx \left(\frac{\tilde{\Gamma}}{2\omega_z}\right)^2 \left(\frac{1}{4} + \frac{\eta_{854}^2 + \tilde{\eta}_{393}^2 + \eta_{397}^2 + \tilde{\eta}_{397}^2}{\eta_{729}^2}\right) \tag{4.76}$$

Before moving to the numerical description, we have to also define the Lamb-Dicke parameters carefully. For the 854 nm absorption, there is no change, however for the 397 nm absorption the Lamb-Dicke parameter is reduced by a factor of $\sqrt{2}$ if we assume an equal scattering rate from the radial laser since a radial absorption won't change the axial phonon number. The decay Lamb-Dicke parameters are modified based on the average probability of decay in the z direction. We use the probabilities listed in figure 4.14 as well as the standard emission patterns of dipole transitions to evaluate the geometric factor given in equation 4.50 to obtain:

$$\eta_{397d} = \sqrt{f_{sz}}\eta_{397} = \frac{\eta_{397}}{\sqrt{3}} \tag{4.77}$$

$$\eta_{393d} = \sqrt{f_{sz}}\eta_{393} = \frac{2}{\sqrt{15}}\eta_{393} \tag{4.78}$$

To find out the discrepancy between this analytical result and one where higher order couplings are considered, we solve the rate equation 4.71 up to $N = 8$ phonon states for $\Delta n = 1, 2, 3$ with $\Omega_0 = 40$ kHz and $\tilde{\Gamma} = 40$kHz. From the resulting plots in figure 4.15, we see that all the models agree to within $\bar{n} \approx 1\%$ for axial frequencies above 250 kHz. At lower frequencies,

when the Lamb-Dicke condition is not satisfied, significant population accumulates outside the ground state due to both higher off-resonant coupling and stronger decay rates that alter the phonon state. The plot also shows that higher order couplings up to the third order are necessary to capture the full population dispersion at low frequencies. To achieve the lowest

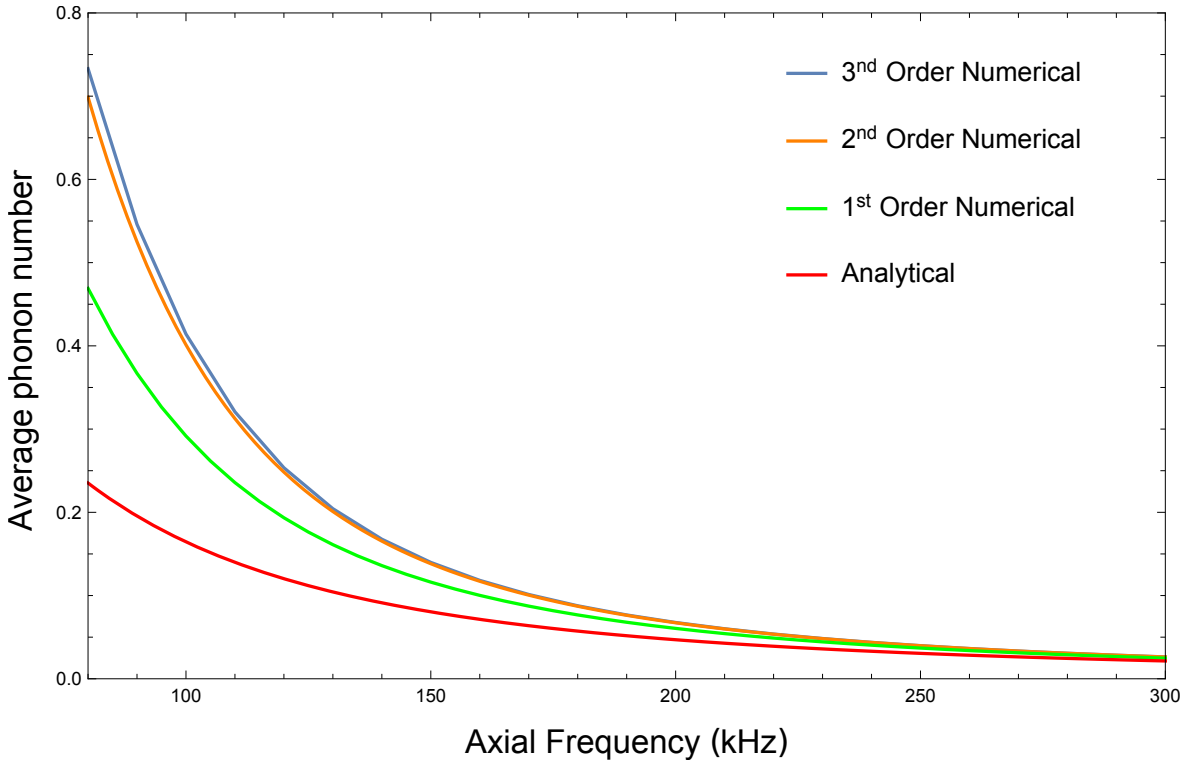

Figure 4.15: Comparison of the analytical cooling limit of equation 4.76 to the steady state solution of equation 4.71 at $\Omega_0 = 40$ kHz and $\tilde{\Gamma} = 40$kHz.

limits, at any trapping frequency, the analytical model prescribes the reduction of the effective linewidth parameter, trading off cooling speed for final temperature. However, the results of the numerical solution suggest that the 729 nm Rabi frequency also begins to be important at lower frequencies. Experimentally it is difficult to change $\tilde{\Gamma}$ during a sequence and not have secondary effects due to the Stark shift change, however turning down the 729 nm laser power for the final stage of the cooling sequence is an easy way to maintain a swift cooling rate and a low final mean phonon number.

4.4.3 Sideband cooling limits with multiple modes

Multiple modes can appear in a Penning trap system either when considering the two radial modes of a single ion, or the modes of ion Coulomb crystals. In both cases we have to consider the total generalised Rabi frequency as the product of the Rabi matrix elements of each mode. This means that when we can drive transitions that cool modes simultaneously such as the red breathing mode sideband of the red centre of mass sideband of the carrier $\Omega_{n,n-1}\Omega_{m,m-1}|n,m\rangle \rightarrow |n-1,m-1\rangle$. For ion chains this is usually unnecessarily slow since the coupling now scales as η^2 hence the bulk of the cooling is performed by alternating between the different red sidebands that only change the motion of one mode at a time, with the pulses that change both modes reserved for pumping out trapped states. On the other hand, the larger starting $\bar{n}$ for the magnetron mode can benefit from the use of these higher order transitions in

the cooling sequence. For the cooling limits we are just interested in the final stage hence we separate the analysis for different scenarios.

- Two-ion chain

  The breathing mode is separated by $\sqrt{3}\omega_z$ away from the carrier and the Lamb-Dicke parameter is scaled by $\eta_B = 12^{-\frac{1}{4}}\eta$. The centre of mass Lamb-Dicke is $\eta_{COM} = 2^{-\frac{1}{2}}\eta$. This means that effectively both modes should cool to a lower limit at the same frequency compared to a single ion. The other major difference is that when cooling on one mode, the re-emission on decay can heat up the other mode. This additional pathway to decay into the other mode actually lowers the cooling rate since higher phonon states in the other mode lower the carrier transition coupling, but it does not affect the final mean phonon number for the mode being cooled. The implication of this fact is that to get both modes near the ground state, the cooling sequence needs to alternate between cooling on the two modes with the one receiving the final cooling steps getting closer to the ground while the other mode heats up. Figure 4.16 shows the linear evolution of the mean phonon number of one mode, given that the second mode is cooled to the ground state and off resonant excitation is dominated by carrier absorption. Due to the lower heating rate on the centre of mass mode, the final cooling step should be performed on the breathing mode and should be as short as possible to achieve the minimum reheating.

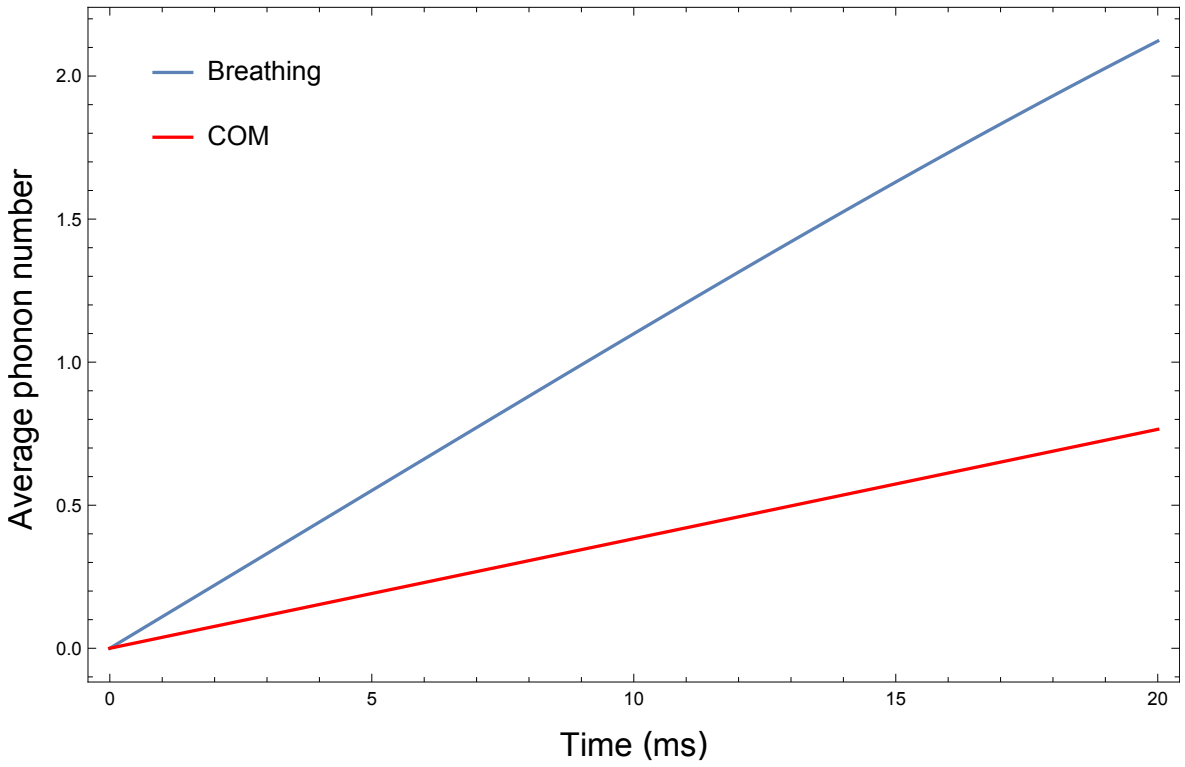

Figure 4.16: Reheating of modes due to off resonant carrier excitation when laser is set to the first sideband of the other mode. Simulation parameters: $\omega_z = 168$ kHz, $\Omega_0 = 40$ kHz, $\tilde{\Gamma} = 40$kHz.

- Axial modes of planar crystals

  The planar modes investigated in this thesis are typically much further in frequency separation from the carrier than from the COM mode. For small ion crystals of 2-5 ions the

mode separation from the COM mode can be set to $\sim \eta\Omega_0$ (by controlling the rotation frequency) allowing for simultaneous cooling of these modes with a laser placed at a single frequency. Since nearby modes cool off-resonantly, they will have slightly larger average phonon limits. Figure 4.17 shows an example of off-resonant cooling limits for parameters typically used in cooling crystals. As the number of ions grows, increasing Ω_0 helps the off resonant cooling process, but eventually the separation is large enough that the modes become well resolved and need to be cooled by sequentially tuning the laser to the appropriate red sidebands.

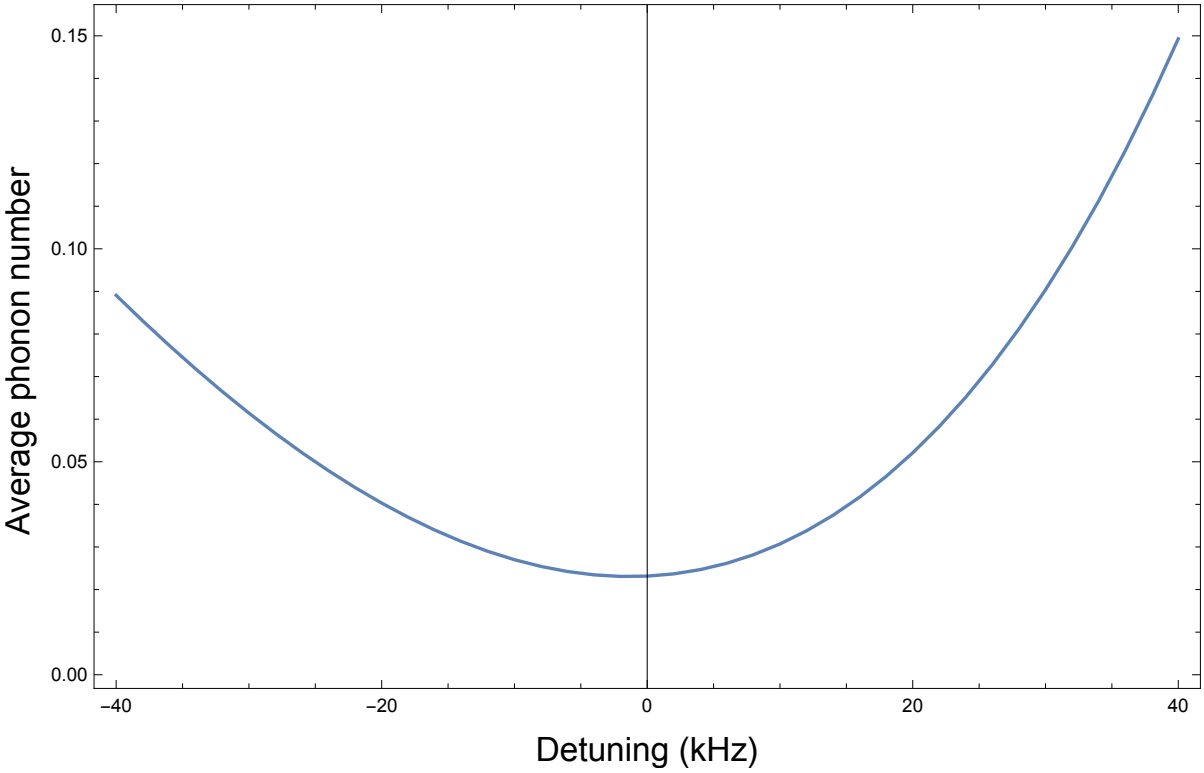

Figure 4.17: Cooling limit as a function of detuning from the first red sideband. Third order simulation parameters: $\omega_z = 168$ kHz, $\Omega_0 = 40$ kHz, $\tilde{\Gamma} = 40$ kHz.

- Radial modes of a single ion

  The cyclotron mode is always well separated from the carrier, with frequencies $> \omega_c/2$, however, the magnetron usually has frequencies $\omega_- < \Omega_0$ hence directly cooling the magnetron introduces significant carrier excitation as well as off-resonant red sideband excitation.[6] The upside is that the Lamb-Dicke parameter of the magnetron depends on the frequency of ω_1 rather than ω_- which means that even at low ω_- frequencies it remains small. Furthermore, we can also assume that all absorption at 854 nm is just from a single axial beam. The emission patterns then give the radial Lamb-Dicke parameters:

$$\eta_{397d} = \sqrt{f_{sx} + f_{sy}}\eta_{397} = \sqrt{\frac{2}{3}}\eta_{397} \tag{4.79}$$

$$\eta_{393d} = \sqrt{f_{sx} + f_{sy}}\eta_{393} = \sqrt{\frac{22}{30}}\eta_{393} \tag{4.80}$$

  which come out slightly higher compared to their axial counterparts. Calculations using

[6] Reminder that for the magnetron mode cooling is performed on the blue sidebands.

the third order numerical model presented above suggest that even for experimentally achievable frequencies of $\omega_- = 50$ kHz the magnetron limit is $\bar{n}_- \approx 1.0$ for the previously used parameters $\Omega_0 = \tilde{\Gamma} = 40$ kHz. Reducing the final stage cooling power to minimise off-resonant carrier excitation becomes paramount. One way to try to achieve a lower cooling limit would be to use a final cooling step on the first order blue magnetron sideband of the first order red cyclotron sideband, which would greatly suppress any carrier excitation. However, the transition rate into the the ground state from this transition calculated using equation 4.71 is 30 Hz for $\Omega_0 = \tilde{\Gamma} = 40$ kHz. This will be insufficient to significantly cool the mode in the presence of heating rates that are of similar magnitude.

CHAPTER 5

EXPERIMENTAL SETUP

This chapter will present the reader with all the relevant information necessary to understand the components of the experimental setup that were used to collect the data in the subsequent sections of this thesis. Since I am a fourth generation student using this setup, there are already theses available that provide very detailed descriptions of the apparatus including theoretical background, design specifications and performance characterisation of various subsystems. Hence my overview of all the established subsystems will reference these results wherever there were no new changes or upgrades. I will give more detailed descriptions of new subsystems that have been installed during my work on the experiment. My main contribution was a major upgrade to the fluorescence detection system. I integrated an electron-multiplying CCD camera (EMCCD) into the setup to obtain spatially resolved spectroscopic information. This was a task that required a large rewriting of our custom experimental control software to communicate with the camera, synchronise exposures and read out data for live display and tracking of the ion signal. Various settings and configurations were explored to find the desired readout settings required to minimise noise. I also added further optical elements to improve the noise of photomultiplier signal measurements. Another hardware upgrade I worked on was prototyping a new feedback circuitry for the laser intensity stabilisation, which was eventually finalised by Manoj Joshi. Throughout the duration of the PhD I became intimately familiar with every bit of equipment in the kit as various failures and malfunctions required intervention at different times. Starting from laser diode maintenance, locking cavity alignment, YAG laser maintenance through to HeNe laser polarisation locking, scanning cavity mirror replacement, RF electronics replacements and many improvements to the experimental control software, no bit of the experiment went untouched except the trap itself which served us faithfully.

5.1 Overview

The experiment can be split into four general areas:

- Trapping apparatus - This includes the trap itself – a set of electrodes with the required geometry to produce the desired field. The trap is set inside a vacuum chamber and placed within the bore of a superconducting magnet. The associated voltage sources for the electrodes, neutral calcium source and ionisation laser all fall under this category.
- Laser Systems - Under this category we have all the diode lasers that are required for laser cooling, two near UV lasers at 397 nm and two IR lasers at 866 and 854 nm for

rempumping. The UV lasers have their own set of cavities that are used for Pound-Drever-Hall locking to reduce their linewidths. All four of these lasers are then locked through a scanning cavity transfer lock to a reference helium-neon laser for long term stability. A spectroscopy and sideband cooling diode laser at 729 nm requires a much finer linewidth for effective coherent manipulation so that it has to be locked to an ultra low expansion high finesse cavity through a Pound-Drever-Hall scheme. To also obtain sufficient power to excite the quadrupole transition a tapered amplifier (TA) is used.

- Experimental control To perform an experiment laser pulses of the correct frequency, intensity and length need to address the ion in a repeatable manner, synchronised to all other subsystems of the experiment such as fluorescence collection and digital storage. For this purpose a field programmable gate array (FPGA) is used to control various radio-frequency sources that power acousto-optic modulators (AOMs) which can precisely adjust the aforementioned laser parameters. The FPGA runs on pre-programmed sequences which are stored in its internal memory. To update the FPGA, change digitally synthesized RF frequencies as well as receive data from detection systems a control software runs on a user controlled desktop computer.

- Light Collection The fluorescence from the ions is collected on either a pair of photomultiplier tubes or an EMCCD. This is a smaller subsystem, but it is especially important when using the EMCCD as the optimal readout noise is obtained when the rest of the experimental sequence is synchronised to the internal clock of the camera. Thus integrating the collection of the camera hardware into the experimental control becomes paramount.

A schematic overview of the main components of the apparatus is shown in figure 5.1.

5.2 The trap, magnet and loading ions

5.2.1 SPECTRAP

The SPECTRAP Penning trap was originally designed by Manuel Vogel and constructed primarily with a focus geared towards spectroscopy of highly charged ions at GSI in Germany. Two identical traps were machined with one of them being installed at GSI and the other at Imperial College by Shailen Bharadia. The trap consists of a cylindrical stack of oxygen-free copper electrodes sepearated by macor rings and sapphire balls. The inner electrode diameter is 21.6 mm, and the distance between the endcap electrodes is 5.9 mm. A positive voltage is applied to each of the endcaps, whereas the central ring electrode is kept near ground. The ring electrode is also split into four segments allowing us to apply time dependent potentials to create rotating dipole or axialization fields. For optical access, 4 mm diameter holes are drilled into each of the four ring segments. The size of this aperture limits the fluorescence collection efficiency. The trap has two compensation electrodes that were originally designed to null anharmonicities for large clouds. However, as we tend to only work in the regime of a few ions at the trap centre where the anharmonicites are negligible, these electrodes are instead used to compensate any unwanted potential on the endcap electrodes that shift the ion away from the trap centre. The four segments of the ring also have small potential offsets on the order of $\sim 10 - 100$ mV for compensation purposes.

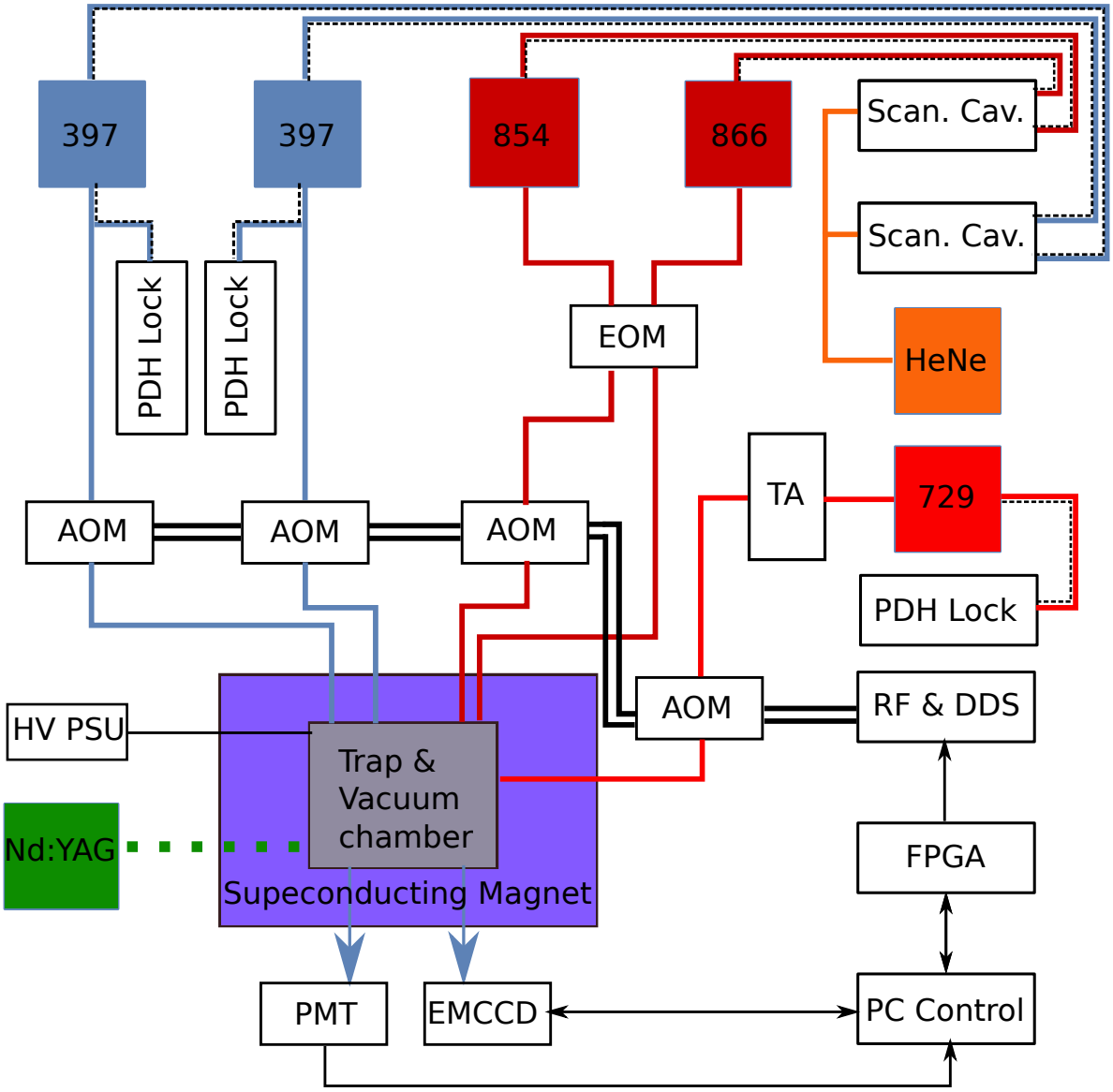

Figure 5.1: Schematic overview of the experiment. Line legend: solid coloured lines – cw lasers, dotted coloured lines – pulsed laser, solid black line – digital and analogue electric signals, double black line – radio frequency signals, dotted black line – feedback electric signals

When the copper electrodes are coated in calcium the voltage on their surface becomes increasingly negative. Experimentally, we observe that if we expose the electrodes to long periods of calcium flux, the ion position will visibly shift from the trap centre at low endcap potential when imaged on a camera. Hence we perform a simple compensation procedure where we localise the precise pixel position of the ion on the camera at high endcap voltage where the effects of these unwanted potentials are negligible and the ion will reside at the geometric trap centre. Then we reduce the voltage to ≈ 3 V and add small positive DC offsets to the compensation electrodes and to the ring segments until we see the ion return to the trap centre. Centering of the ion is particular important in the radial direction as any offset changes the Doppler cooling efficiency for a given radial beam position.

To apply the axialization potential to the radial electrodes, we use a sinusoidal signal generator at ω_c split into four channels, passed through two inverting and two non-inverting op-amps with variable gain. The variable gains allow us to compensate for any micromotion induced by

the RF field when its null is not matched to trap centre. A badly compensated field will act to drive the ion into a large radial orbit which is detectable on the EMCCD camera. We therefore vary the amplitudes on each channel until the radial extent is minimized and then increase the total applied drive voltage. We iterate this procedure until we observe no micromotion at 6 V. Since we typically work with fields up to 4 V, we deem this condition satisfactory.

5.2.2 Vacuum chamber and Breadboard Optics

The trap is housed in a vacuum system that is continuously pumped by an ion pump, achieving vacuum pressure below 10^{-8} mbar. The chamber has four radial viewports and two for axial access – one above and one below with the light entering perpendicular to the vertical axis and reflecting upwards on a 45° mirror. Inside the chamber there is also an effusive calcium oven for producing a neutral atomic vapour. The whole system is mounted on a small optical breadboard which itself sits on a set of three hex bolts emerging from a metal base plate. This base plate is attached to an adjustable height platform (Genie lift). This platform is then raised to insert the trap into the bore of the superconducting magnet. Final adjustments of the position are made using the screws on the base plate. The bore of the magnet is 10.45 cm in diameter, with the collected fluorescence and radial laser beams having to be directed in paths parallel to the bore in a 1.4 cm gap between the vacuum chamber and bore. The bore is also open on the top, allowing for the external Nd:YAG ionisation laser to be sent in from above. Beam steering and fluorescence collection optics are all located on the small breadboard as indicated in figure 5.2.

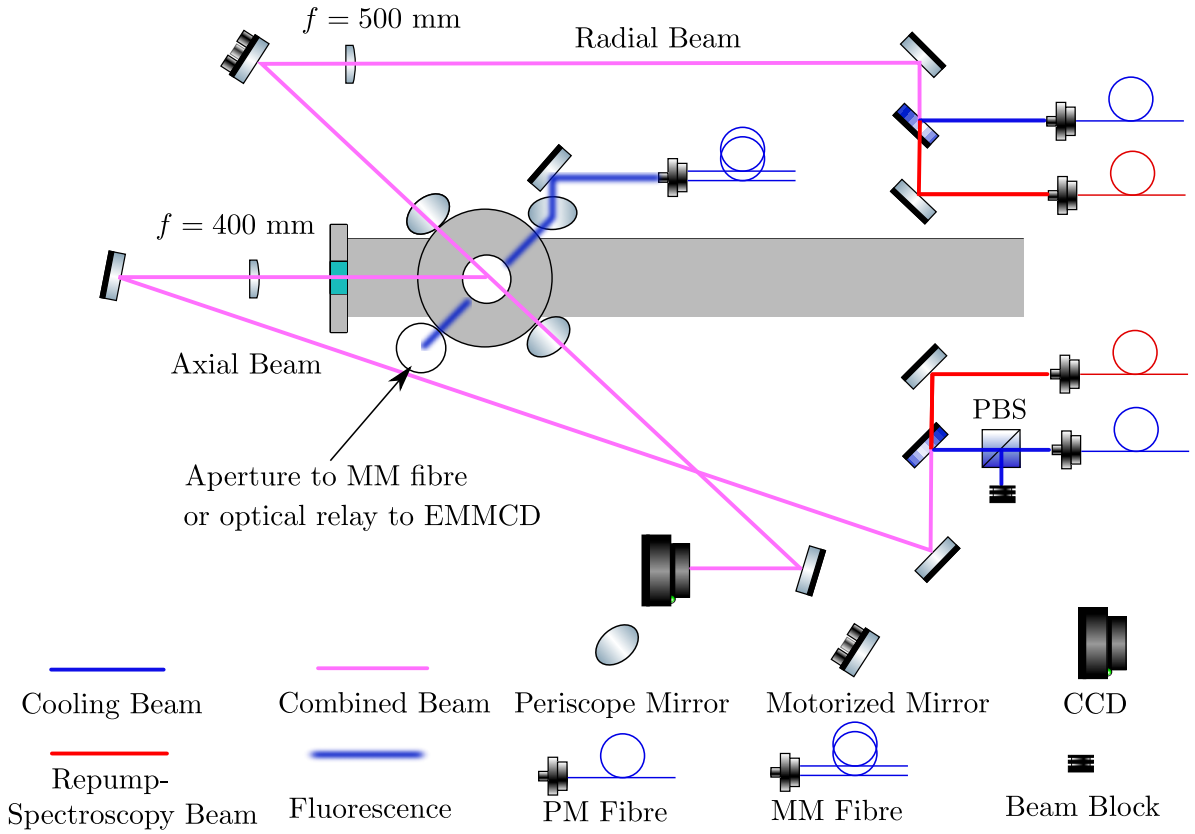

Figure 5.2: Diagram of the optical elements that steer laser beams from the breadboard below the superconducting magnet into the vacuum chamber containing the trap. Also shown is the optical path of fluorescence.

The cooling (blue) lasers are combined with the repump and spectroscopy (red) lasers emerg-

ing from polarisation maintaining single mode fibres on a pair of dichroic mirrors, one each for the axial and radial beams. Additionally, the axial blue beams are passed through a polarizing beam splitter to remove any ellipticity introduced by the fibre. The axial beam is then focused using a $f = 400$ mm lens and sent through a window into the vacuum chamber. Alignment is typically performed by moving the output couplers of the fibres of the red and blue lasers independently rather than using a mirror after they are combined as they have different beam waists at the trap centre. The radial beam is focused by a $f = 500$ mm lens and reflects off a computer controlled motorised mirror before entering a pair of periscope mirrors that send it up along the bore of the magnet and into the trap. Since the radial temperature of the ions is very sensitive to the position of the Doppler cooling beams (changing the position changes the intensity gradient across the ion's trajectory), this motorised mirror is used to give a much finer and reproducible beam positioning. To this end, we have installed a CCD sensor[1] and written a simple matlab live processing software that finds the beam centroid. Since we only use the repump beams in the axial direction, we are usually not worried by a secondary effect on the signal when moving this motorized mirror rather than the coupler, but there is a small effect when performing radial spectroscopy as the Rabi frequency of the 729 beam will change. This effect is not large enough (moving a 230 μm diameter beam 10-20 μm away from the centre) to significantly alter the excitation probability for diagnostic Doppler cooled spectroscopy and once the desired position of blue lasers position is obtained, the red laser can always be optimised from the fibre output coupler.

Another very important consideration is the focus of the radial blue lasers at the trap as this limits the achievable range of the beam intensity parameter and changes the sensitivity to the offset which can be induced by a minimum step of the motorized mirror. Adjusting the beam waist, however, proved to be quite problematic. Since the trap was never removed from the magnet during the whole length of my PhD, we have not been able to make a direct measurement of the distance from the $f = 500$ mm lens to the trap centre. We at first attempted to improve the focus by adjusting the aspheric lens of the output coupler, to change the spot size and divergence on the focussing lens simply by using the ion fluorescence as a reference. This was very difficult to perform without losing alignment of the beam through the trap and thus we also had to adjust the position of the focussing lens to recover good focus. Furthermore, at one point the PM fibre of the radial beam broke and was replaced by a new fibre with a smaller mode field diameter[2], meaning the reference positions of the old aspheric and focussing lenses were no longer valid. From this point on, we attempted to systematically modify the focus and use spectroscopic results to confirm whether the cooling was improving as a proxy measurement for a tighter focus. Based on incomplete information from the lab books of Sandeep Mavadia who last assembled the apparatus combined with direct measurements of beam paths on the breadboard we estimate that at its final position the $f = 500$ mm lens was focussing approximately 4.5 cm short of the presumed trap center. Further improvements were not possible as the focussing lens cannot be moved much closer to the motorized mirror due to space constraints.

Using a fold-out mirror, a set of images was taken around the focus, allowing us to reconstruct the minimum beam waist and find the Rayleigh range as seen in figure 5.3. The fit gives us a beam waist of $67(1)\mu$m and a Rayleigh range of 3.6(2) cm. From this information we calculate

[1] Home hacked old usb webcam

[2] PM-S405-XP with a core diameter of 3 μm replaced by PM-S350-HP with a core diameter of 2.5 μm

the beam waist at the estimated trap centre to be $\approx 100\mu$m.

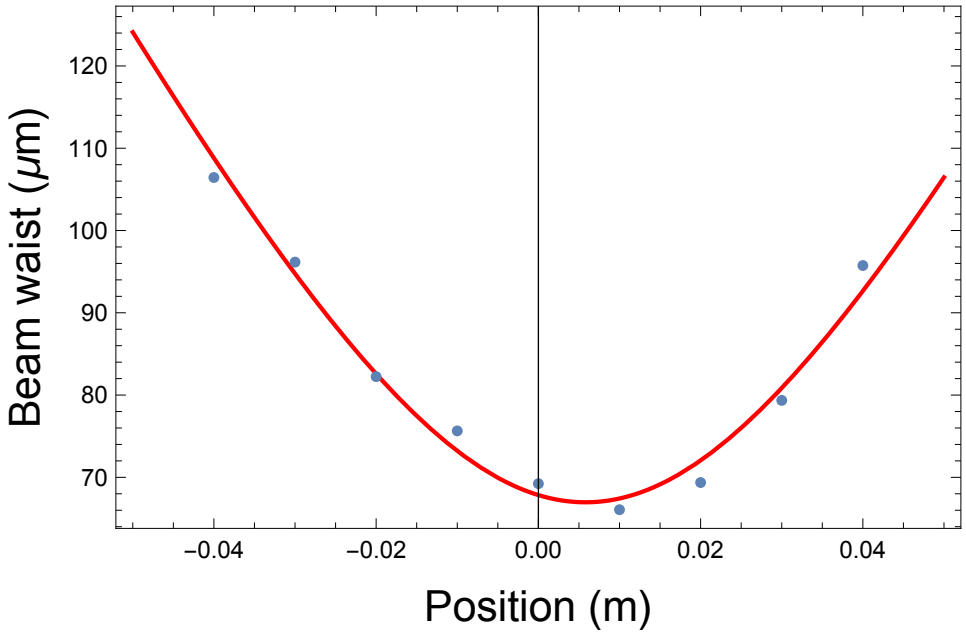

Figure 5.3: Beam waist measurements of the radial blue beam around the nominal lens focus of 500 mm. The beam shapes were recorded on a CMOS camera and fitted to a 2D Gaussian profile to extract the waist data. The fit gives a beam waist 67(1)μm and a Rayleigh range of 3.6(2) cm

The trap also has two apertures with $f = 20$ mm lenses for fluorescence collection glued to the electrode in the vacuum. The light is once again redirected along the bore of the magnet with mirrors and pairs of lenses in a Keplerian telescope arrangement. One output emerges onto the breadboard through a periscope mirror and is then coupled into a multimode fibre and sent to a PMT away from the trap. The second output is instead focused just slightly below a threaded hole in the breadboard, which allows us to either attach a second multimode fibre with suitable telescoping optics or a mirror to send the light through our image relay system to an EMCCD camera. (see section 5.5.1)

5.2.3 Magnet

To create the required magnetic field and achieve high levels of stability, we use a superconducting magnet manufactured by Magnex Scientific. The magnet consists of a vertical bore surrounded by a solenoidal superconducting coil submerged in a liquid helium bath. At the centre of the solenoid the axial strength is maximised while the radial strength is minimised. The maximum field strength of the magnet is 2.5 T, but we operate it at 1.899 T. At fields this large, even very small magnetic field gradients can cause shifts in the Zeeman splittings, which in turn affects our ability to coherently address the $S_{1/2,-3/2} \leftrightarrow D_{5/2,-1/2}$ transition, which has a differential Zeeman shift of 21.26 GHz at 1.899 T. In particular, we will observe significant shifts of the transition frequency for ions in a Coulomb crystal that occupy a different position in the field. At the start of my PhD a minimisation of the axial gradient was performed by raising the breadboard with the trap higher into the bore of the magnet. The procedure is documented in reference [144] and a measurement of the gradient conducted by displacing the ion from the trap centre using small DC offsets potentials before spectroscopically measuring the transition frequency yielded a gradient of 0.003 Tm^{-1}. Further improvements were no longer possible as

a mirror was coming very close to contact with a part of the superconducting magnet's outer body. Since then, we have conducted a spectroscopic measurement of the carrier frequency of each ion in a ground state cooled two ion axial crystal (section 7.2.2) giving a value of 0.01 Tm^{-1}. The accuracy of this value is higher due to the removal of any temporal drifts such as magnetic field decay and laser frequency drift since they affect both ions equally in a single spectroscopic sequence. On the other hand, when measuring various spectra separated in time using a single ion, these drifts can correlate positively or negatively with the field gradient. The magnetic field has a manufacturer listed field drift time of < 0.1 ppm/hr .

5.2.4 Ion Loading

Loading ions is achieved by a two stage process. The first step produces an effusive beam of neutral calcium by heating a calcium filled tube (oven) with an aperture aimed at the centre of the trap. After a warming up period of 1-2 minutes, the oven will be emitting a steady stream of neutral calcium ready to be ionised. In the second step, a three photon non-resonant photoionisation is induced by firing a pulsed, high power, frequency doubled Nd:YAG laser through the trap. This will produce the desired $^{40}Ca^{+}$ ion as well as other calcium ion isotopes and other potentially unwanted species. These ions will be produced at various large orbits around the trap, with only the correct isotopes cooled towards the trap centre by the Doppler cooling lasers. Other isotopes or different species can sometimes get sympathetically cooled into a Coulomb crystal and need to be ejected. One of the 397 nm lasers is typically set to scan from near resonance to about 1 GHz to the red to cool the ions faster.

By adjusting the current through the oven, the Nd:YAG power and the duration of the loading procedure, anywhere from one ion to a large cloud of thousands of ions can be loaded. Despite the optimisations, this procedure remains a stochastic process whereby we often load more ions than desired and then eject them to obtain the desired number. We do this instead of emptying the trap and repeating the loading process as we find that running the oven for prolonged periods of time coats the electrodes with excess calcium, ruining the DC compensation of the trap. To eject ions from the trap, we briefly ground the endcap electrodes for a period of 5-50 μs. Due to the electrostatic potential of the ions suddenly no longer being balanced by the trapping potential, the ions undergo a Coulomb 'explosion' and those closest to the electrodes are lost. The remaining ions quickly re-cool to the trap centre. We keep repeating this procedure until the desired number of ions is reached. Once again, this method is not deterministic, but it is certainly more reliable since we can pulse off one ion at a time from a small Coulomb crystal with high probability. The pulsing procedure is not automated and is performed by an Arduino microcontroller and transistor circuitry controlled by the user from a C# GUI. There is no set prescription on the best method to pulse ions out, but there are some general pointers:

- Reduce the trapping voltage to 10-20 V. For small crystals, try to form a 1D chain.
- For large clouds start with shorter pulses of 5-10 μs as long pulses require a potentially very long recooling time.
- When a large cloud starts recooling, the fluorescence signal will at first increase slowly and then grow exponentially. To eliminate ions faster, observe the fluorescence and pulse again as soon the fluorescence begins to increase.

- Smaller chains will require pulses of 20-50 μs or very fast repeats of shorter pulses.
- Sometimes ions can appear to be lost, but instead have just been pushed out to very large orbits. Patience is needed to allow for recooling time and additional red detuning of the cooling lasers before another loading procedure is attempted.
- The procedure should be almost exclusively performed with the EMCCD camera to monitor the number of ions. If only a single ion is desired, a PMT signal can be sufficient. To verify that only a single ion is present, one can turn off the 854 nm repump lasers and observe quantum jumps. If only a single ion is present there will only be two fluorescence signal levels corresponding to the ion being either dark or bright. Multiple ions will show further quantised levels. This technique does not guarantee that all other non-fluorescing ions were ejected.

5.3 Laser Systems and Optics

In this section, we will describe three separate subsystems: the Doppler, repump and spectroscopy lasers. The scanning cavity lock system that is common to both the Doppler and repump lasers will follow in its own subsection.

5.3.1 Doppler Cooling Lasers

Two lasers that provide light at 397 nm are required to drive the $\sigma^{\pm}$ transitions between $S_{1/2,-1/2} \rightarrow P_{1/2,1/2}$ and $S_{1/2,1/2} \rightarrow P_{1/2,-1/2}$, which are split by 65 GHz. We use two commercial DL100 Extended Cavity Diode Lasers (ECDL) from TuiOptics (now Toptica), with associated temperature stabilisation, current and piezo drive modules. The diodes themselves are non-AR coated Nichia NDV4814T with a typical operating output power of 5-7 mW out of the laser head. A linewidth of $\approx$ 10 MHz was previously measured by beating the pair of lasers on a photodiode [144]. This compares unfavourably to modern diode systems that routinely have linewidths of 100s of kHz. Since we wish to be able to carefully control the absorption profile for Doppler cooling experiments and crystal rotation purposes, we ideally want to make the linewidth much smaller than the transition linewidth of 21.6 MHz. To this end, each laser is locked to individual optical cavities (free spectral range 1.5 GHz, finesse $\approx$ 40 [144]) with piezo-adjustable length. A Pound-Drever-Hall lock scheme is used to generate an error signal, which is fed back to the laser current driver. The linewidth after the cavities is approximately 1 MHz[144]. To further compensate for low frequency noise and drifts an integral gain stage compares the transmitted light intensity to a set value and feeds the difference signal to the piezo driver of the ECDL. This additional stage is also used to monitor the performance of the locks so that when the transmission drops below a certain threshold a digital signal is sent to the FPGA to alert the experimenter that the laser has become unlocked.

While the cavities improve the short time scale linewidth, they are themselves prone to drifts in the 10s of MHz range on time scales of minutes requiring a secondary feedback from the scanning cavity lock (section 5.3.3). There are further issues with a piezo related drift in one of the PDH cavities. As the piezo moves to correct for long term changes such as a steady temperature drift, it tends to carry some inertia even after the error signal has been nulled. This forces the voltage controller to compensate to maintain the lock over a much larger voltage

range. The consequence of this is that on some days when there are significant drifts, the voltage controller reaches either its lower or upper output limit and the lock fails. In this case, the particular cavity mode that was in use has to be replaced by a different one, nearer to the middle of the voltage controller range. This usually requires re-coupling of the cavity modes to find a mode with a suitable transmission lineshape. We have verified this effect by rapidly changing the piezo voltage using a potentiometer and observing the subsequent slow drift in the direction of voltage change. The fact that the other cavity has the exact same control circuitry and none of the above described symptoms leads us to believe that this problem is due to the piezo itself.

The performance of these locks was one of the greatest impediments to smooth operation of the experiment as they tended to fail every few hours at the best of times and often much more frequently. A significant portion of the experimentalist's time operating the setup was spent babysitting this laser system as the lasers would invariably either hop mode completely, broaden in linewidth or drift in intensity all of which cause the scanning cavity to unlock. A significant part of typical daily operation time was devoted to ensuring these lasers were reasonably stable for the purposes of data acquisition. Most frequently, piezo and current adjustments have to be made on a daily basis. When the ability to remain in a stable mode degrades, we increased the mode hop-free range laser of the laser by changing the temperature to maximise the overlap of the gain curve of the internal diode mode with the desired external cavity mode. This adjustment is performed roughly every few weeks. If all these adjustments fail, then the alignment of the extended cavity grating must be modified. Most importantly, the vertical alignment is crucial to get optimal feedback into the diode and achieve stable lasing. Despite all these maintenance tasks, the performance of the current drivers visibly degraded in time. In the final year of the PhD we managed to source a replacement for one of the current drivers from a more modern DL110 Toptica controller, which immediately improved stability, mostly by preventing sharp current jumps that induced mode hopes when adjusting the current. A similar problem can be observed on the other remaining DL100 controller. Ultimately, this laser system was pushed to its limits and for any more demanding experiments that require large data collection runs such as full state tomography a more modern system would be required.

5.3.2 Repumping Lasers

We use two homebuilt ECDL diode lasers to repump the $D_{3/2} \rightarrow P_{1/2}$ transition centred at 866 nm and the $D_{5/2} \rightarrow P_{3/2}$ transition centred at 854 nm. The current drivers and temperature locks are a mix of commercial units from Thorlabs and homebuilt circuits. The two diodes used are ridged waveguide diodes from Eagleyard [3]. The powers at the ion for the 866 and 854 nm lasers are 5 and 0.6 mW respectively. Since we wish to saturate the repump transitions and do not require very fine frequency selectivity, we do not take any additional measures to reduce the linewidth as with the Doppler cooling lasers. Stability against drift is achieved through a scanning cavity transfer lock as with the Doppler lasers.

As discussed in section 3.2.1, the Zeeman splitting of the $D_{5/2}$ and $D_{3/2}$ manifolds is in the 10s of GHz, which is much larger than the linewidth of the lasers. Thus we need to clear out 10 Zeeman sub-levels using $\sigma^{\pm}$ transitions leading to a total of 12 possible transition. Exploiting the fact that the first order Zeeman shifts between the $D_{3/2} \rightarrow P_{1/2}$ transitions and

[3]Models: EYP-RWE-0860-06010- 1500-SOT02-0000 and EYP-RWE-0870-06010- 0750-SOT01-0000

	ν_1 (GHz)	ν_2 (GHz)	ε (MHz)
866 only	10.6263	1.76035	89
All	10.6363	1.7722	195
No σ^+	10.6459	1.7862	142
No σ^-	10.6257	1.7568	128

Table 5.1: Table of optimal modulation frequencies for four different minimisation routines. The bottom two lines exclude either the σ^- $D_{5/2,1/2} \rightarrow P_{3/2,-1/2}$ and $D_{5/2,3/2} \rightarrow P_{3/2,1/2}$ transitions or the σ^+ $D_{5/2,+1/2} \rightarrow P_{3/2,3/2}$ and $D_{5/2,-1/2} \rightarrow P_{3/2,1/2}$ transitions. The error ε is the square root of the sum of the square residuals for the transitions included.

the $D_{5/2} \rightarrow P_{3/2}$ transitions have a fixed integer ratio we can create a comb of sidebands on each laser using a single Electro-Optical modulator (EOM) to address all transitions by simply mixing two frequencies. To first order this corresponds to one frequency at $\nu_1 = 6\mu_B B/15 =$ 10.6371 GHz and a second frequency at $\nu_2 = \mu_B B/15 = 1.7729$ GHz where μ_B is the Bohr Magneton and $B = 1.8996$ T. The situation is slightly complicated by the second order Zeeman shift which breaks the neat symmetry. To incorporate the second order Zeeman shifts, we can run a simple minimisation routine to find what the modulation frequencies should be for the smallest square difference in frequency over the selected sidebands. We can consider four cases: find the optimum frequencies for all 12 transitions, ignore the $D_{5/2,-1/2} \rightarrow P_{3/2,-3/2}$ and $D_{5/2,1/2} \rightarrow P_{3/2,-1/2}$ transitions, ignore the $D_{5/2,+1/2} \rightarrow P_{3/2,3/2}$ and $D_{5/2,-1/2} \rightarrow P_{3/2,1/2}$ transitions or consider just the 866 nm transitions. The results are summarised in table 5.1.

Because we have sufficient power in the 866 nm beam and we wish to maximise the $D_{5/2,-3/2} \rightarrow P_{3/2,-1/2}$ σ^+ transition strength used to quench our qubit state during sideband cooling (giving us more freedom in adjusting detuning) we aim to use the 'No σ^-' frequencies to minimise the error. We used a HP 8650L function generator to precisely set $\nu_1 = 10.6256$ GHz. The second frequency was generated using a Mini-Circuits ZX95-2600-S+ voltage controlled oscillator that did not afford such tuning precision resulting in $\nu_2 = 1.774$ GHz as measured on a spectrum analyser. The residual errors ranging between 1 to ≈ 100 MHz are shown in figure 5.4. We see clearly that the error on the σ^+ transitions on the far right has been minimised compared to the σ^- transitions on the far left of the plot. The power of the HP 8650L was empirically optimised to maximise power into the second and third order sideband by observing the fluorescence of a cloud of ions. These two signals are then summed on a resistive power combiner and fed into a fibre-pigtailed EOM (EOSPACE PM-0K5-20-PFA-PFA-850). The two lasers are combined just before the EOM on a dielectric filter and sent together into a fibre coupler.

5.3.3 Scanning Cavity Locks

The scanning cavity lock system has been developed both to provide long term stability to the cooling and repump lasers as well as to provide for a means to have fine digital control of the lasers frequency at the 1 MHz level. The system is described in detail in the thesis of Joseph Goodwin [145] and thus here we shall just give a brief overview and highlight some of the changes that were implemented and important points for maintaining the setup. The goal

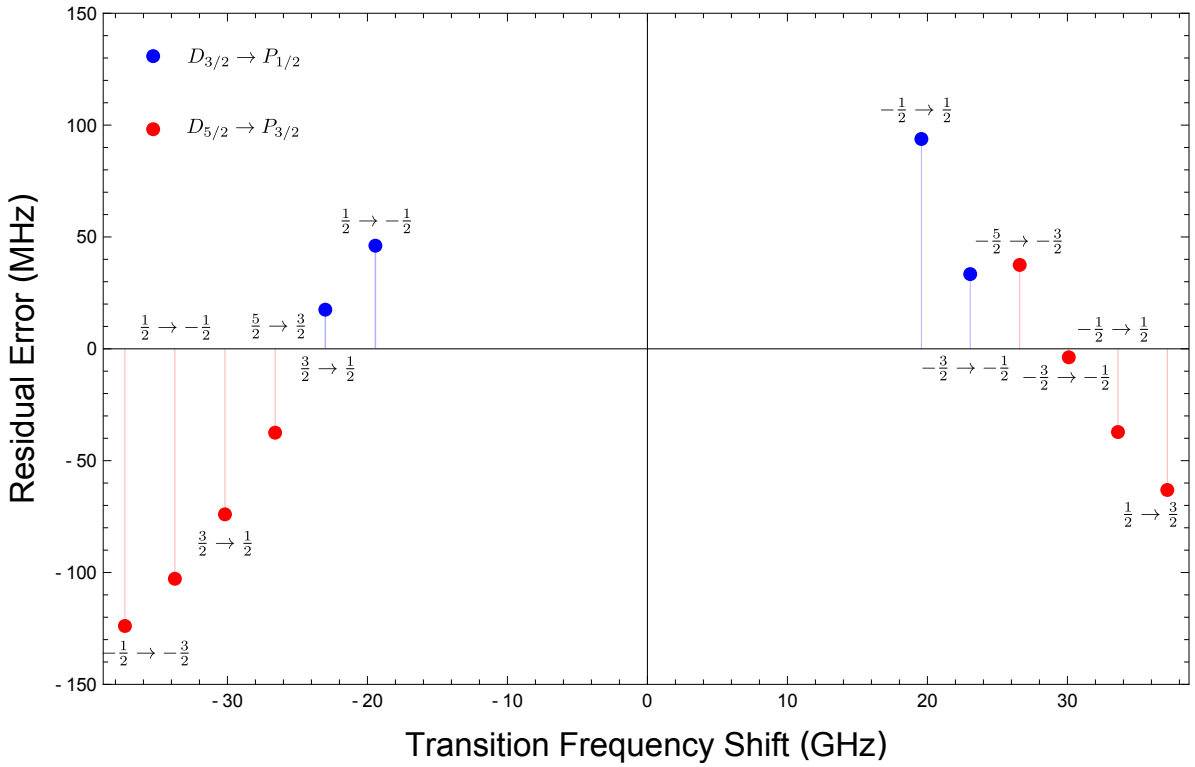

Figure 5.4: A plot of the residual error between the sidebands on the EOM and the actual transition frequencies. The bottom axis plots the shift of each transition relative to their non-Zeeman shifted values. Modulation frequencies: $\nu_1 = 10.6256$ GHz and $\nu_2 = 1.774$ GHz

of the scanning cavity lock is to stabilise the frequency of a 'slave' laser relative to a 'master' HeNe laser, which is independently stabilised using a polarisation lock. The feedback is derived by scanning the length of a cavity to which both lasers are coupled and monitoring the relative arrival time of transmission peaks on a photodetector. To distinguish the master signal from the slave signal, the transmitted light is split on a dichroic mirror and sent to independent detectors. Analogue electrical signals from a transimpedance amplifier stage are converted to TTL pulses with the aid of a 'peak detector' circuit, which uses a differentiator to find signal peaks and a comparator to accept or reject them based on a threshold voltage. The pulse arrival time is then digitised on an Arduino microcontroller. There are two stages to the lock. First, as the cavity is scanned over the length of its free spectral range the arrival time of the first HeNe pulse is stored and feeds back to a DC voltage applied to the cavity piezo to stabilise the cavity from drifts. Second, the arrival time of the slave laser peaks relative to the HeNe peak is converted to a feedback signal using a 16-bit DAC and sent directly to the diode piezos for the red lasers or to the PDH cavity piezos for the blue lasers. In the case of the 866 nm and 854 nm beams one peak each is required between the master peaks, whereas in the case of the 397 nm lasers two peaks corresponding to one laser and one to the other are necessary due to historical design of the system.[4] The Arduino also has a serial link to a digital LCD display and control box that can be used to monitor the relative positions of the slave peaks, assess the state of the lock and modify the lock set points.

The cavities are constructed from pairs of broadband dielectric mirrors attached to brass endcaps with a fine screw thread inserted into a brass cylindrical spacer. The screw thread

[4] If the system were to be reprogrammed, it would work just fine with one peak from each laser.

allows for careful tuning of the cavity length to a near confocal configuration to create a set of degenerate transverse modes spaced half a free spectral range apart. The blue cavity has a single ring piezo stack that both performs the scanning and has a large enough throw to compensate for cavity drifts. The blue cavity is also wrapped in a heater tape to temperature stabilise it to within 0.1 K using a thermistor and transistor circuit. The red cavity has a piezo element on both mirrors, one is a single layer 'AC' piezo to perform the cavity scan and the other a 'DC' piezo stack for the cavity locking. In early 2017, this piezo stack broke and we did not have an immediate replacement to hand. We attempted to run the cavity by combining the scan and cavity lock signal on the AC piezo as in blue cavity, but the throw on the piezo was not sufficient to compensate for the cavity drifts and thus the lock typically lasted only a few hours as opposed to weeks under normal operation. The dead stack was ultimately replaced by a new triple stack with a throw of 9.9 μm (Noliac NAC2123-H08-A01) and we returned to the previous configuration. However, the performance is not as good as previously and the lock is still usually lost every few days. This is because the original broken stack consisted of five layers; a fact that we were not aware of until we opened the cavity. An easy improvement would be to create an identical temperature lock for the red cavity as for the blue as this should remedy these long term drifts.

To ensure that we only see one peak from each laser between the HeNe peaks, we carefully mode match to the TEM_{00} of the cavity to suppress the odd order transverse modes and have a sufficient contrast betweeen the principal mode and higher order longitudinal modes. The red cavity works without any issues, however the blue cavity is very sensitive to a slight mode mismatch where the second longitudinal mode can become prominent enough to register on the peak detector and thus cause errors in feedback. In general, the problems with the unlocking of the blue lasers stem from the interplay between the PDH locks and the scanning cavity. If the PDH lock starts to reach the edge of its feedback range the laser begins to broaden which appears on the cavity transmission signal as a drop in the maximum signal height. If the signal drops below the peak detector threshold, the Arduino reacts by sending a very large incorrect feedback signal to both lasers, typically unlocking both PDH locks and potentially even causing mode hops. Thus it is usually very important to monitor the height of the peaks during locked performance and sometimes manually compensate by changing the current from the laser controller to rectify the problem. Similarly, pure intensity noise on the lasers can cause them to drop below threshold. An improvement in this regard was achieved by removing a polariser that was located in the blue beam path after the output of a polarisation maintaining fibre. This polariser turned any circularity acquired in the fibre due to temperature drifts into intensity noise. These drifts were accentuated by the fact that the two beams did not have the same linear polarisation and hence could not simultaneously be made to correctly align with the slow axis of the PM fibre. The origininal intended role for the polariser was to set a common polarisation for both lasers so that multiple peaks corresponding to orthogonal polarisation components did not appear in the cavity (described in [145] page 92) for a particular orientation of the mirrors. We were not able to reproduce this effect for any polarisation angle hence the polariser was removed. This led to increased total transmission intensity through the cavity and greater differential intensity stability between the two blue lasers.

5.3.4 HeNe Polarisation Lock

The HeNe laser and polarisation lock was set up by Joe Goodwin based on original designs by Dan Crick [146]. We describe the system here as the laser broke in late 2016 and had to be replaced. The laser is essentially a glass tube filled with a HeNe gas mixture with mirrors attached to the anode and cathode endcaps. The tube is powered by a filtered fixed power 1250 V, 4 mA switch mode power supply with 66 kΩ ballast resistors attached to the cathode giving an output of approximately 0.5 mW. In the HeNe gain curve, there are exactly two competing longitudinal modes with orthogonal polarisation that grow and fall in relative intensity as the cavity length changes with temperature. An error signal can thus be derived by splitting the two polarisations on a PBS and recording their intensity on calibrated photodiodes. The difference in voltages from the photodetectors' transimpedance amplifiers is then fed to a transistor based circuit that drives a current through a heater tape wrapped around the HeNe tube. The light used for stabilisation is obtained from the small leakage through the back mirror of the tube. The front output facet is filtered with a PBS so that only one polarisation goes into the scanning cavities.

In September 2016, we noticed that the HeNe peaks on the cavity were jumping about with no discernible pattern and upon inspection of the laser itself we noticed it was flickering. Since we did not have an immediate replacement at hand we tried many different fixes to try to revive the laser including:

- Additional ballast. 99 kΩ and 150 kΩ at 1250 V.
- Stored in a Ziploc bag filled with helium gas for 5 hours.
- Higher voltage power supply - 1750 V with 66 kΩ.

to no avail. In the end we managed to get the laser running by combining a 150 kΩ ballast with a 1750 V supply. However, there were periodic power spikes every 10s which would ruin any locking attempts. Our next attempt was to use a spare HeNe tube of the same model that was recovered from an old experiment. This tube exhibited none of the flashing behaviour and seemed to run stably, but once we coupled the light to the blue scanning cavity, we noticed the peaks flickering even though the power output on a fast photodetector was constant. This suggested the presence of some strong frequency noise, which was later found to be mostly distributed between 10-50 kHz. Upon investigation of the error signal from the temperature lock, it was found that the trace did not follow the expected sinusoidal curve as the tube was heated, but instead had very sharp discontinuities as the orthogonal polarisations instantly flipped (the error signals are shown in appendix A). This left us puzzled for a while until we found that this is indeed sometimes the case for certain HeNe tubes from a different production batch, even for the same model. These 'flipper' tubes are wholly unsuitable for this sort of locking scheme and produce a very noisy lock. Thus we had to order a brand new JDSU 1008 HeNe (same model as before) and this time the tube worked exactly as intended, with the 1250 kV supply and a 66 kΩ ballast resistor.

5.3.5 729 nm Spectroscopy Laser

The 729 nm laser is a home made laser diode system designed and built by Dan Crick [146] with modifications by Graham Stutter and Joe Goodwin. An overview of the optics and electronics

is shown in figure 5.5. The light is produced from a home made ECDL laser in a Littrow configuration with a home made current driver and a commercial temperature lock. The output passess through two stages of optical isolation before some light is picked off and sent through an EOM to an ultra stable cavity to produce a PDH lock error signal to narrow the linewidth, whereas the rest of the light is passed through a tapered amplifier[5] (TA) to boost the output power before the light is coupled to a fibre and sent to the experimental optical table. To form the error signal, reflected light from the cavity is converted to an electrical signal that is demodulated by mixing with a phase shifted high frequency RF signal that drives the EOM and then low pass filtered. The resulting error signal is fed back directly to the laser current and it is also sent to an Arduino micro controller through a 16-bit DAC. The Arduino is then used for slow feedback to the laser piezo and can also hold the piezo voltage in the case of an unlock. The lock is monitored by measuring the intensity of light transmitted through the cavity.

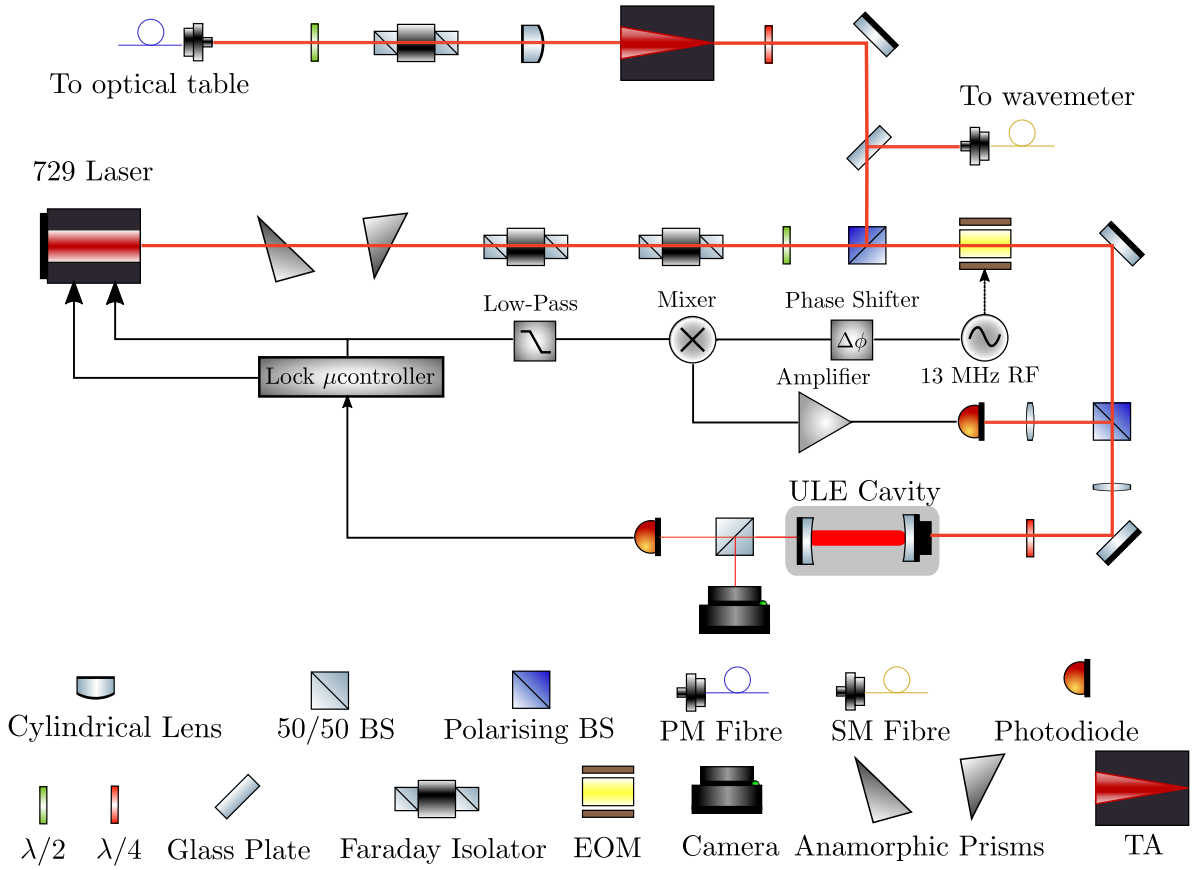

Figure 5.5: Diagram of the optical and major electrical components comprising the 729 nm laser system. The red line shows the laser path, whereas the black line shows electrical signals.

The cavity is made with an ultra low expansion (ULE) glass spacer that has a zero crossing in its expansion coefficient at approximately 17° C i.e. at this point the cavity length dependence on temperature is minimised. It is housed in a vacuum chamber and temperature locked with a Peltier cooler aided by passive cooling and a fan to within 0.2 mK of the zero crossing point corresponding to a frequency stability of $\approx$ 60 Hz. The finesse was measured to be around $F \approx 60000$.

The output of the laser head itself is only around 24 mW leaving only approximately $1-2$

[5]Toptica TA-0735-0500-4

mW of laser power at the ion after 2 sets of optical fibres, AOMs and beam shaping optics. This would not give us enough power to perform fast sideband cooling, hence the tapered amplifier is required to boost the power to ≈ 250 mW. There is one downside to the use of the TA that became evident once we started performing coherent manipulations such as Rabi oscillations. When the TA is run at large currents, within 75-100 % maximum output power, we notice that the Rabi oscillations at longer times tended to appear disproportionately noisy, with large jumps in the excitation that do not seem to follow an expected smooth decay in coherence in the case of simple broad laser linewidth, magnetic field noise or improper ground state cooling as seen in figure 6.11. A possible explanation is laser intensity noise, but we take care to eliminate this effect down to less than 1 % using an AOM for feedback.

This problem was directly correlated to the behaviour of the laser by monitoring the transmission signal through the ULE cavity. When the laser is locked and the TA is either off or run at low power, then the transmission signal is flat and completely insensitive to vibration. As the TA current is increased, the transmission signal begins to respond to knocks to the optical table and ultimately the transmission level begins to drift on a timescale of a few seconds even when locked. The error signal, however, retains the shape corresponding to an optimal lock. We believe that this effect is consistent with optical feedback from the TA into the laser diode. This is reinforced by the fact that to correct this issue, we deliberately introduced a slight misalignment in the input beam coupling to the TA so as to avoid any back-reflection to the laser as well as to avoid amplified spontaneous emission from the TA. The insufficient isolation is most likely a result of using improper optical isolators. One of the pair is an unidentified model while the other is rated for central frequency of 780 nm, thus having only an estimated 18 dB isolation. At the time of writing, we have acquired a new Thorlabs IO-5-730-HP with an estimated 38 dB isolation which we have added in series with the old isolators and have managed to operate the TA at full current with no feedback related noise without the need for misalignment, however, all data involving coherent manipulation in this thesis was taken with the TA misalignment and without the new isolator.

5.3.6 Optics

In this section we describe the optics on the main experimental table that is used to prepare all the laser beams that are sent by optical fibres to the breadboard upon which the trap and superconducting magnet rest. The optical setup is shown in figure 5.6 with the areas that have undergone major changes highlighted in blue and red. The blue laser diodes produce vertically polarised light that is collimated to a roughly Gaussian shape using a pair of cylindrical lenses before passing through an optical isolator. A variable amount of light is split on polarising beam splitters by adjusting a half-wave plate just before them. A small fraction of the light is sent to fibre couplers that send the light to the PDH and scanning cavity locks using PM fibres and to the wavemeter using a single mode fibre.[6]. The majority of the light passes through to a double-pass AOM used for shuttering the lasers with extremely high extinction. A quarter-wave plate ensures that the returning light is reflected and the two laser beams are combined on a 50:50 beam splitter and the two outputs are sent to PM fibres that pipe the light to the trap breadboard.

[6]The use of the wavemeter is kindly provided by the Centre for Cold Matter. Motorised servo shutters are used to select which beam frequency is shown on the wavemeter

The radial coupling branch had a new AOM installed to help with readout fidelity. As will be described further in section 5.5.2, the radial beam causes significant background scatter meaning it has a worse signal to noise ratio than the axial beam. We therefore use a single-pass AOM to dump approximately $70 - 80\%$ of the radial power during readout. Alternatively, by changing the RF amplitude to the AOM we can more easily tune the relative power of the beams without recourse to imprecise neutral density filters, or deliberate misalignment. The challenge of setting up this additional AOM was that the two laser beams were found to have a slightly different spot size and divergence at this point and both were too large to effectively diffract through the active region of the AOM. First, to even out the beam divergence we added a $f = +1000$ mm lens before the 50:50 beam splitter for the path of 'Blue 1'. Subsequently we introduced two plano-convex lenses in a Keplerian telescope configuration to reduce the beam size by $1.5\times$ and achieved up to 80% diffraction efficiency. The beam output from the AOM was, however, unsuitable for fibre coupling and hence a Gallilean beam expander was used to return the beam to its original size.

The repump beams follow an almost identical setup up as the blue laser up to the point where they are combined on a dichroic mirror, with the difference being that the 866 nm laser has no AOM since it is always on during all experiments. After the beams are combined, they are coupled into the fibre-EOM. A small portion of the output light is then picked off to a Fabry-Perot cavity with a 7.5 GHz FSR that is used to monitor the combs of sidebands imprinted on the lasers. The remainder of the light is divided using a half-wave plate and a PBS between PM fibres corresponding to radial and axial beams on the trap breadboard.

The 729 nm laser optics on the main experiment were modified significantly from their original configuration. The first major addition was a laser intensity stabilisation system, where a part of the laser light that emerges from a PM fibre is converted to an electronic signal on a photodiode which is then fed back through a PID lock circuit to the amplitude control of the RF driver of a single-pass AOM. The laser intensity is stabilised by trading off the amount of intensity retained in the 0-th order beam compared to all other diffracted intensity. The electronics for the lock were built by Manoj Joshi, with my help during the prototyping stage, and have a bandwidth up to ~ 100 kHz. The intensity noise is stabilised to less than 1%.

The second major change was when we decided to change the spectroscopy AOM that is used to shift the 729 frequency from a double-pass configuration to a single-pass configuration midway through the PhD. This was necessary since we wanted to have the option of creating bi-chromatic beams by feeding two RF frequencies into a single AOM. A double-pass configuration would include higher order sum and difference terms between the two frequencies resulting in an undesirable poly-chromatic beam. A disadvantage of this change was that it inevitably halved the frequency scan range of the AOM and also introduced a coupling efficiency (and hence Rabi frequency) dependence on the frequency. The large scan range was often necessary to find an appropriate mode of the ULE cavity to lock the laser since the transverse cavity mode spacing is 369 MHz. However, the Isle Optics 250 MHz AOM has a sufficient diffraction efficiency even at 250 ± 80 MHz to allow us to to find a suitable mode. To minimise the beam pointing error and ensure there is no skew in the excitation spectra, we always ensure that the fibre coupling is maximum at the RF frequency corresponding to the ion's carrier transition such that the coupling efficiency/RF frequency curve is symmetric around it. At frequencies up to 2 MHz either side, we observe a 1.3% difference in intensity. After the AOM, we rotate a mirror to

determine whether we wish to couple all the power into the radial or axial beam PM fibre.

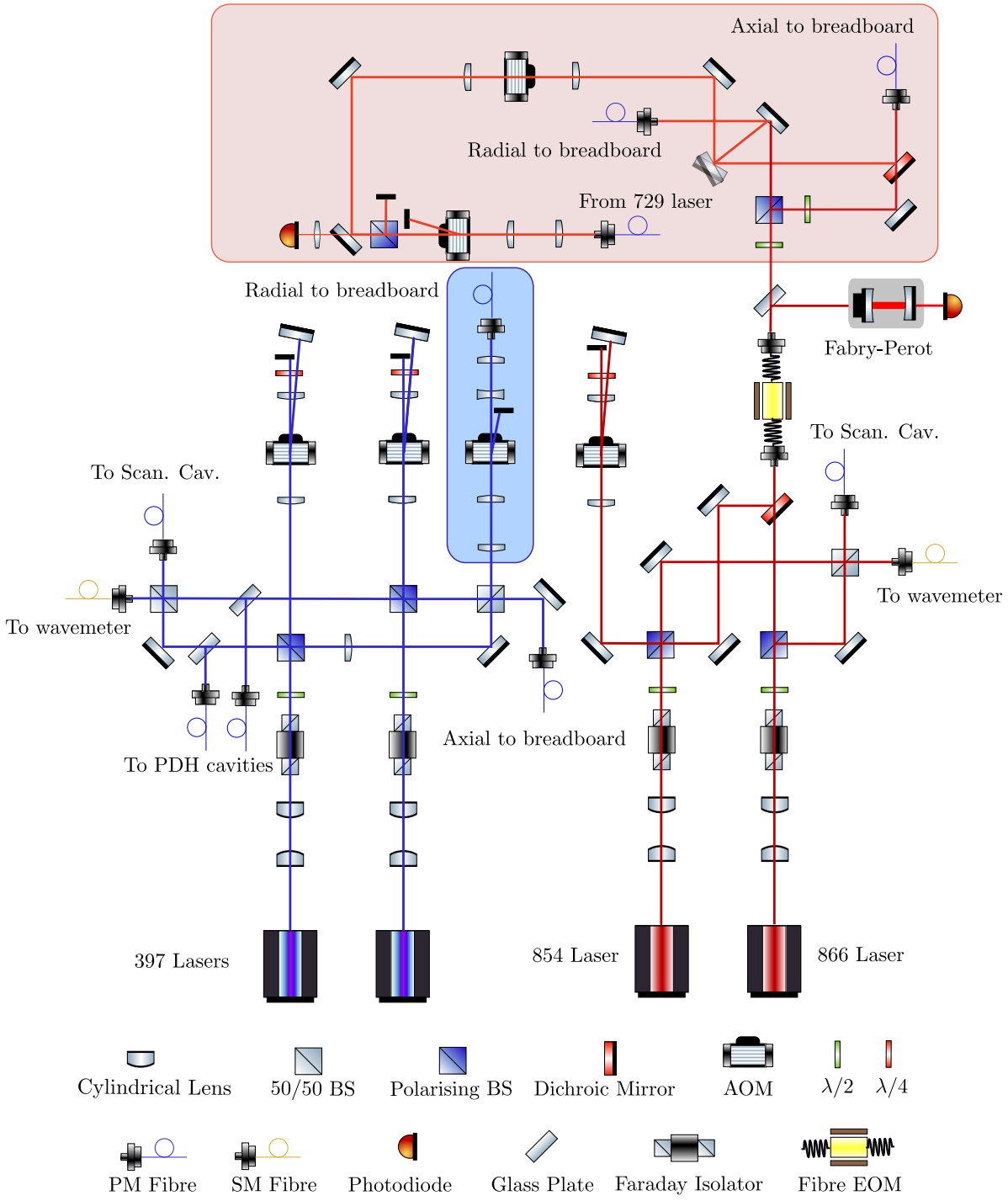

Figure 5.6: A diagram of the optics on the main experimental table. Some mirrors have been removed to improve readability. The blue and red areas correspond to parts of the setup that were added or modified for the 397 and the 729 lasers respectively.

5.4 Experimental Control

5.4.1 Experimental sequencing - FPGA

To run any kind of ion trapping spectroscopy experiment, it is paramount to have a precise synchronisation between all instruments, as well as precise control over their state and to be

able to run the same identical sequence repeatedly. To meet these criteria our experiment uses a field programmable gate array (FPGA) to provide TTL outputs to the various subsystems such as the RF switches which shutter/attenuate laser beams or switch between single frequency and bi-chromatic operation. The FPGA has an internal memory that can store instructions about the state of the TTL outputs at each 'tick'. The tick is simply a time bin that is some chosen integer multiple of the minimum 20 ns period of the internal 50 MHz clock. The size of the memory limits the amount of tick information that can be stored and hence it can be beneficial to increase the tick size if such a fine time resolution is not required. Originally, the experiment was set up with 640 ns tick length, which we later reduced to 40 ns to give us the required precision to resolve high frequency ion excitation oscillations up to 500 kHz.

The instructions are uploaded to the FPGA from a PC using a custom C# user interface and backend. The software allows the user to specify the state of all TTL outputs for a given number of tick segments. After a desired sequence segments is programmed, the user can program a loop to repeat this sequence a set amount of times to accumulate statistics before requesting the FPGA to send the acquired data back to the PC. The user can also programme nested loops to allow for repeated sub-sequencing. If the length of a sequence needs to be different for each data point, as is the case when acquiring Rabi oscillation spectra and in other experiments, the software can automatically create the required instruction set given a tick step. The output is usually saved as an intermediate .xml file so that the instructions are stored in a readable format and the pulse sequence used for a particular experiment can always be retrieved in the future. To send the instructions to the FPGA, the .xml file is converted to a hexadecimal file and sent over a USB connection.

The PC and FPGA have other avenues of communication. The FPGA experimental sequence is always initiated by a start signal from the computer and can also be paused in the outermost loop or stopped from the PC. As alluded to above, data in the form of photon counts that are collected from PMTs in a given time period is sent from the FPGA to the PC for immediate post-processing, storage and visualisation. A logic signal is also sent to the FPGA from the 729 nm laser lock to indicate if the laser has become unlocked. This information is also stored and transmitted along with the photon count data, ensuring that data acquired with an unlocked laser is identified. The FPGA also takes an analogue trigger signal as an input. When this input is grounded, the sequence is essentially free running and the timing between successive loop repetitions is fixed by the loop length. Alternatively, one can use a comparator circuit and trigger the start of each experimental loop from the AC mains to compensate for potential AC induced magnetic noise. A final use of the trigger is to synchronise the loops to an external clock, which is very useful for data acquisition with the EMCCD camera as will be described in section 5.5.4.

5.4.2 The Control Software

The home built spectroscopy control software was originally designed with functionality that was limited to pulse sequence design, sending commands to and retrieving data from the FPGA. Since then it has grown through the efforts of successive PhD students to include a live visualisation window that plots spectra in real time, provides histograms of photon counts and can display previously acquired data, control over various external frequency generators and a more robust data structure allowing for more carefully tailored spectroscopic sequences. One of my

major tasks during the PhD was writing a new control class of the software that would allow live acquisition and processing of spectroscopic data from an Andor iXon-897 EMCCD camera. Unlike the PMT counts which are sent as a simple series of voltage pulses corresponding to each photon, the underlying data structure upon readout from a CCD pixel array is very different and includes spatial information requiring a completely new data handling and processing code. After completing this project, I had acquired a great degree of familiarity with most branches of the codebase of the whole control system and thus for the subsequent years I was in charge of maintaining the code, fixing bugs and adding improvements along the way. Before going into detail about the design of the camera control code, I will list the highlights of the improvements made to the general control code

- Minor data format restructuring to allow the option of skipping a scan over the carrier to minimise acquisition time. This is useful for sideband cooled spectra where the regions of interest are only on the first order red and blue sidebands.
- Fixed a broken part of the old code that wouldn't allow the creation of xml pulse sequences with variable tick lengths. Previously, these had to be created in a separate Python script rather than within the general software.
- Cleaned up data access behaviour that caused crashes if the user tried to view a histogram and the required data wasn't available yet.
- Added capability to quantise each experimental run's count period into small time bins so that users can post process data using a Maximum Likelihood Estimation technique, while still allowing for live visualisation.
- Visiting summer student John Peurifoy added a peak fitting method that allows for fast identification of the width and position of spectral features.

5.4.3 Camera Control Class

The camera control class uses a DLL library with methods to control the various functions of the EMCCD and provides a GUI that displays real time images from the camera both in free running mode or during spectroscopy as seen in figure. I will now provide a summary of the main features of the program.

- **Display Features** The display area in the centre panel can show the full 512×512 pixel array in monochrome 8-bit resolution with auto-scaling contrast. The image can also be cropped for faster readout by selecting the region coordinates in the Sub-image boxes on the left of the window.
- **Acquisition Settings** A portion of the settings have already been optimised for typical spectroscopy operation and are hard coded into the software. Remaining user options are:
  - ◇ EM Gain – Allows the setting of the electron multiplying gain between values of 1-1000. For spectroscopy, this is generally set to 900-1000. Larger gain elevates the signal above the noise floor.
  - ◇ Cooler Temperature – The temperature set point of the Peltier cooler on the camera can be set from 20 to -80 degrees Celsius. Lower values significantly reduce

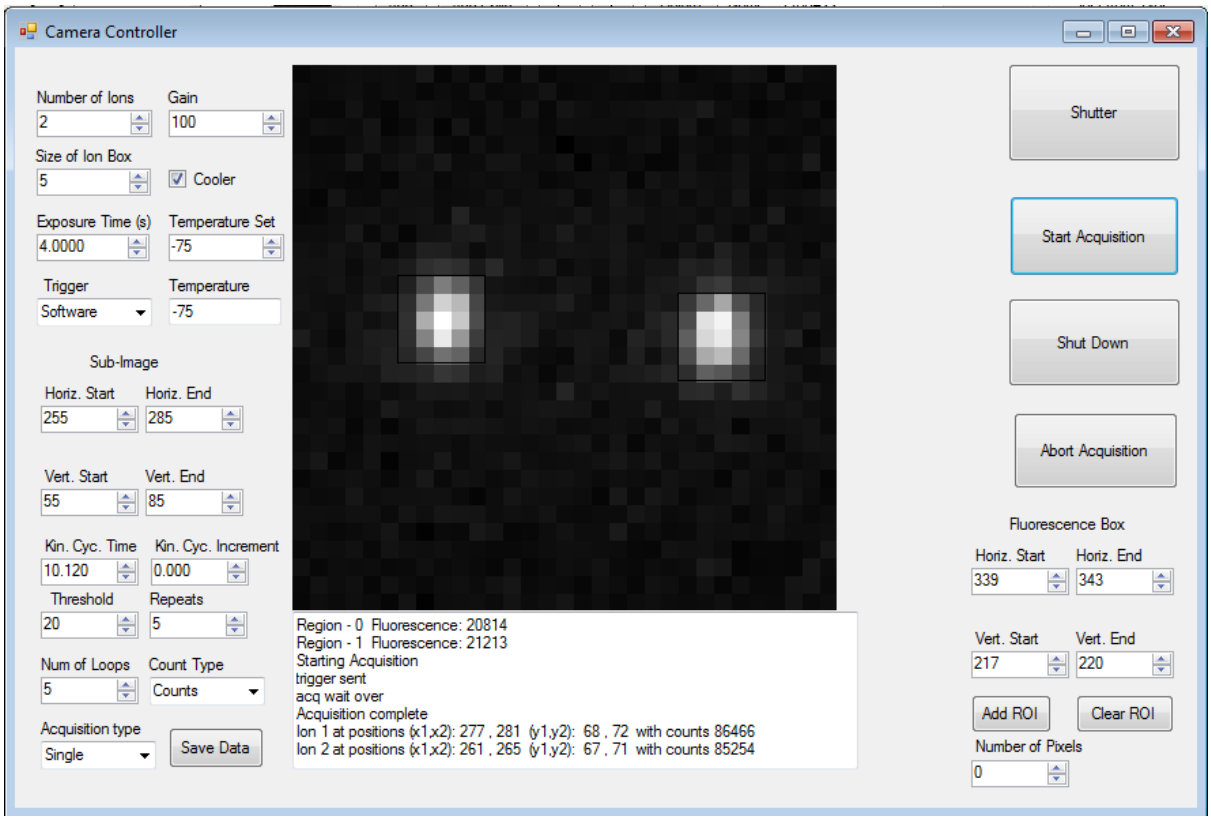

Figure 5.7: Camera software front-end.

dark counts in the pixels hence the lowest temperatures are preferred. Depending on environment temperature, the Peltier might struggle to achieve the minimum temperature, hence we tend to use -70 degrees.

- ◇ Exposure Time – Sets the exposure time for all acquisition types in seconds.
- ◇ Trigger – Change between software(internal) or external triggering. Depending on the acquisition mode, the first option is either a trigger sent digitally from the control software to the camera, or a command to start the internal trigger of the camera. The external option requires a TTL pulse to the camera to initiate image acquisition.
- ◇ Count Type – This option selects whether to output the data as raw counts (total number of electrons after amplification) or whether to use the internal manufacturer calibration of the various gain stages and bias offsets to convert to true initial electrons created in the CCD. A further conversion using the quantum efficiency of the CCD at 397 nm then gives the number of photons. The photon mode is used for spectrum acquisition.

- **Acquisition Modes**
  - ◇ Single – Acquires a single image. This mode can be used to find the ROIs around each ion. Can use either software or external trigger.
  - ◇ Continuous – Allows for continuous display of images on the camera. This uses the camera's run till abort method and can be stopped by the user at any time. The total counts in the pixel ROIs are continuously displayed in the message box. After the acquisition is aborted, the count information in each ROI for all exposures can be saved using the 'Save Data' button. An external or internal trigger can be used.

- ◇ Spectrum – A repeated series of exposures with a fixed cycle time using the kinetic series method of the camera. This option is not user selectable and instead the software defaults to this setting when the camera spectrum option is enabled in the main control window. The count data from the ROIs is directly communicated to the main experimental software for live display in the spectrum viewer and for storage in our standardised data format. This mode always defaults to internal trigger.

- **Spectrum Acquisition Settings**

  - ◇ Kinetic Cycle Time – This is the total time in milliseconds from start of an exposure to the beginning of the next exposure, including readout. The user must make sure that this is long enough to read out the image sensor. If the kinetic cycle time setting is too small, the software defaults to the lowest permitted value by the hardware. The most common cause of this problem is that the selected sub-image size is too big.
  - ◇ Kinetic Cycle Increment – When running a spectrum that has variable length pulses, such as a Rabi oscillation, the kinetic cycle length must be incremented by the same amount as the increase in pulse length per data point so that the exposure doesn't begin too early. This box allows setting an increment to the kinetic cycle time in milliseconds.
  - ◇ Number of Loops – The camera needs to know how many acquisitions there are in a kinetic series corresponding to one data point. This should be set to two[7] times the number of repeats per data point since an exposure is required for both the Doppler cooling and final counting period to conform to our data structure. This value is set automatically at the start of each spectrum from the user input selecting the number of repeats in the main controller pop-up window.

- **Region of Interest (ROI) selection**
  To obtain useful data for spectroscopic purposes, we wish to store the total counts in a pixel region surrounding each individual ion (or in some cases some part of a planar ion crystal). The software provides two methods for this purpose.

  - ◇ Manual ROI setting – In the 'Fluorescence Box' panel the horizontal and vertical position can be used to define a rectangular region that is added by pressing the add ROI button. Any number of regions can be added this way. These ROIs are used when the camera is operated in continuous acquisition mode.
  - ◇ Automatic ROI setting – The software has a built in ion finding algorithm that requires the user to specify only the number of ions and the desired size of the ROI. These regions are always square and hence are only defined by one dimension in the 'Size of Ion Box' box. Any time the single acquisition mode is run, the algorithm finds the brightest box around each ion, displaying its coordinates and storing them in memory, ready to used in a spectrum acquisition. We typically perform this calibration on a single long exposure of a few seconds before the start of data acquisition.

[7] When running interleaved spectra (i.e. multiple cool/count segments in a loop), this becomes 2× the number of interleaves.

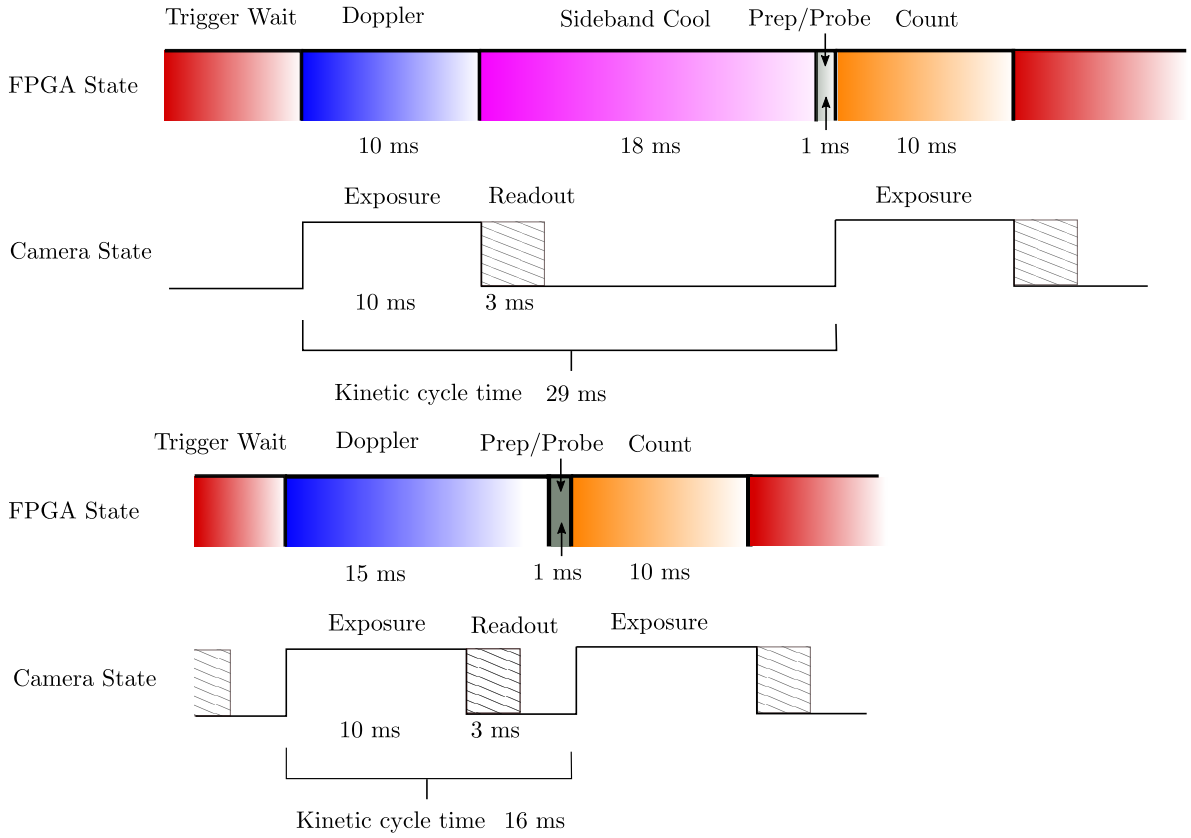

Figure 5.8: Schematic of the synchronisation of the FPGA experiment states and the camera state for two typical sequence types: sideband cooled spectrum (above) and Doppler cooled spectrum (below)

One of the major issues when designing the camera control was the fact that we did not want to use a TTL trigger from the FPGA at the designated count time to initiate a fixed length exposure as this was shown to lead to increased noise (section 5.5.4) compared to when the same exposures were triggered with the internal camera clock. Instead, we used the internal clock of the camera to trigger the start of an FPGA loop. This was accomplished by sending a TTL signal from the 'FIRE' output of the camera to the FPGA trigger input at the start of every exposure. The complication arises from the fact that we always wish to expose twice per FPGA loop, once for diagnostic Doppler cooling and once for the actual electron shelving data readout. Given that the camera has a particular readout time, the second exposure must not occur before this readout is completed. This means that the FPGA loops have to be designed so that the separation between the two exposures is longer than the readout time and that there is no dead time in the loop itself once the experiment has started. Typically this is not a problem in any experiment that involves sideband cooling since the readout time required is on the time scale of 2-3 ms and sideband cooling is always longer and we simply match the kinetic cycle time of the camera to synchronise the initial and final exposures. For all other scenarios, we simply extend the Doppler cooling time by 4 ms and adjust the kinetic cycle time accordingly. An example of the synchronisation for these two experimental sequences is shown in figure 5.8.

One downside of this scheme is that there is a relatively long dead time after the count period equal to the kinetic cycle minus the exposure that isn't present when running with PMTs. For long sideband cooling times and long experimental sequences in general, the total time necessary

to collect a spectrum is almost doubled. A further quirk of the current implementation is that the kinetic cycle time and exposure need to be entered manually by the user based on what spectrum is to be run since the information in the .hex filed that stores the FPGA instructions is never actually unpacked in the PC once it has been compiled. Hence the user must be vigilant to carefully compute the required cycle time, especially when the sequence to be run is complicated with smaller internal loops. One suggestion to fix this issue would be to always initiate a stored spectrum from its associated xml file, from which the required data can be scraped and the hex file recompiled at run time. This would add a minute or two at most (for long sequences), but potentially save a lot of time redoing whole experimental sets if subtle timing errors are present.

5.4.4 RF frequency synthesis

The AOM on the 729 nm spectroscopy laser requires very precise frequency synthesis to perform spectroscopy and coherently drive the ions. We use an Analog Devices AD9910 direct digital synthesis (DDS) chip on an evaluation board interfaced with an Arduino micro controller and the FPGA to generate fast switching of frequencies with 1 Hz precision. The DDS board can store up to 8 profiles with different frequency, amplitude and phase information that can rapidly be switched using TTL signals from the FPGA to three logic pins on the board. These profiles allow us to rapidly alternate between frequencies to do complex pulse sequences such as those employed in multi-stage sideband cooling. To update the profiles, the PC control software first sends the required commands to the Arduino, which then writes to the internal DDS memory.

We also sometimes need to send two frequencies into the AOM to create a bichromatic beam. We do this by combining a second RF frequency from a HP8643A function generator with the DDS output on a resistive summer. The function generator is phase locked to the DDS using a 10 MHz clock signal, but is otherwise free running and not connected to the experimental control software. Thus before each experiment where we wish to use the bichromatic beam, we have to manually set the required frequency and amplitude to the desired values. The generator is then left on, and the signal is passed through an RF switch triggered by a TTL pulse from the FPGA. This system is somewhat impractical and a modest investment into either a dual channel FPGA, an arbitrary waveform generator or even two paired FPGAs would greatly simplify the experimental process.

5.5 Ion Fluorescence Detection

To read out the state of the qubit formed by the $S_{1/2,-1/2}$ and $D_{5/2,-3/2}$ states, we apply near resonant light on the $S_{1/2} \rightarrow P_{1/2}$ transition and collect fluorescence conditional to the ion being in the 'bright' $S_{1/2,-1/2}$ state either using two PMTs or an EMCCD . If the ion was in the 'dark' $D_{5/2,-3/2}$ state ideally we should see very little fluorescence beyond that of background laser scatter or other noise. The challenge is to effectively discriminate between the fluorescence signals of the bright and dark distribution in the presence of additional magnetically induced j-mixing decay from $D_{5/2,-3/2}$ (section 3.2.2).

5.5.1 Geometrical Efficiency

Light from the trap is collected in a relatively small solid angle of 0.22 steradians, limited by the size of the two apertures in the ring electrodes. This gives an ideal maximum collection efficiency of 1.75%. A pair of best form lenses with $f = 20$ mm are placed one focal length away within the vacuum system to collect the light, which is then reflected off 45 degree angled mirrors downwards, parallel to the bore of the magnet. One beam path then uses an achromatic doublet and an aspheric lens to focus the light into a fixed 200 μm multimode fibre. The other beam path uses a pair of singlet lenses to create a new focused image magnified by a factor of 3 directly beneath a screw-threaded aperture on the breadboard. At this point, we can choose to connect either a second 200 μm multimode fibre or a mirror on a rotating elbow mount to send the light to an optical relay and then onto the EMCCD camera. This relay is necessary to protect the camera from the fringe field of the superconducting magnet. The relay system was designed by Jieyi Liu for his Masters thesis with my assistance and consists of a pair of achromatic doublets with $f = 150, 500$ mm separated by 350 mm to create a very sharp focus with minimal aberrations and an additional 3.3x magnification 1076 mm away from the intermediate focus below the breadboard. This design was optimised in a ray tracing software to ensure excellent imaging resolution at a few micrometer level. The EMCCD camera was initially mounted on a micrometer translation stage to carefully fine tune its position and find the optimum focus, before being permanently fixed into place by attaching it to a pair of posts. This allows us to image the fluorescence of a single ion with a spot diameter of less than 5μm, which is much smaller than the typical inter-ion separation for axial ion chains.

Considering all the losses at each optical element including additional bandpass filters at 397 nm and fibre coupling using the PMTs, the total detection efficiency drops to 0.2%. When using the camera, the efficiency is slightly lower at 0.15% since only half the light is imaged, offset by the lack of fibre coupling.

5.5.2 PMT detection of a single ion

The two PMTs used in the experiment are Thorn-EMI 9893-QB models with quantum efficiency of 20% at 397 nm, resulting in a final collection efficiency of 0.04%. When working with typical laser parameters for Doppler cooling (i.e. detuning of $\Gamma/2$ and saturation of $0.1 - 0.2$) we expect to have a photon count rate of $\sim 1500 - 2000$ photons per second. Thus we would expect to be able to accumulate enough statistics to distinguish a fluorescing ion from background in 10s of ms. However we have to be aware of limit on the collection time placed by j-mixing decays, which are a consequence of the large magnetic field as discussed in section 3.2.2. We can use the j-mixing rate from equation 3.6 to estimate the mean lifetime of the ion remaining in the bright fluorescence cycle before decaying to the $D_{5/2}$ which would potentially present itself as a false positive. Assuming a saturation parameter of 0.3, the time constant of the exponential distribution is $\tau_j = 70$ ms. In 10 ms this corresponds to the ion decaying 13% of the time.

To fully quantify the error in our detection, we need to look at how the j-mixing manifests itself in our detection scheme. The laser scattering and detection on the PMTs can be modelled as a series of random, independent events that follows a Poissonian probability distribution of

n photons being detected in a time interval t_D with a mean photon number λ:

$$P(n) = \frac{e^{-\lambda}\lambda^n}{n!} \tag{5.1}$$

When the ion is prepared in the dark $D_{5/2}$ state, the distribution mean $\lambda = R_d t_D$ will consist of counts due to background R_d, which in our experiment are mostly from laser scatter of the radial 397 nm beam from the trap electrodes or vacuum system windows with a small contribution due to ambient light leakage and PMT dark counts. When the ion is prepared in the bright $S_{1/2}$ state, the detected fluorescence count rate R_b is added to the background rate so that the mean is now $\lambda = (R_d + R_b)t_d$. In the absence of j-mixing, the total $P(n)$ distribution would just be the sum of these two Poissonians. If we simply increase t_d so that there is no overlap between these two distributions and then set a threshold value for n to discriminate between the two states the detection fidelity approaches unity. To account for j-mixing we have to consider what happens when an initially bright ion becomes dark during the detection period. The modified bright distribution takes the form:

$$P(n) = e^{-t_D/\tau_j}\frac{e^{(R_d+R_b)t_D}((R_d+R_b)t_D)^n}{n!} + \frac{1}{R_b\tau_j}\int_{R_d t_D}^{(R_d+R_b)t_D} e^{-(\lambda - R_d t_D)/(R_b\tau)}\frac{e^{-\lambda}\lambda^n}{n!}d\lambda \tag{5.2}$$

where the first term is the distribution in the absence of decay weighted by the probability that the ion will not decay and the second term is the distribution after decay integrated over all the possible means based on when the decay occurred. We can see the effect of this j-mixing on real counts in figure 5.9 where the data is taken from a Rabi oscillation experiment where the ion spends, on average, roughly equal amounts of time in the dark and bright state. The figure shows two peaks that look very similar in shape to standard Poissonians, but there is a clear plateau in between the peaks that is a result of the j-mixing. The figure also shows that a fit to the above equation 5.2 follows the distribution more accurately, especially in the j-mixing region. If the j-mixing was absent, then the double Poissonian fit would clearly suggest placing the threshold at $n = 10$ to maximise the state discrimination fidelity. However, if we calculate the dark and bright errors ϵ_d, ϵ_b, defined as the ratio of their respective distribution areas below and above threshold to their total area we obtain $\epsilon_d = 0.01\%$ and $\epsilon_b = 9.6\%$ suggesting a significant fraction of bright counts have been incorrectly identified as dark. By minimising the total error, we find the optimal threshold position to be $n = 7$, yielding $\epsilon_d = 0.7\%$ and $\epsilon_b = 6.2\%$.

We usually have to adjust the threshold based on the experimental conditions. One important case to highlight was the refocussing of the radial beam as detailed in section 5.2.2, which increased our background scatter rate R_d. A fit to a count histogram in 5.10a reveals errors of $\epsilon_d = 3.5\%$ and $\epsilon_b = 7.4\%$, marking a roughly 40% increase in error over the original beam focus. To alleviate this problem, we implemented a technique to attenuate the intensity of the radial 397 nm beam by $\approx 80\%$ during the count period since it contributes almost all of the background scatter to R_d, but also contributes only 20-30% to the fluorescence rate R_b due to being offset from the trap centre. Using the same exact experimental conditions as in 5.10a, we were able to reduce the errors to $\epsilon_d = 2\%$ and $\epsilon_b = 4.8\%$ in 5.10b, thus reducing the total error by almost 40%. To achieve any further improvement would require either to increase the collection efficiency, reduce background or to use detectors with higher quantum efficiency.

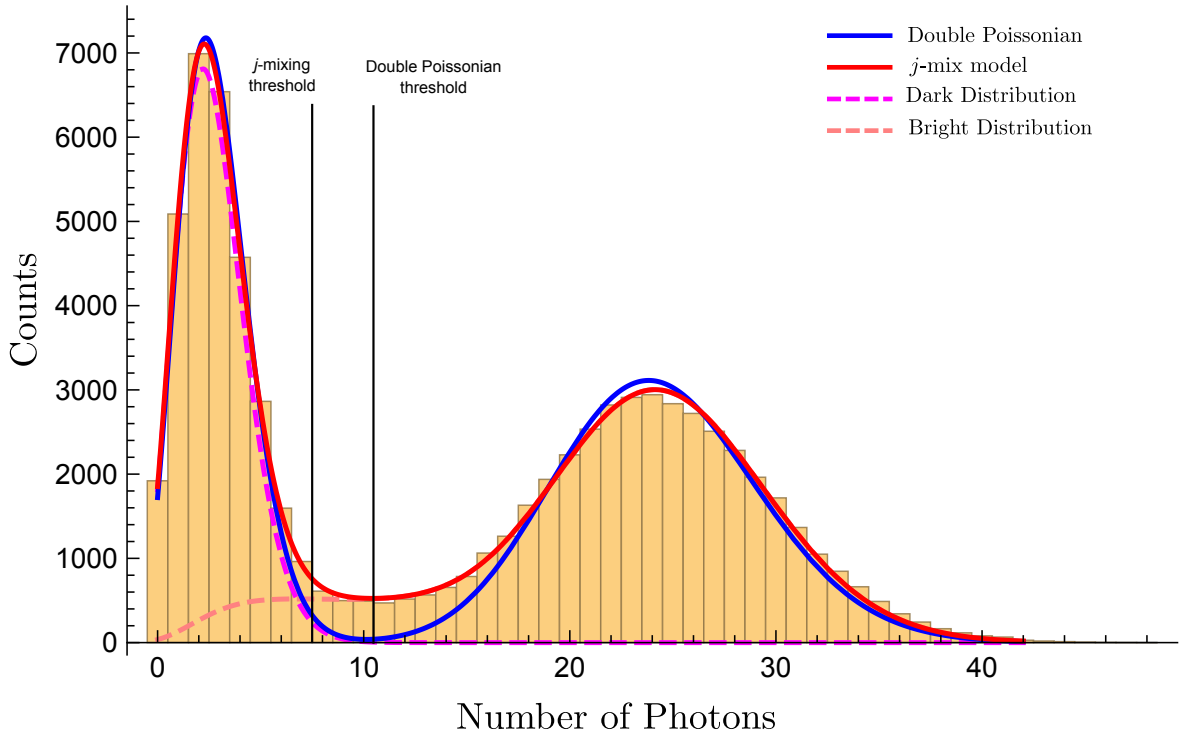

Figure 5.9: Histogram of photon counts in many 8 ms count periods where the ion was prepared in the dark and bright states a roughly equal number of times. The peak between 2 and 3 photons corresponds to mostly counts from the ion in the dark $D_{5/2}$ state whereas the peak at 24 corresponds to counts from the bright $S_{1/2}$ state. A fit assuming the peaks were purely Poissonian is shown along with the associated threshold that would minimise discrimination error. If the full j-mixing expression from 5.2 is used to replace the bright distribution, a better fit to the central plateau region is obtained and the new estimated threshold is lower. The two constituent distributions of the j-mixing fit are also shown.

The first two options are not very practical given the very restrictive optical access conditions imposed by the trap structure and the strict requirements of the beam focus on cooling performance. Improving the quantum efficiency by more than a factor of two could easily be achieved by investing in a new generation of PMTs that boasts quantum efficiencies above 40% at 397 nm[147]. This would allow us to count for a shorter period of time and mitigate the impacts of j-mixing error.

A further option would be to move to techniques such as maximum likelihood estimation. This involves splitting the counting time period into smaller time bins and using the temporal information to better determine if one particular experimental trial resulted from a bright or a dark distribution. This would remove the need for setting a threshold, but slightly increase the acquisition and post-processing complexity and while we have used this technique in a few trial spectra, we did not implement it for the data collection protocols described in this thesis.

5.5.3 PMT detection of multiple ions

So far we have shown that for a single ion, the PMT can provide total errors as low as 6%, but as the number of ions increases this will quickly grow with each additional ion. The count histograms will have an additional bright distribution corresponding to each further ion, but

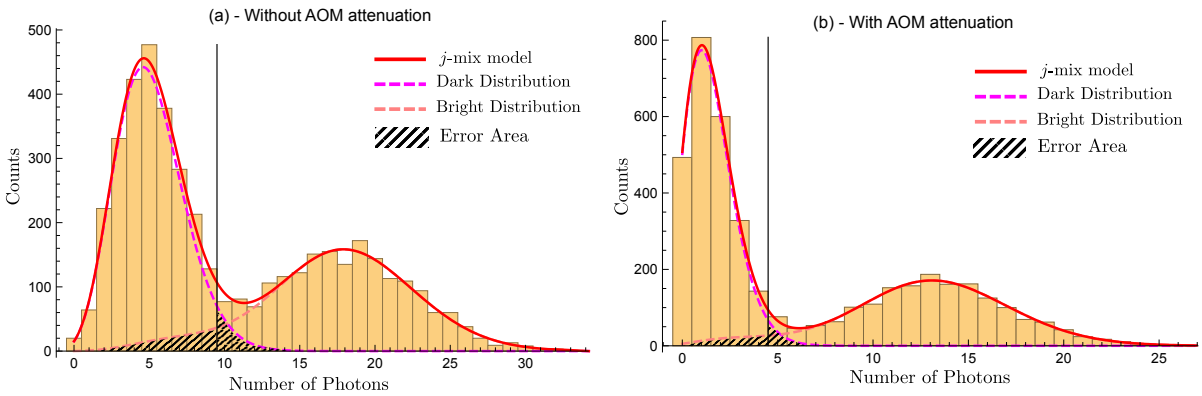

Figure 5.10: Histograms of photon counts in many 10 ms count periods where the ion was prepared in the dark and bright states a roughly equal number of times. Figure (a) shows the distribution in absence of the radial beam attenuating AOM while (b) has the AOM attenuating the radial beam by up to 80% of its intensity. The result is that the shaded area corresponding to the discrimination error is clearly smaller in (b) compared to (a). The total discrimination error is reduced by 40%.

since the separation between the means remains constant[8] while the width of each distribution grows as the root of the mean, the overlaps between these distributions will get progressively larger. We can look at the case of a two ion photon count distribution in figure 5.11 and see that now there are three peaks, the first corresponding to both ions dark, then one ion bright and finally both fluorescing. If we were to threshold as before on the lowest peak, the total error at optimal threshold position of 5.5% remains consistent with the single ion case, since there is no additional source of R_d counts, however the total error in distinguishing at least one ion fluorescing from both fluorescing is already 15% and will continue to get worse with additional ions. Hence for multiple ions, it makes sense to always threshold on the dark distribution for spectra that require minimal error, such as Rabi oscillations, where we expect high excitation probabilities. On the other hand, for spectra where we look for small peaks corresponding to weak transitions, the N-tuple excitation might suppress them excessively since the excitation probability p will scale as p^N.[9] In this case, it can be worth compromising the fidelity of the relative height of the prominent peaks in order to be able to distinguish these weaker features from the background. For larger crystals $N \geq 4$, the N-tuple excitations become very weak and the photon count histograms looks almost completely flat hence setting a threshold becomes problematic. In this case we opt to show the total counts accumulated over all the experimental trials, akin to datasets obtained from absorption spectroscopy, rather than threshold between distributions. In the relevant experimental results section, we will always list the type of state discrimination used in each spectrum.

5.5.4 Spectroscopic EMCCD detection of ions

The benefits of using an EMCCD compared to PMTs are twofold. Firstly, the spatial resolution of the camera allows us to distinguish ions that are in axial chains, mapping fluorescence from

[8]This ignores such effects as unequal illumination of some ions, which will become an issue for certain ion crystal configurations

[9]This is only strictly true on carrier transitions. In general, any transition that changes the motional state of any of the crystal modes will create small levels entanglement altering the excitation probability. See section 7.1 for treatment of the two ion case.

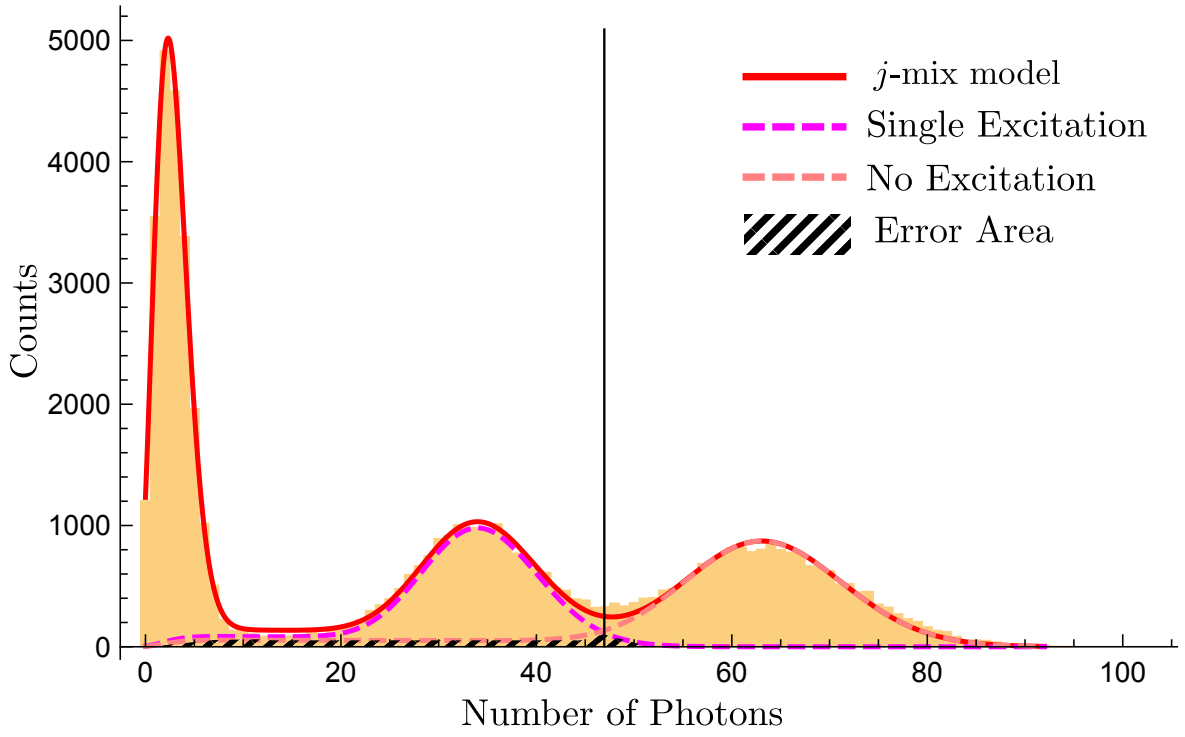

Figure 5.11: Histogram of photon counts in many 12 ms count periods for a two ion Rabi oscillation experiment. The full j-mixing fit is broken down into the two distributions constituting one ion fluorescing and both ions fluorescing. Their mutual overlap area corresponding to the error is highlighted as well as the optimal threshold to distinguish between them is shown.

each ion to its own individual excitation spectrum. This allows us to pick up on effects such as different Rabi frequencies[10] and hence excitation strength between the two ions. This greatly increases the readout fidelity for coherent operations, where the fact that the two ion excitations always get averaged in the PMT data can smear out many important features. For example, a two ion Ramsey spectroscopy experiment that involves a frequency splitting between fringes of 1.5 kHz, same as the difference in Zeeman shifts between the two ions, would lose all contrast on the PMT as the ions' fringes would be out of phase with each other. Secondly, the readout fidelity for axial chains is naturally improved by avoiding the overlap of distributions as seen in the previous section. Furthermore, the spatial resolution also greatly reduces the contribution of the background laser scatter to R_d as the ion signal is generally focused to a few pixels, whereas the scatter is distributed over a large area. This will have to be contrasted with the downside of having only half the geometric collection efficiency compared to two PMTs.

The EMCCD used in the experiment is an Andor iXon 897 Ultra with a nominal quantum efficiency at 397 nm at $\approx$ 50%, which would offset the halving of the geometric collection efficiency. Unlike the PMT, the camera has different sources of noise that need to be considered. To discuss them we will first outline how an EMCCD functions. First, light is collected on a standard CCD array. After collecting the signal for some time, the accumulated charge in each pixel is shifted to a backplane CCD in a process called 'frame transfer' effectively ending the exposure. The readout then proceeds by shifting each row of pixels vertically down into a serial register, which then moves each pixel horizontally through the electron multiplying gain stage,

[10] Mostly due to the ions experiencing slightly different magnetic fields, leading to different Zeeman shifts on the spectroscopy transition

where the signal is greatly amplified above noise and ultimately converted to a count on an analogue to digital converter. The pixels are shifted by applying a potential difference between the register, or across the CCD plane. These shifts are precisely controlled by a 'clock' voltage that is different and independent for the horizontal and vertical shifts.

The speed (frequency) of these clocks and their amplitude (voltage) affect the rate at which spurious charges are created during the shifts. The manufacturers call this 'Clock-induced charge' (CIC). Since this noise depends on a fixed number of readout steps, it is independent of exposure time and is defined per pixel. In principle, pixels at the bottom of the camera should have slightly lower CIC since they need fewer steps to reach the gain stage though we observe most of the noise to originate from the serial register. This type of noise is inevitable and can be minimised by optimising the parameters. In general, increasing the readout speed and decreasing the clock voltage lowers noise. However, at fast readout speeds, some of the charge gets left behind on the sensor recording a smeared or almost completely empty image, requiring larger amplitudes. We have taken care to minimise the error by trialling all different parameters and observing the effects on the noise. This noise is non-Poissonian in nature. [11]

A second consequence of this readout mechanism has implications on the triggering method used in the experiment. While the camera has a mechanical shutter, it is too slow to operate at the required rate, hence the front CCD sensor is constantly exposed to light. This means that before an exposure period starts, all the accumulated charge has to first be cleared from the sensor by what the manufacturers term a 'keep-clean cycle'. In principle, when the camera receives an external trigger, it should perform a full keep clean cycle before initiating exposure, however, despite this claim we notice a higher background noise than when using the internal trigger with its own keep clean cycle. This has been observed by another research group as well with the same camera model [148]. Comparing many acquisitions of background signal, the internal clock erroneous photon per pixel rate is found to be 0.04, whereas for the external triggering it is 2.5 times larger. It is for this reason that we adopted the internal camera triggering in all our experimental data acquisition.

The final effect to consider is the electron multiplication gain stage. Since this is a stochastic process, there is a further non-Poissonian broadening of the count standard deviation by a factor of $\sqrt{2}$. [149] The effect of this broadening is that for the same mean photon count of the bright and dark distributions, the error rate is greater than in a PMT. Figure 5.12 shows a camera count histogram with a 12 ms collection time of a 5x5 pixel region around a single ion with a double Poissonian model overlaid. The data is in clear excess of the curve for both distributions due to the non-Poissonian broadening. The pixel region size was also optimised in a series of experiments comparing the overlap of the bright (with 854 repump on) and dark distribution starting from a 3x3 up to a 10x10 region. The minimum total overlap error was found to be 1.7%. Once j-mixing is included, as in figure 5.12, the error rises to 5% which is similar to the case of two PMTs. This is consistent with the fact that the bright rate is slightly higher due to a higher quantum efficiency despite imaging only half the light of the PMTs and the distribution is broadened. For detection of a single ion, the EMCCD camera performs roughly equivalent to two PMTs when it comes to discrimination fidelity, but has the downside of having longer readout time, which can lead to significant experimental dead time due to the pulse sequencing required for synchronisation to the internal camera clock (see section 5.4.3). This dead time

[11] The parameters used are: Horizontal Clock – 17 MHz, Vertical shift speed – 3.3 μs, Vertical amplitude – +2

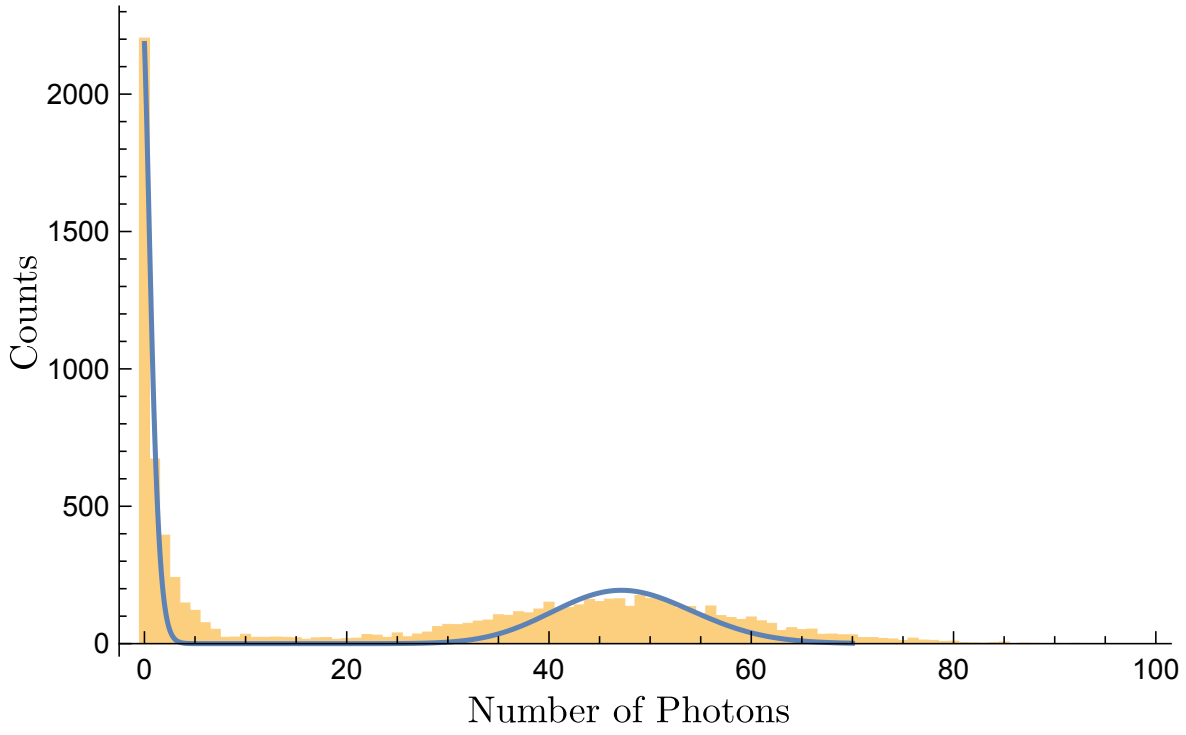

Figure 5.12: Histogram of photon counts in many 12 ms time periods from a 5x5 pixel region-of-interest centred on a single ion of a two ion axial crystal during a Rabi oscillation experiment. The blue overlaid curve is a fit to the data assuming only two Poissonian distributions, highlighting the additional broadening of the counts by EMCCD specific noise processes.

prolongs the length of time required to keep all other experimental systems such as lasers stable over the course of whole spectrum and hence we use PMTs only for single ion spectra.

For axial ion crystals, the camera is the preferred choice due to both an improved detection fidelity that is independent of the number of ions and individual ion readout. For planar crystals, however, the benefits of the spatial resolution are often lost due to the ions constantly rotating around the magnetic field axis which is being imaged side-on with exposure times much longer than the rotation period of the crystal. There are sometimes exceptions where we want to only look at fluorescence from a particular region of an ion crystal, for example the central ion in an $N = 6$ crystal that sits at the trap centre and is orbited by a pentagon of ions. Since the coherent manipulation laser beam will have a different intensity on the central ion compared to the outer ones, we should be able to distinguish different excitation spectra between these regions using the EMCCD (see figure 7.13).

CHAPTER 6

COOLING AND COHERENT STUDIES ON THE AXIAL MODE OF A SINGLE ION

In this chapter we will present results that build on the first ever demonstration of ground state sideband cooling of the axial motion of a single ion in a Penning trap [50]. In terms of cooling we will demonstrate in detail the applications of higher order sidebands to prevent population trapping at low axial frequencies, outside the Lamb-Dicke regime. Then we will show an alternative method using adiabatic trapping potential relaxation to take an ion that was ground state cooled at high axial frequency down to very low trapping frequencies without any heating. Using the ground state cooled ion we then show the results of Rabi and Ramsey type experiments that help us constrain the different coherence times of the system. We determine the optical coherence time of the qubit and then show how we can use a dynamical decoupling sequence of additional laser pulses to effectively extend it. We also measure the motional coherence times of various motional Fock state superpositions and compare the results to the trap heating rates. Finally, we demonstrate the use of a bichromatic laser beam in preparing non-classical states of motion.

6.1 Sideband cooling – Outside the Lamb-Dicke regime

6.1.1 Spectroscopy techniques – Doppler cooling

We begin this discussion by describing how we perform Doppler cooled spectroscopy on the $S_{1/2} \leftrightarrow D_{5/2}$ transition. This type of experiment is the most basic diagnostic that we can perform to help us correctly set the laser frequencies and intensities to achieve the lowest temperature and hence we run these types of spectra daily. A typical experimental sequence of this type is shown in figure 6.1. First, we begin with a cooling pulse where both 397 lasers and the repump lasers are on for a period of 8-12 ms. The cooling length is set to match the readout length for easier diagnostics of potential erroneous data points. During this time the ion should be fluorescing throughout, but if it goes dark for whatever reason, such as collision with a background gas pushing it out of the laser beam or if one of the lasers becomes unlocked, we reject this experimental trial if fewer photons than a set threshold value are detected. In the next step, we prepare the ion in the $S_{1/2,-1/2}$ Zeeman sublevel by turning off the σ_+ 397 nm laser for 100–200 μs. This allows us to initialise the ion in the qubit ground state with almost perfect fidelity. At this point, we turn off the 397 nm lasers as well as the 854 nm repump and tune the 729 nm laser to near resonance with the $S_{1/2,-1/2} \leftrightarrow D_{5/2,-3/2}$ transition for some desired length of time to excite the ion with particular probability given by the detuning, pulse length

and Rabi frequency. Finally, we turn the 397 nm lasers back on and record the fluorescence effectively performing a projective measurement on the qubit. This sequence is then repeated between 100-400 times to build up sufficient statistics to measure the excitation probability to a given degree of accuracy. The spectrum data collection then proceeds by incrementing the frequency of the 729 nm probe laser and repeating the sequence.

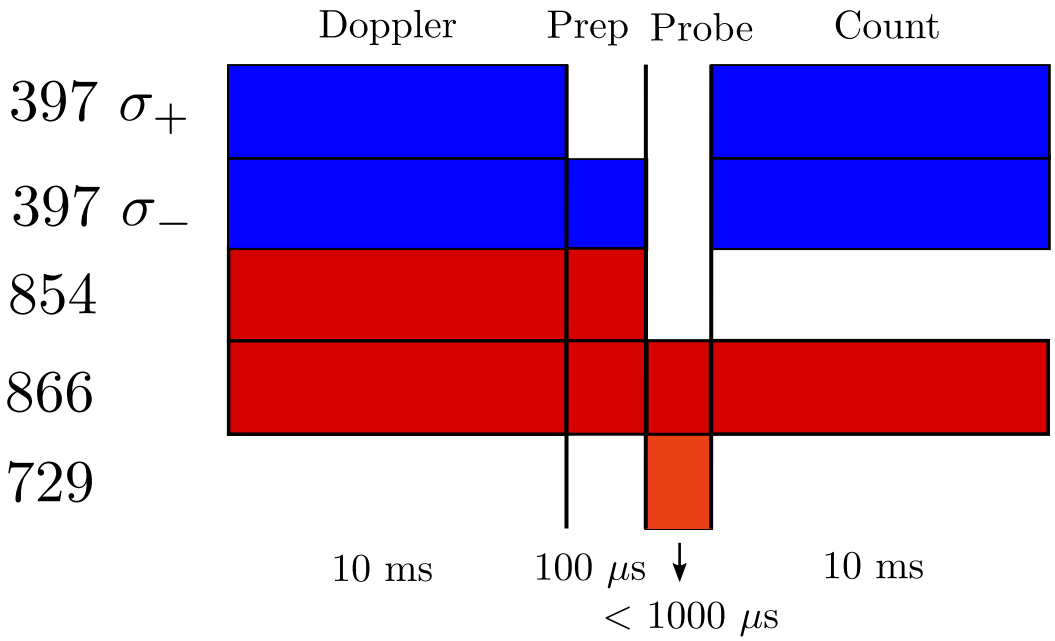

Figure 6.1: Pulse scheme representing a typical Doppler cooling spectroscopy sequence. Probe times depend on the 729 laser intensity.

After Doppler cooling, the ion is in a thermal state given by the Boltzmann distribution with a mean phonon number $\bar{n}$. Throughout one set of repeated measurements we thus probe the ion at various different n states. The excitation probability around a particular k-th order sideband is then given by a sum over all the possible excitation profiles (eq. 4.16) that depend on Rabi frequency $\Omega_{n,n+k}$ (eq. 4.27) weighted by the probability of being in the n state (eq. 4.28):

$$|c_e(t,\Delta)|^2 = \sum_{n=0}^{\infty} \frac{\bar{n}^n}{(\bar{n}+1)^{n+1}} \frac{\Omega_{n,n+k}^2}{\Omega_{n,n+k}^2+\Delta^2} \sin^2\left(\frac{\sqrt{\Omega_{n,n+k}^2+\Delta^2}}{2}t\right) \tag{6.1}$$

In the limit of resolved sidebands, the full spectrum can thus be approximated as an incoherent sum of the excitation probability around each sideband. Using this model we can fit any Doppler cooled spectrum keeping the $\bar{n}$ and Ω_0 parameters free, provided we choose a sensible cut-off for n in the summation. In the interest of preserving computational ease, we usually truncate at $n = 400$, which even for $\bar{n} = 75$ accounts for 99.95% of the population. Using this model we fit two spectra in figure 6.2 to experimental data at axial trap frequencies of $\nu_z = 418$ kHz and $\nu_z = 187$ kHz. The spectra were recorded under similar experimental conditions where the detuning of both Doppler cooling lasers was maintained roughly ≈ 10 MHz below resonance. The radial to axial beam power was kept at an approximate 3/2 ratio, with the axial powers reduced to ≈ 2 μW per beam to prevent any recoil heating from the beams being abruptly turned off. Axialization was kept on during both spectra at 400 mV to keep the radial motion cool. Qualitatively we see that the spectrum (b) has more sidebands within a Gaussian shaped

envelope of the peak heights, yet they still remain well resolved. The fits tell us that both spectra are consistent with their Doppler limited $\bar{n}$ for a 3/2 radial to axial ratio[1] in scattering rate and hence their temperature must be the same ($\approx$ 420 mK), which is also evident when comparing the width of the peak height envelope.

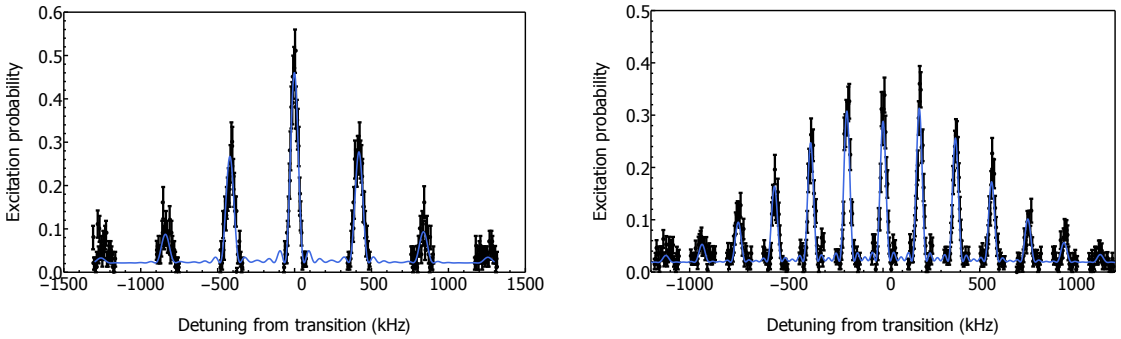

(a) $\nu_z = 418$ kHz **(b)** $\nu_z = 187$ kHz

Figure 6.2: Spectra of a single ion after 10 ms of Doppler cooling. The average occupation obtained from the fits is $\bar{n} = 23(1)$ and $\bar{n} = 54(2)$ for (a) and (b) respectively consistent with the Doppler limits of 23 and 52 respectively at $\gamma_z/\gamma_r = 1.5$ scattering rate ratio.

6.1.2 Sideband cooling

The general scheme of performing sideband cooling (fig. 6.3) begins with a Doppler cooling segment and then adds a time interval of 10–80 ms of the 729 laser targeted at one red sideband (or many in turn) and uses the 854 repump beam to quench the excited $D_{5/2}$ state to broaden the transition and accelerate the cooling. The 397 σ_- beam and the 866 beam are kept on to close the cooling cycle. The spectrum concludes with the usual segments of state preparation, probing and detection. The presence of the 854 beam creates an appreciable Stark shift of $10 - 30$ kHz that needs to be experimentally measured as the 854 beam frequency and power drift. We periodically perform measurements where we set our probe frequency to the un-Stark shifted first red sideband and then scan the 729 cooling pulse around this frequency and look for a drop in excitation corresponding to cooling. The frequency difference between the excitation minimum and the unshifted peak defines that Stark shift that is added to all the cooling profiles including those for higher order sidebands.

Having prepared the ion at or near the Doppler limit, the additional sideband cooling pulses required to bring the ion to the ground state depend on how much of the thermal state n lies above the first or even second order red sideband coupling strength minima as seen in figure 4.12. To remind ourselves of the severity of the problem, figure 6.4 shows a plot of the fraction of population at the Doppler limit that lies above the coupling minima of the first two sidebands as a function of ν_z. We can divide this plot into three regions:

- $\nu_z \gtrsim 300$ kHz
  In this region the population above the minima of both sidebands is below the discrimination error of our apparatus. The error very quickly dips below one percent for the 1st

[1] Since the radial beam is offset from the trap slightly, the ratio should in reality be a bit lower, and consequently the Doppler limit too. Though we can't exactly measure the ratio, this difference would at most lower the limit by a few phonons and thus the slight increase above the limit is not a significant concern.

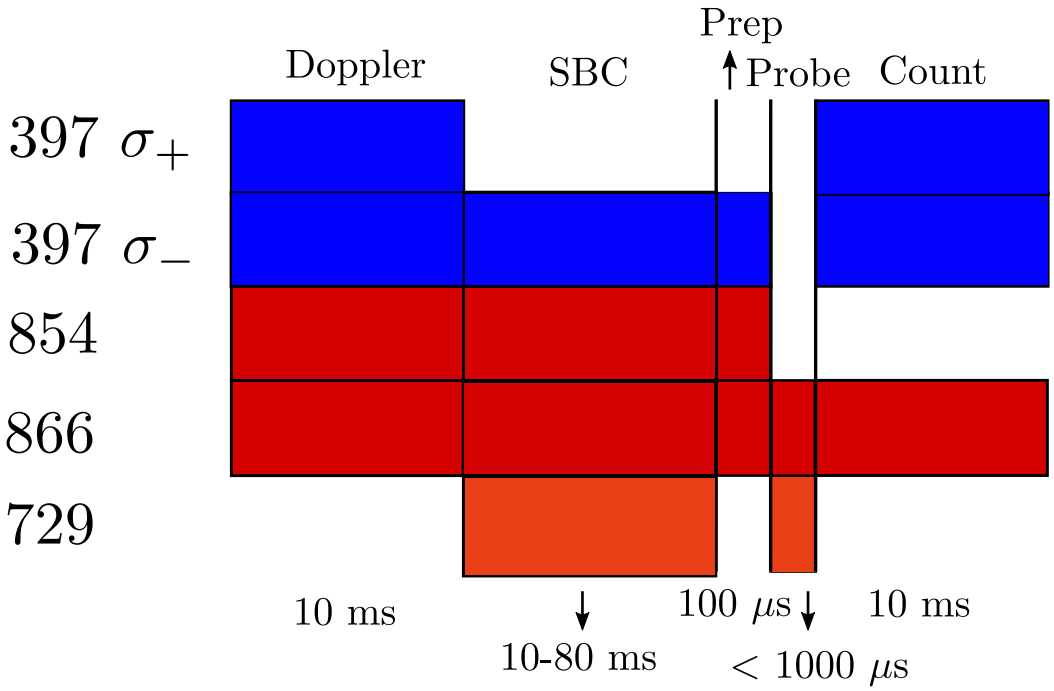

Figure 6.3: Sideband cooling pulse scheme showing the laser states at each step. The length of the cooling stage depends on the complexity of the underlying cooling sequence.

red sideband, hence using it should suffice to get the ion into the ground state.

- $300 \gtrsim \nu_z \gtrsim 80$ kHz
  This intermediate region has appreciable population above the minima of both sidebands that leads to non-thermal phonon distributions where a part of the population is cooled to the ground state and a part remains trapped around the coupling minima when cooled only on one sideband. The use of combinations of sidebands in sequence is required to achieve ground state cooling.

- $\nu_z \lesssim 80$ kHz
  In this region, cooling on one sideband would not bring more than 20 % of the population to the ground state and instead there would also be population accumulation in various trapping minima beyond the first. The Doppler limit becomes large, the minima get very close to each other and even with interleaving many higher order sidebands ground state cooling becomes impractical.

For now, we will focus on the first two regions and return to the third when we discuss adiabatic cooling. To illustrate the effectiveness of single stage sideband cooling in the first high frequency region, we show a spectrum after 10 ms of cooling on the first red sideband in figure 6.5. From the fit we determine $\bar{n} = 0.01(1)$, which is consistent with the ion being 99% of the time in the ground state. In contrast, when sideband cooling is performed for 25 ms at 187 kHz, the picture is quite different as seen in figure 6.6; the first BSB amplitude is reduced to 0.8 and higher order sidebands have appreciable population. To fit this data, the population that is trapped around the first RSB coupling minimum at $n_0 = 72$ is modelled as a Gaussian distribution centred around n_0 with a standard deviation σ_n as a free parameter weighted by a factor q whereas the population near the ground state is modelled by a thermal distribution

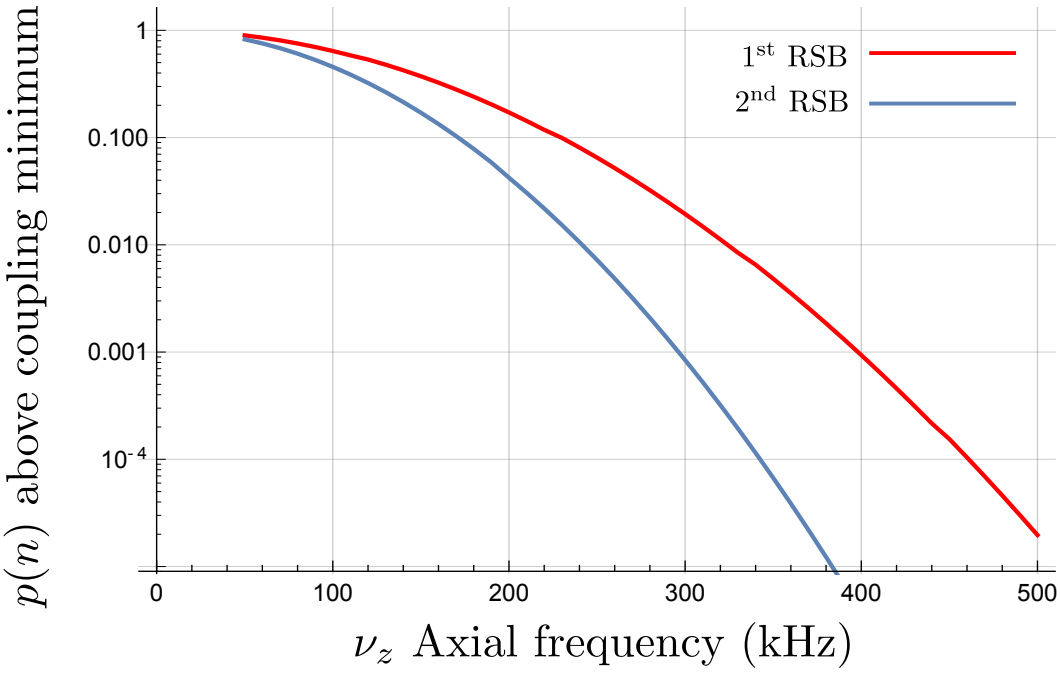

Figure 6.4: Plot showing fraction of population at the Doppler limit that lies above the lowest coupling minima of the first two red sidebands as a function of the trapping frequency.

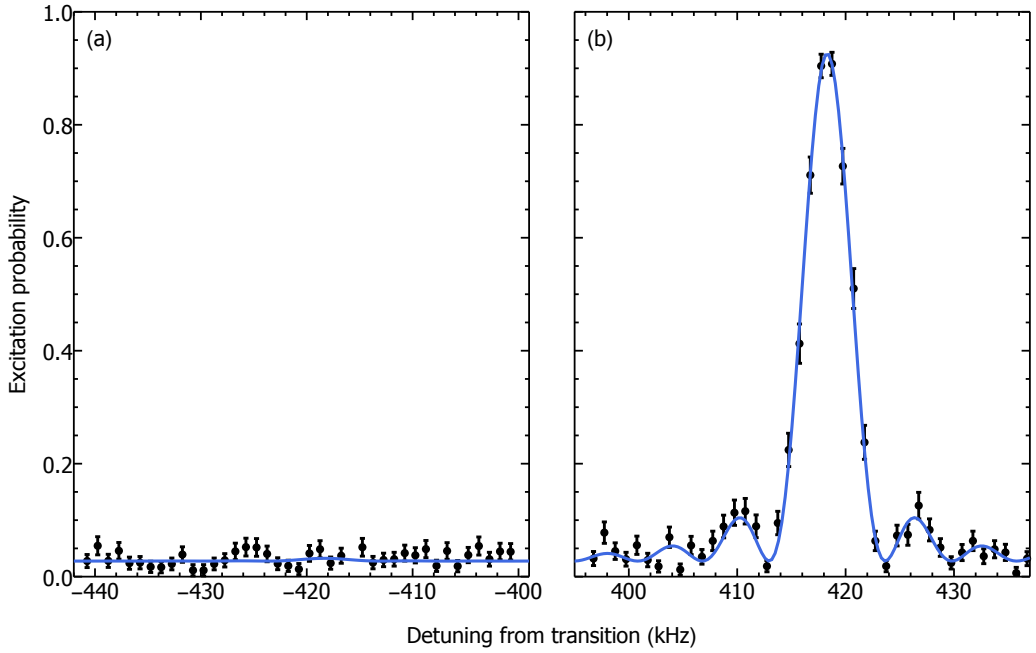

Figure 6.5: Spectrum after 10 ms of single stage sideband cooling for a single ion at 418 kHz trapping frequency. (a) First red sideband. (b) First blue sideband. The final ground state occupation $\bar{n} = 0.01(1)$ is given by the fit ($R^2 = 0.98$). All higher order sidebands are consistent with background. Probe time of 170 μs and $\Omega_0/2\pi$= 11 kHz.

weighted by $(1-q)$. Thus the Boltzmann prefactor in equation 6.1 is replaced with a piecewise

function:

$$p(n) = \begin{cases} q \times \frac{\bar{n}^n}{(\bar{n}+1)^{n+1}} & n < n_0 - 3\sigma_n \\ (1-q) \times \frac{1}{\sqrt{2\pi}\sigma_n} e^{-(n-n_0)^2/2\sigma_n^2} & n_0 - 3\sigma_n \leq n \leq n_0 + 3\sigma_n \\ 0 & n_0 + 3\sigma_n < n \end{cases} \tag{6.2}$$

The result of the combined fit tells us that $q = 0.19(1)$ hence only 81% of the population approaches the ground state, with the rest distributed around $n_0 = 72$. For the population near the ground state, $\bar{n} = 0.12(2)$.

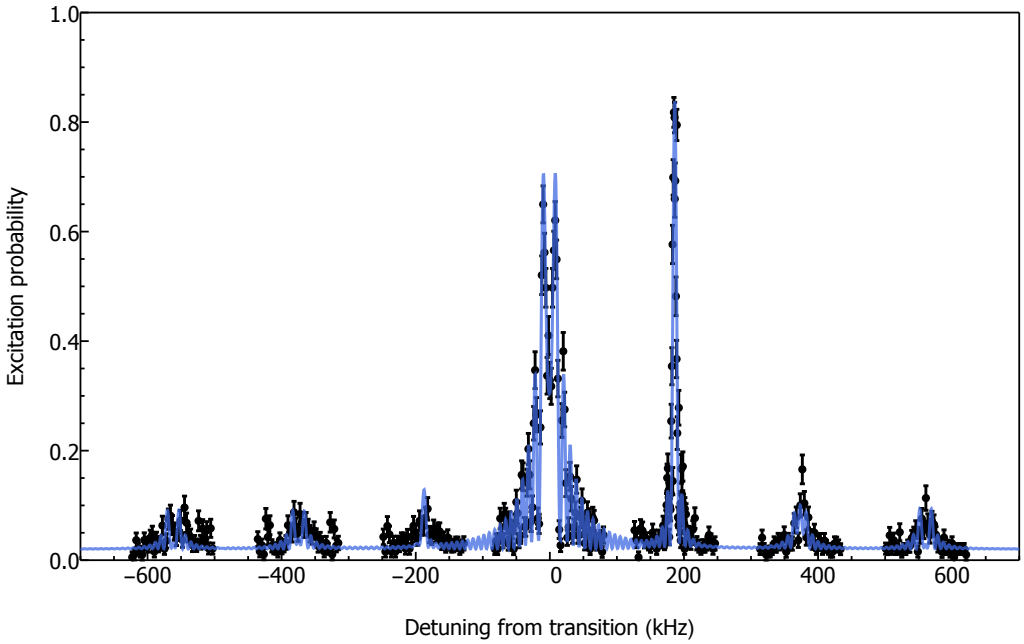

Figure 6.6: Spectrum after 25 ms of single stage sideband cooling for a single ion at 178 kHz trapping frequency. 17% of the population stuck near minimum of first RSB with $\sigma_n = 3$. Remaining ground state occupation $\bar{n} = 0.12(2)$. Pulse area equivalent to π pulse on ground state BSB

In this case, the pulse length was set to maximise the first BSB amplitude, so if one were to just scan first order sidebands, it might not be immediately obvious whether the spectrum looks like that of an imperfectly ground state cooled ion or one with significant population trapping. To make this more obvious, the pulse length was reduced, which should reduce the heights of all the sidebands if the ion was near the ground state. Instead, the higher order sidebands grow as seen in figure 6.7.

It is hence clear that at this frequency single stage cooling is inadequate and will become even less effective at lower frequencies. To overcome this population trapping, a composite pulse sequence that targets different order red sidebands in turn was used. We based our approach on Monte Carlo simulations (paper in preparation) guided by empirical trials. The final sequence we used splits the total 25 ms cool time into 5 ms segments targeting the 2^{nd}-3^{rd}-2^{nd}-3^{rd}-1^{st} sidebands. The advantage in starting from higher order sidebands is that their couplings are strong at high n and since they remove 2 or 3 phonons per pulse they initially cool quicker. Any population that gets stuck in any higher order minimum is also effectively cleared. The last pulse on the first sideband is needed to reach the ground state limit from a point where the population is comfortably below the first zero. Using the same fitting model as before with $\sigma_n = 3$, only 2.5(1.5)% of the population remains in the trapped region near the $n_0 = 72$

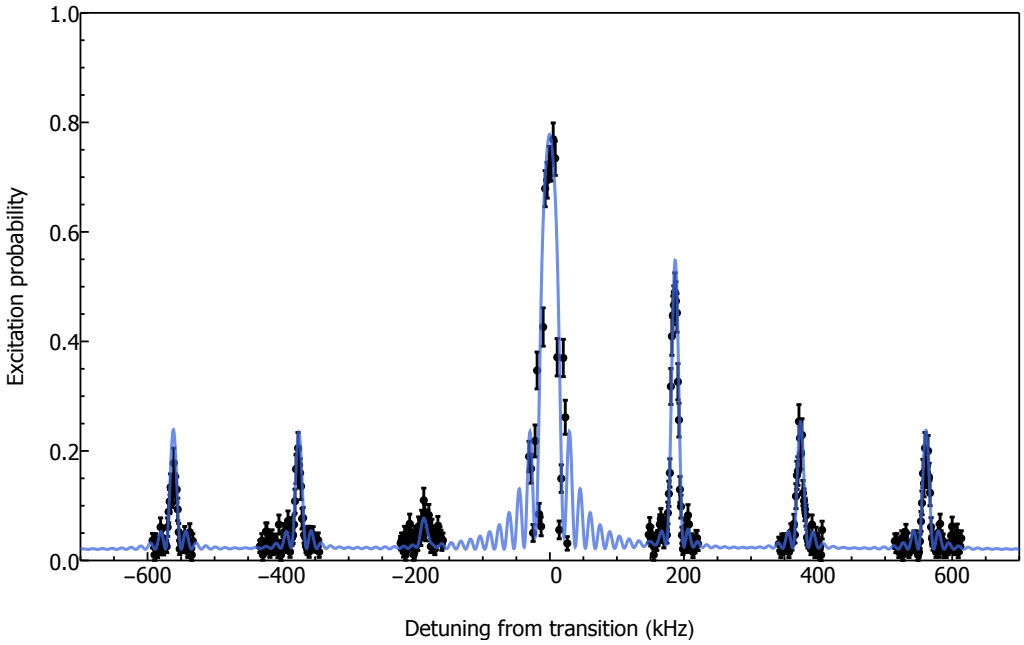

Figure 6.7: Spectrum after 25 ms of single stage sideband cooling for a single ion at 178 kHz trapping frequency. 17% of the population stuck near minimum of first RSB with $\sigma_n = 3$. Remaining ground state occupation $\bar{n} = 0.08(2)$. Pulse width on the sidebands equivalent to 0.56π pulse on ground state BSB; carrier same as in 6.6

minimum with the rest at $\bar{n} = 0.019(10)$ (Fig 6.8). If we restrict the model to ignore the population trapping and just use a thermal state near $n = 0$ we find that $\bar{n} = 0.021(10)$, which differs less than the parameter error from the previous model . The adjusted R^2 of the two fits matches to within 99.94% and thus given the data it is impossible to distinguish between the models with any significant degree of confidence. It is reasonable to assume that the 2.5(1.5)% value gives a conservative upper bound on the remaining trapped population. Figure 6.8 also shows a small second order blue sidedband, highlighting the fact that we are working on cooling outside the Lamb-Dicke regime. Using these interleaved higher order cooling sequences makes this intermediate trapping frequency range amenable to direct ground state cooling. Reaching even lower frequencies without population trapping becomes ever more difficult as the minima get closer, the Doppler limit $\bar{n}$ increases and off resonant excitation of carrier transitions becomes more prominent. Attaining ground state cooling for the lowest frequencies becomes only possible using the adiabatic cooling technique described in the next section.

6.1.3 Adiabatic Cooling

Adiabatic cooling of classical systems such as adiabatic expansion of gases is a very common and established concept that can be extended to the quantum domain. The implementation in a Penning trap was first discussed in the context of cooling thousands of ions, [150] where the authors treated the ion cloud as a classical gas. To further reduce the temperature of a low temperature (few kelvin), high density plasma of weakly correlated particles required a reduction of both the trapping potential and magnetic field. Later on, adiabatic cooling of one motional mode of a single ion was demonstrated in an RF trap [151]. The authors performed a simple procedure of reducing the trapping potential along the weak trapping axis of a linear RF trap on a timescale much longer than the inverse of the final trapping frequency. Since the axial

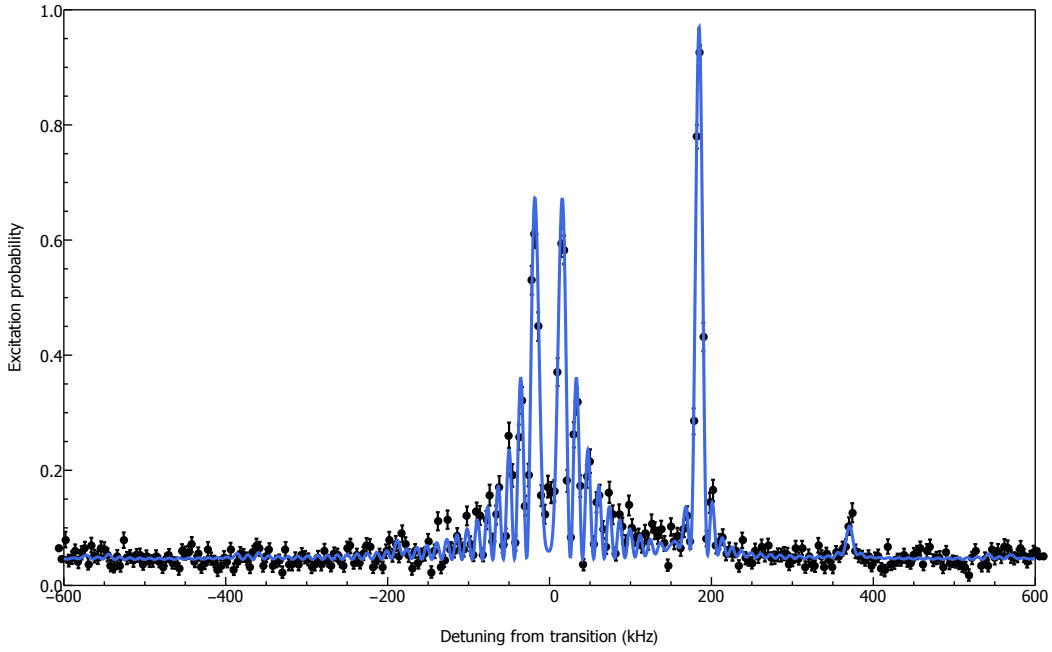

Figure 6.8: Spectrum after 25 ms of multi stage sideband cooling for a single ion at 178 kHz trapping frequency. The cooling sequence consists of 5 ms pulses at the 2-3-2-3-1 sidebands. No strong evidence of population trapping. Remaining ground state occupation $\bar{n} = 0.02(1)$. Pulse width equivalent to 1.1π pulse on ground state BSB

motion ν_z in a Penning trap is also just a simple harmonic motion depending on the endcap electrode potential exactly like in the RF trap, we can replicate this process in our system.

When the trapping potential is lowered slowly enough to satisfy the adiabatic condition $\dot{\nu}_z/\nu_z^2 \ll 2\pi$ then the phonon state n remains unchanged and thus $\delta\nu h$ of energy is removed from the system. This means that we can effectively prepare sup-Doppler limit states at low frequencies by first Doppler cooling at high ν_z and then reducing the potential or alternatively we can sidband cool to the ground state at high ν_z and retain this ground state occupation at any lower ν_z. This avoids any of the population trapping issues that would otherwise be present when attempting direct sideband cooling at low ν_z.

To perform this experiment, we proceed with the usual single stage or multistage sideband cooling sequence, but before the probe we leave a small gap of 1 ms during which the trap potential is lowered. Using this technique we can achieve outstanding results that would be impossible with even the most complex sideband cooling sequences beating the limits set out in section 4.4.2. Figure 6.9 shows the data taken after single stage sideband cooling at $\nu = 418$ kHz followed by an adiabatic drop to $\nu = 94$ kHz with average population $\bar{n} = 0.041(7)$. We can compare it to the expected sideband cooling limit from the rate equation solutions of $\bar{n} = 0.5$ and see we have already exceeded it by a factor of 10. In similar fashion (Figure 6.10), we repeated the same procedure dropping the voltage after sideband cooling from 250 to just 3.6 V giving us a ground state cold ion with $\bar{n} = 0.07(1)$ at $\nu = 67$ kHz. In practice we are limited from going to lower frequencies by the effects of calcium deposits on the electrodes creating stray potentials that displace the potential null from the geometric trap centre resulting in the ion being displaced and hence heated when the potential is adiabatically lowered. To reach these low frequencies shown here already required very careful optimisation of the potentials on the compensation electrodes to re-centre the potential null with the trap centre and thus

further improvements are unlikely without more robust voltage control.

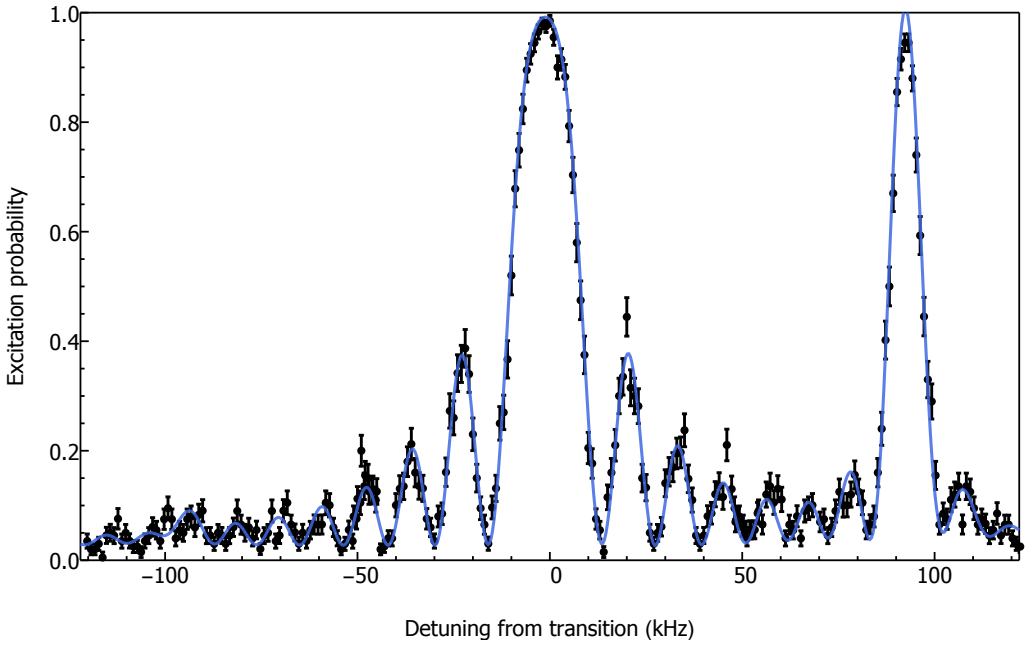

Figure 6.9: Spectrum after 10 ms of single stage sideband cooling at 418 kHz followed by an adiabatic potential relaxation to 94 kHz. Average population $\bar{n} = 0.041(7)$.

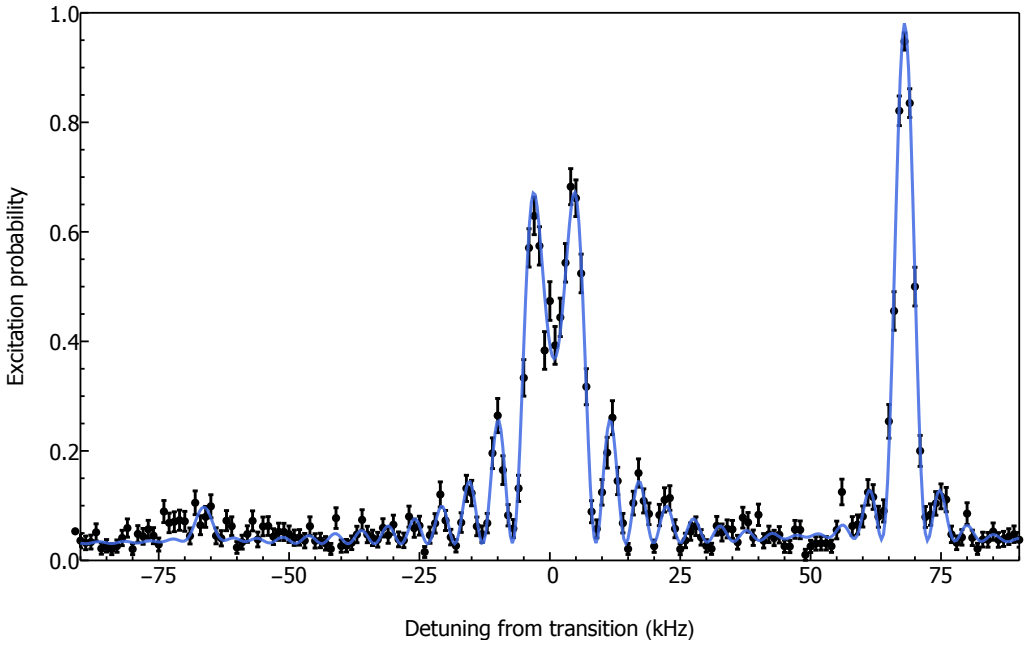

Figure 6.10: Spectrum after 10 ms of single stage sideband cooling at 418 kHz followed by an adiabatic potential relaxation to 67 kHz. Average population $\bar{n} = 0.07(1)$.

While this technique is very well suited to the axial mode of a single ion, it does not naturally extend to the radial modes or to larger crystals. While the cyclotron $\bar{n}$ is always small enough to facilitate simple sideband cooling, the magnetron $\bar{n}$ starts high at low magnetron frequency and only grows higher as the potential is increased. This means that there isn't an equivalent of a potential region where we can perform simple and efficient cooling such as for the axial mode. Likewise, for 1D ion chains we can only perform multi stage sideband cooling at low potentials

and frequencies well outside the Lamb-Dicke regime since the chain begins jumping to a different 2D or 3D configurations at higher potentials (We could of course lower the potential after the chain has been cooled). Conversely, sideband cooling of planar crystals is always performed at high potentials where the ions can be cooled directly to the ground state in a single step without the need for the adiabatic process. In all these cases, once the ions are cooled to the ground state an adiabatic change in the potential does still preserve the $\bar{n}$ of the modes as long as there is no structural change of the crystal, but besides very low frequency 1D chains, there are no frequency regions that can't be reached equally easily without the adiabatic step.

6.2 Optical Coherence Studies

6.2.1 Decoherence overview

One of the biggest challenges of working with quantum systems is preserving the stored information in the presence of environmental noise. In a trapped ion quantum system, noise can enter through various different mechanisms, but can be broadly separated into three major categories:

- Logic Pulse fidelity – Each coherent operation requires the parameters of the addressing field such as polarisation, intensity and pulse length to be very precisely defined. Fluctuations in these parameters degrade the fidelity of any desired operation.

- Spin Decoherence – This corresponds to the information stored in the qubit being affected by external magnetic fields that scramble the phase information between two energy levels leading to imperfect state retrieval. This dephasing error is referred to as a τ_2 time-scale of the qubit. The other decoherence source is spin flip error due to radiative decay from the upper $D_{5/2}$ state of our qubit with a timescale $\tau_1 \approx 1$ s.

- Motional Decoherence – To perform operations such as entangling gates with very high fidelity the motional n state of the ion also needs to be preserved. As with the spin qubit, a τ_2 time-scale is introduced to characterise dephasing between motional states due to fluctuations in the trap frequency. This is typically the consequence of common-mode noise on the electrodes. Other types of noise on the electrodes that cause a fluctuating field at the ions lead to heating, the rate of which defines an analogous τ_1 timescale.

Since we perform all our coherent manipulation through the application of a single 729 nm laser to the $S_{1/2} \leftrightarrow D_{5/2}$ qubit and do not have any other reference laser of similar performance for comparison, we are not able to decouple all contributions from the laser to the spin coherence time. Hence in this section we will treat both the sources of error together to define an experimentally observable 'optical' coherence time. The motional coherence will then be discussed later in 6.3.

6.2.2 Pulse Fidelity and Rabi Oscillations

The most fundamental operation is the on-resonant drive of the qubit transition leading to Rabi oscillations with the excited state population given by:

$$|\langle e|U(\Omega_0,\phi,\Delta,t)|g\rangle|^2 = \frac{\Omega_{n,n}}{\sqrt{\Omega_{n,n}^2+\Delta^2}}\sin^2\left(\frac{\sqrt{\Omega_{n,n}^2+\Delta^2}\times t}{2}\right) \tag{6.3}$$

where we have kept the motional state dependent Rabi frequency from equation 4.27. If the drive is perfectly on resonance and the ion is initiated to a single motional n state then in the absence of noise we should observe full contrast $\sin^2$ oscillations of the excited state population with a π pulse corresponding to maximum excitation at $t = \pi/\Omega_{n,n}$. In our experiments we take a set of 200–400 measurements at increasing pulse lengths for a fixed laser power and detuning to map out the decay of the contrast after many Rabi cycles. We now look at various potential sources of error:

- Laser intensity noise – If the laser intensity I changes then the Rabi frequency changes as $\Omega_0 \propto \sqrt{I}$. We can separate error due to slow drifts and jumps of the mean intensity on timescales much longer than a single experimental trial and error due to fast acoustic noise that broadens the intensity distribution on timescales shorter than the probe time. For the first case, we have a direct measurement of the uncompensated intensity noise at the ion of approximately 10% corresponding to 5% Rabi frequency noise on timescales of minutes. To remedy the problem, we built an AOM and PID electronics based 'noise eater' lock to stabilise the intensity before the final fibre to the trap with a bandwidth of up to 100 kHz to also deal with acoustic noise. The long term drifts were reduced to below 1% of the total power on a time scale of hours.

- Polarisation Noise – Since we require the 729 laser to maintain a linear polarisation at all times to address the transition, we send the light through a polarisation maintaining fibre. Despite careful alignment of the polarisation axis to the polarisation maintaining axis of the fibre, thermal drifts and acoustic noise introduce circularity into the outgoing light. Based on the analysis of section 3.3, we know that the Rabi frequency is strongly sensitive to circularity. To protect against this we place a polarising beam splitter after the fibre to remove the orthogonal polarisation and hence convert the polarisation noise into intensity noise with a weaker $\Omega_0 \propto \sqrt{I}$ dependence. Ideally we would place the noise eater after this PBS, but we were not able to do so due to space constraints on the breadboard under the superconducting magnet. Thus the total intensity noise is a combination of the pure residual intensity noise after the noise eater and the intensity noise after the fibre and PBS.

- Imperfect state preparation – If the ion is not consistently prepared in the same motional state for all trials, then the observed spectrum will have Rabi frequencies corresponding to different motional states. This is why Rabi oscillations on a thermal state decay very quickly. We minimise this issue by ensuring we sideband cool the ion as close to the ground state as possible for results in this section. Later on when we discuss Rabi oscillations near other high n states, the distribution of the different $\Omega_{n,n}$ that contribute will become increasingly important.

- Frequency/phase noise – This broadly includes all noise that causes the laser frequency to deviate from the atomic transition frequency inducing a detuning Δ be it laser frequency noise at the diode, phases noise imprinted on the light in fibres or magnetic field noise changing the transition frequency. Based on equation 6.3 the oscillation frequency and excitation depend on $\Omega_{n,n}^2 + \Delta^2$, but if $\Omega_{n,n} \gg \Delta$ the Rabi oscillations are not very sensitive to frequency noise.

For the purpose of the subsequent analysis we will use the generalised Rabi frequency $\Omega = \sqrt{\Omega_0^2 + \Delta^2}$ since what we experimentally see is ultimately due to the drift of both constituent quantities. To mathematically model the decoherence processes we can first consider what happens when the noise timescale is longer than the probe times used in the experiment. This implies that Ω is approximately constant over the length of each probe. Hence each new experimental trial consists of us sampling from a probability distribution $P(\Omega)$. The resulting data then has the form:

$$P_e(t) = \int_{-\infty}^{\infty} \frac{\Omega_0}{\Omega} \sin^2\left(\frac{\Omega t}{2}\right) P(\Omega) d\Omega \tag{6.4}$$

The decay timescale τ is then given by the constant in the exponent of the Fourier transform:

$$C = \int_{-\infty}^{\infty} P(\Omega) e^{-i\Omega t} d\Omega \tag{6.5}$$

Commonly used distributions to model noise such as the normal distribution or Cauchy distribution give rise to Gaussian and exponential decay of the coherence respectively. An important consequence of this model is that the coherence time depends only on the absolute width of the distribution, not the mean i.e. the coherence is given by the width $d\Omega$ rather than the relative error $d\Omega/\Omega$. To fit the functional form of the decay, we can write a general form:

$$P_e(t) = \sum_{n}^{5} \frac{\bar{n}^n}{(\bar{n}+1)^{n+1}} \left(\frac{1}{2} - \frac{1-a}{2} e^{-t/\tau_e - t^2/\tau_g^2} \cos\Omega_{n,n} t\right) \tag{6.6}$$

that includes contributions from both an exponential decay with timescale τ_e and Gaussian decay τ_g, a sum over phonon states n and a constant a that accounts for imperfect state detection. This corresponds to the noise being distributed according to the Voigt profile. During the fitting routine we always used this general model, but we subsequently found that for all data presented here τ_e grew very large and only τ_g remained to define a relevant timescale. This supports the conclusion that we are observing Gaussian white noise.

Throughout our time in the lab we have worked to minimise the contributions of intensity, polarisation and frequency noise to the decoherence of the Rabi oscillations. Here we will highlight the types of problems we encountered and how we dealt with them. Initially, we encountered problems with noise that resulted from feedback of laser light or amplified spontaneous emission from the TA into the laser causing large drifts of the Rabi frequency on timescales of minutes. Combined with these drifts we had standard intensity noise at timescales of 1-1000 Hz that lead to a smooth decrease in the oscillation visibility. An example of such a spectrum is show in figure 6.11a. Here we can clearly see a smooth decay of the visibility as well as sharp changes in oscillation frequency at longer times resulting from the change of the mean Ω value. In the fit we used the first three cycles to fix $\Omega/2\pi = 17.5(15)$ kHz and the whole data set to find a coherence time of $\tau_g = 0.41(4)$ ms and $\bar{n} = 0.06(5)$. Using the model

from equation 6.4, we find that this corresponds to $d\Omega/\Omega = 0.037$ where $d\Omega$ is the half-width at half maximum of the Gaussian distribution. We were not able to find a clear identifiable pattern to the modulation of the mean as the jumps appeared to be quite sudden at times as corroborated by observations of drifting cavity transmission signal discussed in 5.3.5. The optical feedback from the TA was fixed by very careful misalignment of the optical system, removing the unpredictable modulation, but leaving slow drifts due to thermal effects on fibres and the laser itself.

Next, to asses the contribution of frequency noise we performed a Rabi oscillation at low laser power where $\Omega_0/2\pi = 2.2(1)$ kHz as shown in figure 6.11b. In this case, the laser intensity noise should decrease linearly with a decrease in total laser intensity maintaining the same fractional error dI/I_0 and hence same fractional error $d\Omega_0/\Omega_0$ if $\Omega_0 \gg \Delta$. Thus using the previous results from 6.11a, if all noise were purely due to intensity, then $d\Omega/2\pi = d\Omega/\Omega \times \Omega_0/2\pi = 0.037 \times 2.2 \approx 0.08$ kHz and equation 6.5 then predicts a $\tau_g \approx 3.2$ ms. We can compare this to the value of $\tau_g = 2.90(4)$ ms derived from the fit and notice that the value is only slightly smaller hence the effect of frequency noise must be small even at low Ω_0. Even if all the noise was due to frequency alone, then $d\Delta < 600$ Hz, placing a strong upper bound on the frequency stability of our laser-qubit system. This data shows that even with no additional stabilising measures taken, lowering the Rabi frequency gives a longer coherence time, but no large gains are obtained in terms of how many high fidelity oscillations fit within it. Additionally, the long term drifts also remain present even though their effects are not as severe. In figure 6.11b we used a fit that allowed for a timing variation from the initial Rabi frequency Ω_I by a sinusoidal function $\Omega(t) = (1 - A\cos(f_d))\Omega_I$ with frequency $f_d = 200(3)$ Hz and amplitude $A = 0.046(1)$. Given that the spectrum acquisition took an hour and f_d completed half a period over the data set, we obtain an approximate drift rate $\dot{\Omega}/\Omega_I = 4.6\%\ \mathrm{h}^{-1}$.

To improve the quality of the Rabi oscillations, we made further improvements by transforming any polarisation noise to intensity noise and added an AOM based noise eater system to reduce laser intensity noise. A representative spectrum of these much improved Rabi oscillations is shown in figure 6.11c. The Rabi frequency of the oscillations is $\Omega_0/2\pi = 9.97(1)$ kHz with no discernible drift and a coherence time of $\tau_g = 2.70(5)$ ms corresponding to $d\Omega/\Omega = 0.009$ – a four fold improvement compared to results before the noise eater.

Finally, we also demonstrate that we can coherently drive not just the carrier, but also sideband transitions. Simultaneously, we show that we can also perform these oscillations at $\nu_z = 124$ kHz where the ion was prepared in the ground state by adiabatic cooling following sideband cooling at 418 kHz. In figure 6.12 we perform Rabi oscillations on the blue sideband driving the $|0\rangle \leftrightarrow |1\rangle$ with a $d\Omega/\Omega = 0.009$, in exact agreement with the result of the best carrier Rabi oscillation in 6.11c.

6.2.3 Spin Coherence and Ramsey Spectroscopy

To precisely characterise the τ_2 coherence time of our qubit, we can use the techniques of Ramsey spectroscopy. The principle behind the method is very simple: first the qubit is initialised in its electronic ground state, after which a laser pulse $T_{\pi/2} = \pi/(2\Omega_0)$ is applied to create a balanced coherent superposition between the ground and excited state. The lasers are now turned off and a wait time T_w is introduced, during which the energy eigenstates evolve in time according to their unperturbed Hamiltonian, acquiring a phase $\phi = \omega T_w$. This period ends when a final

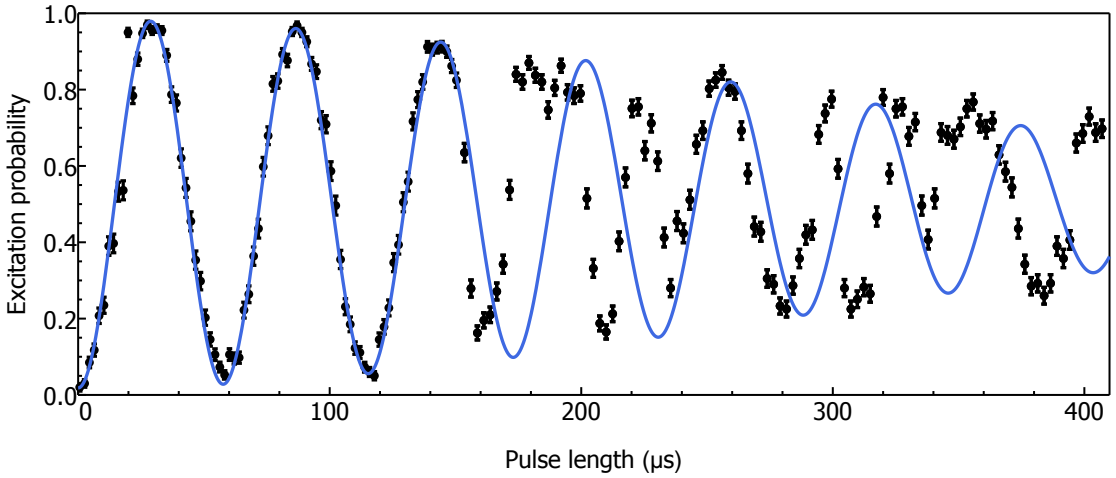

(a) $\Omega/2\pi = 17.5(15)$ kHz, $\bar{n} = 0.06(5)$, $\tau_g = 0.41(4)$ ms, $d\Omega/\Omega = 0.037$

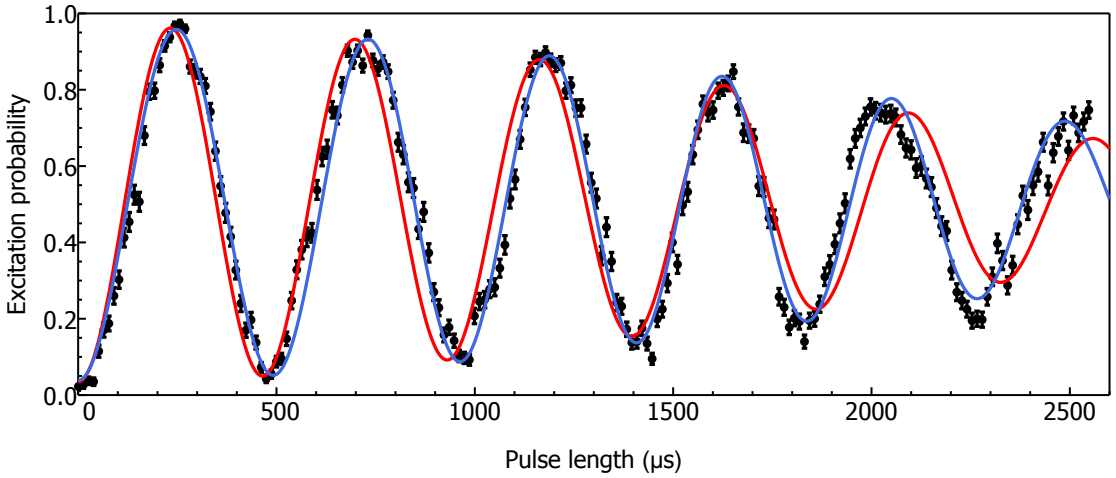

(b) $\Omega_0/2\pi = 2.2(1)$ kHz, $\bar{n} = 0.05(5)$, $\tau_g = 2.90(4)$ ms, $d\Omega/\Omega = 0.032$

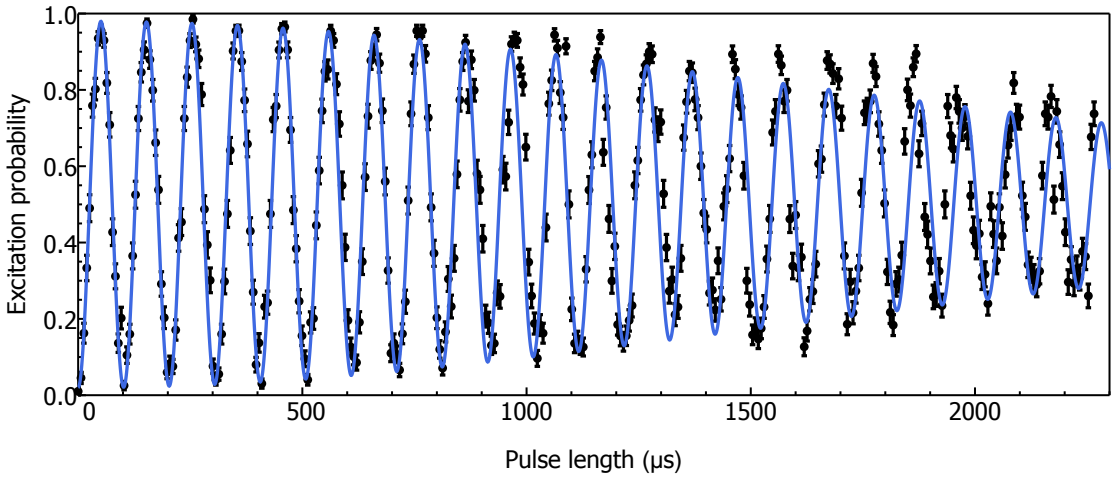

(c) $\Omega_0/2\pi = 9.97(1)$ kHz, $\bar{n} = 0.05(4)$, $\tau_g = 2.70(5)$ ms, $d\Omega/\Omega = 0.009$

Figure 6.11: Rabi oscillations (a) without noise eater and with optical feedback noise, (b) without noise eater and without optical feedback, (c) with noise eater and without optical feed back. Red curve in (b) shows a fit with a fixed Ω to contrast with the time varying Ω fit in blue. All data taken after single stage sideband cooling at $\nu_z = 418$ kHz

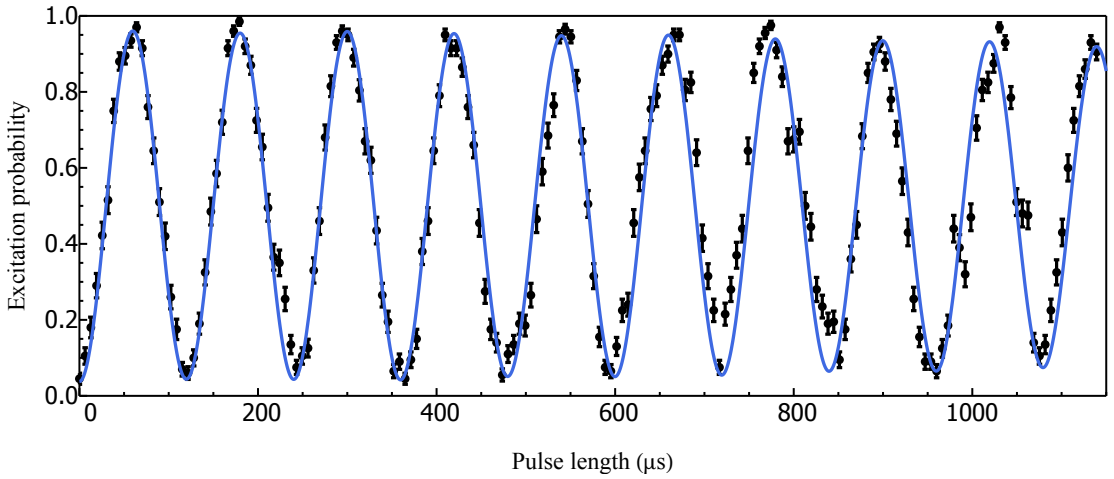

Figure 6.12: Rabi oscillation on the first blue sideband at $\nu = 124$ kHz. $\Omega_0/2\pi = 31.55(1)$ kHz, $\bar{n} = 0.01(1)$, $\tau_g = 3.93(3)$ ms, $d\Omega/\Omega = 0.009$, $\eta = 0.274$

laser pulse $T_{\pi/2}$ identical to the first is applied to close the sequence. The population is then measured for different frequency detunings of the driving laser field. Alternatively, the frequency can remain fixed, but the phase of the second laser pulse can be scanned. A third way is to fix the frequency and phase of both pulses and instead vary the length of T_w. Since the T_w can be much larger than $T_{\pi/2}$, this method provides a sensitive means to observe coherence without relying on long laser pulses that can be subject to intensity or polarisation drifts. Instead, the method precisely measures the phase mismatch between the initial and final laser pulses, ultimately revealing the limits of either the driving laser coherence or the atomic qubit. The laser sequence necessary to generate the Ramsey interferometry experiment is given in figure 6.13. The sequence is preceded by Doppler cooling and sideband cooling to the ground state and initialisation of the qubit in the $|g\rangle$ ground state.

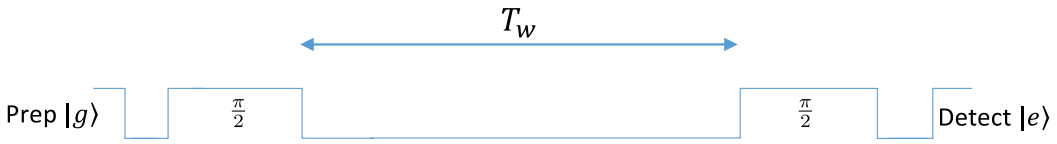

Figure 6.13: Laser sequence for creating Ramsey interference

We can now consider what kind of decoherence response we can expect if we limit ourselves to frequency noise, ignoring intensity. Since the Ramsey experiment translates frequency noise into a phase mismatch, we are interested in the integral of the detuning $\Delta(t)$ over the course of the wait time. In the density matrix representation, the off diagonal coherence elements decay as:

$$C = \exp\left[-\frac{1}{2}\int_0^T dt \int_0^T dt' K(t-t')\right] \tag{6.7}$$

where we have taken a Gaussian random variable with ensemble average mean $\langle\Delta(t)\rangle = 0$ and covariance $\langle\Delta(t)\Delta(t')\rangle \equiv K(t-t')$. To proceed we note that the power spectrum of the noise

$\tilde{K}(\omega)$ is the Fourier transform of $K(t)$, giving:

$$\begin{aligned} C &= \exp\left[-\frac{1}{2}\int_0^T dt \int_0^T dt' K(t-t')\right] = \exp\left[-\frac{1}{2}\int_0^T dt \int_0^T dt' \int_{-\infty}^{\infty} \frac{d\omega}{2\pi} e^{-i\omega(t-t')}\tilde{K}(\omega)\right] \\ &= \exp\left[-\frac{1}{2}\int_0^T e^{-i\omega t} dt \int_0^T e^{i\omega t'} dt' \int_{-\infty}^{\infty} \frac{d\omega}{2\pi}\tilde{K}(\omega)\right] = \exp\left[-\frac{1}{\pi}\int_{-\infty}^{\infty} \frac{d\omega}{\omega^2} \sin\left(\frac{\omega T}{2}\right)^2 \tilde{K}(\omega)\right] \end{aligned} \tag{6.8}$$

To perform this integration, we first assume that if we have Gaussian white noise, then the power spectrum is constant for all frequencies, hence we define $\tilde{K}(\omega) = 2/\tau_2$. Finally, using the standard result $\int_{-\infty}^{\infty} dx \sin(x)^2/x^2 = \pi$, we obtain

$$C = e^{-\tilde{K}(\omega)T/2} = e^{-T/\tau_2} \tag{6.9}$$

The resulting decay is exponential with time constant τ_2.

Another possibility is that the noise occurs on timescales longer than the wait time in each trial of the Ramsey experiment. In this case the noise $\Delta(t) = \Delta$ is constant over each trial and the analysis is exactly the same as for the intensity noise calculation (eq. 6.5) and thus the coherence elements decay according to the underlying noise distribution. To calculate the resulting fringes when the frequency is scanned we define an evolution operator from the propagator $U_{int}(t)$ (eq. 4.14): $R_{\pi/2}(\Delta, \phi, t_i) = U_{int}(t_i + \pi/(2\Omega_0))U_{int}(t_i)^\dagger$. The excitation spectrum then takes the form:

$$\begin{aligned} P_e &= \mathrm{Tr}\left(|e\rangle\langle e| R_{\pi/2}(\Delta, 0, T + \pi/(2\Omega_0)) R_{\pi/2}(\Delta, 0, 0)\rho R_{\pi/2}(\Delta, 0, 0)^\dagger R_{\pi/2}(\Delta, 0, T + \pi/(2\Omega_0))^\dagger\right) \\ &= \frac{\Omega_0^2}{\Omega^4}\sin^2\left(\frac{\pi\Omega}{4\Omega_0}\right)\left[2\left(\Delta^2 + \Omega_0^2\cos^2\left(\frac{\pi\Omega}{4\Omega_0}\right)\right) + C(T)\left(\cos(\Delta T)\left(\Omega_0^2 + \left(2\Delta^2 + \Omega_0^2\right)\cos\left(\frac{\pi\Omega}{2\Omega_0}\right)\right)\right.\right. \\ &\quad \left.\left. -2\Delta\Omega\sin(\Delta T)\sin\left(\frac{\pi\Omega}{2\Omega_0}\right)\right)\right] \end{aligned} \tag{6.10}$$

where $C(T)$ represents the decay function of the visibility. An example of two data sets at 200 and 700 μs wait times is shown in figure 6.14. The data shows an excellent agreement with the model in figure 6.14(a) with the fringes exhibiting full contrast oscillations. In 6.14(b) we begin to see evidence of decoherence which we model with a decay function $C(T) = e^{-T^2/\tau_2^2}$ obtaining $\tau_2 = 1.8(1)$ ms. While these types of experiment yield conclusive proof that we can perform high resolution spectroscopy measurements, they do not individually reveal the true nature of $C(T)$, which would give us information about the underlying noise sources. To do this, we require a data set with visibility information as a function of time for which these types of spectra are not as appropriate since they take a relatively long time to acquire. Instead, we can fix the frequency near resonance and then scan the phase of the second $T_{\pi/2}$ pulse by changing the phase of the RF field sent to the spectroscopy AOM. In this case we can restrict ourselves to the region where $\Delta \ll \Omega_0$ and obtain a simple sinusoidal oscillation as a function

of ϕ given by:

$$\begin{aligned} P_e &= \mathrm{Tr}\left(|e\rangle\langle e| R_{\pi/2}(0,\phi,T+\pi/(2\Omega_0)) R_{\pi/2}(0,0,0)\rho R_{\pi/2}(0,0,0)^\dagger R_{\pi/2}(0,\phi,T+\pi/(2\Omega_0))^\dagger\right) \\ &= \frac{1}{2}\left(1+C(T)\cos(\phi+\Delta T)\right) \end{aligned} \tag{6.11}$$

A sample of such phase scan Ramsey measurements is shown in figure 6.15 where the visibility

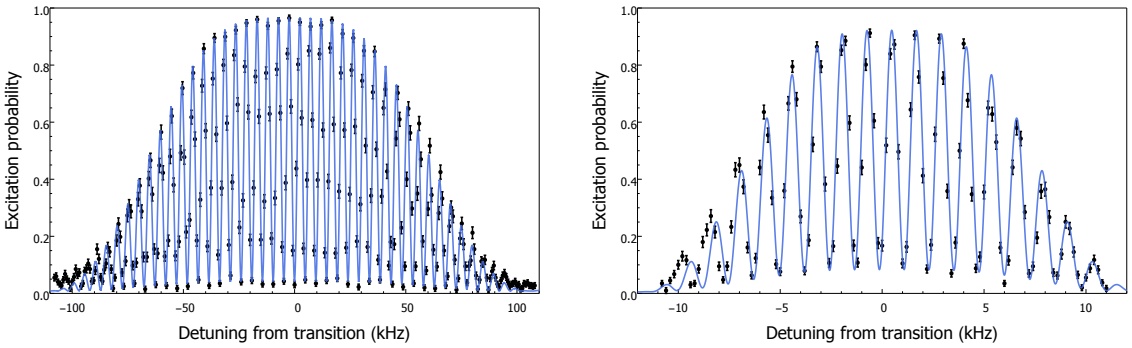

(a) $T_w = 200\mu$s, $\Omega_0/2\pi = 28$ kHz **(b)** $T_w = 700\mu$s , $\Omega_0/2\pi = 3.2$ kHz

Figure 6.14: Two Ramsey interference spectra for a ground state cooled ion at ν_z= 418 kHz. Laser intensity was reduced in (b) to reduce the width of the envelope to better resolve the fringes. Spectrum (a) shows full coherence, whereas (b) shows a characteristic loss of visibility with $\tau_2 = 1.8(1)$ based on a $C(t) = e^{-T^2/\tau_2^2}$ model.

C was extracted from the fit each time. This set was acquired sequentially within a 30 minute time period, following an initially careful alignment of the laser frequency to the centre of the carrier transition. It is evident that as T_w is increased, there is a significant phase $T_w\Delta$ acquired. Based on the fit to the $T_w = 500\mu$s data, we estimate a detuning of $\Delta = 300(10)$ Hz is initially present assuming that less than 2π of phase was accumulated. None of the other wait time measurements are consistent with this value, suggesting that there are drifts of the transition or laser frequency on the order of 10-1000 Hz per minute.

The visibility values are plotted in figure 6.16. We found that the data appears to best fit a Gaussian function $C(T_w) = C_0\exp(-T_w^2/\tau_2^2)$, giving a coherence time of $\tau_2 = 1.78(4)$ ms. This implies a frequency width $\sigma_\Delta = 125(3)$ Hz. The fact that the data does not follow an exponential trend seems to suggest that the coherence time is limited by noise on timescales greater than T_w. Gaussian visibility decay has been observed in RF traps with optical qubits before [28, 152]. To further investigate the nature of the noise, we shall look at dynamical decoupling techniques that seek to extend the coherence time of the qubit.

6.2.4 Dynamical Decoupling

Dynamical decoupling is a quantum control technique that uses additional laser interaction pulses to suppress decoherence. The first evidence of the coherent refocusing of nuclear spins in magnetic resonance experiments was observed by Hahn in 1950 [153]. In the context of our optical qubit the Spin echo eliminates any acquired phase when there is a constant mismatch between the qubit transition frequency and the driving laser radiation. If we assume a small detuning $\Delta \ll \Omega_0$ so that we have almost full population transfer, then the first $T_{\pi/2}$ places

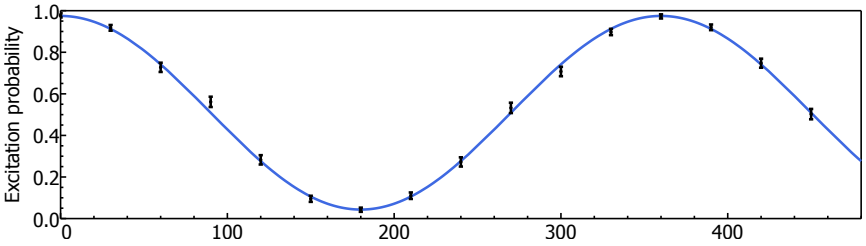

(a) $T_w = 0\mu$s, $C = 0.93(1)$

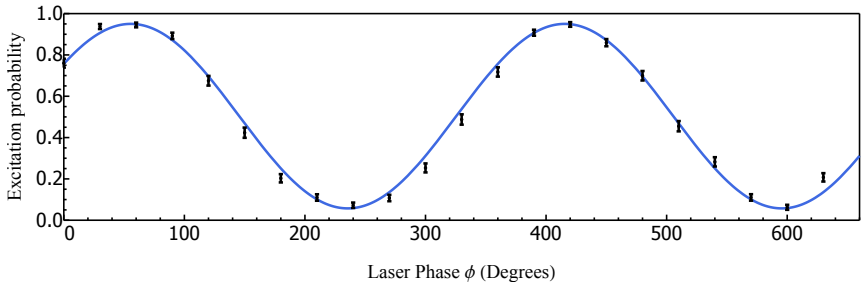

(b) $T_w = 500\mu$s , $C = 0.89(1)$

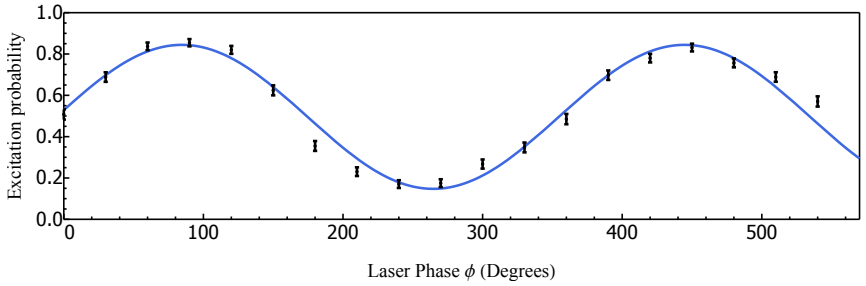

(c) $T_w = 1000\mu$s , $C = 0.70(1)$

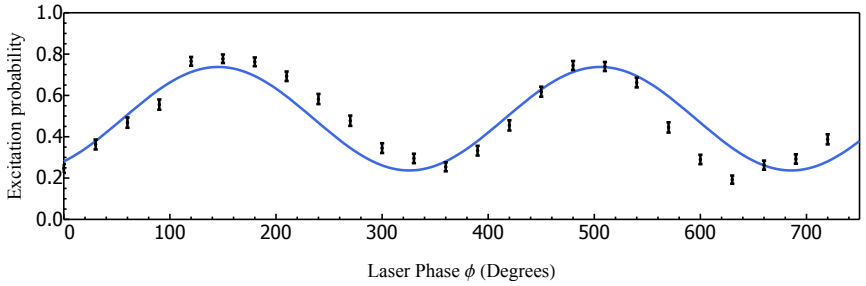

(d) $T_w = 1500\mu$s , $C = 0.5(1)$

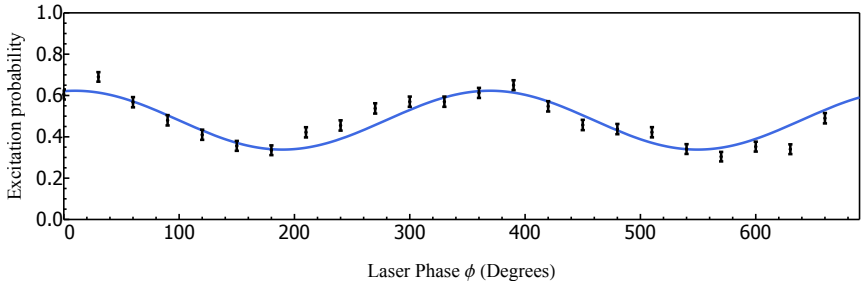

(e) $T_w = 2000\mu$s , $C = 0.28(2)$

Figure 6.15: A set of Ramsey interference measurements taken at ν_z= 418 kHz with the phase of the second $\pi/2$ pulse scanned.

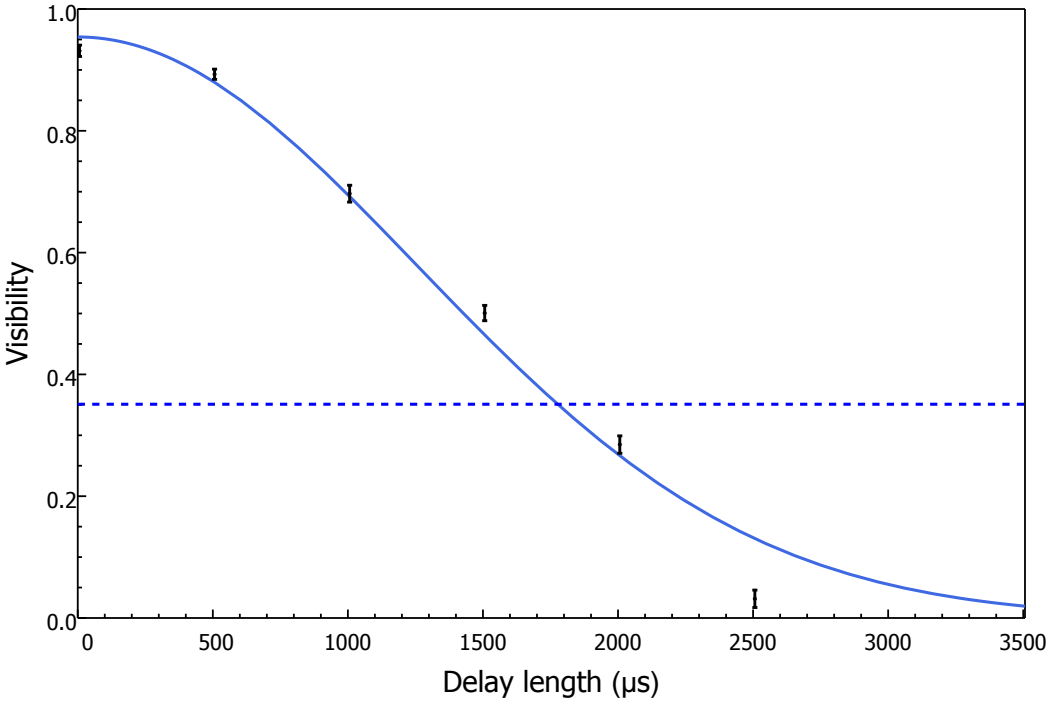

Figure 6.16: Visibility of Ramsey phase scan experiments at different delay times T_w. The data is fitted on a Gaussian model. The dotted line indicates the $1/e$ of the maximum visibility.

the ion in the $|g\rangle + |e\rangle$ superposition followed by a wait period during which a relative phase $\phi_a = \Delta T_w$ between the states is acquired.[2] Setting the second $T_{\pi/2}$ pulse to the same phase with respect to the first, we note that any acquired phase lowers the maximum excitation probability proportional to $\cos\phi_a$. In the Bloch sphere picture, the initial $T_{\pi/2}$ pulse rotates the state vector to coincide with the x axis. Then during the wait period, the state vector rotates in the x-y plane by ϕ_a. Finally, the second $T_{\pi/2}$ pulse attempts to bring the state vector back in line with the z axis pointing to the $|e\rangle$ position on the south pole, with a fidelity proportional to the projection of the state vector on the x axis. For each new realisation of this experiment with a different Δ there will be a distribution of state vectors near the $|e\rangle$ pole that will average and hence reduced the visibility. Spin echo counteracts this problem by inserting an additional laser pulse of length $T_\pi = 2T_{\pi/2}$ in the middle of the wait time. This has the effect of rotating the state vector 180° about the y axis. Now during the first wait $T_w/2$ a phase of $\phi_a/2$ is acquired, but in the second wait the phase acquired is $-\phi_a/2$ as the vector rotates in the x-y plane back to meet the x axis. To best complete the picture, figure 6.17 shows the Bloch sphere schematic of the sequence.

Figure 6.18 shows the laser pulse sequence and an additional schematic to illustrate the effect of the spin echo. The phase accumulated can be thought of as the area between a detuning versus time plot. The spin echo effectively changes the sign of the detuning and hence creates an equal sized negative area in the second half of the sequence that adds to zero.

We can also ask what happens if Δ is not constant throughout the experiment. The simplest case is to consider a linear drift. In this case, the phase accumulated will be larger or

[2]We have assumed here that the $T_{\pi/2} \ll T_w$ so that the phase acquired during the laser interaction time is negligible to simplify the argument and the associated illustrations, but spin echo works just as as well if it doesn't hold.

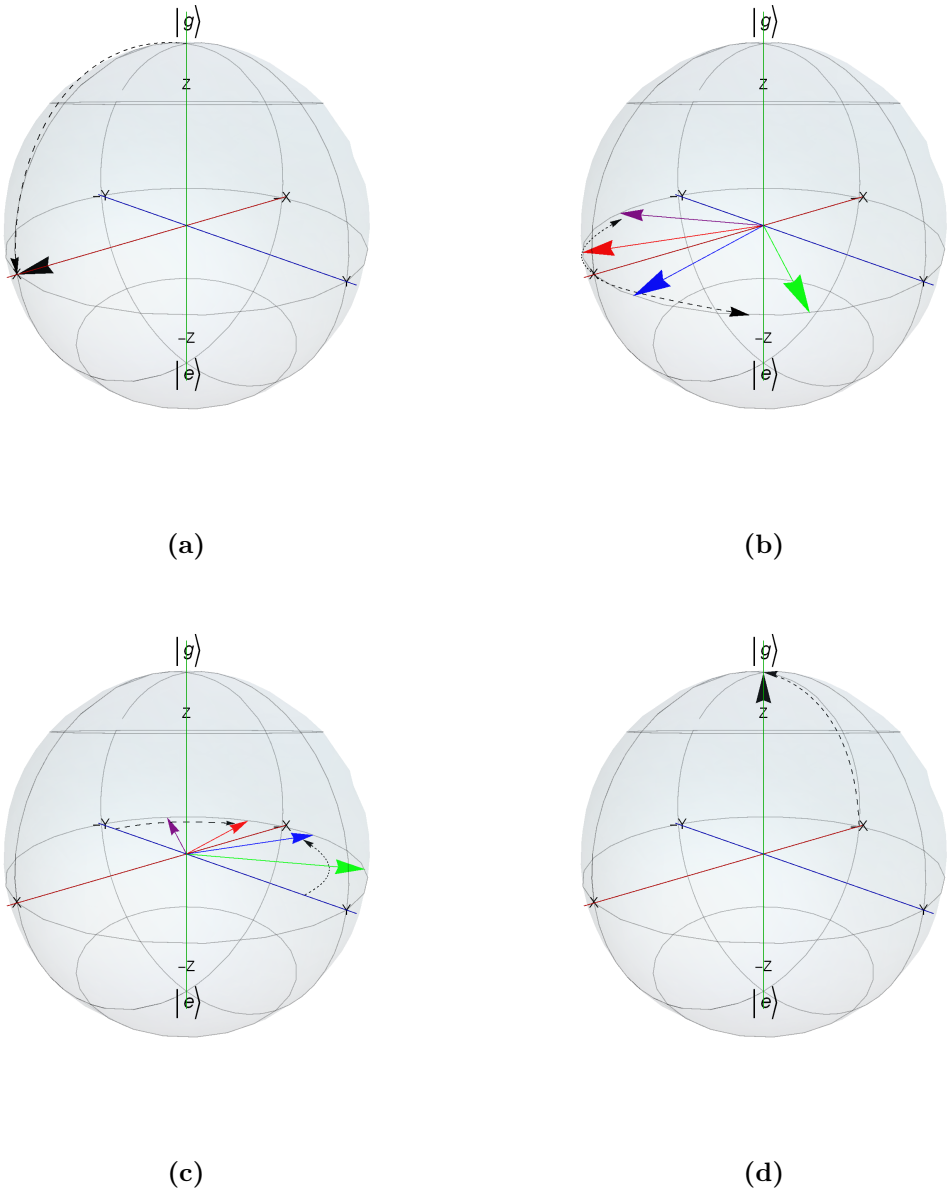

Figure 6.17: Spin echo representation on the Bloch Sphere. In (a) the state vector is rotated from $|g\rangle$ along the dotted line to $|g\rangle + |e\rangle$ initiating the Ramsey sequence. For each trial there is some random detuning that causes a dephasing in the x-y plane, represented by the four coloured state vectors in (b). Immediately after a T_π pulse, the state vectors are rotated 180° through the y axis as seen in (c). They continue their phase evolution until they recombine at $|g\rangle - |e\rangle$ and a final $T_{\pi/2}$ brings all the states back to $|g\rangle$ in (d).

smaller (depending on the direction of the drift) after the T_π than in the first wait gap, and hence will not cancel. However, we can cancel the phase by using two T_π pulses. This is best understood geometrically as seen in figure 6.19. In principle, to correct noise from an N-th order polynomial, we would require N+1 pulses. Schemes of this sort are a form of dynamical decoupling, which was first proposed by Carr and Purcell for NMR systems in 1954 [154]. A further refinement by Meiboom and Gill followed [155], establishing the Carr-Purcell-Meiboom-Gill (CPMG) decoupling scheme where an additional T_π pulse is added at equal time intervals. Today there are many new decoupling schemes around that seek to find optimal sequences of pulses to correct for higher order noise, but here we will focus on one that was investigated

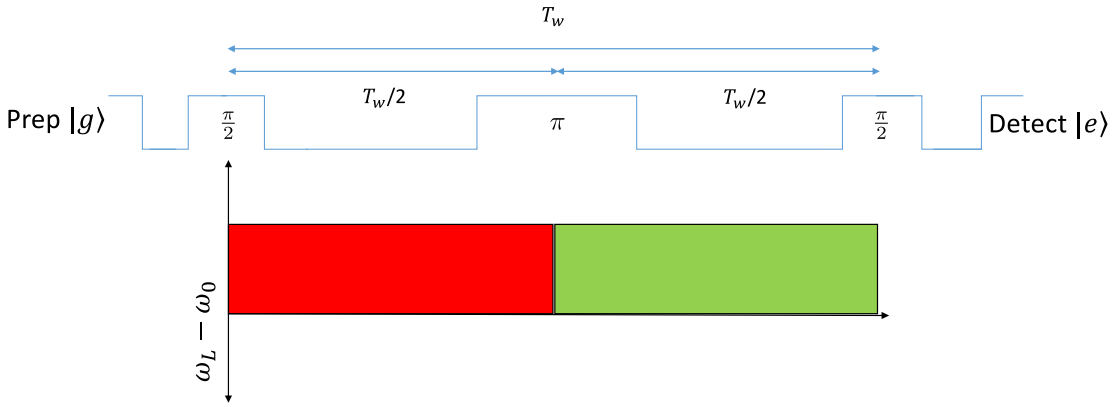

Figure 6.18: Pulse sequence for a spin echo experiment. The wait time T_w is defined between the middle of the initial and final pulse. The schematic underneath shows the phase accumulated before and after the pulse. The red and green areas exactly cancel to give zero total phase accumulated.

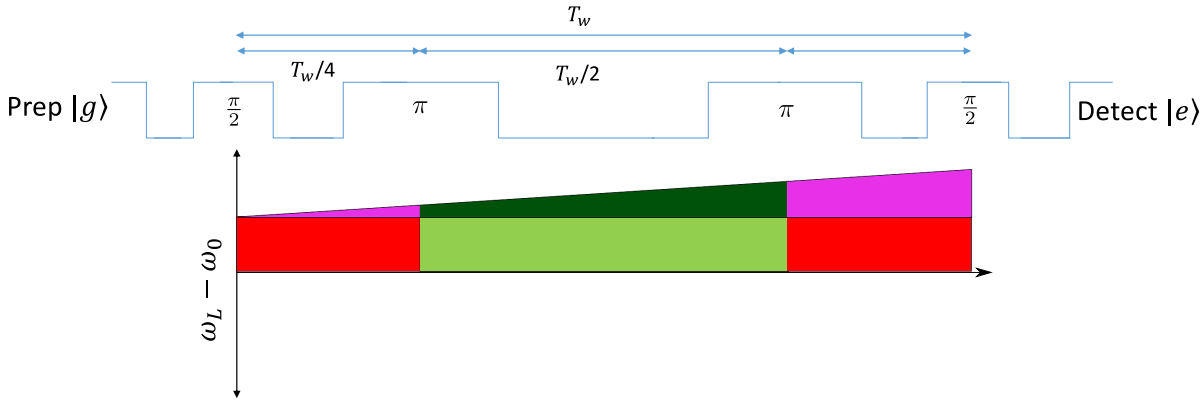

Figure 6.19: Pulse sequence for a two T_π dynamical decoupling experiment. The schematic underneath shows the phase accumulated before and after the pulses. The two pink areas have the same area as the dark green area showing the cancellation of error due to linear drift. Similarly, the green rectangle has the same area as the sum of the two red ones. The net phase is thus eliminated.

theoretically by Uhrig (UDD) [156, 157] and experimentally with trapped ions in both RF [158] and Penning traps [159]. This scheme has been proven to be optimal for any dephasing Hamiltonian for sufficiently short times T_w and a finite number of pulses[160]. The sequence consists of n T_π pulses centred at τ_n between the the initial and final $T_{\pi/2}$ pulses:

$$\tau_n = T_w \sin\left(\frac{\pi}{2}\frac{n}{N+1}\right)^2 \tag{6.12}$$

We performed the spin echo and UDD sequence Ramsey type experiments with up to three T_π pulses, each time scanning the phase of the final $T_{\pi/2}$ pulse to produce data (found in B.1) from which the visibility is extracted. The results are compiled in figure 6.20. We extract the coherence times using a Gaussian decay model for $C(T_w)$ to fit the 0–2 pulse data and use a linear interpolation for the 3 pulse data to find the $1/e$ point assuming an initial visibility consistent with a no delay spectrum. Plotting the resulting coherence times versus the number

of pulses in figure 6.21 gives a clear linear relationship indicating an additional 3.9(3) ms of coherence per T_π pulse.

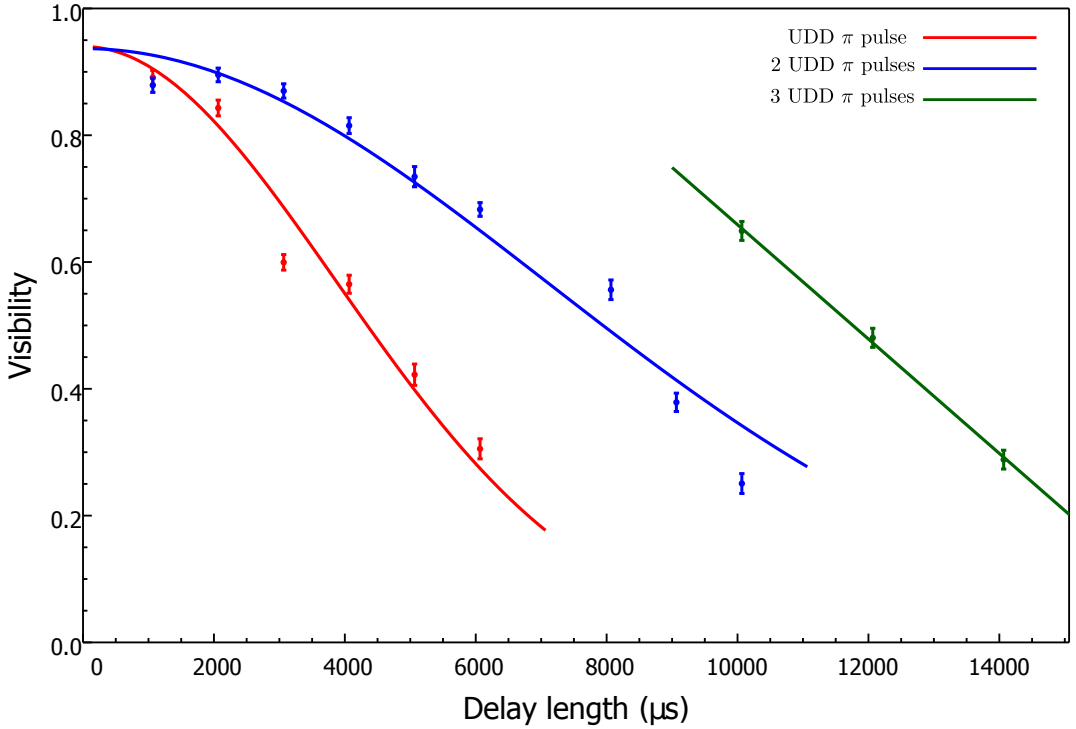

Figure 6.20: Visibilities of Ramsey and UDD sequence phase scans for different wait times. All experiments performed at $\nu_z = 418$ kHz

The above results are very encouraging and suggest that with sufficient pulses we can extend the optical qubit lifetime to timescales of hundreds of milliseconds, which would be at least an order of magnitude longer than standard gate operations. The practical limit will be the errors accrued due to imprecise pulse length (or alternatively Rabi frequency noise/drift), which means that after many slightly imperfect pulses the visibility will drop even without a delay, as well as optical decay from the excited state as the τ_1 time is approached.

Returning to the question of the underlying noise spectrum, it is clear that there is significant noise at timescales longer than the Ramsey wait time as evidenced by both the visibility decaying in a Gaussian rather than exponential fashion and the fact that low order dynamical decoupling is very effective. Further investigation into the nature of the noise spectrum is necessary to help us understand the qubit response. This could be done by artificially generating noise profiles that are imprinted on the AOM that shifts the frequency of the probe laser. The effects of dynamical decoupling could then be more methodically investigated for noises at different power spectra.

At the moment we do not know exactly what is limiting our coherence time. To investigate further we must try to characterise the contributions of the following potential noise sources:

- The linewidth of the laser is currently unknown since we do not have a second laser for a beatnote measurement. If the laser was the largest contributing factor, then the FWHM linewidth would be estimated to be approximately 250 Hz. This is not an unreasonable estimate for a homebuilt laser, but is not competitive with state of the art commercial systems that can reach linewidths of < 10 Hz. [161]. The linewidth might also be further

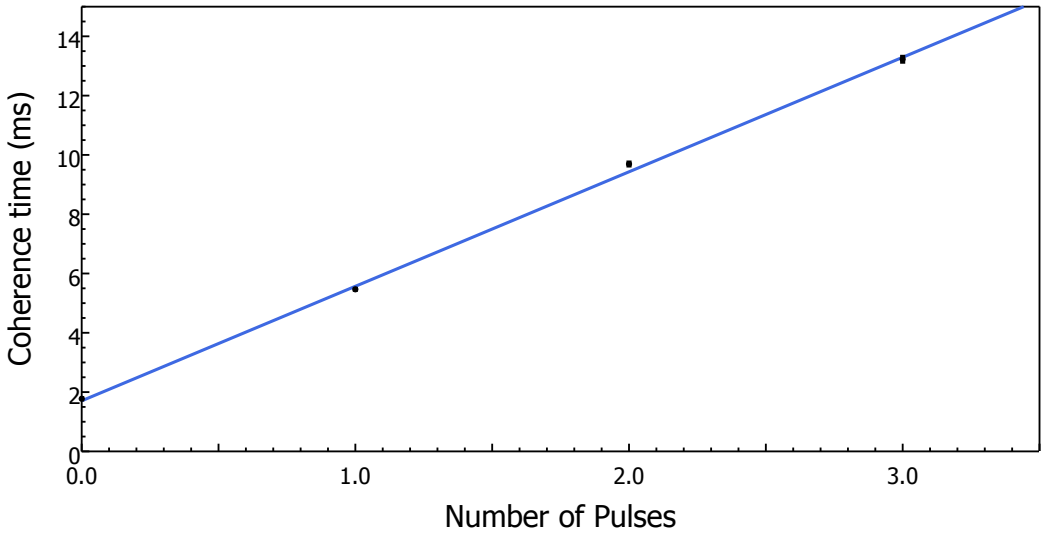

Figure 6.21: Coherence time fitted to a linear relationship against the number of T_π pulses in a UDD sequence. Each pulse adds 3.9(3) ms to the τ_2 coherence time.

broadened by phase noise introduced by birefringence in the fibres caused by acoustic noise.

- The magnetic field of the superconducting coil itself should be completely stable on the timescale of the experimental trials, but slow drifts due to temperature induced changes of the magnetic susceptibility of trap and magnet materials coupled with a unidirectional field decay do occur. While we have not conducted systematic measurements to measure the drifts, based on the above measurement sets we are well below the manufacturer quoted limit of < 0.1ppm hr^{-1} corresponding to < 2.1 kHz hr^{-1}. In general, we can correct drifts by re-measuring the transition frequency after each Ramsey measurement.

- Stray magnetic fields from the environment can affect the transition frequency on a much faster timescale. We do not have any systematic additional shielding of the trap, but we have observed that adding a roughly 30 by 80 cm sheet of mu-metal around an optical table corner that is within 40 cm of the magnet's outer dewar shifts the carrier frequency by ~ 10 kHz, without affecting the coherence time. To minimise any effects due to noise in nearby equipment such as power supplies, we attempt to place them as far away as possible. We also attempted to reduce noise by synchronising the start of each experimental sequence to the 50 Hz signal of the AC mains, but found no noticeable improvement, suggesting that this is not the limiting factor.

- Vibrations of the trap within the bore of the magnet will also appear as magnetic field noise. Reference [162] reports an improvement of coherence time from 6 to 50 ms by vibrationally isolating their superconducting magnet from the floor using rubber pads. We do not currently know how severe this problem is in our experiment, but it is worth investigating if gains of a similar magnitude might be achievable in our experiment as well.

6.3 Motional Coherence and Fock state manipulation

The axial motion of a single ion in a Penning trap is a very high fidelity realisation of an ideal quantum harmonic oscillator. Akin to the τ_2 of the spin qubit, we can characterise the coherence time of the harmonic oscillator τ_z by measuring the stability of the trapping frequency. We have demonstrated in section 6.1 that we are able to prepare the ion in the $n = 0$ Fock state with 99% fidelity and in section 6.2.2 that we can coherently manipulate both the electronic and motional states of the ion by driving carrier or sideband transitions. With these tools, we can place the ion in a low lying Fock state with high probability or coherently engineer superpositions of these states. Using these superposition states, we can then perform Ramsey type interference experiments that measure the contrast loss caused by noise in the trapping frequency. The other coherence limiting effect is direct heating where a phonon is absorbed by the system and n increases. Characterisation of these effects is important not only for quantum information processing operations, which are adversely affected by both, but also is of fundamental interest for the study of coherence time scaling with respect to location in Fock space and the distance between the superposition states.

6.3.1 Heating Rates

When the electric field at the ion fluctuates, there is a small coupling to the electric charge of the ion that can induce direct transitions between motional states. Near the ground state, Fermi's golden rule can be used to calculate the rate Γ_h at which the ion leaves the $n = 0$ state into the $n = 1$ state, which we will assume is a good approximation for the measured heating rate $\dot{\bar{n}}$ as long as n is far below the environment temperature. The heating rate is thus given by [163]

$$\dot{\bar{n}} \approx \Gamma_h = \frac{e^2 S_E(\omega_z)}{4M\hbar\omega_z} \tag{6.13}$$

where $S_E(\omega_z)$ is the spectral density of the field noise at the ion as a function of the trapping frequency:

$$S_E(\omega_z) = 2\int_{-\infty}^{\infty} d\tau \langle \delta E_t(\tau)\delta E_t(0)\rangle e^{-i\omega_z\tau} \tag{6.14}$$

To measure this rate in our trap we prepare an ion in the ground state either by direct sideband cooling or sideband cooling at a high trap potential followed by an adiabatic potential relaxation and then turn of all lasers for a defined wait period before performing a spectral thermometry measurement. To measure the temperature, we follow the same approach as in section 6.1 where we measure the excitation probability profiles around the first red and blue sidebands and fit them with the thermal model of equation 6.1. To obtain the heating rate, we perform a linear fit to the measured temperatures as a function of wait time. We interleave the data acquisition at each new frequency point for different wait times so that we avoid comparing spectra acquired under different experimental conditions. This is particularly important since these spectra can include delays of up to 50 ms repeated 400 times per data point so full data set acquisition can take well over an hour at a time, whereby all 397 nm cooling lasers and 854 re-pump need to be remain drift free to maintain consistent cooling performance in order to not bias the result.

A typical heating rate measurement following direct multi-stage sideband cooling at $\nu_z =$

184 kHz is shown in figure 6.22, yielding $\dot{\bar{n}} = 1.1(3)$ phonons s^{-1}. This was found to be consistent with a more systematic study of heating rates in our trap reported in [50] where a measurement at 190 kHz was reported with $\dot{\bar{n}} = 0.6(6)$ phonons s^{-1} and an average of heating rate measurements from 150 to 400 kHz was found to be $\dot{\bar{n}} \approx 0.3$ phonons s^{-1}. Since the data agreed, we did not seek to repeat the measurements at various trapping frequencies and instead accepted that there was little to no dependence on ω_z suggesting that either our experiment is not sensitive enough to measure the rates with sufficient precision or that there are some noise sources not accounted in the simplified model presented above such as soft collisions with background particles or external electromagnetic noise pick up.

To compare our result to that of the wider ion trap community we translate the heating rate to a scaled spectral noise density and obtain $S_E(\omega_z) = 1.4(4)$ V^2 m^{-2} Hz^{-1} which is almost an order magnitude smaller than any value for a room temperature trap reported in a 2015 meta-study of heating rates [164]. This result is, however, not entirely surprising as the ion to electrode separation is also the largest in the whole study[3] at 10.3 mm hence the effect of any field noise is greatly diminished at the ion. The noise scales with electrode to ion separation d as a power law $S_E \propto d^{-\alpha}$, with values of alpha between 2 and 4 plausibly supported by the aggregate community over all d data [164]. A d^{-4} scaling is theoretically derived from a model of fluctuating patch potentials while pure thermal noise in the electrodes would lead to a d^{-2} scaling [165]. Our result is consistent with the latter, but not the former though given the paucity of data at this length scale we are only left to speculate as to the potential origin of the noise. It is not unreasonable to believe that the effects of patch potentials on the electrodes are much more severe at small d, whereas Johnson noise in the electrodes or electromagnetic pickup becomes dominant for large d. This is still a very active area of research where nothing is conclusively settled, but the evidence for a d^{-4} scaling in the $10^{-5} - 10^{-3}$ m range is gaining support in experiments where d can be controllably varied in a single trap. [166]

While the above result is typical of trap operation under direct sideband cooling, we have observed the heating rate to increase in certain conditions. When performing a set of measurements at 124 kHz with the ion prepared by the adiabatic cooling method, we measure $\dot{\bar{n}} = 9.2(4)$ phonon s^{-1} as seen in figure 6.23. The most likely explanation is that the introduction of the additional transistor circuitry to adiabatically lower the voltage adds a small amount of noise onto the electrode voltage, however a resonance at this particular frequency cannot be ruled out without an independent measurement without the circuitry installed. We include this result here because we use this increased heating rate in the following section to study its effects on a motional superposition.

6.3.2 Motional Superposition on Fock States

To further investigate the motional coherence of our trapped ion, we can perform Ramsey type experiments by creating superpositions of motional Fock states. We can create simple superpositions $|gn\rangle + |gm\rangle$. Starting from the state $|g0\rangle$ we first apply a $\pi/2$ pulse on the m'-th blue sideband (or carrier for $m' = 0$) to create:

$$|\psi\rangle = \frac{|g0\rangle + |em'\rangle}{\sqrt{2}} \tag{6.15}$$

[3] $\approx 3\times$ bigger than the next largest trap.

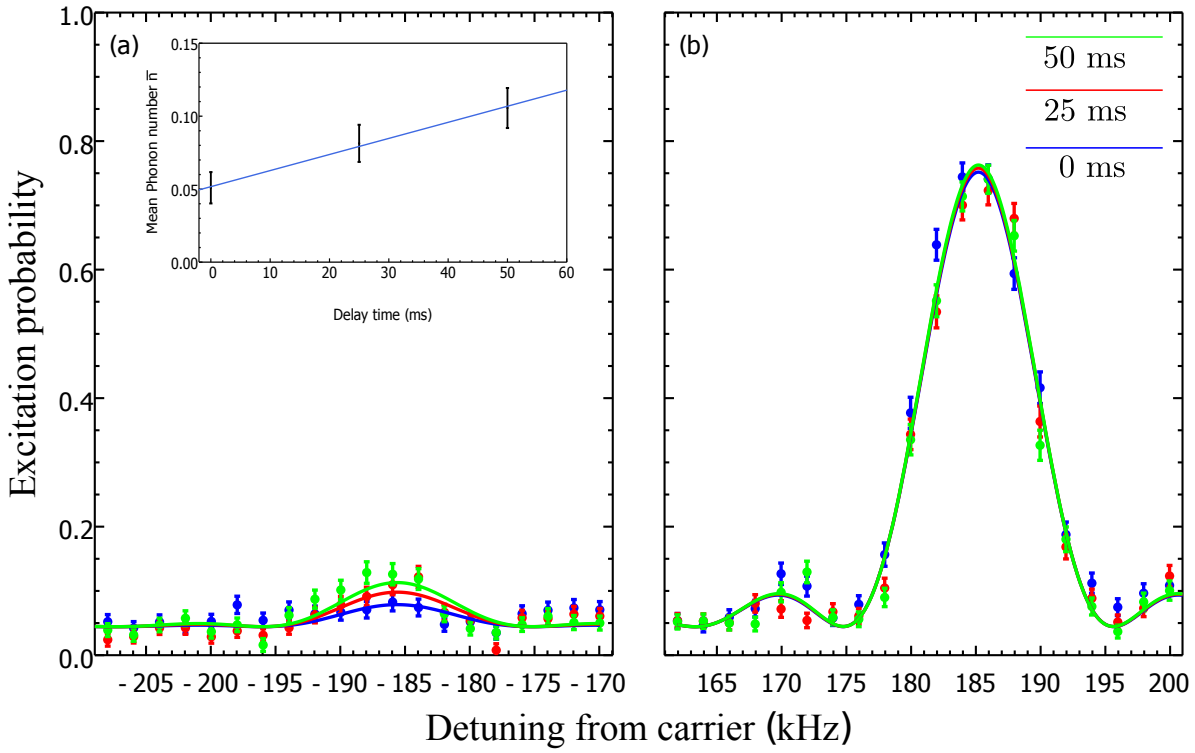

Figure 6.22: Heating rate measurement at $\nu_z = 184$ kHz on a ion prepared in the ground state by a 25 ms sideband cooling sequence targeting the 3^{rd}-2^{nd}-3^{rd}-2^{nd} -1^{st} sidebands for 5 ms each. The inset contains a linear fit to the $\bar{n}$ derived from the sideband fits as a function of wait time where all lasers are off giving $\dot{\bar{n}} = 1.1(3)$ phonons s^{-1}

then we subsequently apply a π pulse on the red $(m - m')$-th sideband to reach the desired state:

$$|\psi\rangle = \frac{|g0\rangle + |gm\rangle}{\sqrt{2}} \tag{6.16}$$

Having shown how we can achieve a particular state, let us assume we have prepared an arbitrary ground state superposition of states n and m to derive a more general result. After some wait time T_w, the state evolves to:

$$|\psi\rangle = \frac{e^{-in\phi(T_w)}|gn\rangle + e^{-im\phi(T_w)}|gm\rangle}{\sqrt{2}} \tag{6.17}$$

where the eigenstates acquire a phase due to the change in trap frequency $\delta\omega_z(t)$:

$$\phi(T_w) = \int_0^{T_w} (\omega_z + \delta\omega_z(t))dt \tag{6.18}$$

The first retrieval pulse of the interferometer creates a spin-motion superposition state:

$$|\psi\rangle = \frac{e^{-in\phi(T_w)}|gn\rangle + e^{-im\phi(T_w)}|em'\rangle}{\sqrt{2}} \tag{6.19}$$

The final $\pi/2$ pulse creates the state:

$$|\psi\rangle = \frac{1}{2}\left[\left(e^{i(-n\phi(T_w))} - e^{i(\xi - m\phi(T_w))}\right)|gn\rangle + \left(e^{i(\xi - n\phi(T_w))} + e^{-im\phi(T_w)}\right)|em'\rangle\right] \tag{6.20}$$

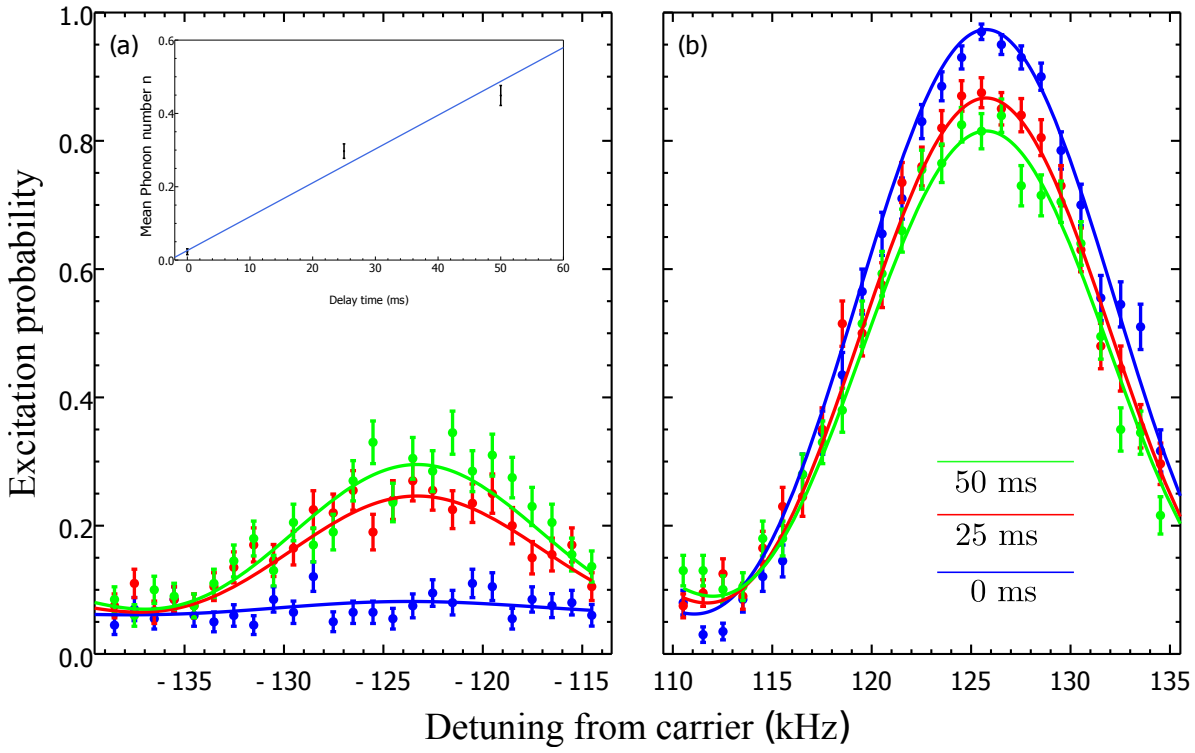

Figure 6.23: Heating rate measurement at $\nu_z = 124$ kHz on a ion prepared in the ground state by a 20 ms sideband cooling sequence at $\nu_z = 418$ kHz, follow by an adiabatic potential relaxation. The inset contains a linear fit to the $\bar{n}$ derived from the sideband fits as a function of wait time where all lasers are off giving $\dot{\bar{n}} = 9.2(4)$ phonons s^{-1}

where ξ is the phase between the final two pulses of the interferometer. This is an important point since the optical coherence time of the laser can be orders of magnitude smaller than the wait time hence all phase information encoded in the $|e\rangle\langle g|$ coherences is lost. Projecting as usual on $|g\rangle$ gives us sinusoidal oscillations:

$$P_e = |\langle e|\psi\rangle|^2 = \frac{1}{2}\left[1 + \cos(\xi + m\phi(T_w))\right] \tag{6.21}$$

Let us now consider the usual procedure of assuming that the trap frequency is constant over the course of one experiment, but varies from repeat to repeat according to a Gaussian distribution with standard deviation σ_ω. The excitation probability is then given by:

$$\begin{aligned} P_e &= \int_{-\infty}^{\infty} \frac{1}{2\sqrt{2\pi\sigma_\omega^2}} e^{-\frac{(\omega_z-\omega)^2}{2\sigma_\omega^2}} \left[1 + \cos(\xi + (m-n)T_w\omega_z)\right] d\omega \\ &= \frac{1}{2}\left[1 + e^{-(m-n)^2\sigma_\omega^2 T_w^2/2} \cos(\xi + (m-n)T_w\omega_z)\right] \end{aligned} \tag{6.22}$$

Immediately we notice an important result that the coherence time scales with the square of the distance $m-n$ between the superposition states. This is in agreement with a more rigorous derivation using a full master equation treatment [167]. In the same reference, the authors also considered how the coherence is affected by heating through direct phonon absorption deriving an approximate expression for the visibility:

$$C_{0,m} \approx \frac{1}{(1 + \dot{\bar{n}}T_w)^{(1+m)}} \tag{6.23}$$

A difficulty in performing an exact calculation lies in the fact that once the two superposition states are displaced, the pulse length of the retrieval pulses of the interferometer no longer form exact π and $\pi/2$ angles due to a change in the strengths of the Rabi coupling to the excited electronic state. This effect is exacerbated for larger Lamb-Dicke parameters. For the simple purpose of distinguishing between a Gaussian decoherence trend and one given by 6.23, we shall neglect these concerns.

We begin by first studying the motional coherence of $|0\rangle + |1\rangle$ and $|0\rangle + |2\rangle$ superposition states at two different motional frequencies – 418 and 124 kHz. We exploit the fact that we observe an almost order of magnitude greater heating rate at 124 kHz when the ion is prepared in the ground state using the adiabatic cooling technique (section 6.3.1) to study and compare motional decoherence in the presence of amplitude noise. In both cases the ion is first prepared into the ground state by 10 ms of sideband cooling at 418 kHz. Immediately afterwards, or after the adiabatic relaxation step to reach 124 kHz, we perform a $\pi/2$ pulse on the carrier followed by a π pulse on the first red sideband to prepare the $|g0\rangle + |g1\rangle$ state or a π on the first blue sideband followed by a π pulse on the first red sideband to prepare the $|g0\rangle + |g2\rangle$ state. After some wait time T_w we reverse the order of the last two pulses and measure the population in the excited state. To obtain fringe contrast for the 418 kHz data we scan the phase of the final carrier pulse, whereas for the 124 kHz data we add a short time t_d on top of T_w in increments of 640 ns. These methods are equivalent since $t_d \ll T_w$ and we can thus think of each visibility measurement as being performed at a fixed T_w.[4] Figure 6.24 summarizes the experimental technique for each of the two experiment types.

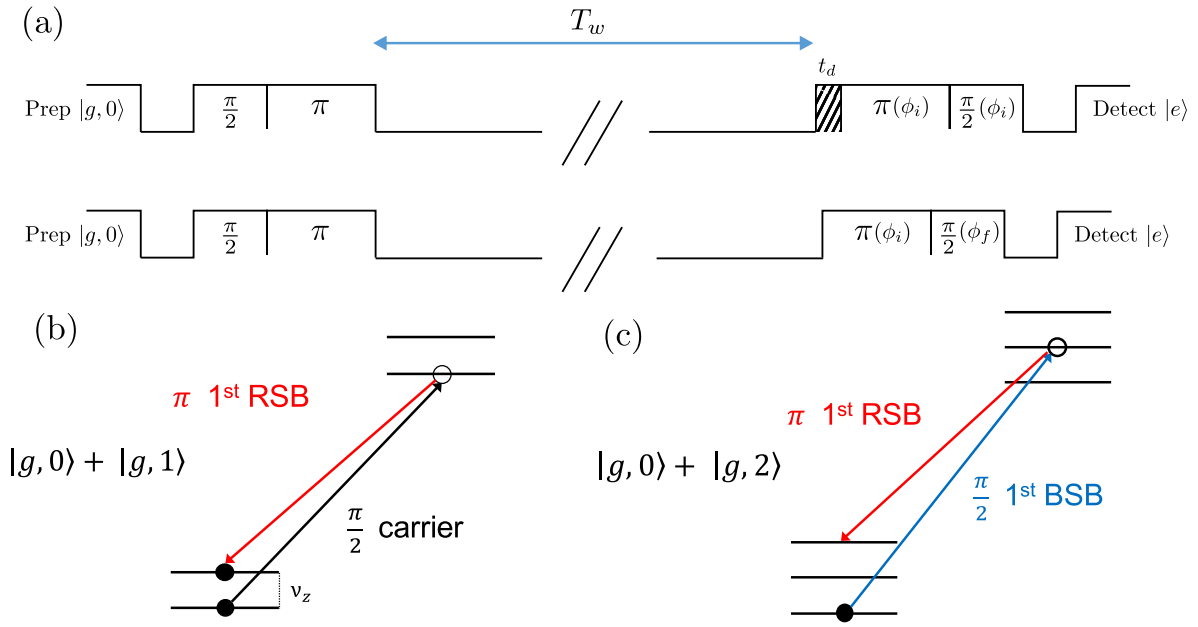

Figure 6.24: (a) - The two methods for performing motional coherent state interferometry. In the top sequence, a small additional wait time $t_d \sim 10\mu$s is incremented to produce fringes. In the second sequence, the wait time is fixed and the phase of the final laser pulse relative to the second π pulse is fixed. (b) Diagram depicting the creation of the $|g0\rangle + |g1\rangle$ superposition. (c) Diagram depicting the creation of the $|g0\rangle + |g2\rangle$ superposition.

[4]The reason for the two experimental sets using different methods is that at the time, we could not set the time increments on our FPGA that controls all the laser pulses below 640 ns, which would result in us under sampling the fringe pattern.

The $|g0\rangle + |g1\rangle$ visibilities are presented in figure 6.25a while the individual fringe fits are found in Appendix B. The first important difference to note is that the higher frequency data exhibits a Gaussian trend whereas the low frequency data appears exponential. Using a fit to the visibility function 6.23 we obtain a value of $\dot{\bar{n}} = 8.3(3)$ s^{-1} for the 124 kHz data which is within 2 sigma of the value determined from sideband thermometry. A Gaussian fit to the 418 kHz data yields a corresponding trap frequency noise of $\sigma_\nu = 0.40(1)$ Hz. This is well within the upper bound of $\sigma_\nu = 0.8$ Hz set by measuring the power supply stability of the endcap power supply which is 4 ppm at 250 Volts. The quality of this fit constrains the heating rate to less than a phonon per second, once again consistent with the sideband thermometry, however to extract a true measure of σ_ν and $\dot{\bar{n}}$ in a region where both have a similar timescale would require a more rigorous derivation of the combined response function and much more precise measurements than presented here. The $1/e$ coherence times are $\tau_{418} = 590(12)$ ms and $\tau_{124} = 84(2)$ ms. The implication for coherent quantum operation state is clear – the motional coherence time is significantly long enough to be comparable to the heating rate and hence is not a limitation. In fact, our motional coherence time is better than those reported in RF traps designed for quantum information processing, which observed times of 100 ms ($\nu_z = 4$ MHz) [28], 157(34) ms ($\nu_z = 800$ kHz) and 76(30) ms ($\nu_z = 500$ kHz) ms [168], both of which were heating rate limited.

Since the results of the 0 and 1 state superposition at 418 kHz suggested that we are operating in a region where motional dephasing is not completely dominated by the heating rate, we undertook a study of how different superposition states are affected. The next data set of visibilities was taken for the $|g0\rangle + |g2\rangle$ superposition (fig. 6.25b) exhibiting the same behaviour; the 418 kHz remains Gaussian in shape while the 124 kHz data is more appropriately fitted by the heating rate model. The trap frequency noise is measured to be $\sigma_\nu = 0.31(2)$ Hz from the Gaussian model while the heating rate is $\dot{\bar{n}} = 6.8(2)$. In both cases the measured values are slightly smaller than those extracted from the $|g0\rangle + |g1\rangle$ superposition fits, suggesting that the visibility decrease is not as strong as the scaling predicts, but it is still higher than what would be seen in the case if the dephasing were linear rather than quadratic in $m - n$ or if the heating didn't scale with $\dot{\bar{n}}^{-m}$. This could be, as suggested above, because we are in a regime where both effects contribute and hence lead to a modified scaling or, owing to the relatively small scale of the discrepancy, simply due to natural fluctuations in noise level as the sets were collected on different days. Ideally, we would attempt to collect all the data in one short session, but owing to the length and the difficulty of maintaining the same experimental conditions over the course of day this was not possible.

One way of further trying to discriminate between heating and dephasing is to perform a 'phonon echo' experiment akin to that of the spin echo for the optical qubit. The procedure is similar in that we wish to swap the population between the $|g0\rangle$ and $|gm\rangle$ states in the middle of the wait time, such that the phase acquisition is cancelled to first order. We performed this experiment on the 418 kHz $|g0\rangle + |g2\rangle$ superposition by inserting three π pulses in succession on the 1$^{\text{st}}$ red, blue and red sidebands in order to swap the population. The process is graphically depicted in figure 6.26 and shows the state after each pulse. Though we have not conducted a calculation to show this, we conjecture that this procedure should not improve the coherence time significantly if it is limited purely by heating since any change in the phonon state in the first half of the wait will cause a pulse angle mismatch on the three population swap pulses,

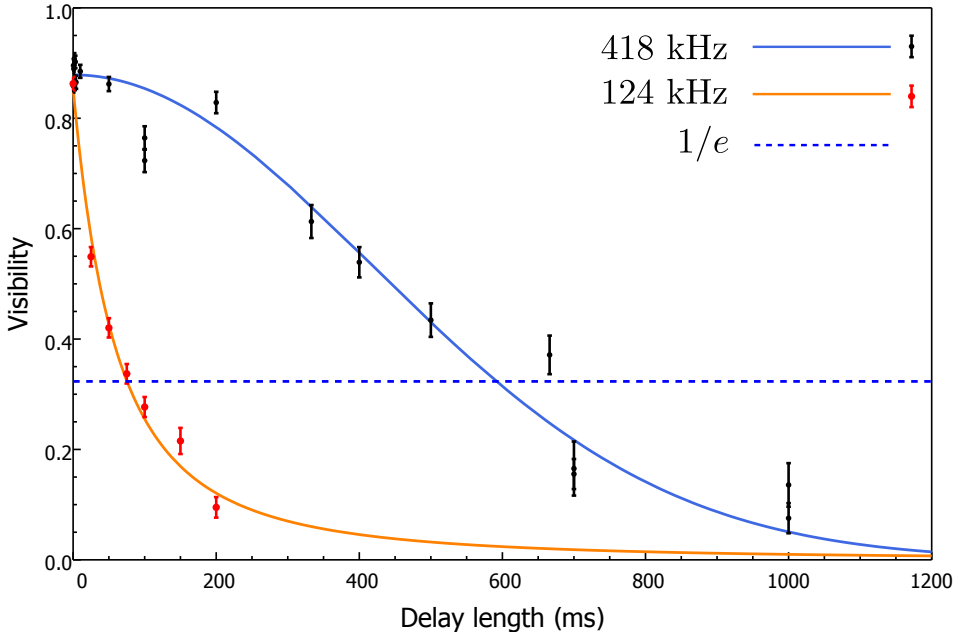

(a) $|g0\rangle + |g1\rangle \quad \tau_{418} = 590(12), \quad \tau_{124} = 84(2)$

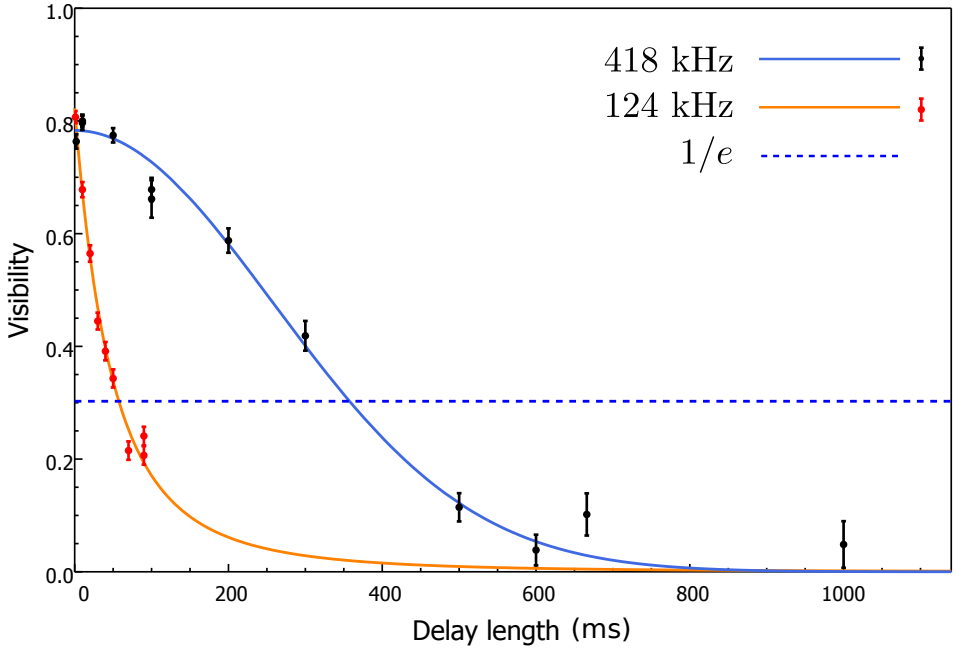

(b) $|g0\rangle + |g2\rangle \quad \tau_{418} = 366(11), \quad \tau_{124} = 59(1)$

Figure 6.25: Visibility versus delay time plots of an interferometry measurement on the (a) $|g0\rangle + |g1\rangle$ and (b) $|g0\rangle + |g2\rangle$ superpositions. The 418 kHz data is fitted with a Gaussian function while the 124 kHz data is fitted with the heating model of equation 6.23. τ expresses the $1/e$ visibility indicated on the plot.

reducing fidelity. The results of the experiment show an increase in the coherence time by approximately a factor of two to $\tau_{418} = 790(30)$ ms, while also changing the distribution of the data from Gaussian to a distribution better described by the heating model. The fit suggests a heating rate of $\dot{\bar{n}} = 0.5(1)$ consistent with our sideband thermometry and therefore we are led to believe that the procedure removes most of the dephasing noise. While this procedure might be of limited interest within quantum computation algorithms, it can be useful as a way to preserve motional superpositions in the presence of strong phase noise.

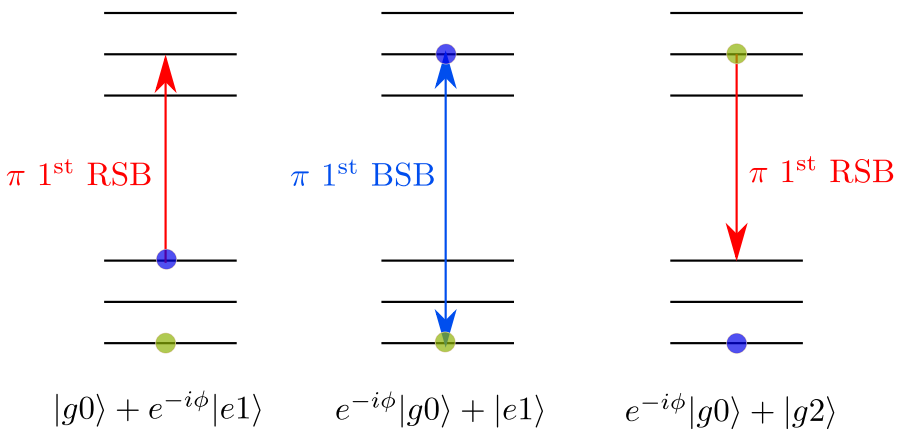

Figure 6.26: The phonon echo pulse sequence applied to a state $|g0\rangle + |g2\rangle$ with the state after each pulse indicated below each step. The sequence proceeds left to right.

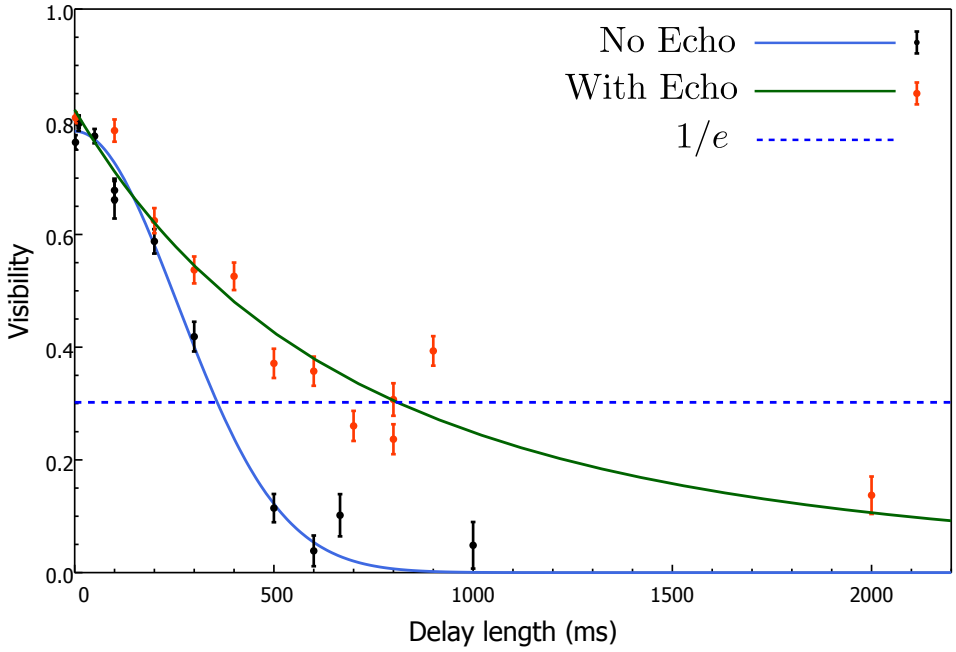

Figure 6.27: Data comparing the visibility with and without the phonon echo on an interferometry measurement of the $|g0\rangle + |g2\rangle$ superposition.

To complete our studies of low n superspositions, we examine the coherence time of a three state superposition $(|g0\rangle + |g1\rangle + |g2\rangle)/\sqrt{3}$. The scheme to prepare this state (illustrated in figure 6.28) begins with a pulse angle of $t_{02}^{\pi} = \Omega_0 t/2 = 0.955$ on the carrier to drive two third of the population to the excited state. We then apply a $\pi/2$ pulse on the first red and π pulse on the second red sidebands in succession to prepare the desired state. At this point we have created the state:

$$|\psi_{123}\rangle = \frac{1}{\sqrt{3}}\left[|g0\rangle + e^{-it_r^{\pi}\omega_z}|g1\rangle + |g2\rangle\right] \tag{6.24}$$

Then after a wait time T_w and the first retrieval π pulse on the 2^{nd} red sideband we end up with the state:

$$|\psi\rangle = \frac{1}{\sqrt{3}}\left[|g0\rangle + e^{-i\omega_z(2t_r^{\pi}+T_w)}|g1\rangle + e^{-i2\omega_z T_w}|e0\rangle\right] \tag{6.25}$$

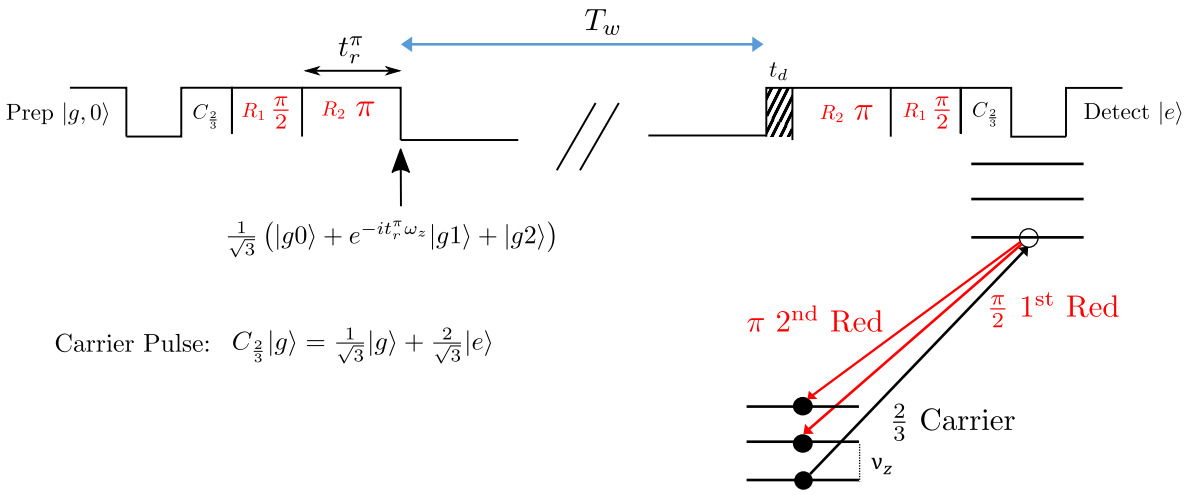

Figure 6.28: Pulse sequence and schematic diagram for preparing a three state superposition of the form $|g0\rangle + |g1\rangle + |g2\rangle$.

The next $\pi/2$ pulse with phase ϕ_r on the first red sideband creates the state:

$$|\psi\rangle = \frac{1}{\sqrt{6}}\left[\sqrt{2}|g0\rangle + \left(e^{-i\omega_z(2t_r^\pi+T_w)} - e^{-i(2\omega_z T_w+\phi_r)}\right)|g1\rangle + \left(e^{-i\omega_z(2t_r^\pi+T_w)+i\phi_r} + e^{-i2\omega_z T_w}\right)|e0\rangle\right] \tag{6.26}$$

Lastly, the 2/3 excitation pulse with phase ϕ_c on the carrier creates the state:

$$\begin{aligned}|\psi\rangle = \frac{1}{3}\left[1 - e^{-i(\omega_z(2t_r^\pi+T_w)-\phi_r+\phi_c)} - +e^{-i(2\omega_z T_w+\phi_c)}\right]|g0\rangle \\ +\frac{1}{3\sqrt{2}}\left[e^{-i\omega_z(2t_r^\pi+T_w)} - e^{-i(2\omega_z T_w+\phi_r)}\right]|g1\rangle \\ +\frac{1}{3}\left[\sqrt{2}e^{i\phi_c} + \frac{1}{\sqrt{2}}\left(e^{-i(\omega_z(2t_r^\pi+T_w)-\phi_r)} + e^{-i(2\omega_z T_w)}\right)\right]|e0\rangle \\ +\frac{1}{3}\left[e^{-i(\omega_z(2t_r^\pi+T_w)-\phi_c)} - e^{-i(2\omega_z T_w+\phi_r-\phi_c)}\right]|e1\rangle\end{aligned} \tag{6.27}$$

To complete this derivation, we have made the approximation that the action of the carrier pulse is the same on the $|0\rangle$ and $|1\rangle$ states; while this is generally true in the Lamb-Dicke regime, for the $\eta = 0.27$ used in our experiment, the error is 7%. If we now perform a projective measurement on the $|e\rangle$ state, we obtain

$$P_e = \frac{1}{9}\left[5 + 2\cos(\phi_c + 2\omega_z T_w) - \cos(\phi_r + \omega_z(T_w - 2t_r^\pi)) + 2\cos(\phi_r - \phi_c - \omega_z(T_w + 2t_r^\pi))\right] \tag{6.28}$$

The most important feature here is that we will observe oscillations at $2\omega_z$ that will interfere with oscillations at ω_z. The shape of the pattern will also be sensitive to the phase difference between the beams. In our experiments we synthesize all frequencies from a single source that is phase continuous, but we also experience frequency detunings that will effectively look like phase shifts of the pulses. To fit our experimental data, we use a model of the form:

$$P_e(T_w) = B + \frac{1}{9}\left[5 + 2C_2\cos(\phi_1 + 2\omega_z T_w) - C_1\cos(\phi_2 + \omega_z T_w) + 2C_1\cos(\phi_1 - \phi_2 - \omega_z T_w)\right] \tag{6.29}$$

with offset B, the phases ϕ_1, ϕ_2 and the visibilities C_1, C_2 as fit parameters. The full data set is presented in figure 6.29, where we have interleaved T_w delayed interferometry measurements

with measurements without a delay to account for potential stray phases due to detunings that change the shape of the interference pattern. It is clear that for example the data set in (e) has a much more pronounced asymmetry between the blue no delay peaks than in (a). We therefore used the no delay data sets to normalise the visibilities of the delayed spectra. Before moving on, we remark on the fact that the fits from the model 6.29 fit remarkably well even in the presence of decoherence and we clearly observe the behaviour characteristic of two frequency components interfering.

To characterise the decoherence as a function of wait time, we extract the C_1 and C_2 amplitudes independently and also find the average decoherence C_A by setting $C_A = C_1 = C_2$ as a fit constraint. Since we do not have a full theoretical model of decoherence, we conjecture that the decoherence under the presence of heating of each amplitude will follow the form of 6.23 while the exponent of the average visibility will be the average of the independent exponents. We thus expect to see the higher frequency oscillations due to the $e^{-i2\omega_z T_w}$ terms die faster. Due to the fact that we only have 5 data points and we wish to extract three exponents and a normalisation we fix the heating rate to $\dot{\bar{n}} = 9$ s^{-1} based on the sideband height measurements from section 6.3.1. The resulting parameters from the fits in figure 6.30 are summarised in table 6.1. From the coherence times, we observe that the visibility of the higher frequency component indeed decays faster. The exponents of both the C_1 and C_2 visibility are larger by ≈ 1 compared to the heating noise model prediction for an individual $|g0\rangle + |g1\rangle$ or $|g0\rangle + |g2\rangle$ state, but their relative difference is also ≈ 1 suggesting the scaling dependence on the difference in n is preserved. The absolute difference in the exponents could be simply because the heating rate was slightly different than the one that was assumed as the function is very sensitive to this parameter and with few data points it is difficult to be quantitatively accurate.

Alternatively, this simplified model may not capture the full extent of the physics, but it nonetheless clearly shows that we observe different timescales of decay for the two frequency components. One potential technical cause of the decoherence appearing faster is that preparing the $|g2\rangle$ state with high fidelity is more difficult. It requires a very precise measurement of the sideband peak frequency because the Rabi frequency at this sideband is typically only ≈ 2 kHz and we observe Stark shifts of a similar magnitude. This low Rabi frequency also means that the π pulse has to be $\approx 150\mu$s long and at this point we lose some fidelity due to laser addressing error. Reducing the laser linewidth and further stabilising its intensity so that larger Rabi frequencies can be achieved would help eliminate this problem.

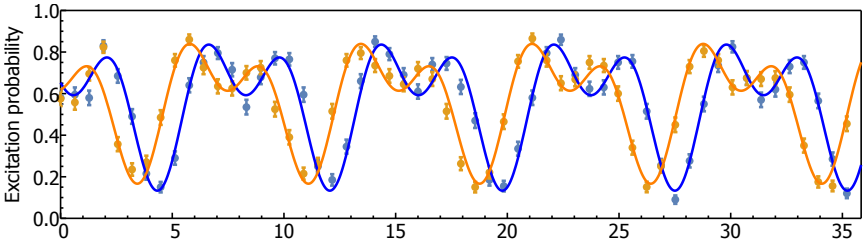

(a) $T_w = 1$ ms

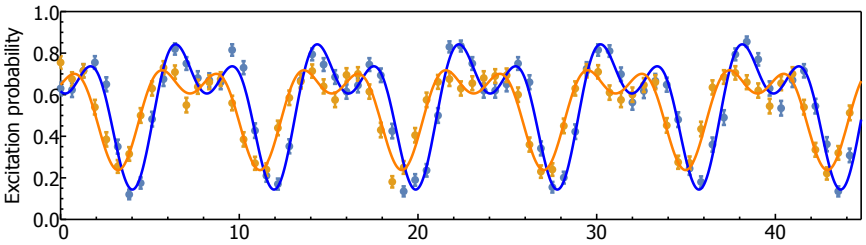

(b) $T_w = 10$ ms

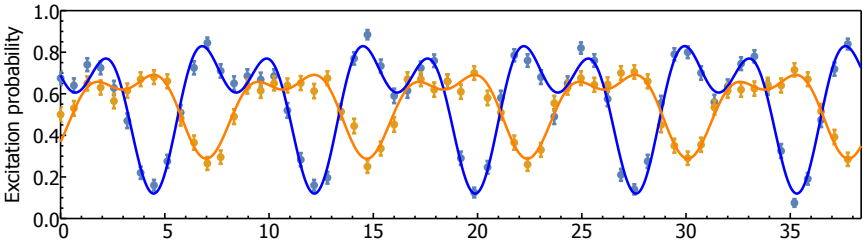

(c) $T_w = 20$ ms

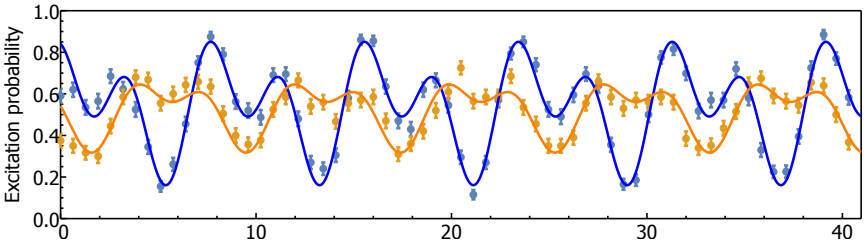

(d) $T_w = 30$ ms

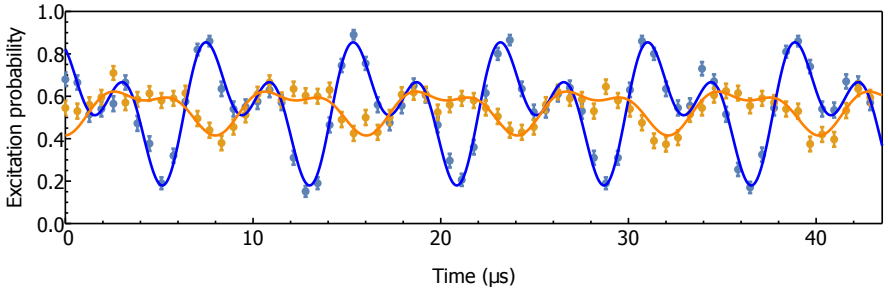

(e) $T_w = 50$ ms

Figure 6.29: An interleaved set of interference measurements of the $|g0\rangle + |g1\rangle + |g2\rangle$ superposition taken at ν_z= 124 kHz with a short time scan added to the T_w wait time. The blue data are all taken with $T_w = 0$ to provide a reference for the initial phase conditions during the experiment, whereas the gold data have the wait time listed in the captions.

	τ (ms)	m
C_1	42(2)	2.0(3)
C_2	30(2)	3.0(3)
C_A	35(2)	2.5(2)

Table 6.1: Table of fit parameters for the visibility of the three state superposition to the heating model, giving the coherence time τ and the exponent m of the decay.

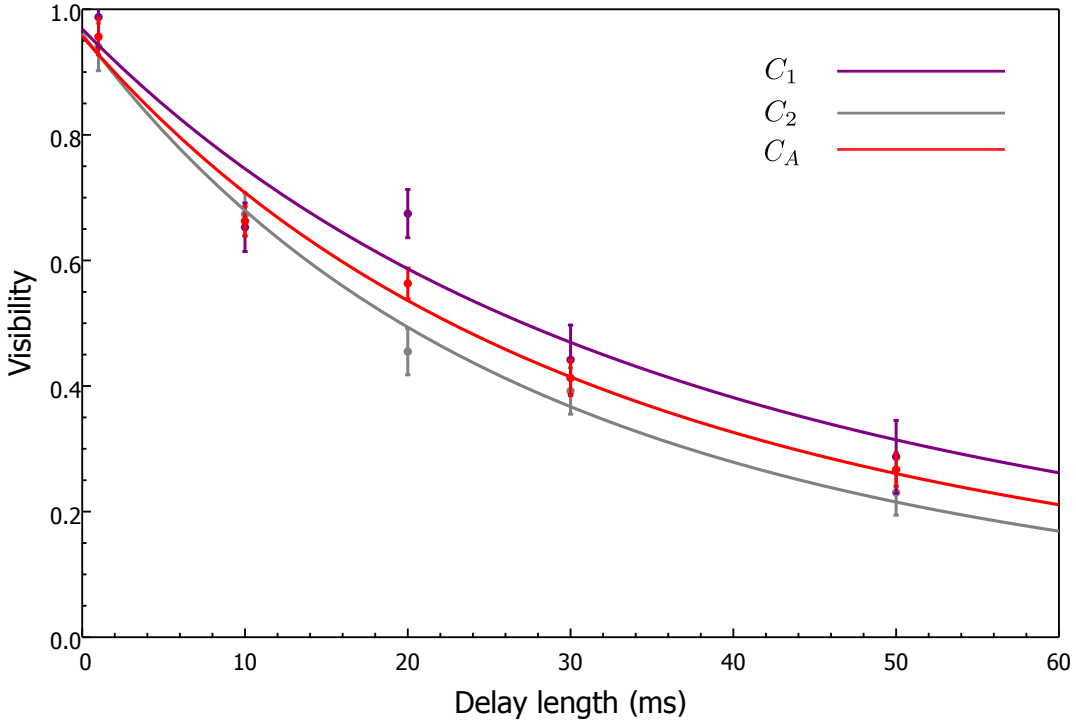

Figure 6.30: Visibility of the interference measurements of the $|g0\rangle+|g1\rangle+|g2\rangle$ as a function of wait time. The fits use the heating model from equation 6.23 where the exponent and initial amplitude is allowed to vary, while the heating rate is fixed to $\dot{\bar{n}} = 9$ s^{-1}.

6.3.3 Motional Superposition outside the Lamb-Dicke regime

One interesting question is to establish experimentally whether there is not only decoherence scaling with the distance between Fock states, but also whether the absolute value contributes significantly. A general scheme to coherently prepare any arbitrary superposition of Fock states was devised [169] and later experimentally implemented to genereate the state $|g0\rangle + |g3\rangle$ [170]. However, as discussed in the previous section, generating superpositions of the form $|n\rangle + |m\rangle$ far from ground state with high fidelity is difficult due to the error accumulated from power and phase imprecisions in each pulse. Reference [171] simulates a large superposition of up to $n = 29$ and concludes that a Gaussian error of 2.5% in the laser parameters reduces the state fidelity by $\approx 50\%$. There is, however, one technique that we can exploit that can prepare quasi-pure high lying states incoherently that uses the coupling strength minima of the sidebands that posed us problems during sideband cooling (see 6.1.2) to our advantage. Just as population could get trapped in a particular Fock state during sideband cooling, we can start with a ground state

cooled ion and 'sideband heat' [5] it into the same state. By simply reversing the cooling process and driving the ion on the first or second blue sideband with the 854 nm quench laser turned on we can produce an arbitrary[6] high n Fock state by selecting the appropriate trap frequency since the minima locations scale with the Lamb-Dicke parameter.

The full picture is of course not as simple. Once the ion begins to reach higher n states, the coupling to higher order sidebands gets progressively stronger and since the heating process relies on additional decay and incoherent repump steps (discussed in the context of sideband cooling in 4.4.2), the ion can leapfrog over the coupling minimum on a higher (or lower) order transition as seen in a schematic illustration in figure 6.31. Hence the population will slowly leak through and not perfectly accumulate in the minimum Fock state. The resulting population will thus have some non-standard distribution near the minimum n state. The key part of preparing a state that is very narrowly distributed around the desired minimum is to empirically measure the cooling dynamics parameters such as the 854 nm laser detuning and the 729 nm laser power that can prepare a ground state cooled ion given a particular Doppler cooled thermal distribution. We can then estimate an appropriate sideband heating time using these parameters and then optimise the final time empirically. For a more rigorous treatment using a Monte-Carlo simulation of the heating process see the PhD thesis of Manoj Joshi.

Our technique is similar to one proposed in reference [172] where the blue sideband pulse and the 854 quench are applied in sequence rather than simultaneously. The pulse length on the blue sideband is selected such that it is a 2π pulse for the desired Fock state, hence it will not transfer any population while only adding a trivial phase, but it will shift some population from all lower Fock states at each iteration. By adding more iterations, the desired Fock state population approaches unity. The major drawbacks of this scheme are that it is significantly slower, taking approximately 3 ms to reach the $n = 6$ with a 96% fidelity compared to $n \approx 150$ for the same laser parameters in our scheme. Furthermore, it also cannot be used to create any Fock states above $\frac{d\Omega_{n,n+1}}{dn}(n_{max}) = 0$. For the purposes of reaching much larger states in a shorter amount of time, our technique is superior if very high preparation fidelities are not demanded.

To find out the purity of a quantum state, the gold standard is full state tomography that maps out the elements of the density matrix. To do this with the motional states of a trapped ion, following the scheme of [173], requires a coherent displacement to be applied to the ion to shift it in phase space followed by a measurement of excitation on the blue sideband. We are currently not able to do this with the required degree of control, but we report in section 6.3.4 our progress towards achieving this goal. Since we cannot analytically predict the distribution of the Fock states, we will simply assume a normal distribution around a mean $\bar{n}$, with a standard deviation σ_n which, as we will see shortly, is adequate for the purposes of our modelling.

We first perform two spectroscopic measurements of the 7 lowest order sidebands after sideband heating of an ion prepared in the ground state at $\nu_z = 418$ kHz. To reach the first blue sideband coupling minimum at $n_1 = 162$ we heat for 10 ms of the first blue sideband only, and to reach the second minimum at $n_2 = 292$ we follow up the 10 ms heating period of the first blue sideband with 20 ms of heating on the second with $\Omega_0/2\pi = 40$ kHz and $\Omega_{854}/2\pi = 80$ kHz. We do not begin immediately on the second sideband since the coupling near $n = 0$ is very weak.

[5] In this chapter we will take sideband heating to specifically mean increasing the phonon by incoherent driving to higher phonon states – the reverse of sideband cooling. We stress that we are not creating a thermal state.

[6] Within the limits of our trapping parameters and inital ground state cooling capabilities

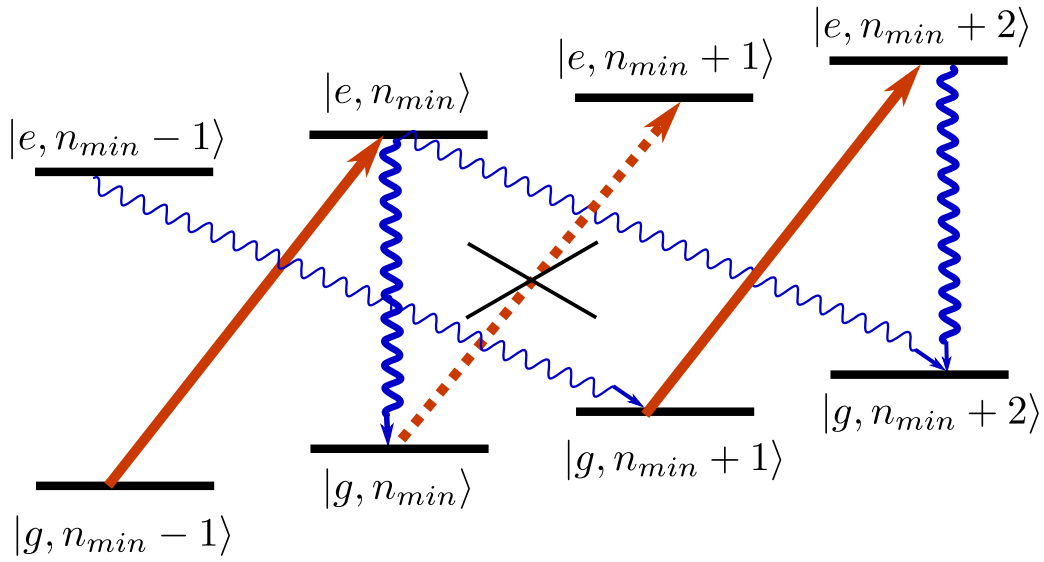

Figure 6.31: Simplified schematic of the sideband heating process using the first blue sideband. The pumping out of the n_{min} state is effectively blocked due to the almost negligible coupling, but decay processes on the second order allow transitions to higher states, where the first blue sideband coupling begins to grow again. Higher order processes are not shown for clarity, but also contribute.

The results of the experiments in figure 6.32 show a strong excitation suppression on the $1^{st}/2^{nd}$ order sidebands for plots (a) and (b) respectively showing a clear signature that the majority of the population is located near the minima. For the first sideband heating case, the value of $\bar{n} = 145(1)$ is below the minimum by more than the standard deviation of $\sigma_n = 10(1)$, which could suggest that we might have terminated the heating slightly prematurely. The $\chi^2_R = 1.5$ value, however, implies that despite the crude approximation of the model, it seems to follow the data fairly accurately. In the second sideband heating case, we obtain a distribution centred at $\bar{n} = 291(1)$, which is only 3 Fock states away from the coupling minimum, with a standard deviation of $\sigma_n = 12(1)$. In this case a goodness of fit test yields a value of $\chi^2_R = 1.6$ once again supporting the validity of the model. A skew-Gaussian distribution defined as

$$P(n) = \left(1 + \left(\mathrm{erf}\left[\frac{\alpha(n-\bar{n})}{\sqrt{2}\sigma_n}\right]\right)\right) e^{-\frac{\alpha(n-\bar{n})^2}{2\sigma_n^2}} \tag{6.30}$$

fit was also attempted, but for both cases, the skewness parameter alpha was smaller than its associated error and consistent with zero.

While that Gaussian modelling of the distributions might not give us an accurate measure of the underlying state distribution, we can take a pragmatic approach and ask how well we can perform coherent manipulations on the states that we create. To this end we drive Rabi oscillations on transitions that show the least dependence on n near the state we created (fig. 6.32). In figure 6.33 we perform Rabi oscillations on the carrier transition both after sideband cooling to the ground state and after 10 ms of sideband heating on the 1^{st} BSB to near the first coupling minimum in an interleaved spectrum to maintain the same Ω_0 for both spectra and to ensure we don't observe excessive laser intensity noise that would exacerbate the decoherence due to the n state spread. We fit the ground state function using the standard form of equation 6.6 whereas for the heated spectrum, we replace the thermal distribution with a sum over a

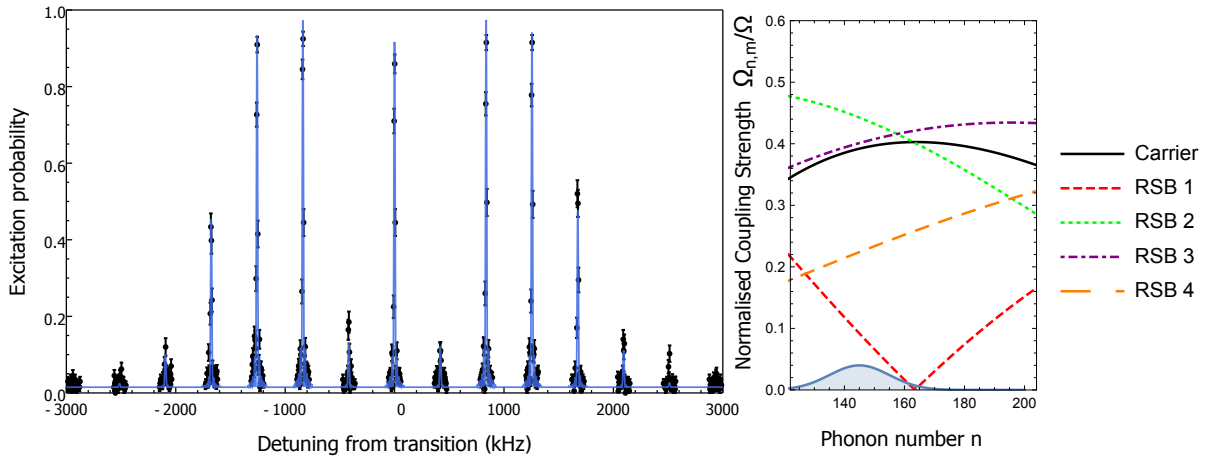

(a) $\bar{n} = 145(1), \quad \sigma_n = 10(1)$

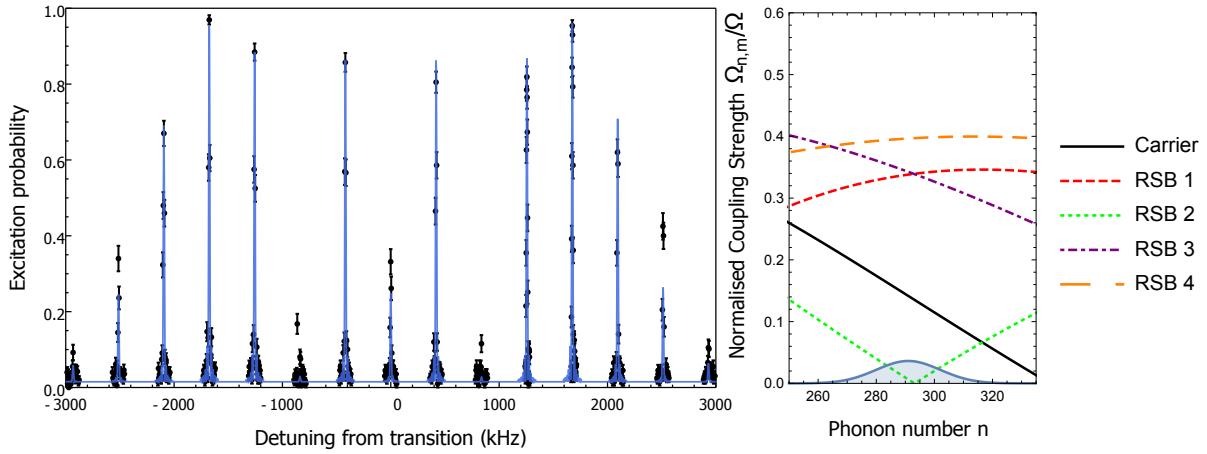

(b) $\bar{n} = 291(1), \quad \sigma_n = 11(1)$

Figure 6.32: *Left* – Spectra after (a) 10 ms heating on 1st BSB probed for 65 μs and $\Omega_0/(2\pi) =$ 16.5 kHz. (b) 10 ms on 1st BSB followed by 20 ms on 2nd BSB probed for 70 μs and $\Omega_0/(2\pi) = 16.5$ kHz. *Right* – Sideband coupling strengths in the vicinity of the coupling minimum with the probability distribution from the fit overlaid in blue. Fits are to a sum of excitation probabilities weighted by a normal distribution with parameters under each plot. The sum is truncated to $\approx \pm 3\sigma_n$. Trap frequency $\nu_z = 418$ kHz

normal distribution of Rabi frequencies as for the sideband excitations, obtaining $\bar{n} = 146(2)$ and $\sigma_n = 17.2(2)$. Encouragingly, we have a very good agreement on the mean phonon number with the previous spectroscopic method even though we see a slightly larger spread in the distribution. This might simply be due to the fact that the Rabi frequencies do not change very much over the span of the distribution hence the method is not as sensitive to the distribution width as oscillations on sidebands with a steeper coupling strength dependence on n near $\bar{n}$. The important conclusion for our goal of creating a coherent superposition is that we can perform a π pulse on the carrier with almost 90% fidelity .

We demonstrate a similar experimental result near the minimum of the 2nd blue sideband coupling driving the 4th red sideband depicted in figure 6.34. This result highlights the highly non-thermal and relatively narrow distribution of phonon states near $\bar{n} = 291$ since we see high contrast coherent oscillations on such a high order sideband. To our knowledge this is the first demonstration of coherent driving on sidebands of higher order using this preparation technique. It was only as recently as 2016 that coherent driving on sidebands of up to 5th order

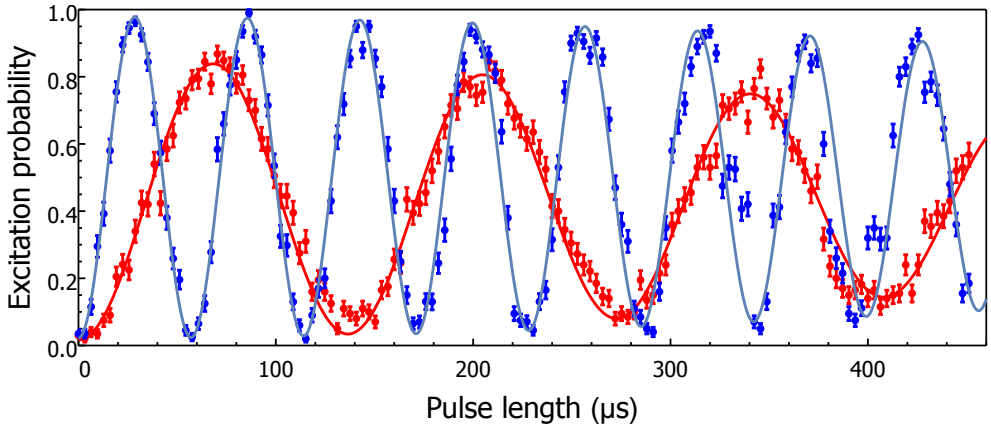

Figure 6.33: Rabi Oscillations of the carrier on the ground state population (Blue) with a thermal $\bar{n} = 0.08(2)$ and $\Omega/2\pi = 17.75(5)$ kHz and on a high lying state with a Gaussian distribution of motional states. $\bar{n} = 146(2)$, $\sigma_n = 17.2(2)$.

was demonstrated in an RF trap using a very different approach where by the ion is displaced in space by a very rapid switching (≈ 4 ns) of the potential on a set of auxiliary electrodes to create large coherent states up to ≈ 10000 phonons [174].

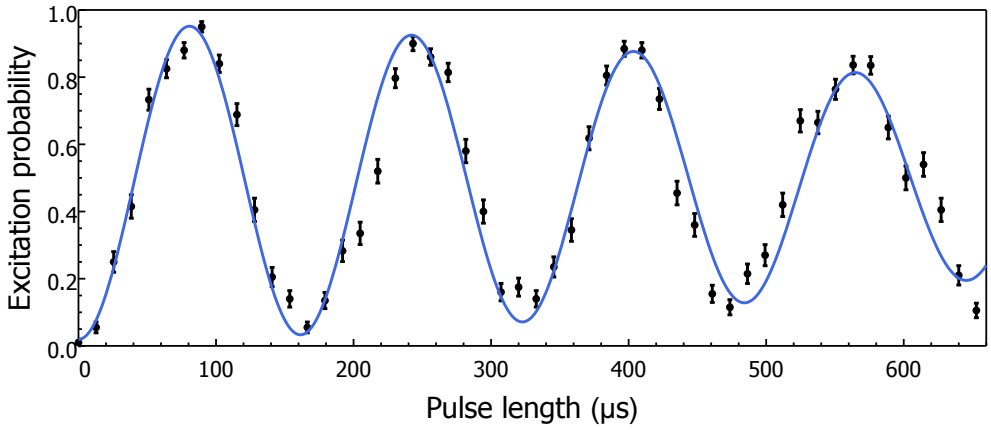

Figure 6.34: Rabi Oscillations of the 4^{th} red sideband on a high lying state with a Gaussian distribution of motional states. $\bar{n} = 297.5(2.5)$, $\sigma_n = 11(1)$ and $\Omega_0/2\pi = 15.6(2)$ kHz

Armed with the sideband heating state preparation technique, we turn to preparing motional superpositions on these high lying states. Unlike the ground state, we do not have the convenience of creating all the desired motional state superpositions in the ground state only since any k-th sideband pulse on a superposition of the form $|gn\rangle + |em\rangle$ will drive it to the state $\cos\theta|gn\rangle + e^{i\phi}\sin\theta|e(n \pm k)\rangle + \cos\theta|em\rangle - e^{-i\phi}\sin\theta|g(m \pm k)\rangle$, leaving some residual population in the excited state. As we shall soon see, this type of state preparation will limit the maximum visibility of interferometric fringes at timescales beyond the optical coherence of our system, but does not prevent us from studying the long term decoherence behaviour. First we write the

general form of a superposition state:

$$|\psi_n\rangle = \cos\frac{\pi\Omega_{n,n\pm m}}{2\Omega_{n_c,n_c\pm m}}\left[e^{i\phi_r}\sin\frac{\pi\Omega_{n\pm m,n\pm m\mp k}}{2\Omega_{n_c\pm m,n_c\pm m\mp k}}|en\mp k\rangle + \cos\frac{\pi\Omega_{n\pm m,n\pm m\mp k}}{2\Omega_{n_c\pm m,n_c\pm m\mp k}}|g,n\rangle\right] + \sin\frac{\pi\Omega_{n\pm m,n\pm m}}{2\Omega_{n_c\pm m,n_c\pm m}}\left[-e^{-i\phi_r}\sin\frac{\pi\Omega_{n\pm m,n\pm m\pm k}}{2\Omega_{n_c\pm m,n_c\pm m\mp k}}|gn\pm m\pm k\rangle + \cos\frac{\pi\Omega_{n\pm m,n\pm m\pm k}}{2\Omega_{n_c\pm m,n_c\pm m\mp k}}|e,n\pm m\rangle\right] \tag{6.31}$$

where ϕ_r is the phase of the pulse on the k-th red sideband relative to the initial pulse and n_c is the Fock state corresponding to the mean of the Gaussian distribution of states after heating. This expression is equally valid for preparation on the blue sideband with a simple interchange of $\pm \rightarrow \mp$. For each experimental trial, a slightly different superposition will be created based on the mismatch between the pulse time and Rabi frequency selected to make $\pi/2$ pulses for the n_c state. Furthermore, there is going to be a fundamental unavoidable imbalance in the two arms of the interferometer even when the $n = n_c$ due to the fact that the sideband pulse coupling will be slightly different as seen in the arguments in the second line of 6.31 ($\mp$ instead of $\pm$). To obtain the expected interference pattern, we would need to complete this general interferometry derivation and then average over the distribution of n states. The final expression of this form is not very enlightening, hence we instead assume an ideal Fock state preparation with a carrier $\pi/2$ pulse and a $\pi/2$ pulse on the k-th sideband to derive the shape of the interference pattern and consider all the errors mentioned above as a visibility reduction of the fringes. Starting from 6.31 and adding a period of free evolution T_w where we accumulate a spin dependent phase ϕ_s, we obtain the state:

$$|\psi_{n_c}\rangle = \frac{1}{2}\left[|gn\rangle - e^{-i(\phi_r - k\omega_z T_w)}|gn+k\rangle + e^{i\phi_s}|en\rangle + e^{i(\phi_r+\phi_s-k\omega_z T_w)}|en-k\rangle\right] \tag{6.32}$$

After applying retrieval pulses with phase ϕ_r' and ϕ_c and projecting on to the $|e\rangle$ state we obtain the excitation probability:

$$P_e = \frac{1}{8}\left[4 + \cos(\phi_c - \phi_s) + \cos(\phi_c + 2\phi_r - 2\phi_r' + \phi_s - 2k\omega_z T_w) - 2\cos(\phi_c + \phi_r - \phi_r' - k\omega_z T_w)\right] \tag{6.33}$$

The expression contains two oscillatory terms that depend on the wait time at frequencies $k\omega_z T_w$ and $2k\omega_z T_w$, but only the latter has a dependence on ϕ_s. During the wait time our laser is set to the carrier frequency so $\phi_s = 0$. From our Ramsey experiments in section 6.2.3 we know that this phase becomes randomised on ≈ 1 ms timescale, hence for much longer wait times, we average over this phase, and the excitation probability takes the form :

$$P_e = \frac{1}{2}\left[1 - \frac{1}{2}\cos(\phi_c + \phi_r - \phi_r' - k\omega_z T_w)\right] \tag{6.34}$$

thus we will be limited to oscillations with an ideal maximum visibility of 0.5. The first scheme we implement on the state near the first sideband coupling zero consists of a $\pi/2$ pulse on the carrier followed by a $\pi/2$ pulse on the 3$^{\text{rd}}$ red sideband to prepare the state as shown in figure 6.35. Here we note that the carrier and the red sideband both have a weak coupling strength dependence on n (see figure 6.32): 5.7% and 7% across the region $\pm\sigma_n$ from the fits for the carrier and the 3$^{\text{rd}}$ red sideband respectively. As before, we scan the wait time between the retrieval pulses, but we also include a second interleaved measurement where we set the

phase of the final carrier pulse to $\phi_c = \pi$ before measuring the population of the excited state. A sample of the data is shown in figure 6.36 with the fit of both data sets (blue and gold curves) performed simultaneously to 6.33 using the same parameter set where we allow the amplitudes in front of the cos terms with ϕ_s to vary independently of the amplitude of the term without it, while also allowing ϕ_s and ϕ_c to vary; the red sideband phases are set equal to each other and hence do not contribute in our experiment. The curves reproduce the data very well showing clear interference of $6\omega_z$ and $3\omega_z$ frequencies at short wait times that washes out as the optical coherence time is exceeded leaving only the $3\omega_z$ component. The $\cos(\phi_c - \phi_s)$ term also accurately accounts for the change in offset between the two curves following the π phase shift. Furthermore, the initial total visibility is 85(3)%, attesting to our ability to produce a high contrast fringe pattern despite the fact that we do not have a perfect Fock state preparation.

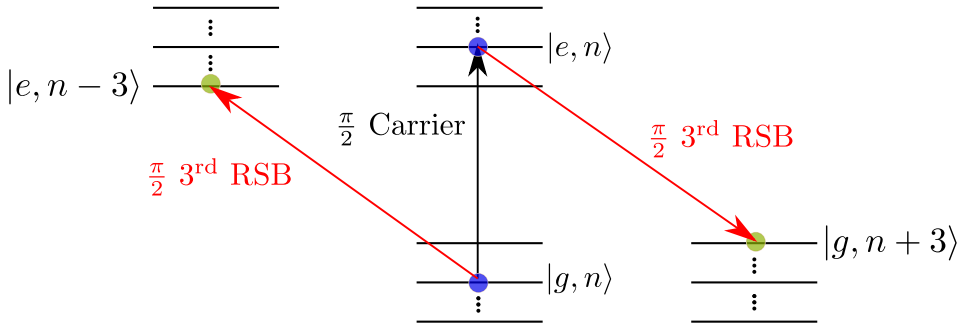

Figure 6.35: Scheme for preparing superpositions at n near the first blue sideband coupling minimum. The interference between the green circles creates a oscillations at $6\omega_z$ as the wait time between the retrieval pulses is incremented, twice the frequency of the oscillations due to the interference of the blue and green circles.

The full visibility data set in figure 6.37 is fitted to a sum of two Gaussian functions yielding an optical coherence time $\tau_{opt} = 0.7(1)$ ms and a motional coherence time of $\tau_{mot} = 160(20)$ ms. Using the noise model where scaling of the coherence time with trap frequency noise depends on the values of $(n-k)^2$ yields $\sigma_\nu = \sqrt{2}/(2\pi(n-k)\tau_{mot}) = 0.45(6)$ Hz, which is in remarkable agreement with the value measured for $\sigma_\nu = 0.40(1)$ Hz in the $|0\rangle + |1\rangle$ superposition state. This result clearly suggests there is no significant scaling with the absolute position of the superposition in the Fock space. We also observe that despite the relatively poorly characterised initial state, our interferometry experiment has proven robust to the variations in the coupling strength of the sidebands used to perform it.

To confirm the above result we took a further data set near the second blue sideband coupling minimum. Examining the coupling strengths near the $\bar{n}$ state in 6.32b suggests using the 1^{st} and 4^{th} red sidebands to prepare the superposition. However, at the time of data collection we decided to try what would happen if we used the 3^{rd} sideband instead given that it has a variation of 10% in coupling strength over $\pm\sigma_n$. The pulse sequence now consists of a $\pi/2$ pulse on the 1^{st} red sideband followed by a $\pi/2$ pulse on the 3^{rd} red sideband to prepare the state that after free evolution takes the form:

$$|\psi_{n_c}\rangle = \frac{1}{2}\left[|gn\rangle - e^{-i(\phi_r - 2\omega_z T_w)}|gn+2\rangle + e^{i(\phi_s - \omega_z T_w)}|en-1\rangle + e^{i(\phi_r + \phi_s - 3\omega_z T_w)}|en-3\rangle\right] \tag{6.35}$$

In this experiment, the laser is set to the first red sideband during the wait time leading to $\phi_s = -\omega_z T_w$ in the absence of dephasing, resulting in an interference pattern that has frequency

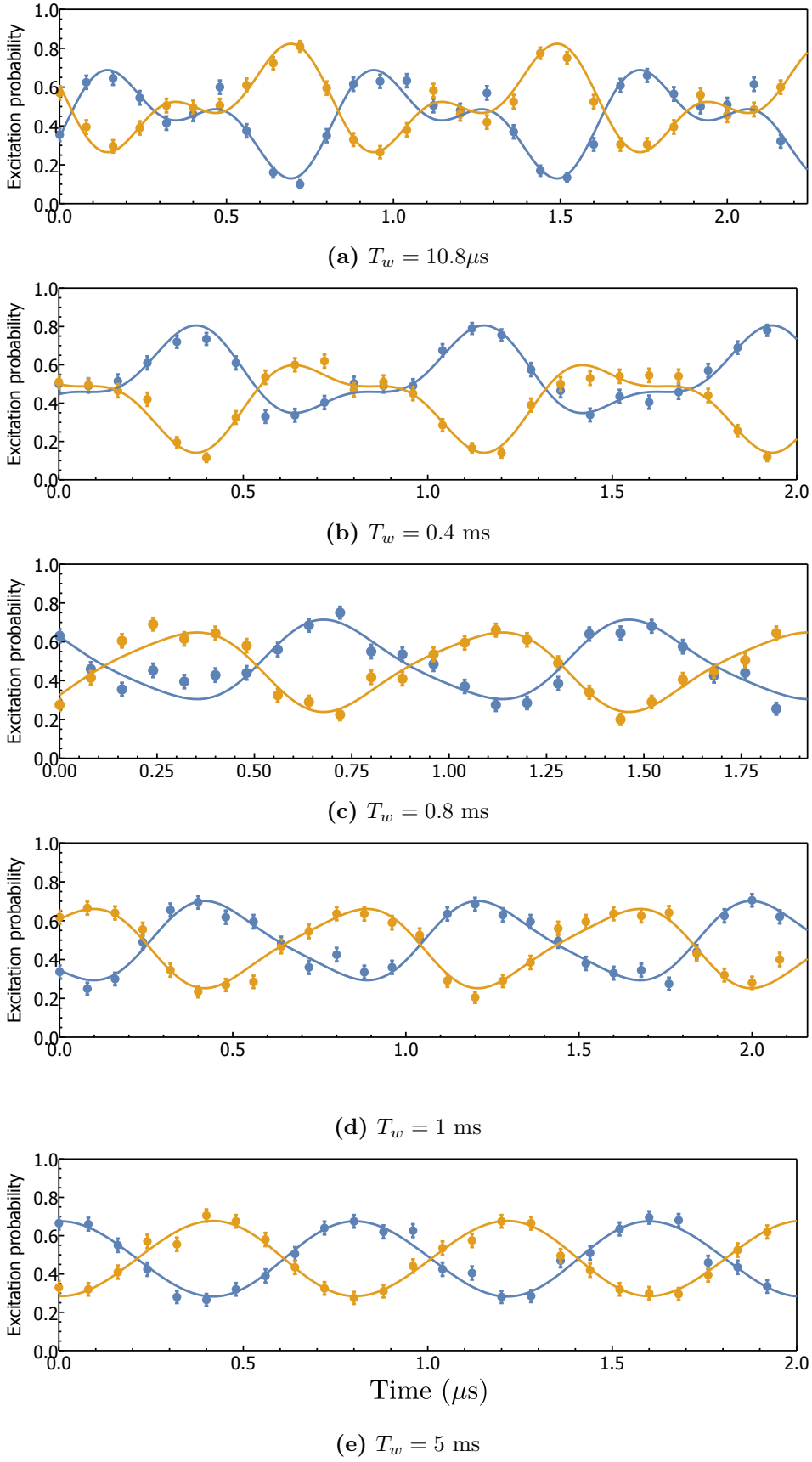

(a) $T_w = 10.8\mu$s

(b) $T_w = 0.4$ ms

(c) $T_w = 0.8$ ms

(d) $T_w = 1$ ms

(e) $T_w = 5$ ms

Figure 6.36: An interleaved set of interference measurements of a $(|gn\rangle + |gn+k\rangle + |en\rangle + |en-k\rangle)/2$ type superposition formed on a state reached after 10 ms of first sideband heating at ν_z= 418 kHz for different wait times T_w. The gold data have a π phase shift applied to the final carrier pulse.

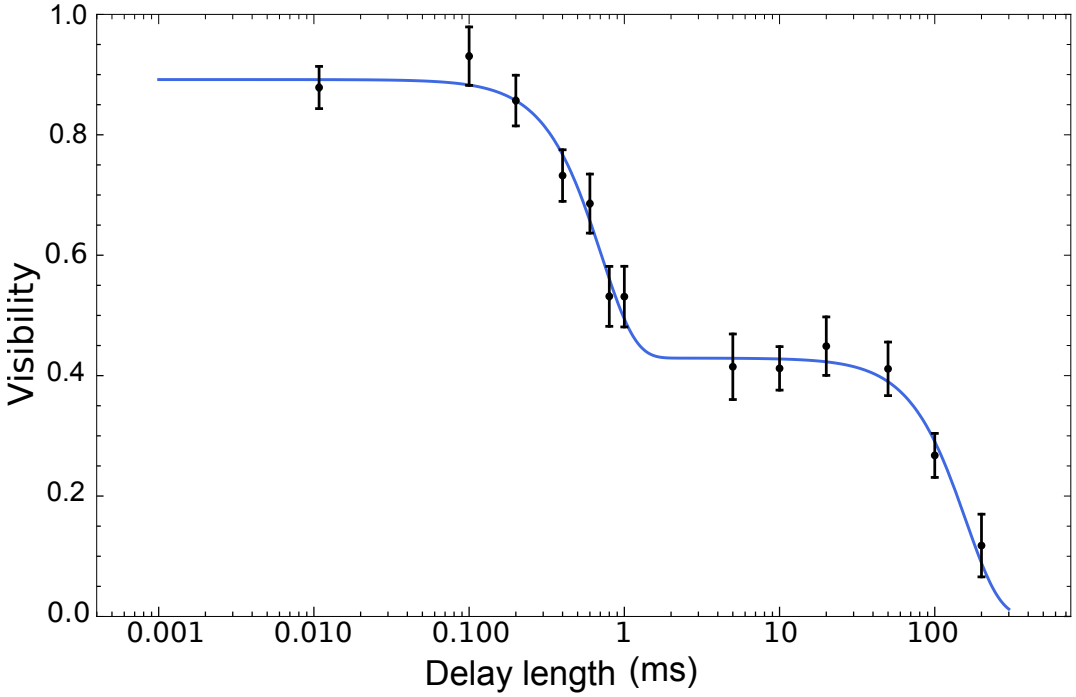

Figure 6.37: Total visibility (average of amplitudes) as a function of wait time for a $(|gn\rangle + |gn+3\rangle + |en\rangle + |en-3\rangle)/2$ type superposition formed on a state reached after 10 ms of first sideband heating at ν_z= 418 kHz. The fit is performed to a sum of Gaussians giving an optical coherence time $\tau_{opt} = 0.7(1)$ ms and a motional coherence time of $\tau_{mot} = 160(20)$ ms.

components at $2\omega_z$ and $4\omega_z$. Once again, the higher frequency component that depends on ϕ_s is washed out after a loss of optical coherence. The full data set is in Appendix C. As done previously, we use a double Gaussian model to fit the total visibility of both components in figure 6.38 measuring $\sigma_\nu = 0.41(4)$ Hz, which is once again in excellent agreement with previous measurements. Thus we have shown without a doubt the consistency of the noise model even when applied to superpositions created on a state distribution with a moderate coupling strength dependence on the phonon number.

6.3.4 Coherent and Squeezed States

Coherent states and squeezed states have garnered significant theoretical [175] and experimental interest over the years. Coherent states have been used to demonstrate purely quantum phenomena in the Jaynes-Cummings model such as the collapse and revival of population oscillations in a single atom maser [176], Bose-Einstein condensate matter waves [177] or superconducting qubits [178]. Superpositions of coherent states are known as Schrödinger cat states with applications as resource in quantum information processing[179, 29], superresolution phase measurement [180] and for studies of decoherence[181]. Squeezed states are useful for improving measurement precision by reducing uncertainty in either the phase or amplitude quadrature of light [182] and similarly can improve sensitivity in atom interferometry [183]. While coherent states squeezed states and cat states are not novel by themselves and have all been successfully realised in ions [181, 184, 174] we are motivated to study them for two reasons:

- The bichromatic (simultaneous addressing at two optical frequencies) interaction that we use to create these states is the same type of control pulse that is required to realise a

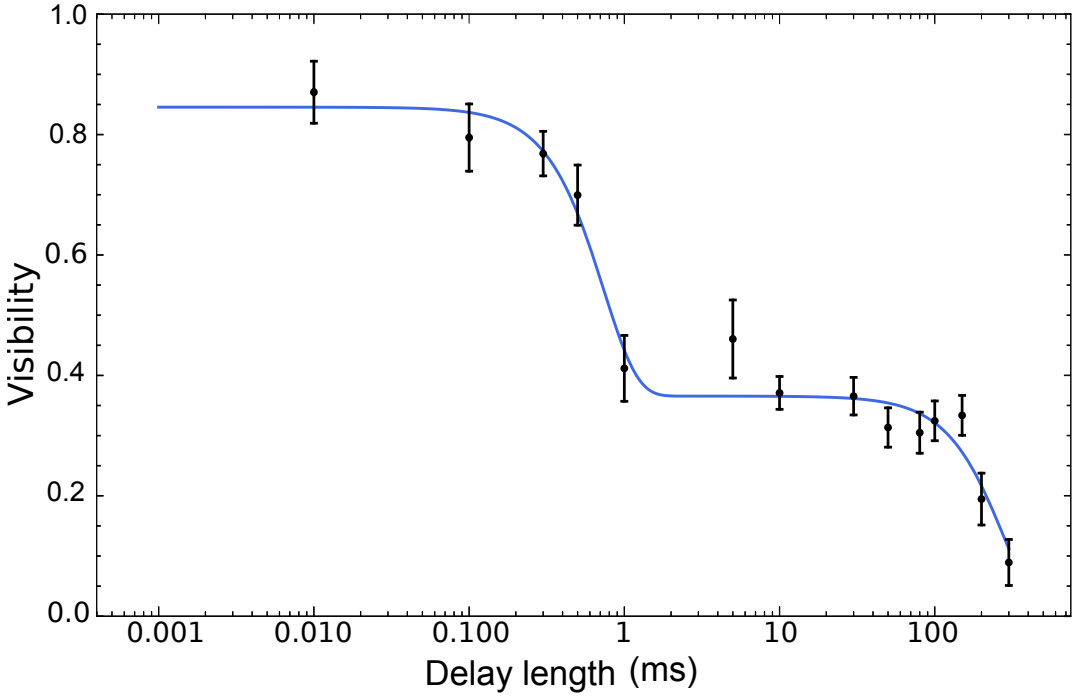

Figure 6.38: Total visibility (average of amplitudes) as a function of wait time for a $(|gn\rangle + |gn+2\rangle + |en-1\rangle + |en-3\rangle)/2$ type superposition formed on a state reached after 10 ms of first sideband heating, followed by 20 ms of second sideband heating at ν_z= 418 kHz. The fit is performed to a sum of Gaussians giving an optical coherence time $\tau_{opt} = 0.74(4)$ ms and a motional coherence time of $\tau_{mot} = 270(30)$ ms.

Mølmer-Sørensen type entangling gate, which remains a long term goal of our research group, both as a demonstration of the Penning trap's capabilities in the field of quantum information as well as for future research into more complicated poly-chromatic sequences that can be made faster and more robust against errors.

- The ability to create coherent displacements allows us to map out the density matrix of the motional states allowing us to more precisely characterise the states we can create through our sideband heating method as well as to map out the Wigner function according to the scheme by Leibfried et. al. [173].

Starting from the interaction picture Hamiltonian from equation 4.8 and expanding it assuming we are in the Lamb-Dicke regime keeping only terms resonant with the first order red and blue sidebands yields the Hamiltonian:

$$\begin{aligned} H_B =& \hbar\eta\Omega_0 \left[\sigma_x \cos\left(\frac{\phi_r+\phi_b}{2}\right) - \sigma_y \sin\left(\frac{\phi_r+\phi_b}{2}\right)\right. \\ & \left. \otimes \left((a+a^\dagger)\cos\left(\frac{\phi_b-\phi_r}{2}\right) + i(a^\dagger - a)\sin\left(\frac{\phi_b-\phi_r}{2}\right)\right)\right] \end{aligned} \tag{6.36}$$

with phases ϕ_r, ϕ_b for the red and blue sidebands respectively. [184]. Written in this form, we can recognize the position and momentum operators $2\hat{z} = a + a^\dagger$, $2i\hat{p}_z = a - a^\dagger$. The displacement operator that creates a coherent state is defined as:

$$D(\alpha) = e^{\alpha a - \alpha^\star a^\dagger} \tag{6.37}$$

It is easy to see that if we exponentiate the Hamiltonian, we will obtain a propagator of the same form with the magnitude of the coherent state given by $|\alpha| = \eta\Omega t/z_0$ and a complex phase dependence on ϕ_r and ϕ_b that can sweep out the complete $z - p$ plane.

Experimentally, we generate the bichromatic field by directly combining two RF frequencies offset $\pm\Delta$ from the carrier on a resistive power combiner before sending the signal through an amplifier to the spectroscopy AOM. The biggest limitation of our experimental capabilities is a result of the fact that we cannot synthesise both frequencies from one master DDS with full digital phase/power control of both signals. Instead one frequency is sourced from the single channel DDS that is controlled from our experimental computer whereas the other is taken from a standalone HP function generator that requires manual tuning of parameters. The two frequencies are phase locked using a 10 MHz master clock, but we cannot modify the phase on a timescale relevant to the experiment. This prevents us from being able to vary the complex phase of α and hence we are limited to the scenario $\phi_b = \phi_r = 0$, which gives us a state dependent propagator:

$$U_B(t) = e^{-i|\alpha(t)|(a+a^\dagger)\sigma_x} \tag{6.38}$$

Applying the propagator to a ground state yields:

$$D(\alpha)|g0\rangle = |g\alpha_+\rangle + |e\alpha_-\rangle \tag{6.39}$$

where we create a cat-like superposition of even and odd coherent states $|\alpha_+\rangle, |\alpha_-\rangle$. To create a proper coherent state of the form:

$$|\alpha\rangle = e^{-\frac{\alpha^2}{2}} \sum_{n=0}^{\infty} \frac{\alpha^n}{\sqrt{n!}} |n\rangle \tag{6.40}$$

we need to remove the spin motion entanglement by turning on the 854 nm repump laser to excite the population in $|en\rangle$ to the $P_{3/2}$ state and return to the ground state through spontaneous decay. Since multiple transitions can occur if a decay to the wrong Zeeman sub-level occurs requiring further repumping, the ion has an appreciable chance to change motional state spoiling the fidelity of our coherent state hence we need to work at high trap frequency to minimise the Lamb-Dicke parameter[7]. We will not attempt to fully quantify this behaviour, but qualitatively the resulting effect should be a spreading of the state, resulting in a super-Poissonian distribution in n.

To generate a coherent state, we prepare an ion in the motional ground state by sideband cooling then apply the bichromatic interaction for 150 μs and finally add a 200 μs 854 repump pulse. To verify the creation of the state, we then drive Rabi oscillations on the first blue sideband since it has a much stronger frequency dependence on n than the carrier. The resulting oscillations can be modelled with a sum of oscillations weighted by the Poissonian distribution:

$$P_e = \sum_{n=0} e^{-\alpha^2} \frac{\alpha^{2n}}{2n!} \left(1 - e^{-t^2/\tau_g^2} \cos\Omega_{n,n+1} t\right) \tag{6.41}$$

Alternatively, we can assign a free coefficient to each frequency term and allow the fit to reconstruct the weight of all the frequency components. The data fitted using both models is shown in figure 6.39a with the frequency decomposition shown in 6.39b. We first note the expected qual-

[7]See section 4.4.2 for a discussion of the factors involved

itative behaviour of a coherent state, where the oscillation contrast collapses after $\approx 200\mu$s, but then revives at $\approx 400\mu$s. The fit to the model of equation 6.41 yields a value of $\alpha = 1.729(22)$, with only a slight mismatch to the fit from the frequency decomposition curve. In 6.39b we can see that the distribution appears slightly broadened compared to a true Poissonian, most likely as a consequence of the incoherent transfer of the excited state population to the ground state. A Poissonian distribution fit to the population gives $\alpha = 1.731(21)$ in excellent agreement with the first method. The mean phonon number is then $\bar{n} = \alpha^2 = 3.00(7)$.

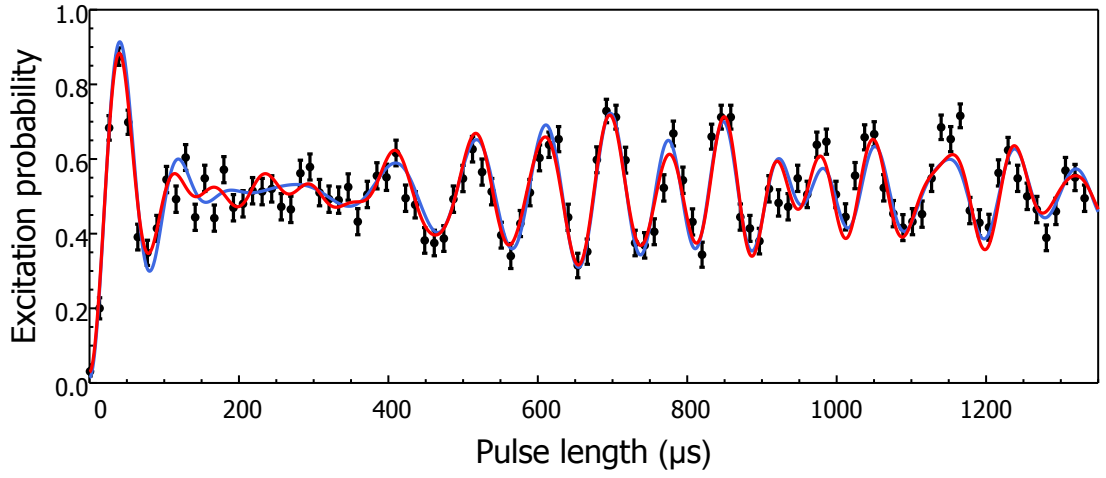

(a)

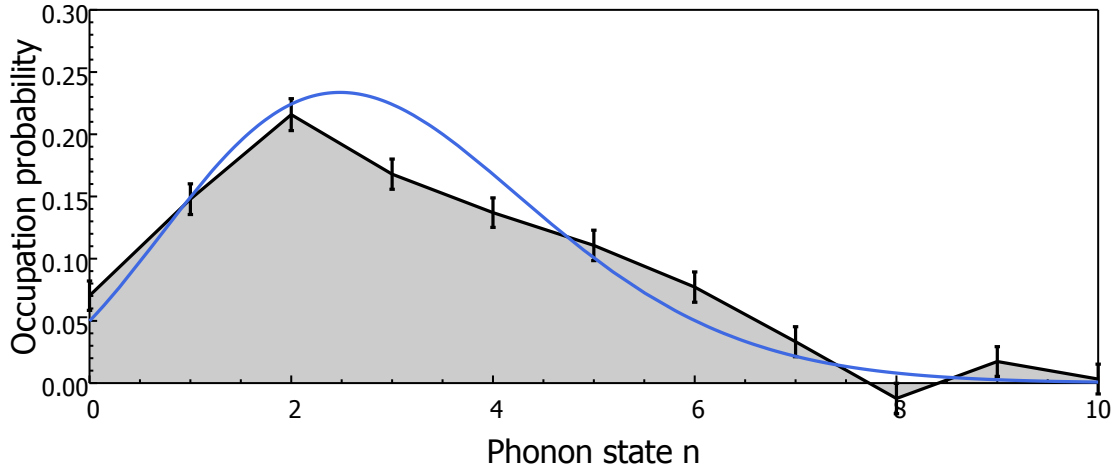

(b)

Figure 6.39: (a) - Blue sideband Rabi oscillations on a coherent state prepared with a 150 μs bichromatic pulse length. The curve in blue is fitted to equation 6.41 giving $\alpha = 1.729(22)$, while the curve in red is fitted to a model where all the cos coefficients are free to vary. Both sum are truncated at $n = 10$. The coefficients of this model are shown in (b) with a fit to a Poissonian distribution yielding $\alpha = 1.731(21)$.

While we have demonstrated that we can create a phonon distribution that appears to match one expected of a coherent state, a more rigorous test would be to perform interferometric Ramsey type experiments on our initial cat state. Unfortunately, the incoherent spin-recombination method destroys any phase information and ruins the measurement. To prove that we are indeed creating a coherent state and not just exciting the ion into a mixed state that mimics one, we slightly detune the bichromatic beam symmetrically from the sidebands. This results in the

ion being driven in a loop in phase space, analogous to an off resonant classical driving of a harmonic oscillator where at a time $2\pi/\Delta$ the state will be returned back to the origin [185]. Thus if we show that the ion returns back to the ground state we will have definite proof that we are indeed performing a coherent displacement pulse. To show this experimentally, we sweep the pulse length of the detuned bichromatic beam and after recombination of the electronic states probe for $t_p = 4\pi/\Omega_{0,0}$ on the carrier or $t_p = \pi/\Omega_{0,1}$ on the first blue sideband. As the ion gets driven to a larger value of $|\alpha|$ the excitation probability for each pulse will change in accordance with the variation of Rabi coupling strength with phonon number. For any given coherent state we can use equation 6.41 to predict the expected excitation for both pulses and hence map out the evolution of $|\alpha|$ with time. The general behaviour of $|\alpha(t)|$ needs to be sinusoidal with frequency $\dot{\alpha}_1$, but drifts in the laser intensity provide a further modulation of the driving force which we include empirically with a $\dot{\alpha}_2$ frequency to give the form:

$$|\alpha(t)| = \alpha_{max} \sin(\dot{\alpha}_1 t)(1 + \sin(\dot{\alpha}_2 t)) \tag{6.42}$$

The largest coherent displacement α_{max} is a function of Ω_0 and Δ, but here we will just measure it empirically. The experimental data is presented in figure 6.40 and show a clear reflection at $\approx 940\mu$s. At this point a coherent state with $\alpha_{max} = 7.0(1)$ is reached. Return to the ground state, which occurs at $\approx 1880\mu$s, is not with perfect fidelity due to frequency noise in our system and the additional heating effects of the spin transfer to the ground state. Despite this, it is incontrovertible proof that we are indeed applying a coherent displacement because if we were simply heating, we would not see the symmetry of excitation about a particular point on both the carrier and blue sideband simultaneously as their coupling strengths will change at different rates.

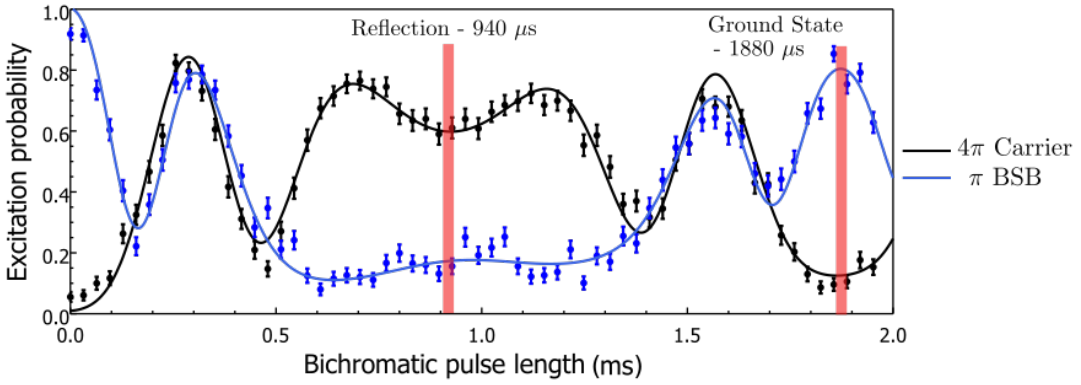

Figure 6.40: Excitation probability for two fixed probe pulses set to the probe the carrier and first blue sideband with pulse angles of $4\pi/\Omega_{0,0}$ and $\pi/\Omega_{0,1}$ respectively as a function of an off-resonant bichromatic drive. The data are fitted to the excitation probability of equation 6.41 with the time dependent $\alpha(t)$ from equation 6.42 substituted in. The averaged parameters from both fits are: $\dot{\alpha}_1 = 1.68(1), \dot{\alpha}_2 = -0.018(2), \alpha_{max} = 7.0(1)$. The bichromatic drive detuning is estimated to be $\Delta = 3.3(1)$ kHz.

The final demonstration in this chapter is the application of the bichromatic beam resonantly to the second order sidebands which acts as a squeezing operator[186]:

$$S(\xi) = e^{(\xi^\star a^2 - \xi a^{\dagger 2})/2} \tag{6.43}$$

where we have the squeezing parameter $\xi = re^{i\phi}$. Applying the displacement operator to the ground state once again creates a spin-motion entanglement so we use the 854 repump to bring all the population to the ground electronic states after which we would have in an ideal case a phonon distribution without any odd states populated:

$$S(\xi)|0\rangle = \frac{1}{\sqrt{\cosh r}} \sum_{n=0} \tanh^{2n}(r) \frac{(2n!)}{(2^n n!)^2} |2n\rangle \tag{6.44}$$

As before, we analyse the data by fitting to a sum over the Rabi oscillation functions weighted by the above distribution and compare the results to a fit where all the Fock state occupation amplitudes are floated, even the odd ones. Figure 6.41a shows data of Rabi oscillations on the first blue sideband after a 900 μs bichromatic pulse. Unlike the coherent state, we do not see any identifiable pattern that immediately identifies it as a squeezed state. Based on the fit to the distribution we obtain a squeezing parameter of $|r| = 1.76(3)$. To really see the squeezing in action, the decomposition in the Fock basis in 6.41b shows the characteristic suppression of the odd motional states. There also seems to be excess population in higher states than expected, potentially due to the power of the beams being imbalanced. In conclusion, we have demonstrated the ability to create a bichromatic laser pulse that can effectively drive first and second order sidebands to create non-classical motional states. The measured fidelity of the states is limited by both the preparation method due to the previously documented laser intensity noise and qubit dephasing, and the detection due to motional state change upon electronic state re-combination.

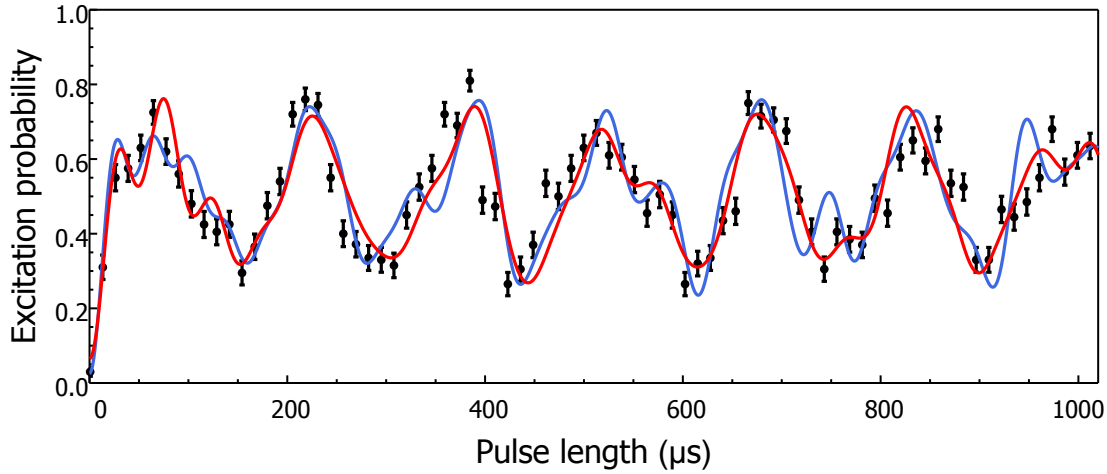

(a)

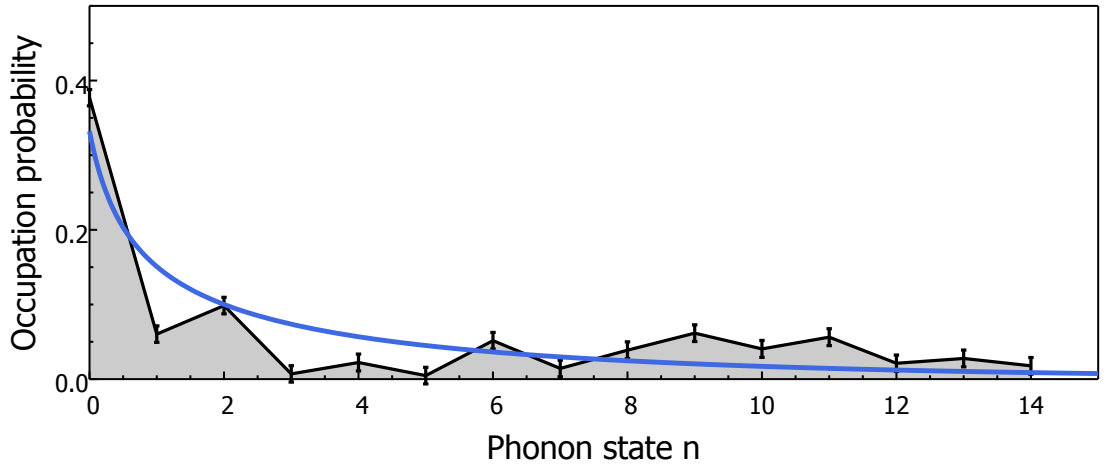

(b)

Figure 6.41: (a) Blue sideband Rabi oscillations on a squeezed state prepared with a 900 μs bichromatic pulse length. The curve in blue is fitted to a sum of Rabi oscillation functions weighted by the distribution in equation 6.44 giving $|r| = 1.76(3)$, while the curve in red is fitted to a model where all the amplitudes are free to vary. The sum in the blue curve is truncated at $n = 70$ whereas for the red model states up to $n = 15$ are included. Based on the estimated r parameter, up to 7% of the population might reside above this cutoff. The coefficients of this model are shown in (b) with a fit to the distribution of equation 6.44 yielding $|r| = 1.81(3)$.

CHAPTER 7

SIDEBAND COOLING OF COULOMB CRYSTALS

Ion Coulomb crystals are promising candidates for the development of a digital quantum information processor [187, 188]. The most common architecture currently implemented consists of a linear string of ions where each ion is spatially well separated so that it can be addressed by a laser beam to perform single qubit rotations and its state read out with high fidelity, while global beams that overlap with the whole chain excite the motional modes to generate entanglement – a fundamental resource for computation [36, 189]. Although entanglement can be generated on low $\bar{n}$ thermal states [190], all scalable schemes rely on the motional mode of the computation ions being cooled to near the ground state for optimal entanglement fidelity. In this chapter we will demonstrate for the first time sideband cooling of a two ion chain in a Penning trap. We perform the cooling starting from thermal state with population outside the Lamb-Dicke regime where we have strong coupling on higher order motional sidebands. The technique described here is equally applicable to RF or Penning traps and may motivate further work in this regime where stronger coupling to the motional sidebands can lead to faster gate operation.

Coulomb crystals, specifically 2D planar crystals with hundreds of ions created in Penning traps, have also been successfully used in quantum simulation experiments of the Ising interaction [56, 108] and spin-squeezing entanglement [57]. In the second part of this chapter we will demonstrate ground state sideband cooling of the axial modes of these planar crystals of up to 15 ions opening up the possibility of running similar simulations, create entanglement [54] or performing quantum computation [53].

7.1 Interaction of two ions with laser light

In this section we will describe the coherent dynamics of two ions when probed with a narrow linewidth laser on either the carrier, red or blue sideband after sideband cooling. Starting from the N ion Hamiltonian in equation 4.39 and taking the Lamb-Dicke approximation[1] to simplify

[1]Since we will only need to consider motional states up to $n = 4$ to study behaviour after sideband cooling with reduced Lamb-Dicke parameters we estimate that in the worst case that we analyse – COM mode at $\nu = 161$ kHz, $\bar{n} = 1$ – the average Rabi frequency error is 0.7%

expression 4.38 we can write the interaction Hamiltonian:

$$\begin{aligned} H_I =& \frac{\hbar\Omega_0}{2}\sum_{j=1}^{2} e^{i(\Delta_j t+\phi_j)}|e_j\rangle\langle g_j|\Big[(1-\eta_n^2(n+\frac{1}{2})-\eta_m^2(m+\frac{1}{2}))|n,m\rangle\langle n,m| \\ &+i\eta_n(e^{i\omega_n t}\sqrt{n}|n-1,m\rangle\langle n,m|+e^{-i\omega_n t}\sqrt{n+1}|n+1,m\rangle\langle n,m|) \\ &+(-1)^j i\eta_m(e^{i\omega_m t}\sqrt{m}|n,m-1\rangle\langle n,m|+e^{-i\omega_m t}\sqrt{m+1}|n,m+1\rangle\langle n,m|)\Big] \\ &+h.c. \end{aligned} \tag{7.1}$$

The first case to consider is when the laser is tuned to the carrier transition. In this situation only the term appearing in the first line is resonant and since there is no change in motional state, there is also no spin-motion entanglement. This means that the two ions evolve independently. If we instead try to drive the red or blue sideband of one mode, the excitation probability of one ion is conditional on the excitation of the other since the motional state and hence coupling strength changes as soon as one ion spin is flipped. This results in a weak form of spin-motion entanglement which modifies the dynamics. To solve for the dynamics we will consider the ions evolving in the basis $\{|ee,n\pm2\rangle,|eg,n\pm1\rangle,|ge,n\pm1\rangle,|gg,n\rangle\}$ when driven on the n mode first order sidebands. The Hamiltonians for the blue and red sidebands can then be written as matrices:

$$H_{b,n}=\frac{i\eta_n\hbar\Omega_0}{2}\begin{bmatrix} 0 & -e^{-i(\Delta_1 t+\phi_1)}\sqrt{2+n} & -e^{-i(\Delta_2 t+\phi_2)}\sqrt{2+n} & 0 \\ e^{i(\Delta_1 t+\phi_1)}\sqrt{2+n} & 0 & 0 & -e^{-i(\Delta_2 t+\phi_2)}\sqrt{1+n} \\ e^{i(\Delta_2 t+\phi_2)}\sqrt{2+n} & 0 & 0 & -e^{-i(\Delta_1 t+\phi_1)}\sqrt{1+n} \\ 0 & e^{i(\Delta_2 t+\phi_2)}\sqrt{1+n} & e^{i(\Delta_1 t+\phi_1)}\sqrt{1+n} & 0 \end{bmatrix} \tag{7.2}$$

$$H_{r,n}=i\eta_n\frac{\hbar\Omega_0}{2}\begin{bmatrix} 0 & -e^{-i(\Delta_1 t+\phi_1)}\sqrt{n-1} & -e^{-i(\Delta_2 t+\phi_2)}\sqrt{n-1} & 0 \\ e^{i(\Delta_1 t+\phi_1)}\sqrt{n-1} & 0 & 0 & -e^{-i(\Delta_2 t+\phi_2)}\sqrt{n} \\ e^{i(\Delta_2 t+\phi_2)}\sqrt{n-1} & 0 & 0 & -e^{-i(\Delta_1 t+\phi_1)}\sqrt{n} \\ 0 & e^{i(\Delta_2 t+\phi_2)}\sqrt{n} & e^{i(\Delta_1 t+\phi_1)}\sqrt{n} & 0 \end{bmatrix} \tag{7.3}$$

These Hamiltonians can only be solved analytically if they are made time independent, requiring the detuning for both ions to be zero. To illustrate the spin-motion entanglement, the state wavefunction can be found easily by solving the Schrödinger equation with the above Hamiltonian for a resonant blue sideband pulse of length t with the population initialised in $|gg,n\rangle$:

$$\begin{aligned} |\psi\rangle =& \frac{2+n+(1+n)\cos\Omega_B t}{3+2n}|gg,n\rangle-\sqrt{\frac{1+n}{6+4n}}\sin\Omega_B t\left(e^{i\phi_1}|ge,n+1\rangle+e^{i\phi_2}|eg,n+1\rangle\right) \\ &+e^{i(\phi_1+\phi_2)}\frac{\sqrt{(n+1)(2+n)}}{3+2n}(1-\cos\Omega_B t)|ee,n+2\rangle \end{aligned} \tag{7.4}$$

where $\Omega_B=\sqrt{\frac{3+2n}{2}}$. If we now apply a pulse $t=\pi/\Omega_B$ to maximise the excitation probability of the $|ee,n+2\rangle$ term, we see that for $n=0$ we only get $|\langle ee,2|\psi\rangle|^2=8/9$ with the remaining

population in the $|gg, 0\rangle$ state. Thus unlike for carrier oscillations we will never achieve full population transfer and for accurate sideband profile modelling this entanglement needs to be included.

Outside the Lamb-Dicke regime, the entanglement becomes negligible and the excitation on each sideband is well approximated by a single ion lineshape with the correct $\Omega_{n,k,n',k'}$ Rabi frequency. For a thermally distributed state we then get an excitation lineshape on a single ion:

$$P_e = \sum_{k=0}^{\infty}\sum_{n=0}^{\infty} \frac{\bar{n}^n}{(\bar{n}+1)^{n+1}} \frac{\bar{k}^k}{(\bar{k}+1)^{k+1}} \frac{\Omega^2_{n,k,n',k'}}{\Omega^2_{n,k,n',k'}+\Delta^2} \sin^2\left(\frac{\sqrt{\Omega^2_{n,k,n',k'}+\Delta^2}}{2}t\right) \tag{7.5}$$

For a double excitation, this expression is simply multiplied by the excitation lineshape of the other ion.

7.2 Two Ion 1D Chain Cooling

7.2.1 Doppler and Sideband Cooling

When we work at sufficiently low trapping potential, the ions will align in a one dimensional chain along the magnetic field axis. In principle, as soon as the condition[191] $6\nu_z^2/\nu_c^2 < 1$ ($\nu_z = 298$ kHz for our system) is fulfilled the axial chain configuration becomes energetically allowed, but empirically we see that the trapping frequency needs to be significantly lower ($\nu_z \lesssim 200$ kHz) to achieve stability against transition to the radial plane configuration. We can understand this when we consider the criterion for forming planar crystals:

$$\beta = \frac{\nu_z^2}{\nu_{eff}^2} = \frac{\nu_z^2}{\nu_c\nu_r - \nu_r^2 - \frac{1}{2}\nu_z^2} \gg 1 \tag{7.6}$$

There is always some value of the planar crystal rotation frequency ω_r that will bring the denominator very close to zero and hence make the whole expression much larger than one. In our experiment this corresponds a very low rotation frequency $\nu_r \approx \nu_-$. Thus if at any time the ions get perturbed out of a chain, for example by a collision with a background gas particle, we require the effective radial trapping frequency to be large to allow the ions to fall back into a chain. In between the radial beam laser parameters such as spatial offset, detuning and intensity as well as the strength of the axialization drive we have many degrees of freedom that can affect the stability of the chain as they all contribute to the torque felt by the crystal which in turn affects ν_r. The lower the frequency ν_z is set, the smaller the range of ν_r values for a stable radial crystal and thus the weaker the constraints on the above parameters becomes. In general, we wish to increase ν_r to increase stability by imparting more torque, hence we need a larger scattering rate difference between when the ions are moving away from the laser than when they are moving towards it implying a larger beam offset, and frequency detuning closer to resonance. Because we do not have independent frequency control between the radial and axial 397 nm Doppler cooling beams, the range where we can effectively cool the axial motion while retaining stability is again narrowed.

Taking all the above limitations into consideration and contrasting with the fact that if we work at very ν_z frequencies sideband cooling will become more and more difficult, we settled on a trap frequency of $\nu_z = 162$ kHz to perform the demonstration of sideband cooling. We remind

ourselves that in this configuration we have two modes of motion, the centre of mass mode at ν_z and the breathing mode at $\sqrt{3}\nu_z$ with corresponding Lamb-Dicke parameters η_{COM} and η_B given by:

$$\eta_{COM} = \frac{\eta}{\sqrt{2}}, \quad \eta_B = \frac{\eta}{\sqrt{2\sqrt{3}}}, \tag{7.7}$$

Figure 7.1 shows a typical two ion chain as seen through our EMCCD imaging system. Before

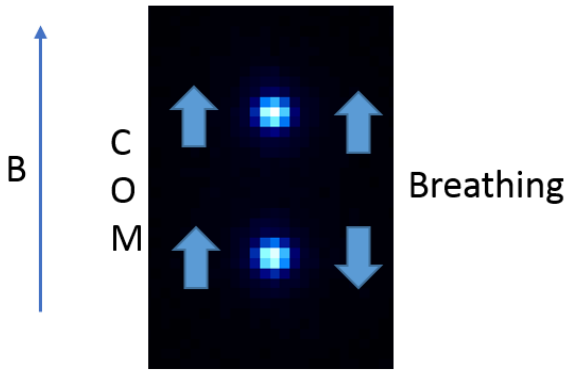

Figure 7.1: EMCCD image of two ions in a chain along the magnetic field B with two modes of oscillation highlighted. Taken at axial endcap potential of 50 V, $\nu_z = 187$ kHz. Scale - approximately 1 μm per pixel.

sideband cooling we typically Doppler cool for 15 ms with the standard 397 nm detunings of $\Gamma/2$, but we use a much higher axialization drive amplitude of 2 V compared to the single ion case. Figure 7.2 shows a representative spectrum after Dopppler cooling, with a dense forest of sidebands due to the low ν_z frequency and Lamb-Dicke parameters of $\eta_{COM} = 0.17$ and $\eta_B = 0.13$. From the fit we obtain $\bar{n}_{COM} = 89(4)$ and $\bar{n}_B = 45(2)$, both of which are approximately 1.5 times above the Doppler limit. This is most likely a consequence of the detuning of the cooling beams being set closer to resonance to maintain chain stability. Despite this, the number of phonons does not pose an insurmountable problem; we can still resolve individual sidebands and hence design a sequence of sideband cooling pulses that picks out different red sidebands of either mode in turn to cool both modes to near the ground state.

The issue with cooling a two ion crystal starting from outside the Lamb-Dicke regime have been discussed at length in section 4.4.1. Broadly speaking, we wish to address a set of sidebands that will, on average, always have some appreciable coupling across the 2D coupling map as in figure 4.13e. To find the length and order of application to obtain the highest cooling efficiency, our efforts were guided by Monte-Carlo simulations described in detail in the thesis of M. Joshi and a paper that is in preparation. Motivated by these results and refined by empirical trials, we designed a 35 ms long cooling sequence that avoids trapping in the sideband coupling minima Fock states involving three COM sidebands and two breathing mode sidebands as well as an intermodulation sideband that changes the motional state of both modes simultaneously. Table 7.1 lists all the pulses in detail for the scheme that we used. Figure 7.3 shows a spectrum of one of the ions as recorded on an EMCCD camera after applying this sequence to a Doppler cooled ion resulting in a greatly simplified spectrum where the first order red sidebands are strongly suppressed compared to the blue sidebands, suggesting a high ground state occupation for both. To extract the $\bar{n}$ from the sideband heights we assume a thermal distribution among the five lowest Fock states of each mode and construct the lineshapes around the sidebands

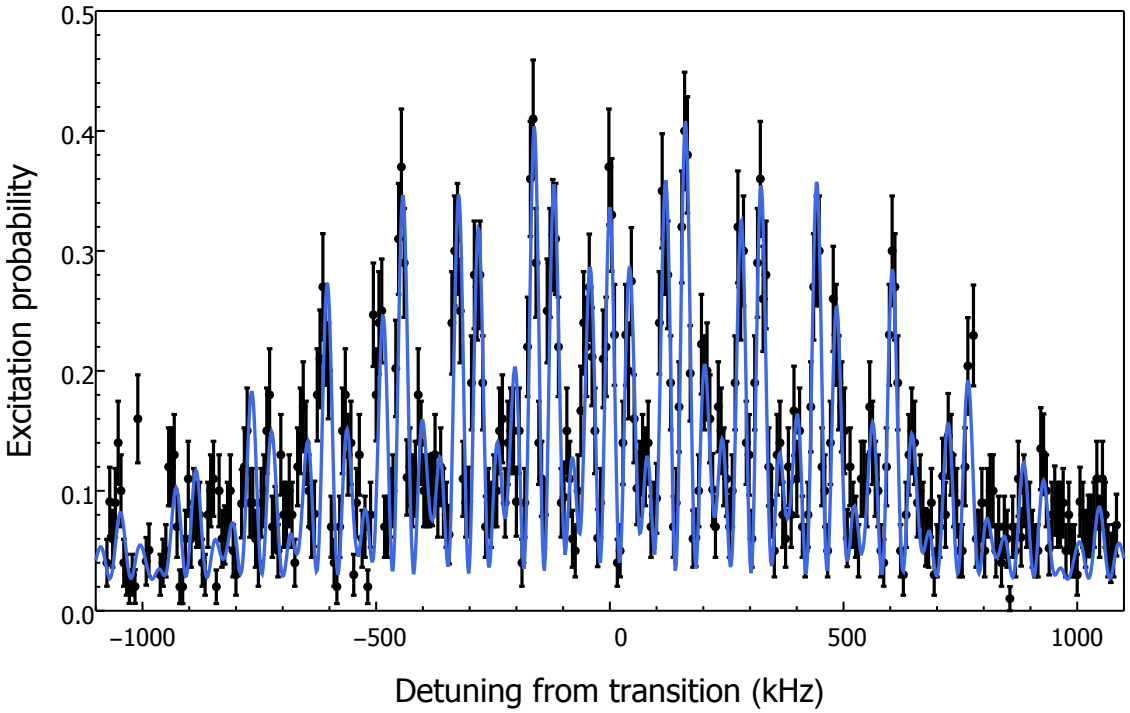

Figure 7.2: Spectrum after a 40 μs probe of one ion obtained from an EMCCD, after Doppler cooling a two ion chain at $\nu_z = 162$ kHz. A fit was performed by considering 5 COM and 4 breating mode sidebands and all their combinations with lineshapes given by equation 7.5. The sums are truncated at $n_{COM} = 300$ and $n_B = 200$ and the Rabi frequency is fixed to $\Omega_0/2\pi = 28$ kHz. The mean occupational numbers are found to be $\bar{n}_{COM} = 89(4)$ and $\bar{n}_B = 45(2)$

by numerically integrating the Hamiltonians of 7.3 to correctly account for the spin-motion entanglement and calculating $P_e = |eg|^2 + |ee|^2$ for one ion and $P_e = |ge|^2 + |ee|^2$ for the other, where we allow for a different detuning between the two ions since their transition frequencies are not equal. The carrier excitation is fitted according to standard single ion dynamic 6.1.

By averaging the parameter values across the fits to both ions, we determine the final mean occupation numbers to be $\bar{n}_{COM} = 0.30(4)$ and $\bar{n}_B = 0.07(3)$. The breathing mode value is consistent with the cooling limit of $\bar{n}_B = 0.04$ derived from the numerical simulation ($\Omega_0/2\pi = 40$ kHz, $\tilde{\Gamma}/2\pi = 50$ kHz) in section 4.4.2, while the COM value is slightly higher than the simulated value of $\bar{n}_{COM} = 0.13$ due to reheating on the final breathing mode pulse. These results show that we can reliably cool two ions in a chain to the ground state in approximately 35 ms.

While the sequence works well for two ions there are many challenges to scaling this procedure to multiple ions. Firstly, the more ions are added, the less likely they are to stay in a 1D configuration at a particular value of the endcap potential. To maintain stability, the potential needs to be relaxed further, which increases the density of sidebands making them harder to pick out without off resonant excitation that can heat other modes, makes population trapping more problematic and increases the total number of phonons in the system for a given Doppler cooled temperature. Furthermore, the scheme is already slow relative to coherent operation timescales and cooling more modes is going to make it even slower. One encouraging fact is that the Lamb-Dicke parameter for the COM mode scales as $\eta/\sqrt{N}$ and the additional higher order modes will appear at higher frequencies with smaller Lamb-Dicke parameters. With enough

Repeats	Sideband	Pulse length (μs)
15×	2^{nd} COM	500
	2^{nd} B	500
	3^{rd} COM	300
	1^{st} B	200
	2^{nd} COM-1^{st} B	200
2×	1^{st} B	200
	2^{nd} COM	500
	1^{st} COM	200
	2^{nd} COM-1^{st} B	200
1×	2^{nd} COM-1^{st} B	500
	1^{st} COM	2000
	1^{st} B	500

Table 7.1: 35 ms sideband cooling sequence for two ions in a chain

effort and clever pulse design, few ion chain cooling might be attainable in the near future, but longer chains will remain the domain of RF traps, where much higher motional frequencies can be attained.

7.2.2 Heating rate and Coherent Driving

We measure the heating rates of the crystal using the standard technique of inserting a delay between the end of the cooling and the probe pulse as described in section 6.3.1. The fits in figures 7.4a and 7.4b suggest heating rates of $\dot{\bar{n}}_{COM} = 9(4)\ \mathrm{s}^{-1}$ and $\dot{\bar{n}}_B = 0.7(8)\ \mathrm{s}^{-1}$. The heating rate of the breathing mode is consistent with zero, with the error larger than the measured value. Even with a wait time of 100 ms we weren't able to measure a significant increase in $\bar{n}_B$ and extending the length of the wait time makes the experimental acquisition time too long to keep all parameters stable. This low heating rate is consistent with the fact that the breathing mode only couples to out-of-phase noise on the end cap electrodes, which suppresses the heating. On the other hand, the COM heating rate is almost an order of magnitude larger than the single ion heating rate. This suggests that the breathing mode is more suitable for performing operations such as entangling gates.

One of the biggest issues with performing coherent operations on the sideband cooled ion chain is the field inhomogeneity along the axis leading to different Zeeman shifts of the $S_{1/2}$ and $D_{5/2}$ levels and subsequently different carrier transition frequencies for the ions. In a Rabi oscillation on the carrier, this difference is not easily observed for Ω_0 larger than the shift frequency. To accurately measure this separation, we perform a Ramsey experiment as in section 6.2.3, and fit the excitation of the two ions separately as seen in figure 7.5. The difference in carrier frequencies obtained from the fit is 2.16(1) kHz, giving us a gradient of 0.01 T/m. This splitting is particularly problematic when we try to drive sideband transitions, which are necessary for performing entangling gates. In figure 7.6 we perform a Rabi oscillation on the blue COM mode sideband at $\nu_{COM} = 162$ kHz with $\Omega_0/2\pi = 25.5$ kHz and notice that the quality of oscillations on one of the ions (orange data) is severely compromised when we tune the laser close to resonance with the other ion (blue data), compounded by the average

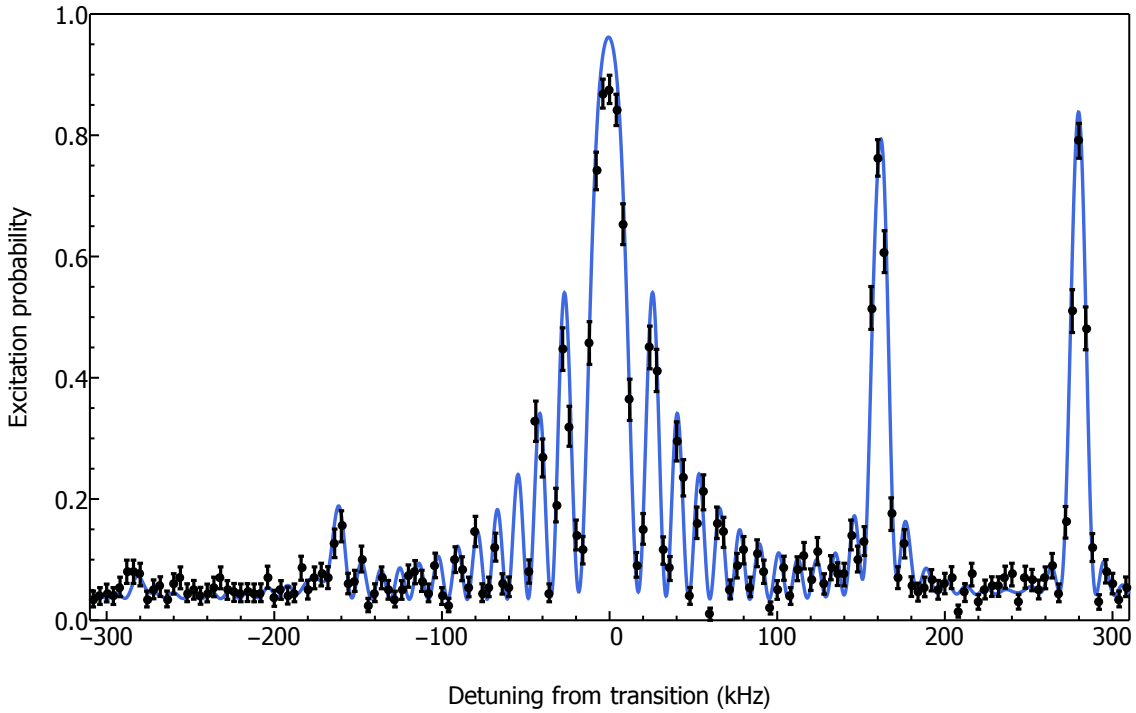

Figure 7.3: Spectrum of one ion obtain from an EMCCD, after sideband cooling a two ion chain at $\nu_z = 162$ kHz using the sequence in table 7.1. Detuning relative to second ion is 2.6 kHz. Average motional state occupation of $\bar{n}_{COM} = 0.30(4)$ and $\bar{n}_B = 0.07(3)$ is obtained from averaging with the parameters from the second ion fit (not shown).

motional occupation of $\bar{n} = 0.39(2)$. We also have a residual Stark shift of 2 kHz which we did not fully compensate at the time. This of course makes the effect more pronounced, but the point remains that the two ions follow a very different excitation curve. The conclusion from these data sets is that our ability to be able to perform quantum entangling operations which use the motional modes is limited by our ability to coherently address them with a single laser. If we had two independent lasers focussed to address each individual ion, we could avoid the problem of different transition frequencies, however, such a laser configuration is not realistically achievable with the current design of the Penning trap and the very limited optical access.

7.3 Two Ion Planar Crystal Cooling

In some sense, the two dimensional configuration where ions rotate around the magnetic field in a plane is the most natural for Penning traps. As explained at the start of the previous section, above a threshold axial frequency, two ions are guaranteed to reside in the radial plane hence we don't have to be concerned about the ions being knocked into a different configuration during the experiment. In this configuration we again have two axial modes: the centre of mass mode as well as a tilt mode with frequency given by:

$$\nu_T = \sqrt{\nu_z^2 - \nu_{eff}^2} = \sqrt{\frac{3}{2}\nu_z^2 - \nu_r(\nu_c - \nu_r)} \tag{7.8}$$

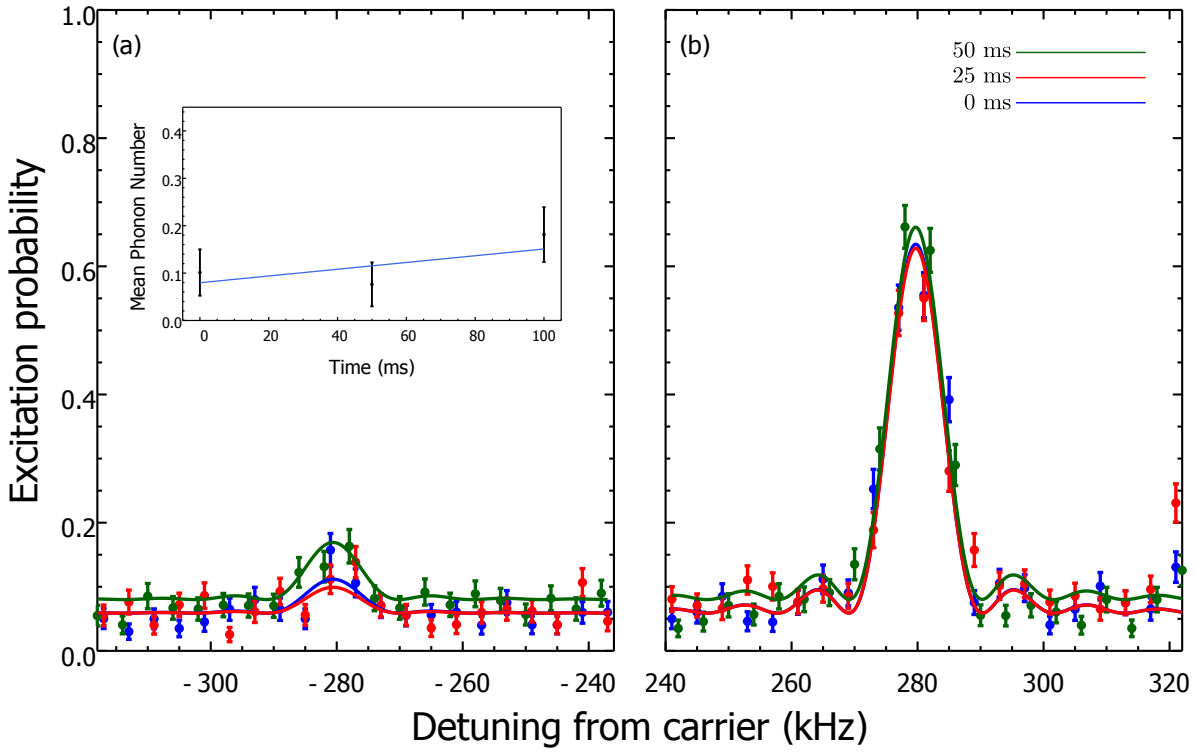

(a) Breathing mode

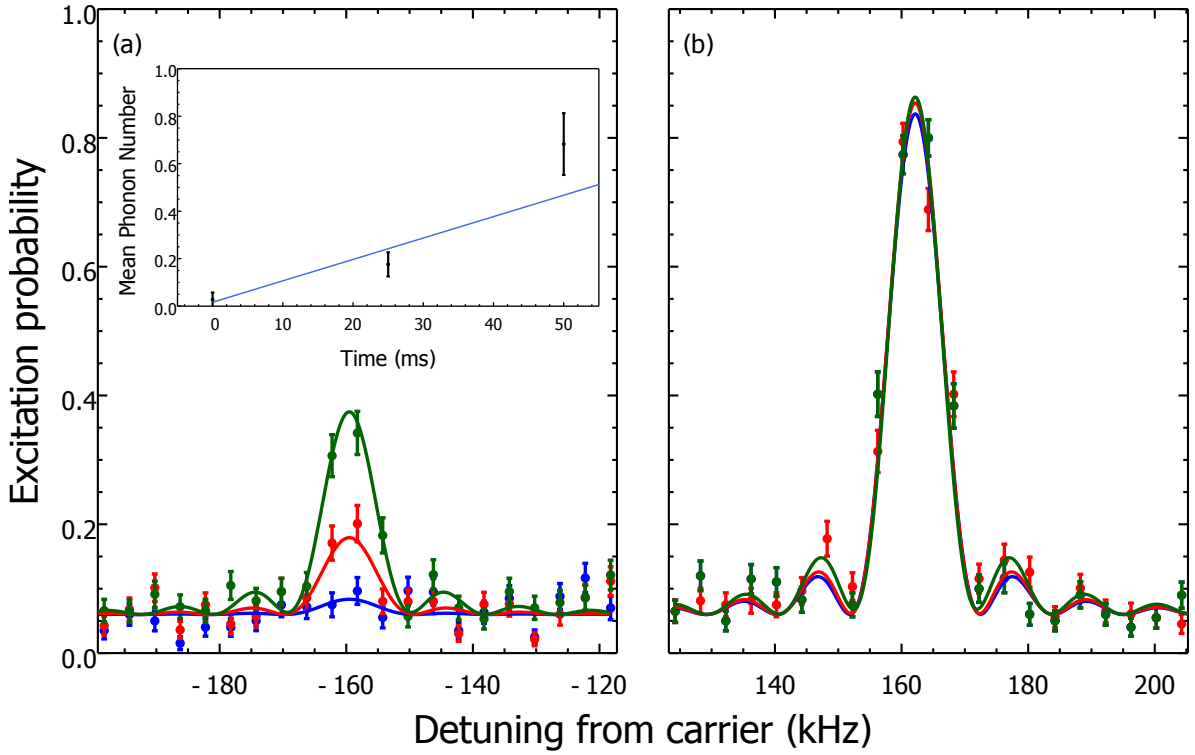

(b) COM mode

Figure 7.4: Heating rate measurements of the (a) breathing and (b) COM modes. The insets contains a linear fit to the $\bar{n}$ obtained from the sidebands fits as a function of time giving $\dot{\bar{n}}_B = 0.7(8)$ s^{-1} and $\dot{\bar{n}}_{COM} = 9(4)$ s^{-1}

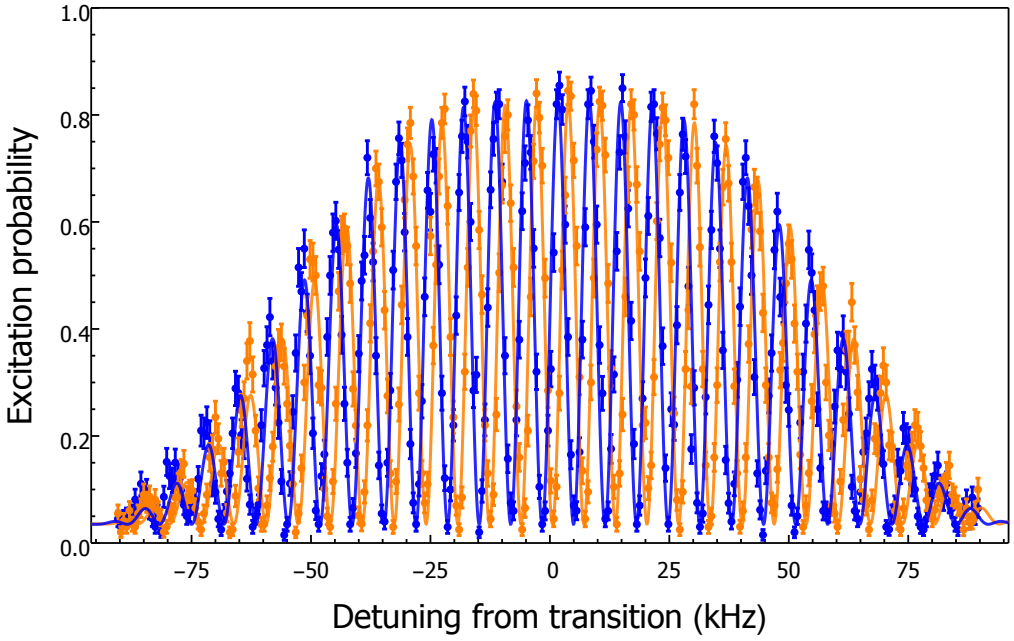

Figure 7.5: Ramsey spectroscopy of the carrier transition of a two ion chain at $\nu_{COM} = 162$ kHz with a wait time of 140 μs. The excitation spectra of each ion are measured individually on an EMCCD. A clear shift in the pattern from one curve to the next is visible, corresponding to a carrier frequency difference of 2.16(1) kHz.

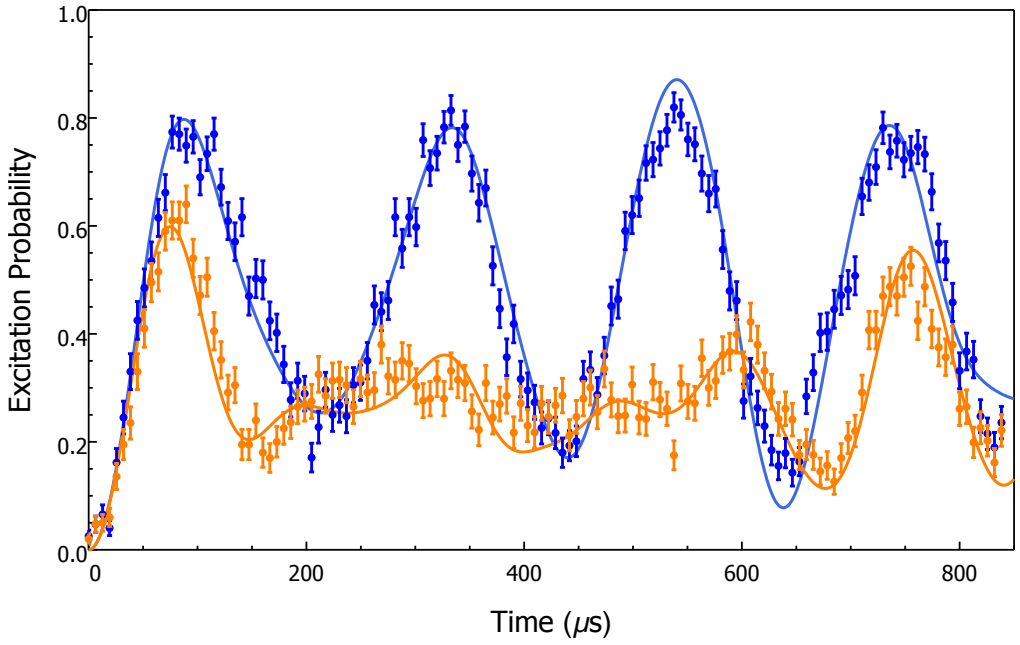

Figure 7.6: Rabi oscillations on the blue COM mode sideband of a 2 ion crystal with the blue and orange data corresponding to the two different ion excitation probabilities. The laser frequency is set to be resonant with one ion (blue data). These data are fitted using a thermally weighted sum of solutions of the BSB Hamiltonian up to $n = 4$ (eq. 7.3) to allow for detuning. The resulting fit parameters give $\Omega_0/2\pi = 25.5(1)$ kHz, $\bar{n}_{COM} = 0.39(2)$, $\Delta_1/2\pi = 2(1)$ kHz and $\Delta_2/2\pi = 3.9(1)$ kHz corresponding to the detuning to ions represented by the blue and orange data respectively

and the Lamb-Dicke parameter thus becomes:

$$\eta_T = \frac{\eta\sqrt{\nu_z}}{\sqrt{2\sqrt{\nu_z^2 - \nu_{eff}^2}}} \tag{7.9}$$

where both depend on the rotation frequency ν_r of the crystal around the z axis

The rotation frequency is dependent on many parameters, mainly the photon scattering rate from and offset of the radial Doppler cooling beam providing torque and the strength of the quadrupole RF axialization field used to periodically squeeze the radial potential. By changing these parameters we can reduce the orbit diameter, corresponding to a particular rotation frequency, from anywhere between $\approx 13-30$ μm. However, we noticed it is not easy to maintain a particular frequency due to the instability of our laser powers (due to polarisation noise through fibers), beam pointing and frequency. Under optimal Doppler cooling parameters for a single ion, we typically observe the rotational frequency to be near its minimum, which corresponds to approximately 10 kHz above the magnetron frequency leading to a mode separation $\nu_z - \nu_T \approx 7$ kHz. This turns out to also be the most stable configuration in order to fix the rotational frequency and hence the tilt mode frequency so that it does not drift throughout the spectrum acquisition. While we can force the crystal to rotate at higher frequencies and thus separate the modes by tuning the Doppler cooling lasers closer to resonance and increasing the radial beam scattering rate, both of these actions cause the axial motion that we are interested in cooling to heat up significantly. For our experiments we thus seek to maintain a stable low rotation frequency near the magnetron frequency and accept that the two modes may not always be well resolved.

The advantage of this quasi degeneracy is that sideband cooling on the first ν_{COM} red sideband appreciably cools the tilt mode as well. Unlike the two ion chain crystals, the trapping frequency can be set significantly higher, leading to a smaller Lamb Dicke parameter and lower $\bar{n}$ for the same Doppler temperature. Consequently, the vast majority of the population of motional states lies below the minimum of the first red sideband coupling making population trapping negligible and allowing for very straightforward sideband cooling.

Figure 7.7 shows a typical two ion planar crystal imaged side on through our EMCCD. The ions appear as a line with varying intensity as their fluorescence is averaged over many periods of rotation. The lack of single ion spatial resolution complicates the state readout. Since we can't image the ions individually, we can only reliably record the double excitation

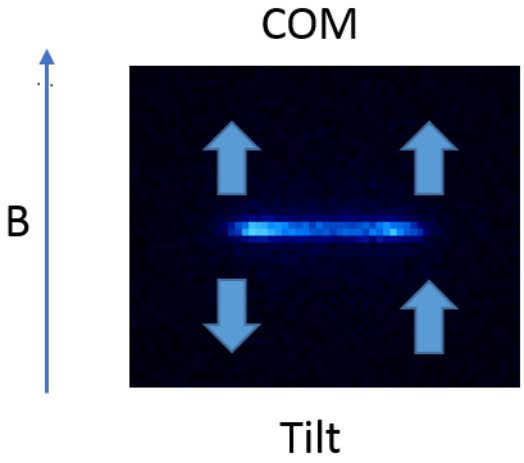

Figure 7.7: EMCCD image of two ions in a plane perpendicular to the magnetic field B with two modes of oscillation highlighted. The image was taken at axial endcap potential of 50 V, $\nu_{COM} = 380$ kHz. The width of ≈ 30 μm is consistent with the spectrally measured $\nu_T = 370$ kHz. Scale - approximately 1 μm per pixel.

spectrum corresponding to both ions being shelved to the $|ee\rangle$ state. Furthermore, our probe laser is slightly misaligned with the magnetic field axis, hence it also sees the radial excitation spectrum with a much reduced Lamb-Dicke parameter. In all spectra so far, for a single ion and two ions in a chain, these radial excitations were negligible at the relevant pulse times, but in principle they can be easily detected for longer probe times. However, for the two ion disk, the radial rotation frequency ν_r sidebands become visible after sideband cooling. Because we don't have a direct measurement of the misalignment angle, we don't know the Lamb-Dicke parameter and hence can't effectively fit the whole spectrum. Figure 7.8 shows the spectrum after Doppler cooling in (a) and after sideband cooling on the COM mode in (b) with the rotational modes appearing ≈ 110 kHz each side of the carrier, very close to the magnetron frequency, consistent with the tilt mode $\nu_T \approx \nu_{COM}$ and hence appearing unresolved from the COM sideband.

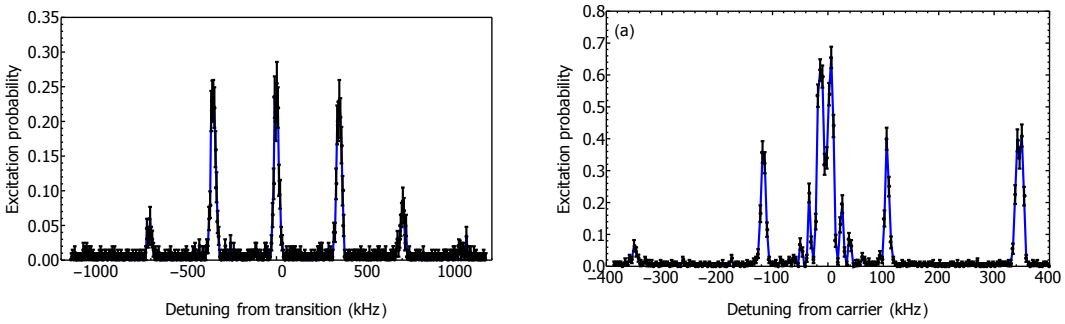

Figure 7.8: Double excitation spectra of two ions in a radial plan (a) after Doppler cooling and (b) after 25 ms total sideband cooling on 1st-2nd-1st RSBs of ν_{COM}.The tilt mode appears degenerate with the COM mode in both plots. The innermost sidebands of the carrier in (b) are at ν_r very close to ν_-. Points are only connected, not fitted.

To effecitvely poulate the ground state we use a simple cooling sequence that has 10 ms of cooling on the 1$^{\text{st}}$ RSB of the ν_{COM}, with the tilt mode cooled off-resonantly. To resolve the modes, we reduce the probe power to $\Omega_0/2\pi = 14$ kHz and sideband cool a crystal at $\nu_z = 346$ kHz with 4 V of axialization voltage. The resulting spectrum of the probability of both ions being shelved is seen in figure 7.9 showing a total suppression of the red sidebands compared to a strong excitation on the blue sidebands. This is not altogether surprising since any excitation to the $|ee\rangle$ state on the red sideband would require the ion to have at least two phonons in the relevant mode. Another clear feature is the reduction in the apparent tilt mode height compared to the the COM that is not explained by the very small difference in their Lamb-Dicke parameters. This is most likely caused by a small residual instability in the rotating frequency that broadens the peak. To extract information about the motional state population, we once again consider a thermal distribution across the 5 lowest motional states of each mode and numerically integrate the Hamiltonians of equation 7.3 to obtain the $|ee|^2$ lineshapes around each sideband, which we sum incoherently. Additionally, we perform a convolution of each peak with a normalised Gaussian function keeping the standard deviation as a free parameter to model the broadening. Unsurprisingly, when using a constrained numerical χ^2 minimisation for $\bar{n}_{COM} \geq 0, \bar{n}_T \geq 0$ algorithm, we find both these quantities to be exactly zero. A jacknife resampling was applied to this data set and found these parameter variances to be consistent with zero. This is a reflection of the fact that the data we are fitting effectively contains no

information on the $n = 1$ Fock state on the red sideband. We can set an upper bound on the $\bar{n}$ by taking the false negative error rate for the double excitation threshold discrimination (see section 5.5.3) of 0.7% and assuming that this is the maximum population that can be left behind in the $n = 2$ state of either mode. This results in $\bar{n}_T = \bar{n}_{COM} < 0.1$. This estimate is lower than the one cited in our paper [192] where the upper bound was more conservative because it considered the total error of 4%. Either way, to get a conclusive measurement would require an improvement to our detection efficiency in order to distinguish the Poissonian corresponding to both or one of the ions fluorescing. The fit also reveals that the tilt mode peak is broadened by $\sigma = 1$ kHz, while the COM also appeared broadened by 0.7 kHz. The broadening of the COM mode is not explained by a change in the rotation frequency, but is commensurate with the linewidth of our laser. Using the residual broadening on the tilt mode, we can estimate the stability of the rotation frequency during this spectrum to ≈ 0.7 kHz. From the measured tilt mode frequency of $\nu_T = 339.5$ kHz we obtain a rotation frequency $\nu_r = 104.5$ kHz, which is 8.2 kHz above the magnetron. We also measure the heating rate immediately after this spectrum for both modes to be 0.7(5) phonons per second consistent with the single ion case.

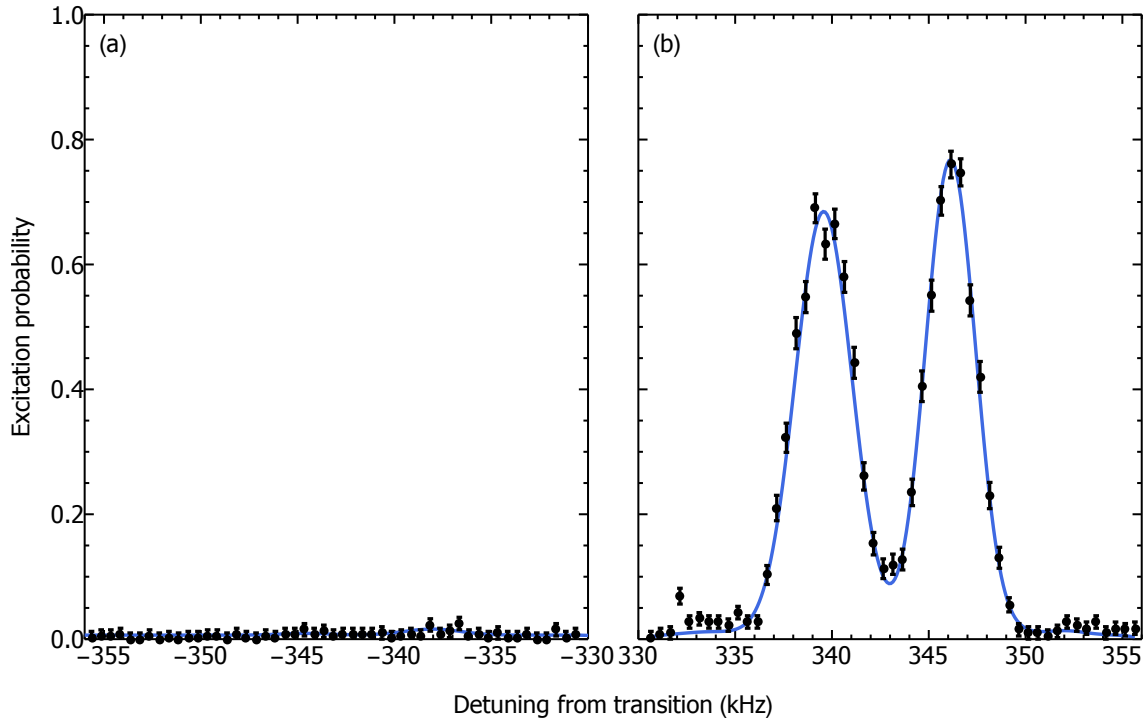

Figure 7.9: Double excitation probability spectrum of two ions in a planar crystal after sideband cooling for 10 ms on the first red sideband of the COM mode at $\nu_{COM} = 346$ kHz. The curves are fitted according to the model described in the text, constraining $\bar{n}_T$ & $\bar{n}_{COM} < 0.1$. Rotational frequency of $\nu_r = 104.5$ kHz measured from tilt mode frequency.

One of the techniques employed is the aforementioned axialization which periodically squeezes the potential such that the rotation is altered. While we found it useful to slightly increase the rotation speed of the crystal by applying a 4 V potential, it does not offer us a reliable method to set the rotation frequency of the crystal. To do this, we would need to modify the trap to include additional electrodes. With at least 6 electrodes we could apply a rotating quadrupole field of the form [108]:

$$\phi_w = V_w \cos(2\pi\nu_w t)(x^2 + y^2) \tag{7.10}$$

which would allow us to lock the rotation frequency of the crystal to the applied drive frequency ν_r. This method has been successfully applied to large Coulomb crystals in a Penning trap to aid coherent manipulation [55]. Without the rotating wall we could still look to improve the control of the laser torque by changing the focus of the radial Doppler cooling beam. Currently we use a moderately focused beam offset from the trap centre; a more focused beam would give us higher torques and allow more effective cooling of the magnetron motion, but will rely on very good beam pointing stability, whereas a less focused beam will have reduced sensitivity to any intensity and pointing fluctuations, but might not be able to effectively apply a strong torque.

7.4 N–Ion 2D Crystal Cooling

Naturally, we explore the limits of this simple scheme as applied to larger 2D ion crystals in the plane. The equilibrium position of the ions can always be determined using the set of coupled equations 2.39 and used to calculate the mode frequencies 2.43.

The simplest case to first consider is that of three ions. The ions form a triangle and by cylindrical symmetry the two tilt modes are degenerate in frequency. By maintaining a low rotation frequency $\nu_r \approx \nu_- + 10$ kHz, we can keep both these modes to within a few kHz of the COM mode allowing us to once again cool them off resonantly by cooling at the red sidebands of the COM mode. Figure 7.10 shows a sample spectrum of the excitation probability of at least one ion[2] taken after 30 ms of sideband cooling split into 10 ms segments on the 1^{st}-2^{nd}-1^{st} sidebands in turn[3]. Due to the complexity of the spectrum, the degeneracy of the modes and the large error in selecting a threshold we do not attempt a fit, but we can attribute near total suppression of excitation relative to background in the vicinity of the red sidebands and the very high excitation of the blue sidebands to a high ground state occupation of all axial modes. The spectrum also shows additional radial features due to the misalignment of the probe beam that are clearly identified. We can use the rotational sidebands to directly obtain a measurement of the rotational frequency $\nu_r = 133$ kHz, which is 13 kHz above the magnetron frequency and hence estimate that the tilt modes are 6 kHz below the COM mode and hence are not resolved.

We now show that we can cool larger crystals with very similar cooling sequences without requiring us to resolve all the additional sidebands by exploiting the small mode separations to off resonantly cool them simultaneously. To get a sense of scale for the mode separation, table 7.2 lists the axial mode frequencies and crystal configuration for a typically observed rotation frequency of $\nu_r = \nu_- + 10$ kHz. It is clear that the modes are very tightly clustered just below the COM frequency, with even the lowest frequency mode for 10 ions being separated by just 26 kHz. Thus our general cooling strategy to cool these crystals is to maximise the cooling rate by having as high an Ω_0 as possible and a $\tilde{\Gamma} \approx 50$ kHz to broaden the transition since we are ultimately not worried about off resonant carrier excitation or heating of the nearby radial modes. We cooled various numbers of ions with different cooling sequences, including cooling on the second order sideband and sequentially cooling at different frequencies just below the

[2]The threshold was optimised empirically by setting the background when the laser is far off resonance from any spectral feature to be in the 2-3% noise region to aid the detection of weak resonances.

[3]The 2^{nd} order sideband was not necessary and other measurements without it verify this. It was coincidental that this wide spectrum was taken with this sequence.

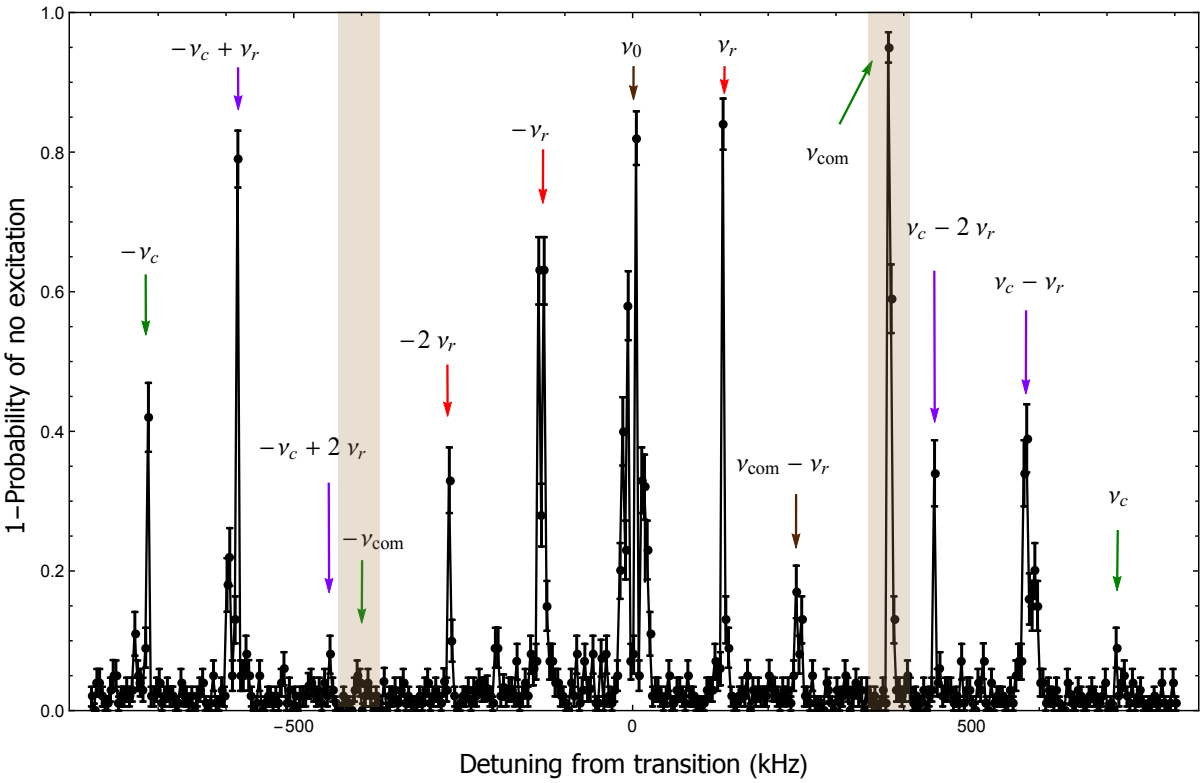

Figure 7.10: Single excitation probability spectrum of three ions in a planar crystal after sideband cooling for 30 ms split into 10 ms segments on the 1^{st}-2^{nd}-1^{st} red sidebands of the COM mode. The points are joined to guide the eye. The pink regions highlight the axial modes, with the individual labels showing additional radial features. Frequencies: $\nu_{COM} = 383$, kHz $\nu_r = 133$ kHz, $\nu_T = 377$ kHz

COM red sideband to increase overlap with the additional modes. Since we did not perform a systematic study of different cooling sequence instead rather choosing them in a heuristic manner based on our experiences, we don't have an optimised prescription but can only offer the general observations that larger crystals require more power, longer cooling times and additional cooling at a frequency below the COM.

In figure 7.11 we present a cross section of spectra obtained after sideband cooling different sized crystals using various cooling sequences. Since we can no longer effectively select thresholds without introducing a larger error, we choose to present the data as an absolute value of background subtracted total fluorescence, defining an effective 'dark count' that corresponds to the ion shelving rate. In this way the spectra maintain a consistent look with the ones shown in the rest of the thesis. Once again we don't perform any quantitative fits, but by comparing the dark counts in the red sideband region to background and noting the large asymmetry with respect to the blue sideband region in figures 7.11(a)-(e), we once again have evidence that suggests a significant fraction of the population is in the ground state for all the modes for crystals of up to 10 ions. We also observe a coherent lineshape in the vicinity of the carrier which would be washed out in a thermal state. In 7.11(f) we applied the scheme to 15 ions and were not able to achieve similar results as for smaller crystals, but there is a small degree of asymmetry and the red sideband region features below the COM frequency appear further suppressed. Without further data it is difficult to conclude that we are approaching the limits of our sideband cooling approach in terms of crystal size, but the 15 ion result is at least evidence that without a less naive approach cooling large crystals will not be as effective and reliable. One of the reasons for

Ions	N_1, N_2	Frequency (kHz)	
4	4,0	$\nu_4 = 345.968$	
5	5,0	$\nu_4 = 343.990$	$\nu_5 = 343.990$
6	1,5	$\nu_4 = 346.210$	$\nu_5 = 346.210$
		$\nu_6 = 338.678$	
7	1,6	$\nu_4 = 344.993$	$\nu_5 = 344.993$
		$\nu_6 = 343.346$	$\nu_7 = 339.023$
8	1,7	$\nu_4 = 343.972$	$\nu_5 = 343.972$
		$\nu_6 = 340.798$	$\nu_7 = 340.798$
		$\nu_8 = 339.409$	
9	2,7	$\nu_4 = 344.998$	$\nu_5 = 344.979$
		$\nu_6 = 342.144$	$\nu_7 = 341.983$
		$\nu_8 = 338.864$	$\nu_9 = 330.827$
10	2,8	$\nu_4 = 344.311$	$\nu_5 = 344.189$
		$\nu_6 = 341.521$	$\nu_7 = 339.439$
		$\nu_8 = 339.106$	$\nu_9 = 338.900$
		$\nu_{10} = 330.361$	

Table 7.2: Occupation of inner and outer shells N_1, N_2 and mode frequencies for small planar Coulomb crystals. $\nu_2 = \nu_3 = 349.242$ kHz for all the above.

this is that the radius of the crystals grows with the addition of further ions, and hence the ions in the outer shell see a lower intensity from the cooling lasers slowing down the process. The radius can be reduced by rotating the crystal faster either through additional torque or using a rotating wall drive, but the modes will then move further away from the COM and the off resonant cooling rate will be affected. Another contribution might be a higher initial Doppler temperature which we have not characterised here.

To confirm that we have cooled ions to near the ground state, and get a a weak thermometric estimate of the ground state population, we perform Rabi oscillations on the carrier transition to avoid the issue of nearby modes interfering. We first perform a measurement on a three ion crystal at $\nu_{COM} = 356$ kHz prepared with 10 ms of cooling at $-\nu_{COM}$. The result in figure 7.12 is thresholded on a triple excitation and hence fitted to the standard Rabi excitation formula of equation 6.6 where the bracketed term is raised to the third power since the excitation spectrum is just the product of three independent ions undergoing oscillations. The result of the fit give an estimated $\bar{n} = 1.0(1)$ distributed between all the modes indicating a 50% occupation of the ground state. There is an additional modulation that is not quite explained by the fit, that is most likely due to laser intensity fluctuation since at the time of this data acquisition the noise eater wasn't working.

The final result of this chapter is a Rabi oscillation spectrum of a six ion crystal. We chose this number because it is the first configuration to have a two shell configuration in which a single ion is orbited by the outer five ions. Thus the outer ions will see a lower average laser intensity compared to the central ion and we will observe an interference effect due to the presence of two distinct Rabi frequencies. We can measure the Rabi frequency of only the outer ions by using the EMCCD to collect position sensitive fluorescence from a region of interest

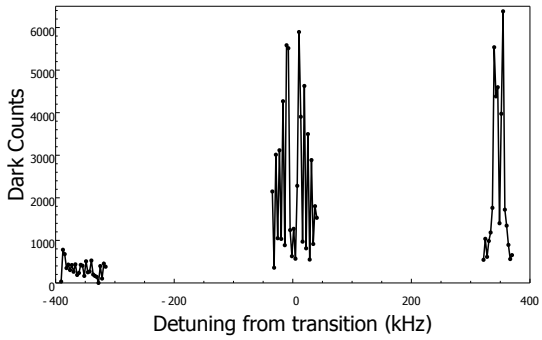

(a) 4 Ions. $\nu_{COM} = 356$ kHz

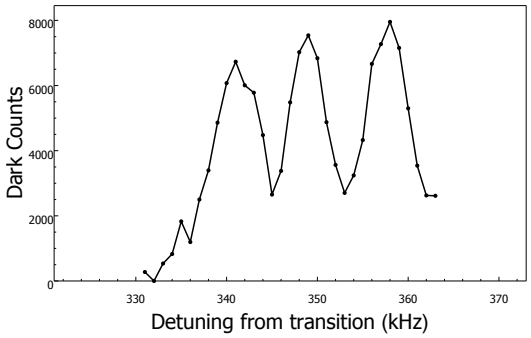

(b) 4 Ions. $\nu_{COM} = 356$ kHz. Zoomed BSBs.

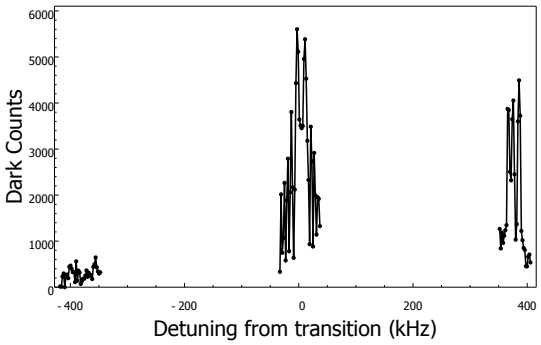

(c) 5 Ions. $\nu_{COM} = 385$ kHz

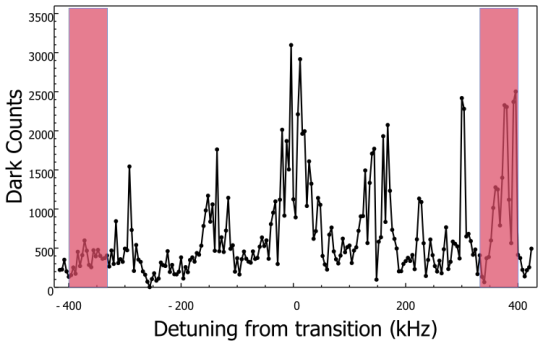

(d) 6 Ions. $\nu_{COM} = 393$ kHz

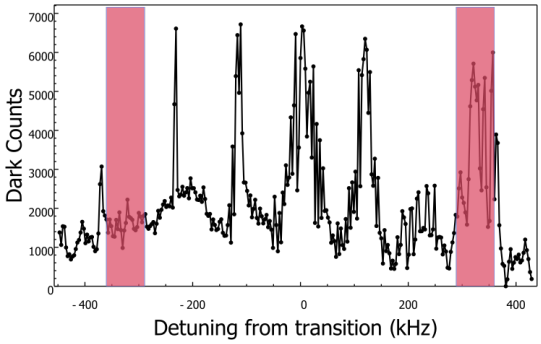

(e) 10 Ions. $\nu_{COM} = 356$ kHz

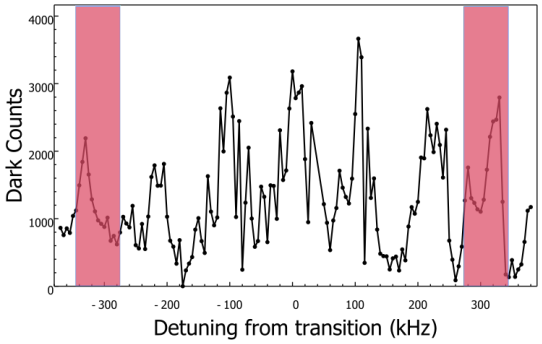

(f) 15 Ions. $\nu_{COM} = 356$ kHz

Figure 7.11: Fluorescence spectra of dark counts (see text) of ion crystals after sideband cooling sequences: (a) 30 ms at $-\nu_{COM}$, (b) 30 ms at $-\nu_{COM}$, (c) 5 ms at $-2\nu_{COM}$ and 15 ms at $-\nu_{COM}$, (d) 30 ms at $-\nu_{COM}$, (e) - 5 ms at $-\nu_{COM}$, 15 ms at $-\nu_{COM}$ + 27 kHz, 10 ms at $-\nu_{COM}$ + 42 kHz 1 ms at $-\nu_{COM}$, (f) - 20 ms at $-\nu_{COM}$, 20 ms at $-\nu_{COM}$+ 20 kHz. Red regions show the axial modes that are being cooled.

defined at the bright extrema of the planar disk, while the PMT records the fluorescence from all the ions. The outer region signal can be fitted as for the three ions, but for the PMT data we use a model of the form:

$$P_e(t) = \sum_n^5 \frac{\bar{n}^n}{(\bar{n}+1)^{n+1}} \frac{A}{2} \left(1 - e^{-t/\tau_e} \cos \Omega^o_{n,n} t\right)^5 \left(\frac{1}{2} - \frac{1}{2} e^{-t/\tau_e} \cos \Omega^i_{n,n} t\right) \tag{7.11}$$

where we have allowed for a Rabi frequency $\Omega^i_{n,n}$ for the inner ion and $\Omega^o_{n,n}$ for the outer ones. The resulting spectra are showed in figure 7.13, demonstrating excellent fits both for the outer ion rings in (a) and the combined oscillations of all ions in (b). The Rabi frequency ratio of inner to outer Rabi frequency of 1.4 tells us that the average laser intensity seen by the outer ring is almost half that of central ion.

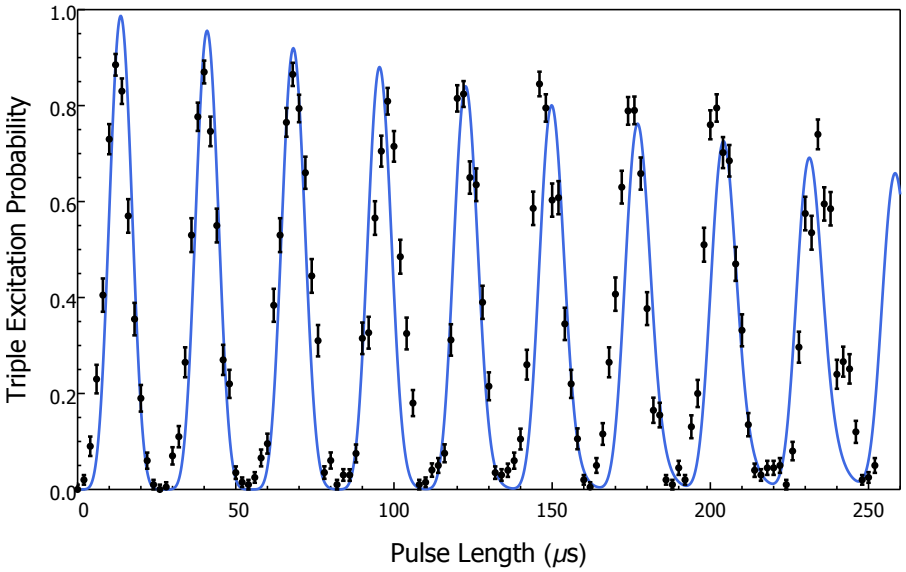

Figure 7.12: Carrier Rabi oscillation on a 3 ion planar crystal at $\nu_{COM} = 356$ kHz, with $\nu_r \approx 120$ kHz. Fitted parameters: $\Omega_0/2\pi = 37.6(2)$ kHz, $\tau_e = 1730(130)$ μs, $\bar{n} = 1.0(1)$

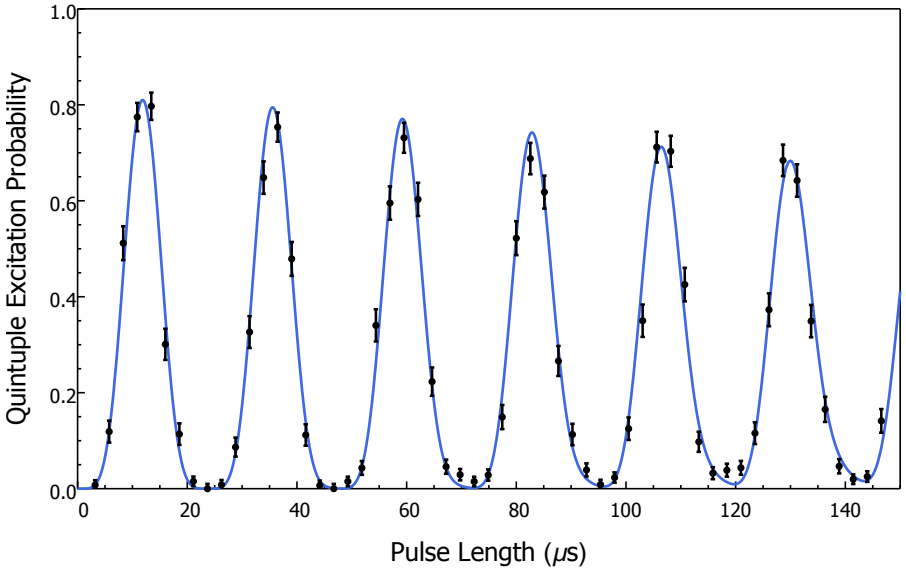

(a)

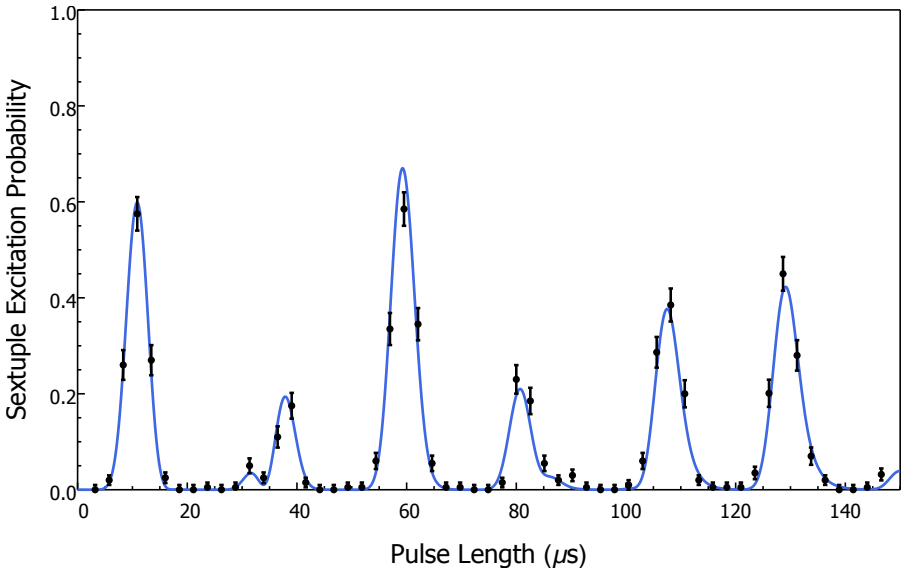

(b)

Figure 7.13: Carrier Rabi oscillations on a 6 ion planar crystal at $\nu_{COM} = 356$ kHz, with $\nu_r \approx 120$ kHz (a) quintuple excitation on the outer 5 ions using EMCCD fluorescence $\Omega_0^o/2\pi = 42.96(5)$ kHz. (b) sextuple excitation of all ions using PMT data. $\Omega_0^o/2\pi = 42.81(6)$ kHz, $\Omega_0^i/2\pi = 59.6(1)$ kHz, $\bar{n} = 0.6(1)$

CHAPTER 8

COOLING THE RADIAL MOTION OF A SINGLE ION

One of the big appeals of a Penning trap is that there is no micromotion present since the RF fields have been replaced by a static magnetic field. The trade-off is that radial motion has a negative total energy magnetron mode since the ion travels around a potential hill in the radial plane due to the magnetic confinement from the Lorentz force. The consequence is that to cool the ion (defined as reducing its orbital radius, or confining it closer to the trap centre), we have to push it up this potential hill. If standard Doppler cooling techniques are applied with a red detuned laser in the plane through the centre of the trap, we will begin to remove energy from the magnetron mode moving the ion down the potential hill and hence heating rather than cooling it. Simultaneous Doppler cooling of both motions with an offset beam is possible, but the efficiency of cooling the magnetron is limited as was discussed theoretically in section 4.3.1. Furthermore, the metastable mode oscillation frequency is typically very low, in the tens of kHz, hence even near the Doppler limit, there can be thousands of phonons in this mode. Due to these reasons, no one has yet successfully demonstrated simultaneous ground state cooling of the radial modes of motion in a Penning trap. In the first section we show numerical simulations of Doppler cooling under the presence of the axialization drive – the technique that uses an RF drive at the true cyclotron frequency to resonantly couple the cyclotron and magnetron motions together. This technique proved crucial in achieving a significant reduction in the average magnetron phonon number. We will experimentally show the effects of the axialization drive on the Doppler temperature and will then go on to present the first evidence of a significant occupation of the ground state of motion of the magnetron and cyclotron modes simultaneously after sideband cooling.

8.1 Simulations of Doppler Cooling

The goal of this section is to highlight general trends that inform us about the behaviour of the classical ion trajectories in the radial plane under the influence of Doppler cooling using an offset Gaussian laser beam both with and without an axialization RF field. Specifically, we are interested in learning about the cooling limits rather than the cooling rates as we seek to find optimal parameters that will yield mean phonon numbers of both modes of motion that are low enough to allow sideband cooling techniques to further cool the ion to the ground state of radial motion.

8.1.1 Simulation Method

We begin by writing explicitly the coupled radial equations of motion for a single ion under the presence of an axialization drive of amplitude V_a given by equation 4.61

$$\ddot{x}(t) = \frac{\omega_z^2}{2}x(t) - \frac{V_a e}{2Mr_0^2}\sin(\omega_c t + \phi_i)x(t) + \omega_c \dot{y}(t) \tag{8.1}$$

$$\ddot{y}(t) = \frac{\omega_z^2}{2}y(t) + \frac{V_a e}{2Mr_0^2}\sin(\omega_c t + \phi_i)y(t) - \omega_c \dot{x}(t) \tag{8.2}$$

If we set $V_a = 0$ these equations exactly reduce to those of equation 2.7 for the static trapping case. Integration of equations 8.1 & 8.2 will yield solutions to $x(t)$ and $y(t)$, which can reconstruct the ion's trajectory in the radial plane, but tell us very little about the behaviour of each mode. Instead we rearrange the analytical solutions from equations 2.16 to find the square amplitudes of the motion:

$$r_+^2 = \frac{1}{4\omega_1^2}\left[(\omega_- x(t) + \dot{y}(t))^2 + (\omega_- y(t) - \dot{x}(t))^2\right] \tag{8.3}$$

$$r_-^2 = \frac{1}{4\omega_1^2}\left[(\omega_+ x(t) + \dot{y}(t))^2 + (\omega_+ y(t) - \dot{x}(t))^2\right] \tag{8.4}$$

In the absence of axialization, these amplitudes are constants of motion that are fixed by the initial conditions and the trap parameters. When the axialization is turned on, the amplitudes evolve sinusoidally in time at a frequency given by equation 4.68. To model the laser-ion interaction, we will consider discrete scattering and absorption of photons by a laser with wave vector $\mathbf{k}$ that leads to an instantaneous velocity change $\Delta\mathbf{v} \equiv \mathbf{v} - \mathbf{v}' = \frac{\hbar}{m}(\mathbf{k} - \mathbf{k}')/m$ after emitting a photon with wave vector $\mathbf{k}'$ as in section 4.3.1. This approximation holds since the timescale for the emission process is orders of magnitude smaller than any of the trapping frequencies under consideration. Even though the Penning trap Doppler cooling is performed with two lasers to repump both $S_{1/2}$ Zeeman sublevels, we will assume just a single monochromatic cooling laser on the 397 nm transition ignoring any repumping by the 854/866 nm lasers. This should not affect the results of the simulation significantly since in practice we always set approximately the same detuning and power on both the lasers. The monochromatic assumption also follows from the linewidth of the laser being much smaller than the transition linewidth. For the decay, we average over all the possible transitions as in equation 4.50 resulting in an isotropic emission pattern. We do not consider re-heating due to scattering of photons from an axial laser beam.

The laser has a Gaussian intensity profile given by:

$$I = \frac{2P_0}{\pi w_0^2} e^{-2(y-y_0)/w_0^2} \tag{8.5}$$

where P_0 is the total power, w_0 is the beam waist and y_0 is the offset from the trap centre (not to be confused with the beam offset parameter used in the linear approximation in section 4.3.1). The laser wave vector is fixed to be $\mathbf{k} = k\hat{\mathbf{x}}$. The scattering rate due to the radial beam including the time dependent Doppler shift is then given by:

$$\gamma_g(t) = \frac{I\sigma_0}{\hbar\omega_L}\frac{(\Gamma/2)^2}{(\Gamma/2)^2 + \frac{I\sigma_0\Gamma}{2\hbar\omega_L} + (\delta + \dot{x}(t)k)^2} \tag{8.6}$$

where the scattering cross-section is [140]:

$$\sigma_0 = \frac{3\lambda^2 |\langle g|rC_q^{(1)}|e\rangle c_i^{(q)}\epsilon_i|^2}{2\pi} \tag{8.7}$$

where we recognize the dipole transition matrix defined in equation 3.10. In our experiment we address both $\sigma^{\pm}$ transitions with optimal linear polarisation and hence obtain $\sigma_0 = \lambda^2/(2\pi)$ (see section 3.3 for discussion of polarisation and beam geometry). Finally, we assume that the laser statistics are Poissonian and thus we can define a probability of seeing n photons in a time interval dt as $P_n(\gamma_g(t)dt)$.

The integration algorithm then proceeds as:

1. Integrate the equations of motion 8.1 and 8.2 using an 8^{th} order Runge-Kutta by a time step dt.

2. Sample the Poissonian distribution $P_n(\gamma_g(t)dt)$ to find how many n photons arrived in the time step.

3. Generate two uniform random numbers $\theta[0,\pi]$ and $\phi[0,2\pi]$ to define the scattered photon wave vector.

4. Update the velocity coordinates by the corresponding velocity kicks:

$$\dot{x}(t) \to \dot{x}(t) + \frac{n\hbar k}{M}(1 + \sin\theta\cos\phi)$$
$$\dot{y}(t) \to \dot{y}(t) + \frac{n\hbar k}{M}(\sin\theta\sin\phi)$$

This algorithm is implemented in the *Mathematica* software package and hence the output after total integration time T is a set of interpolating polynomial functions for all the position coordinates and their derivatives. As mentioned above, we are interested in the average square amplitudes $\langle r_+^2\rangle$ and $\langle r_-^2\rangle$ which can be obtained by substituting the integrated interpolation functions into equations 8.3 and 8.4. There is an important correction that must be made to the x coordinate before the substitution. Since the laser exerts a constant force in the $\hat{x}$ direction, it offsets the ion trajectory from the centre and would hence give much larger values $\langle r_+^2\rangle$ and $\langle r_-^2\rangle$. We therefore subtract the constant force term offset: $\frac{2\hbar k\gamma_g(t_0)}{M\omega_z^2}$ from the x-coordinate solution. The mean phonon numbers can then be expressed in terms of the amplitudes as:

$$\bar{n}_{\pm} = \frac{\langle r_{\pm}^2\rangle M\omega_1}{\hbar} \tag{8.8}$$

The numerical and physical accuracy of the simulation is closely tied to the selection of the time step dt. Firstly, in the absence of any laser scattering, the numerical integration should preserve the sum of the amplitudes of both modes of motion. Here the choice of algorithm and dt combine together both contribute to any error. We have found that to achieve no divergence after 20 ms to within a part in 10^{-3} using the 8^{th} order Runge-Kutta integrator, we required the time step to be at $dt = 10^{-8}$ s (2×10^6 steps). This is also a reasonable choice physically since for typical simulation beam intensities and detuning, we obtain maximum scattering rates on the order of 10^6 photons s^{-1} so that we have only a very small probability that two photons arrive within the time step avoiding any problems with saturation and correlated emission.

8.1.2 Simulation Results

Before moving on to the presentation of the results, we will define the scope of the simulation. Broadly, we were interested in qualitatively finding out the following:

1. Given a particular laser power and detuning, how does $\bar{n}$ change with beam waist and position with/without axialization?
2. What is the scaling of $\bar{n}$ with axialization voltage?
3. How is the $\bar{n}$ scaling proportional to the trapping potential for Doppler cooling with/without axialization?
4. What are realistic parameters that can achieve efficient cooling within our experimental cycle?

There are various difficulties that we shall now discuss that come with the fact that we are presented with a 6 dimensional parameter landscape that cannot be effectively mapped out due to finite computing time. Firstly, points 1–3 are concerned with the equilibrium conditions whereas one iteration of the algorithm yields one trajectory in time that may or may not reach equilibrium depending on the integration time. Since we cannot integrate indefinitely due to numerical error and most importantly computational time, we must set a reasonable cut-off. This cut-off can be informed by experiment where we have typical cooling cycles between 8-20 ms and the fact that any set of cooling parameters that takes too long to reach equilibrium is inevitably not going to be suitable for real experiments where it must also overcome heating and be robust at re-cooling ions that collide with background gas particles, directly connecting with point 4. One temptation is to set the initial conditions near the cooling limit so that the dynamic cooling time is short, but this is not practical as the limits of the magnetron mode span orders of magnitude and thus no matter the choice there will always be a strong dynamical evolution for some parameters. Increasing the scattering rate to achieve the limit faster is also not an option since any change in the laser power affects the limit itself in the presence of axialization as we will show later (figure 8.2b).

In a real experiment we sample the ensemble of final amplitudes 100-200 times after a fixed cooling period given some starting amplitude distribution of which we do not have direct knowledge of and thus we can also measure an out of equilibrium temperature. In principle, we could try this same approach in the simulation, but at great loss of speed since the differential equation solving is very costly. Instead, if one solution trajectory is in equilibrium we can find the time average of the amplitude and use the ergodicity of the system to draw a conclusion about the average ensemble of amplitudes. Since the interpolating polynomials are saved as the result of the integration, this is a cheap and precise way to estimate the average amplitude. Furthermore, with the presence of axialization, some solutions can show oscillatory behaviour in the amplitude over the whole cooling time. In this case, the averaging needs to be performed over a fixed period of the oscillation to get an accurate estimate of the amplitude that is likely to be measured in experiment. Since the period depends on the axialization drive voltage, and trap frequency and the phase is sensitive to initial conditions, it is not possible to easily automate any such averaging process. For all these reasons, we will first present plots of individual solutions for various parameters to get qualitative responses to the questions posed above and to also

highlight the discussed problems. Then to plot more quantitative trends, we shall extract the mean phonon number by taking the average square amplitude between 10 to 20 ms of cooling time. To keep all the results consistent, we always initialise the system to the same initial conditions: $x_i = -4 \times 10^-6$ m, $v_x = 1$ ms^{-1} and $v_y = 2$ ms^{-1}, which corresponds to $r_+ = 0.31$ μm, $r_i = 3.77$ μm and in terms of phonon number $n_+ = 121$, $n_- = 17622$.

We begin by considering cooling at a trap potential of 100 V ($\nu_z = 265$ kHz, $\nu_- = 52$ kHz) with a weak axialization drive $V_a = 0.2$ V, cooled by a Gaussian beam with a beam waist $w_0 = 100$ μm and a detuning $\delta = \Gamma/2$. The plots in figure 8.1 show the evolution of the amplitudes for different beam offset and laser power. The first conclusion that can be drawn

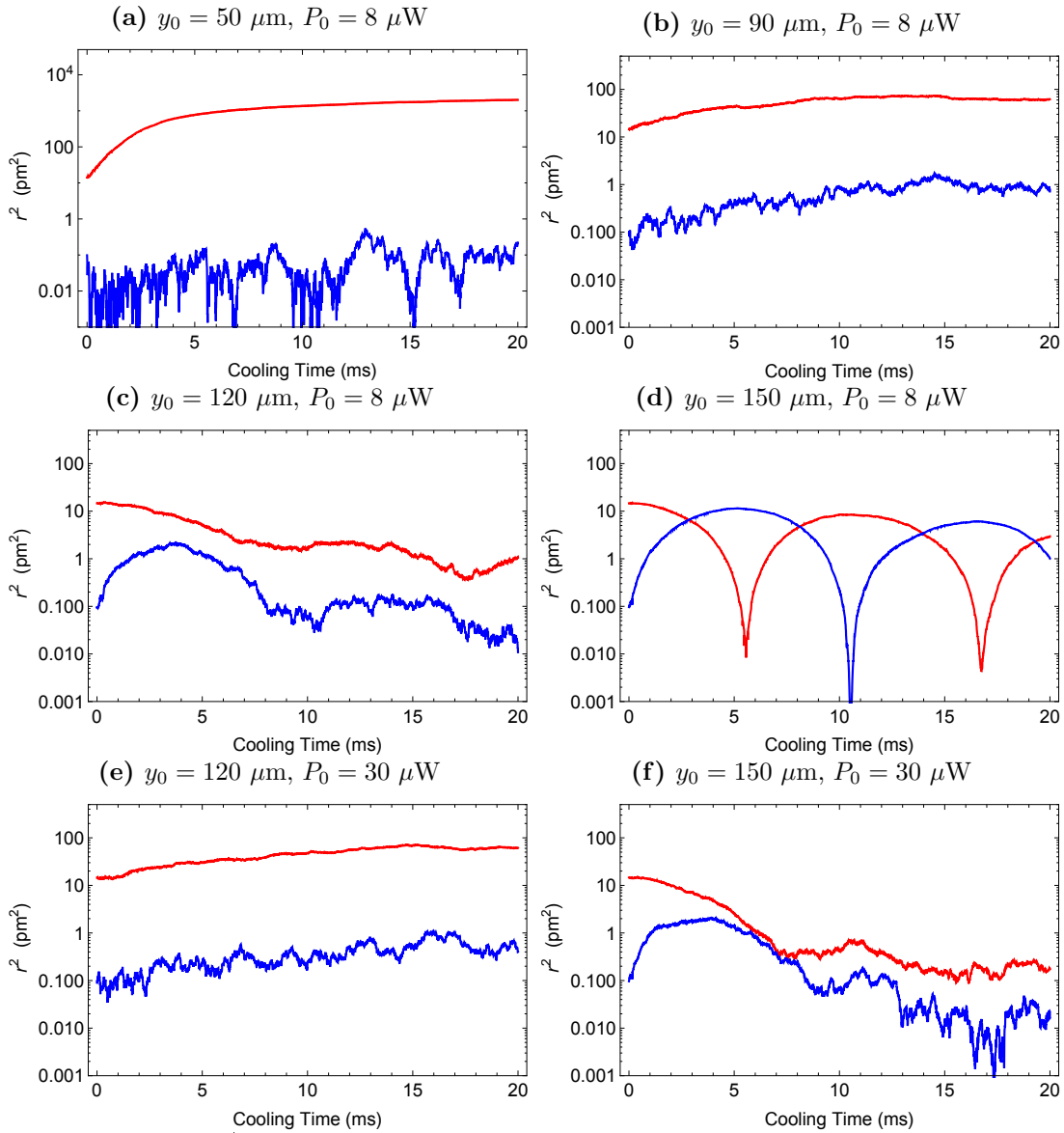

	(a)	(b)	(c)	(d)	(e)	(f)
$\bar{n}_+$	2722	1157	104	4290	651	53
$\bar{n}_-$	4.14×10^5	81×10^4	1625	3915	74×10^4	319

Figure 8.1: Amplitudes of motion for the magnetron (red) and modified cyclotron (blue). The average motional states is calculated between 10-20 ms. Parameters: Trap potential 100 V, $\nu_z = 265$ kHz, $\nu_- = 52$ kHz, $\nu_+ = 677$ kHz,$V_a = 0.2$ V, $w_0 = 100$ μm, $\delta = \Gamma/2$

from plots (a) and (b) is that if the offset is not large enough, the magnetron amplitude gets

heated to a new equilibrium amplitude. The heating gets worse the closer the beam is moved to the trap. The modified cyclotron is also heated due to the axialization coupling, but it is clear that the two quantum numbers are still orders of magnitude different at equilibrium. To begin to see cooling of the magnetron motion, the beam needs to be offset by more than a beam waist as seen in plot (c). After 10 ms, the two motions once again seem to be in equilibrium, but their quantum numbers are still not equalised as predicted, suggesting higher axialization voltages are required. Once the beam is offset by 1.5 times the beam waist as in plot (d), the scattering rate becomes very low and we observe mostly just amplitude exchange due to the axialization drive. Now if we keep the same beam positions of (c) and (d) but increase the beam power, the behaviour drastically changes as seen in plots (e) and (f). The beam offset of 120 μm that previously showed cooling now shows heating and the 150 μm now cools to the lowest amplitude so far. This behaviour clearly differs from the intensity independent cooling limits in the absence of axialization that were derived in section 4.3.1. This is not due to saturation effects since for a beam waist of 100 μm with the beam offset by 150 μm the power at the trap center where the ion resides is approximately a factor of 100 lower, much below the saturation power on the cooling transition of 8 μW.

To further investigate this effect, we compare the results obtained at low axial frequency $\nu_z = 87$ kHz, where cooling is more efficient, against results at $\nu_z = 265$ kHz while varying P_0 at $V_a = 0.5$ V and $V_a = 0$ V. Reassuringly, the results of 8.2a clearly show that there is no intensity dependence in the investigated region whether axialization is on or off. There is only a residual transient effect at low power where equilibrium has not been reached. On the other hand at high axial frequency, figure 8.2b shows a clear dependence on the beam power when axialization is on. At low powers $< 1\mu$W, the scattering rate is low and there is little appreciable cooling/heating within the 30-50 ms time range. Then as the power is increased the mean total phonon number drops with the major contribution being the reduction of the magnetron mean phonon number. A minimum is reached at ≈ 4 μW after which the total phonon number begins increasing. At approximately 16 μW the magnetron phonon number becomes larger than the initial condition. In contrast, when there is no axialization, additional power simply heats the mangetron motion faster. For the remainder of this section, we will fix the power to $P_0 = 8$ μW to correspond to the typical value used in our experiments.

We now turn to investigate the optimal beam position as a function of beam offset without axialization. Figure 8.3 shows curves obtained at a trap voltage of 10 V with a beam waist of 50 μm. Firstly, as expected, the cyclotron cooling has no discernible dependence on the beam position. For the magnetron mode the optimal cooling is obtained when the beam is offset by approximately one beam waist. When the beam is close to the trap centre, as in 8.3a and 8.3b, the cooling dynamics are extremely fast and over 10^4 phonons are removed from the magnetron mode in less than a millisecond at the cost of higher equilibrium $\bar{n}_-$. In 8.3b the equilibrium is reached in ≈ 4 ms, with approximately four times lower $\bar{n}_-$. Moving the beam further out to 1.6 times the beam waist doesn't significantly improve the cooling limit, while also decreasing the cooling rate. The dynamical behaviour in this case is not sufficient to protect against the re-heating due to scattering from the axial beam and parametric heating from the electrodes. This data set gives a flavour of the behaviour that we can expect. The cooling limits improve as the beam is moved outward, but the cooling rate steadily decreases until there is very little scattering. This trend is reproduced for different beam waists and trap voltages as shown in

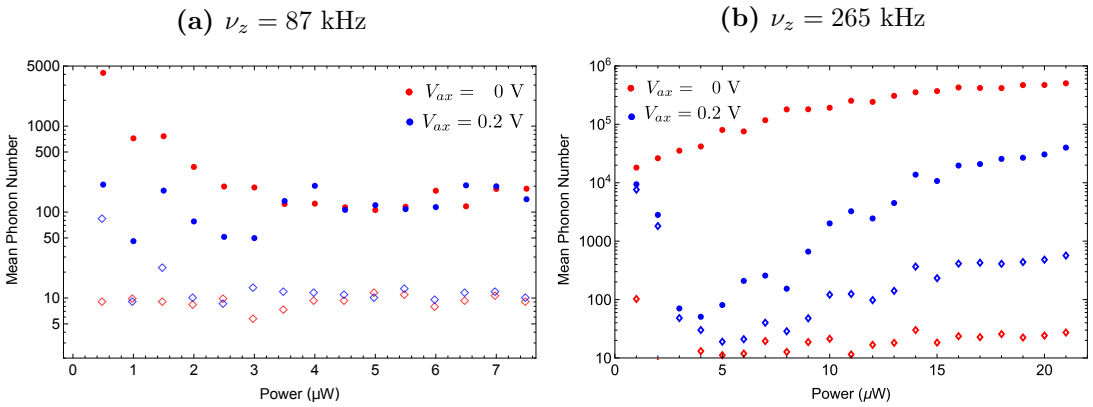

Figure 8.2: Average phonon numbers for the magnetron (circles) and modified cyclotron (diamonds) motions between as a function of beam power for 0 and 0.2 V of axialization voltage. Parameters: (a) $\nu_z = 87$ kHz, $\nu_- = 5$ kHz, $\nu_+ = 724$ kHz,$w_0 = 50$ μm, $y_0 = 50$ μm, $\delta = \Gamma/2$, averaging region 10–20 ms (b) $\nu_z = 265$ kHz, $\nu_- = 52$ kHz, $\nu_+ = 677$ kHz, $w_0 = 100$ μm, $y_0 = 120$ μm, $\delta = \Gamma/2$, averaging region 30–50 ms.

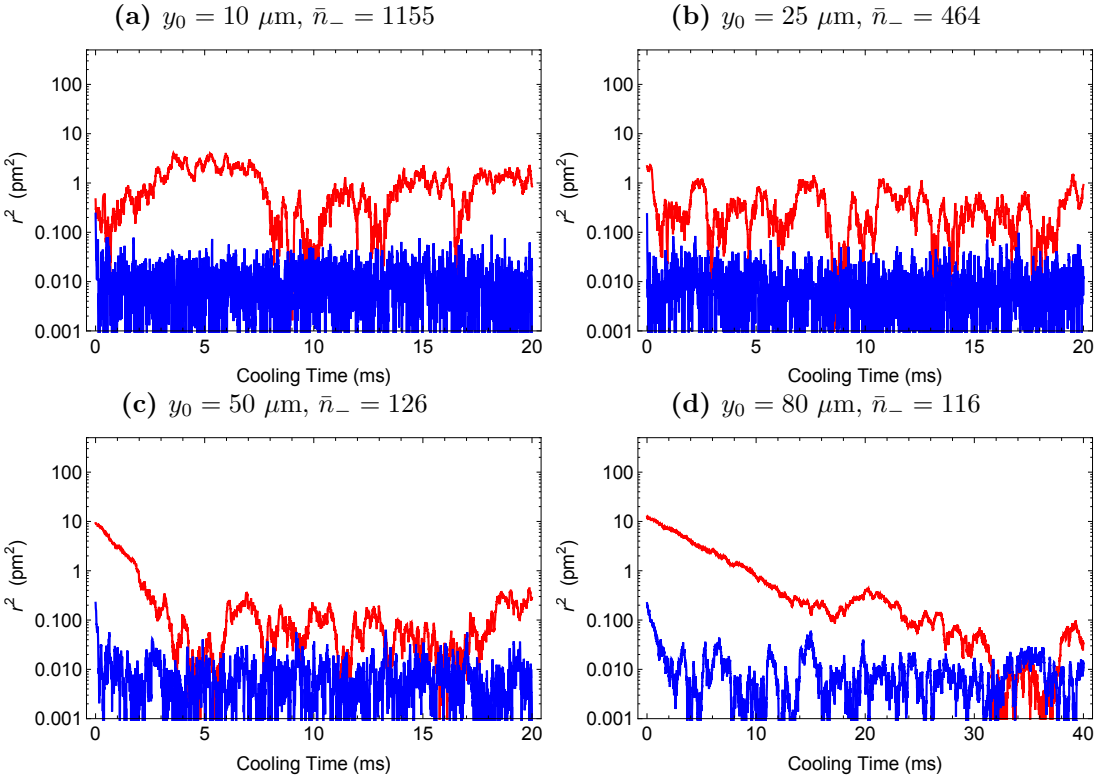

Figure 8.3: Amplitudes of motion for the magnetron (red) and modified cyclotron (blue). The average motional states is calculated between 10-20 ms (a)-(c) and between 20-40 ms for (d). Parameters: Trap potential 10 V, $\nu_z = 87$ kHz, $\nu_- = 5$ kHz, $\nu_+ = 724$ kHz,$V_a = 0.0$ V, $w_0 = 50$ μm, $P_0 = 8$ μW, $\delta = \Gamma/2$. All plots have the same initial conditions, but due to under sampling (a) and (b) starting points are missing.

figure 8.4. For both beam waists, all the magnetron phonon numbers converge when the beam offset gets large corresponding to almost no scatter. For the 50 μm beam waist the optimal position is in the $60 - 70$ μm region for all voltages, with the effective cooling range growing larger as the voltage is lowered. When the beam is broadened to a waist of 100 μm, no cooling is possible at 100 V and the ion is heated to a larger orbit. At 50 V, the ion remains in a stable state for offsets between $90 - 130$ μm whereas once the trapping potential becomes sufficiently

relaxed at 10 V cooling across a wide range of smaller offsets becomes effective. These data sets already suggest that for higher trapping voltages that are desirable for resolved sideband cooling, the beam gradient cooling method results in mean magnetron phonon numbers in the $10^3 - 10^4$ range without moving to even smaller beam waists.

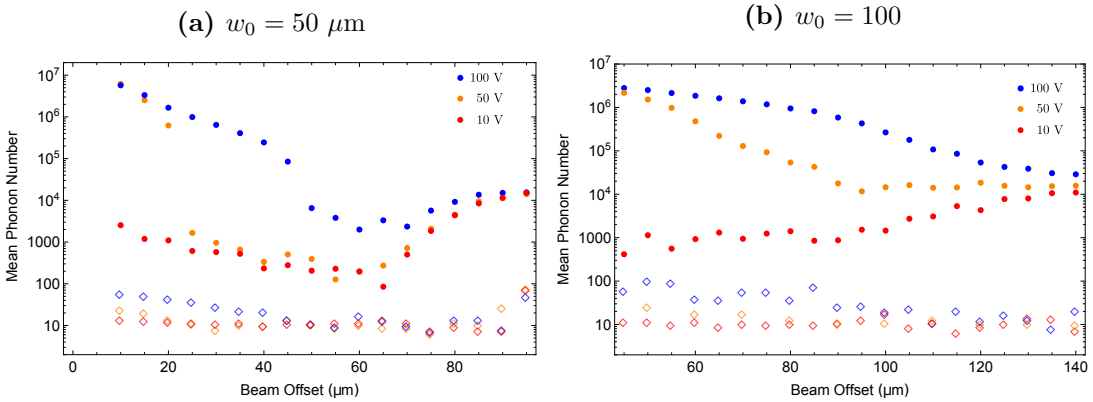

Figure 8.4: Average phonon numbers for the magnetron (circles) and modified cyclotron (diamonds) motions between 10–20 ms as a function of beam position for different trap voltages with beam waists (a) $w_0 = 50$ μm, (b)$w_0 = 100$ μm. Parameters: $V_{ax} = 0$ V, $P_0 = 8$ μW, $\delta = \Gamma/2$.

We now look at the effects of axialization on the cooling limits. We begin by showing the results of cooling as a function of axialization voltage for different beam waists where the beam is not offset from the trap centre in figure 8.5. The addition of even a modest amount of axialization already reduces the total amount of phonons in the system by orders of magnitude. As the axialization voltage increases, the coupling acts to reduce the difference between the phonon numbers of the two modes rather than their ratio resulting in the characteristic shape of the trend. In all these instances, however, the amplitude of the motions is never equalised. It is also clear to see that increasing the beam waist leads to more efficient cooling with lower demands on the axialization voltage. Thus unlike the gradient cooling that requires small beam waists, if no offset is included, a wider beam is preferable.

Ideally, we aim to combine axialization with an offset beam and hence we search for the optimal offset to achieve the lowest cooling limit. Using a moderate amplitude of 0.5 V on the axialization drive, we find in figure 8.6 that with beam waists of either 50 or 100 μm, we can comfortably reach limits below 100 phonons in each mode when offset to near the optimal positions from figure 8.4. The tolerance for remaining between the minimum and the 200 phonon mark is ≈ 20 μm after which the mean phonon numbers grow exponentially. The behaviour for offsets below optimum and above is different in that in the latter case the two mode amplitudes are nearly equalised. This is a consequence of a a residual oscillating amplitude exchange implying the steady state has not been reached due to the slow scattering rate at this particular power. The behaviour for larger offsets looks like that of figure 8.1d.

At these minimum offset positions, we can investigate the mean phonon number as a function of axialization voltage. From figure 8.7 we see that the mean phonon number gets exponentially smaller as a function of the voltage converging to $\bar{n}_{+,-} \approx 50$. The smaller beam waist offers a faster cooling rate, but the limit at large voltage appears to be independent of the beam shape for the cases considered.

If we now consider the optimal offset of $y_0 = 120$ μm for the best estimate of the physical

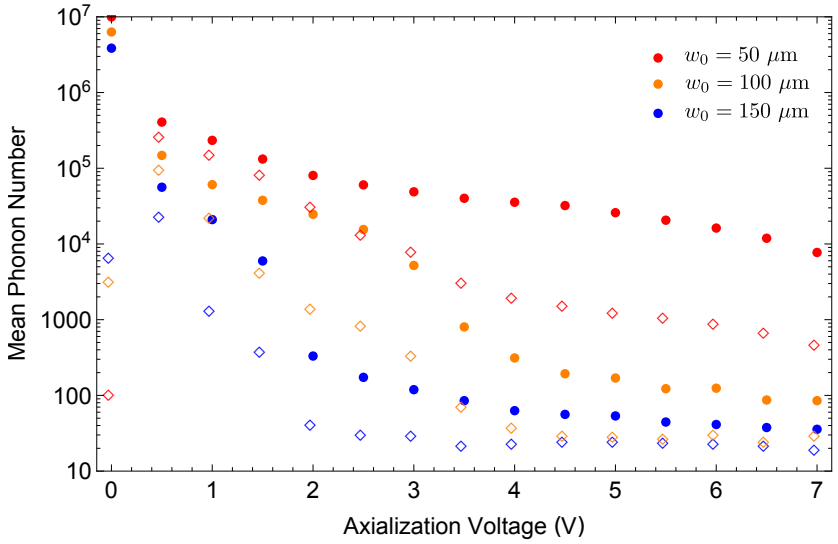

Figure 8.5: Average phonon numbers for the magnetron (circles) and modified cyclotron (diamonds) motions between 10–20 ms as a function of axialization voltage for different beam waists. Parameters: Trap potential 100 V, $\nu_z = 265$ kHz, $\nu_- = 52$ kHz, $\nu_+ = 677$ kHz, $y_0 = 0\ \mu$m, $P_0 = 8\ \mu$W, $\delta = \Gamma/2$.

beam waist $w_0 = 100\ \mu$m of the cooling lasers in our experiment, we can look at the mean phonon numbers as a function of trap voltage. Figure 8.8 tells us first that without axialization the magnetron motion grows exponentially with the voltage until it reaches a steady state at a large orbit 10s of μm in size. The modified cyclotron $\bar{n}$ remains low and only starts to grow at around 300 kHz. Including as little as 100 mV of axialization amplitude already results in an order of magnitude smaller magnetron motion plateau beginning around 300 kHz. The 0.5 and 1 V of axialization data show that a mean phonon number for both motions approaches the lower limit (within 10s of phonons) set by the modified cyclotron motion without axialization over the whole frequency range. Adding additional axialization above 0.5 V provides little to no additional gain.

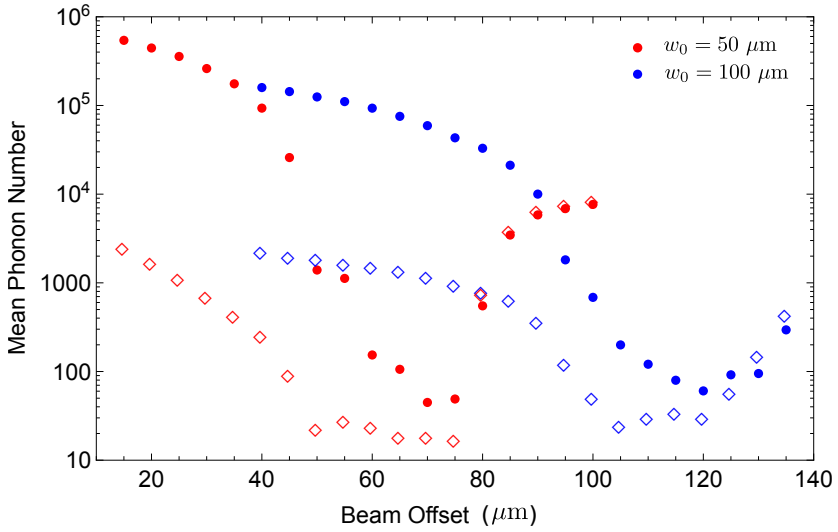

Figure 8.6: Average phonon numbers for the magnetron (circles) and modified cyclotron (diamonds) motions between 10–20 ms as a function of beam offset for different beam waists. Parameters: Trap potential 100 V, $\nu_z = 265$ kHz, $\nu_- = 52$ kHz, $\nu_+ = 677$ kHz, $V_a = 0.5$ V, $P_0 = 8\ \mu$W, $\delta = \Gamma/2$.

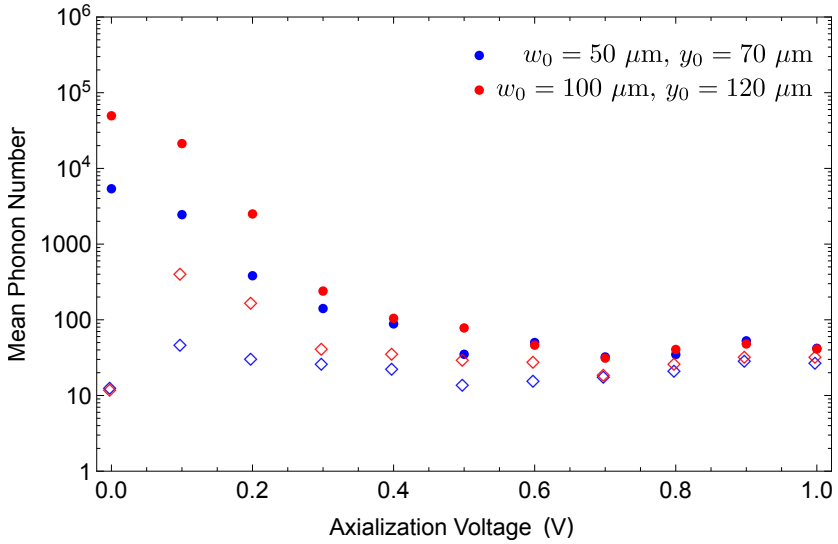

Figure 8.7: Average phonon numbers for the magnetron (circles) and modified cyclotron (diamonds) motions between 10–20 ms as a function of axialization voltage for different beam waist and offset combinations. Parameters: Trap potential 100 V, $\nu_z = 265$ kHz, $\nu_- = 52$ kHz, $\nu_+ = 677$ kHz, $P_0 = 8$ μW, $\delta = \Gamma/2$.

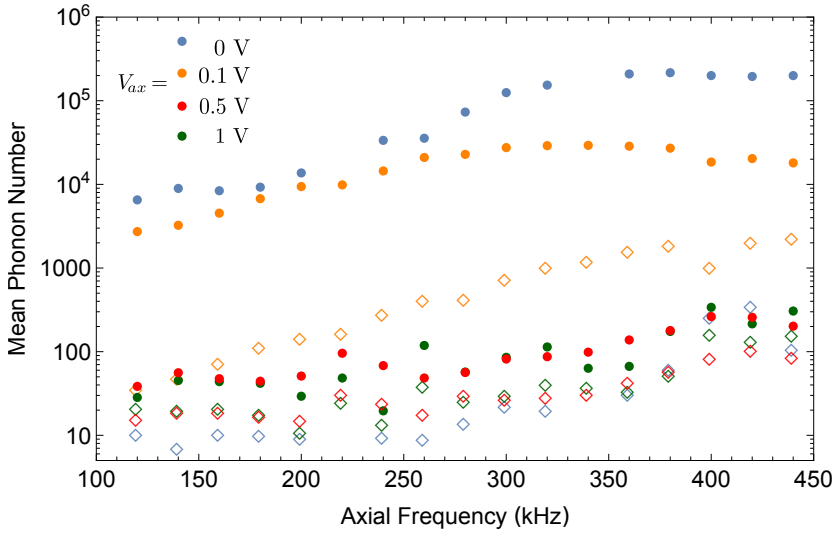

Figure 8.8: Average phonon numbers for the magnetron (circles) and modified cyclotron (diamonds) motions between 10–20 ms as a function of axial frequency ν_z for different axialization voltages. Parameters: $w_0 = 100$ μm $y_0 = 120$ μm, $\delta = \Gamma/2$.

To conclude, we summarize the general observations:

- When using gradient cooling without axialization, smaller beam waists allow for lower mean phonon numbers, with the optimal offset at $y_0 = 1.2 - 1.4 \times w_0$.
- These offsets are appropriate when including axialization as well. The beam waist is not as crucial to achieve low limits as a moderate amount of $V_{ax} = 0.5$V already yields mean phonon numbers below 100 for both modes, which is over an order of magnitude improvement in most cases.
- When there is no beam offset, axialization can still work but requires a larger V_{ax} to achieve the same mean phonon number at the same beam waist as if an offset is included for the beam waists studied. Unlike when an offset is present, larger beam waists cool more efficiently.
- When axialization is used with $w_0 = 100$ μm and $y_0 = 120$ μm, the whole frequency range of our trap becomes accessible with both modes remaining many orders of magnitude colder than if the axialization was not present. Even modest amounts of axialization ≈ 100 mV are sufficient to to confine the magnetron motion to $\bar{n}_- \sim 1000$ phonons.

8.2 Experimental Results

8.2.1 Doppler Cooling

The laser cooling sequence for performing radial Doppler cooling is much the same as the one used in the axial cooling section (6.1.1). There are, however some key differences in the experimental method that we summarise here.

- The radial beam power is significantly increased compared to the axial beam. For axial cooling, the radial/axial ratio was typically kept between 1.5-2, whereas for radial cooling it is around 10. This helps ensure a low scattering ratio of γ_z/γ_r that lowers Doppler limit for both motions as per equations 4.58, 4.59 even when the beam offset from the trap centre increases.
- Related to the previous point, we still require a high axial scattering rate to obtain a good signal to noise ratio during the readout phase. This can't be achieved by the radial beam alone since it is also the source of large background scatter. To overcome this problem, we repurpose the AOM that was used to attenuate the radial beam during the readout period to instead attenuate the axial beam during cooling and increase the power during readout.
- The beam offset that changes the gradient of intensity across the ion now has to be set much more carefully to obtain the lowest temperatures. During axial cooling, the beam pointing and consequently the radial temperature were optimised by eye, making sure the ion on the camera had no radial extent beyond that given by the optical resolution of our system. Motorised control of the beam pointing and an auxiliary CCD that records the beam position as it exits the trap are used in conjunction to make fine adjustments and obtain repeatable results.

- When working with axial modes, the axialization drive is kept on throughout the whole experimental sequence since we only require it to prevent the magnetron motion from ever growing too large. In the case of radial cooling, we wish to obtain an equilibrium between $\bar{n}_+ \approx \bar{n}_-$ which can only occur when the Doppler cooling lasers are on. Once they are turned off, the coherent exchange of phonons between the two modes will change the amplitude of each mode and since the drive will have a different phase during each experimental trial we will not be probing the distribution created during cooling. While the total $\bar{n}$ of both modes might be the same, the variance will be much larger. Hence it is crucial that the axialization drive is turned off simultaneously with the cooling lasers and must remain off during state preparation, probing, sideband cooling or for any other coherent operations.

After Doppler cooling in the absence of axialization, we expect both modes to be in a thermal state. As with a two ion crystal, we can thus model a well resolved sideband spectrum as a sum of excitation probability lineshapes given by equation 7.5. However, when the sidebands are not resolved, this approach is not valid as can often be the case for the magnetron motion when $\omega_- < \Omega_0$. One way to quickly assess the temperature (and $\bar{n}$) is to look at the width of spectral features, which should, in the limit of low saturation, look as a comb of sideband heights modulated by a Gaussian envelope that is dependent on the Doppler shift. When an ion is in a thermal state, its Fock state occupation probability distribution is proportional to the Maxwell-Boltzmann factor [120]

$$P_n \propto e^{-E_K/(k_B T)} \tag{8.9}$$

where E_K is the kinetic energy of the radial motion, k_B is the Boltzmann constant and T is temperature. The energy for an ion with velocity v is given by Mv^2 as we have two radial modes contributing a degree of freedom. Combining this with the Doppler frequency shift $v = d\nu c/\nu_0$ of the spectroscopy transition f_0, the exponential factor is equal to:

$$\exp\left[-\frac{Mc^2}{k_B T \nu_0^2}(d\nu)^2\right] \tag{8.10}$$

which now takes the form of a Gaussian in frequency. For a Gaussian envelope with zero mean and standard deviation $\sigma_\nu = d\nu$ we obtain the temperature and mean occupation numbers

$$T = \frac{M\lambda^2\sigma^2}{k_B} \tag{8.11}$$

$$\bar{n}_+ \approx \frac{M\lambda^2\sigma_\nu^2\omega_1}{2\hbar\omega_+^2} \tag{8.12}$$

$$\bar{n}_- \approx \frac{M\lambda^2\sigma_\nu^2\omega_1}{2\hbar\omega_-^2} \tag{8.13}$$

where λ is the wavelength of the 729 nm laser. Our first radial spectroscopy was performed without any axialization at 10 V where $\omega_m = 4.86$ kHz and is smaller than the Rabi frequency of the probe beam used hence it remained unresolved. The results in 8.9 highlight the importance of the relative powers of the radial and axial cooling beams. As equation 4.58 makes clear, the radial motion Doppler cooling limit depends on the relative scattering rate γ_z/γ_r. Going from (a) to (b) the laser intensity ratio was reduced by a factor of 5, for a an approximate four fold

improvement in the final $\bar{n}_+$ from approximately 110 to 30. The latter value approaches the calculated value of $\bar{n}_+ = 18$ for the Doppler limit when the radial scattering rate is equal the axial scattering rate and $y_0 \to \infty$. Focussing now on the magnetron, we get $\bar{n}_- \approx 1900$ for

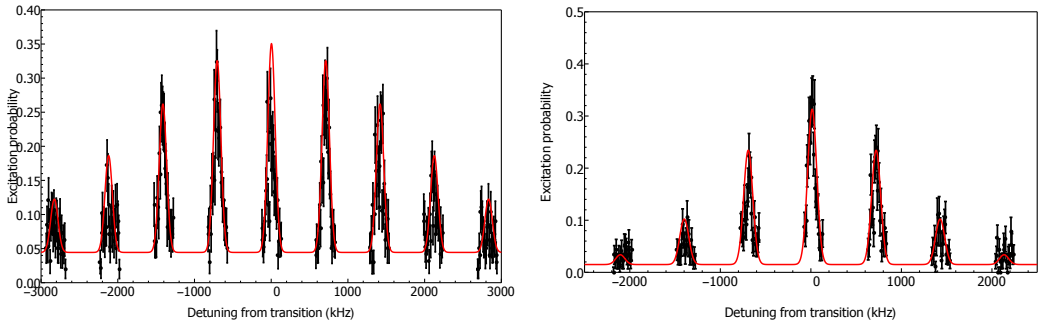

(a) **(b)**

Figure 8.9: Radial Spectra of a single ion after Doppler cooling at $\nu_+ = 708$, $\nu_- = 5.3$ kHz. The average occupation obtained from matching the data for a comb of Gaussian sidebands modulated by a Gaussian envelope gives $\bar{n}_+ \approx 110$ and $\bar{n}_+ \approx 30$ for (a) and (b) and $\bar{n}_- \approx 1900$ for both. In (a) the beam intensities are 8 μW and 18 μW for axial and radial respectively, whereas for (b) they are 0.9 μW and 19 μW. No axialization used.

both plots, indicating that the scattering ratio is not the limiting factor in this case. Since we don't have a way to directly measure w_0 and the modified cyclotron is largely insensitive to it, we don't have a direct $\bar{n}_m$ Doppler limit comparison value. Assuming we have a beam waist of $w_0 = 100$ μm as estimated in section 5.2.2, our measurement is then consistent with the simulation result in figure 8.4b for beam offsets in the 100 μm range.

From these results it is clear that even at very low endcap voltage, where the magnetron cooling with the beam offset is most efficient, we are still left with a $\bar{n}_-$ that is much too high to sideband cool to the ground state. To significantly reduce the magnetron mode's mean phonon number we thus require the axialization technique. To highlight the effects on both the cyclotron and magnetron modes we perform four measurements in sequence, two without axialization and the other two with 500 mV of RF applied to the ring electrodes. Figure 8.10 shows this technique achieving a reduction of the magnetron phonon number by almost a factor of 10, while only increasing the modified cyclotrons' by 50% yielding a large net reduction of the total phonon number. This is a much more promising starting position for sideband cooling. From the spectra in figure 8.10 we also see that at a Rabi frequency $\Omega_0/2\pi = 28$ kHz, the individual magnetron sidebands are still not adequately resolved. As a consequence, cooling on a blue magnetron sideband of the carrier with a large Ω_0 (required for fast cooling) will produce a strong off resonant excitation of the carrier and even heating on the red sidebands. To prevent this, we want to be able to work at trap voltage where ω_- is larger than Ω_0, but not so large that the Doppler cooling even with axialization becomes inefficient. Motivated by the simulation results of section 8.1.2, we performed Doppler cooling at 100 V where $\nu_- = 52$ kHz is and thus should yield sufficiently resolved sidebands. Using 1 V of axialization we obtain very promising mean phonon numbers for both modes of $\bar{n}_+ = 96(5)$ and $\bar{n}_- = 136(8)$ from a fit to the full sideband dynamics in figure 8.11. This result is representative for the typical Doppler cooling that we achieve and forms the starting of our sideband cooling studies.

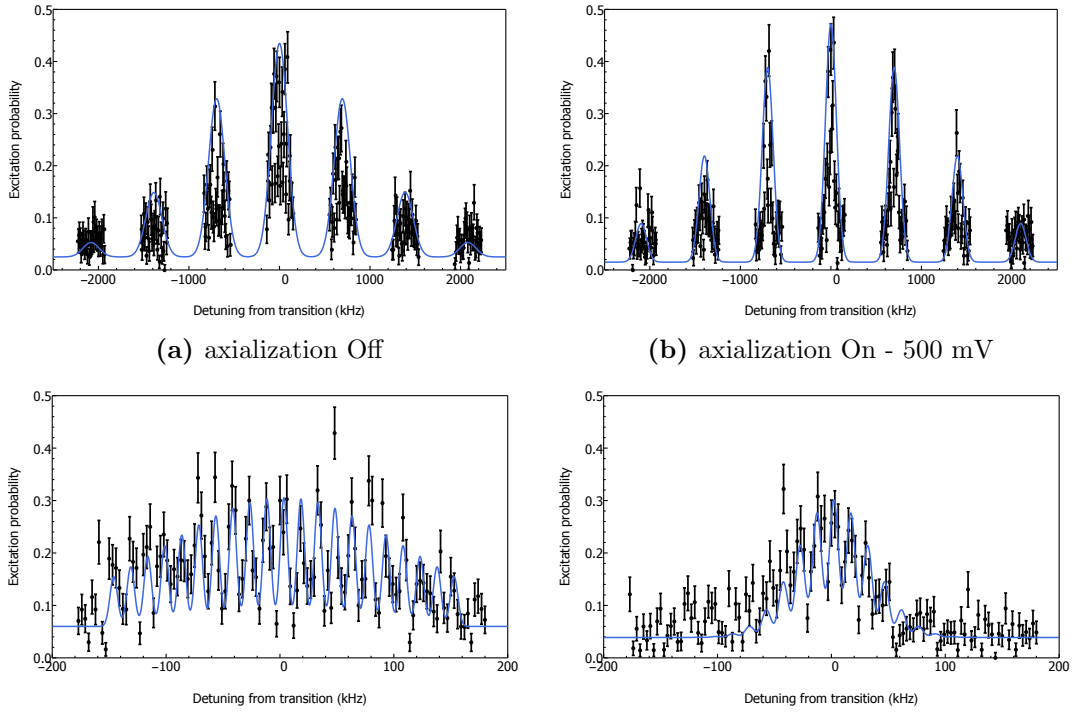

(a) axialization Off **(b)** axialization On - 500 mV

(c) axialization Off **(d)** axialization On - 500 mV

Figure 8.10: Radial Spectra of a single ion after Doppler cooling at 30 V, $\nu_+ = 693$ kHz, $\nu_- = 14.8$ kHz. The average occupation obtained from matching the data for a comb of Gaussian sidebands modulated by a Gaussian envelope: from (a) and (b) $\bar{n}_+ \approx 31$ and $\bar{n}_+ \approx 45$, and from (c) and (d) $\bar{n}_- \approx 900$ and $\bar{n}_- \approx 100$ respectively. All other parameters are kept same between figures. 500 mV of axialization RF is applied in (b) and (d)

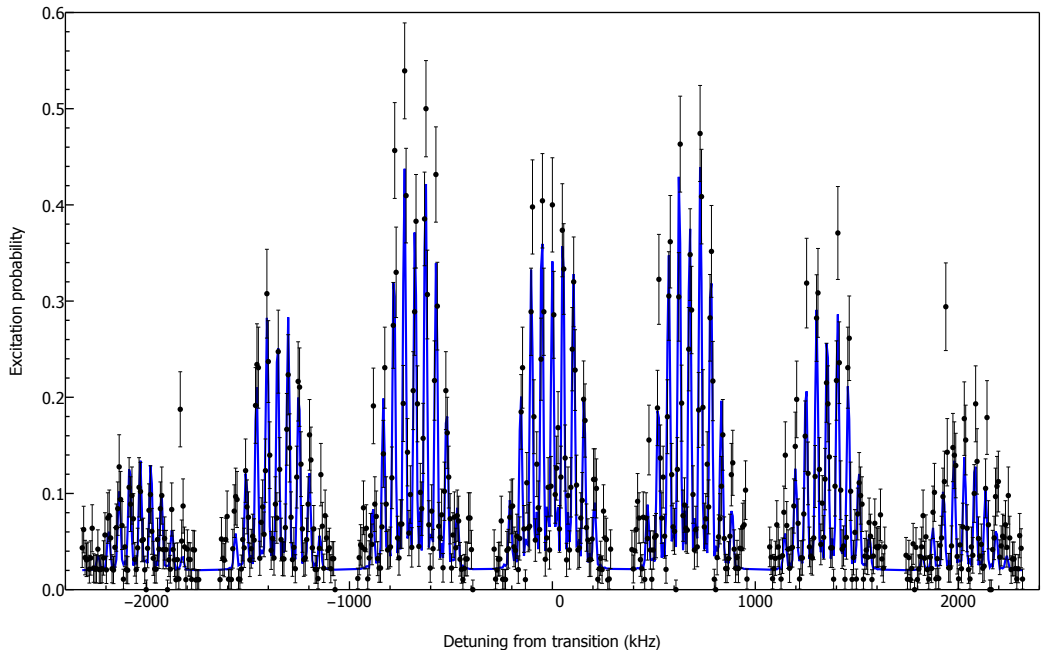

Figure 8.11: Radial Doppler spectrum at 100V with $\nu_+ = 677$ kHz, $\nu_- = 52$ kHz taken with 1 V axialization. Full fit to two mode dynamics of equation 7.5 gives the mean phonon numbers $\bar{n}_+ = 96(5)$ and $\bar{n}_- = 136(8)$ and $\Omega_0/2\pi = 26$ kHz

8.2.2 Sideband Cooling

As the previous section showed us, the axialization technique helps us reach states with $\bar{n} \sim 100$ in each mode, which is still far outside the Lamb-Dicke regime and will require a judicious application of higher order sidebands to ensure there is no population trapped in the coupling minima of the sidebands. Taking the mean phonon number of $\bar{n}_- = 136$ from the result in figure 8.11, there is almost 25% of the population left above the first order sideband coupling minimum at $n = 196$, which is very similar to that of the COM mode for two ions in a 1D chain at $\nu_{COM} = 162$ kHz, which we have managed to successfully cool to the ground state. The approach we thus took is again very similar in that we want to address a set of sidebands that on average always have appreciable coupling to all possible phonon states. In the interest of keeping cooling rates high, we also did not cool on sidebands that change the phonon numbers of both modes simultaneously, as they are usually a factor of ≈ 10 weaker.

Our main experimental result was obtained with a 68 ms long cooling sequence shown in in table 8.1 at a trap potential of 100 V where $\nu_- = 52$ kHz. To prevent off resonant excitation of the carrier when cooling on the first magnetron sideband, the intensity of the 729 nm laser was reduced by approximately 50% (The AOM RF power was reduced by exactly 50%, but there is some residual non-linearity) and the effective excited state linewidth was usually maintained at around $\tilde{\Gamma}/2\pi = 5 - 10$ kHz by appropriately detuning the 854 nm laser. The third order magnetron sideband was also included to add additional cooling for states in high n without much off resonant carrier excitation. As with the axial sideband cooling, careful compensation of the Stark shift induced by the 854 nm laser is crucial to accurately target all sidebands. Applying this sequence to an ion Doppler cooled under 1 V of axialization with $\Omega_0 \approx 30$ kHz, we obtain the spectrum shown in figure 8.12. The asymmetry of the modified cyclotron modes is very pronounced with a fit to a thermal model estimating a mean phonon number of $\bar{n}_+ = 0.30(6)$. Looking at 8.12(b) we can also see an asymmetry present in the magnetron sidebands with the blue sideband now rising higher as expected due to the negative total energy of the magnetron. The mean magnetron phonon number given by the thermal model fit is $\bar{n}_- = 1.7(2)$ implying a ground state occupation probability of $P_0 = 40\%$. However, looking at the continuous spectrum there are some potential spurious features. There appear to be single data point excesses in the vicinity of $2\nu_-$ and $3\nu_-$, which are not accounted for in the thermal model given the estimated $\bar{n}_-$. On the other hand, these features are not mirrored at $-2\nu_-$ and $-3\nu_-$ casting doubt as to whether they correspond to real shelving events. A population trapping model with a fraction of the population left at the coupling minimum of $n_- = 196$ would not account for these excitations without also creating visible magnetron sidebands at $\nu_+ - 2\nu_-$ and $\nu_+ - 3\nu_-$ which are also not observed. Another possible explanation is that there is some non-thermal distribution to the magnetron phonon states, which we cannot rule out, but the rate equation simulation of section 4.4.2 does not support this hypothesis even when considering strong carrier excitation and all third order decay pathways.

Due to the time constraints, we were not able to return to further investigate these higher order carrier sidebands as they only became apparent in one of our final experimental runs. As things stand, the data supporting a non-thermal distribution is not conclusive either way and the asymmetry of the first order sidebands requires a significant population in the $n_- = 0$ state hence we will for now assume that we can keep using a thermal model for the phonon distributions in its vicinity. This result would thus suggest the first ever demonstration of a

Sideband	Pulse length (ms)	AOM RF Power(%)
2^{nd} Cyc.	5	100
1^{st} Cyc.	10	100
3^{rd} Mag.	5	100
2^{nd} Mag.	5	100
1^{st} Mag.	5	50
2^{nd} Cyc.	5	100
1^{st} Cyc.	5	100
3^{rd} Mag.	5	100
2^{nd} Mag.	5	100
1^{st} Mag.	5	50
1^{st} Cyc.	10	100
1^{st} Mag.	2	50
1^{st} Mag.	1	100

Table 8.1: 68 ms sideband cooling sequence for both radial modes.

simultaneous ground state occupation for both modes of 32%. There are two excess data points that also stand out near $-\nu_+ - \nu_-$ and $-\nu_+ + \nu_-$, though they do not exactly align with the expected magnetron peak positions and they are not seen in a separate measurement with a similar cooling sequence (see table 8.2) shown in figure 8.13. The thermal model seems to account for the data better this time around, resulting in mean phonon numbers: $\bar{n}_+ = 0.28(6)$ and $\bar{n}_- = 1.9(4)$. Although this data set lacks the carrier and its magnetron sidebands, the extracted parameters are consistent with those of figure 8.12.

We have one further measurement using a sequence almost identical to the one in table 8.1 where we scan over both the first order carrier magnetron sidebands and the cyclotron sidebands. The resulting fit to the data, shown in figure 8.14 gives the lowest measured mean phonon numbers of $\bar{n}_+ = 0.01(7)$, $\bar{n}_- = 0.4(1)$. The parameters errors are larger in this case due to the data only having 100 repeats per point, but the reduced Rabi frequency of $\Omega_0/2\pi = 7.3(4)$ kHz should ensure that there is no residual excitation of the carrier at the magnetron sidebands. While the numbers might appear too low due to excess random suppression of the red sidebands, the red(blue) cyclotron or magnetron sidebands have an unambiguously strong asymmetry. Considering all three results together, we can make a convincing case for the ground state cooling of both modes to near the ground state without any significant population trapping. To support this conclusion we will assess our ability to perform coherent Rabi oscillation in section 8.2.4, but first we will turn our attention to characterising the heating rate since it can have a potential direct impact on the motional coherence.

8.2.3 Heating Rate

In section 6.3.1 we established that we observe a very low heating of ≈ 1 phonon per second for the single ion axial mode irrespective of trap frequency. This attested to a low electric field noises at the ion mostly as a consequence of large endcap electrode to ion distance and low Johnson noise in the endcap potential. For the radial heating rate, the ion still has the same electrode-ion distance, but the noise on the split ring radial electrode can be quite different as

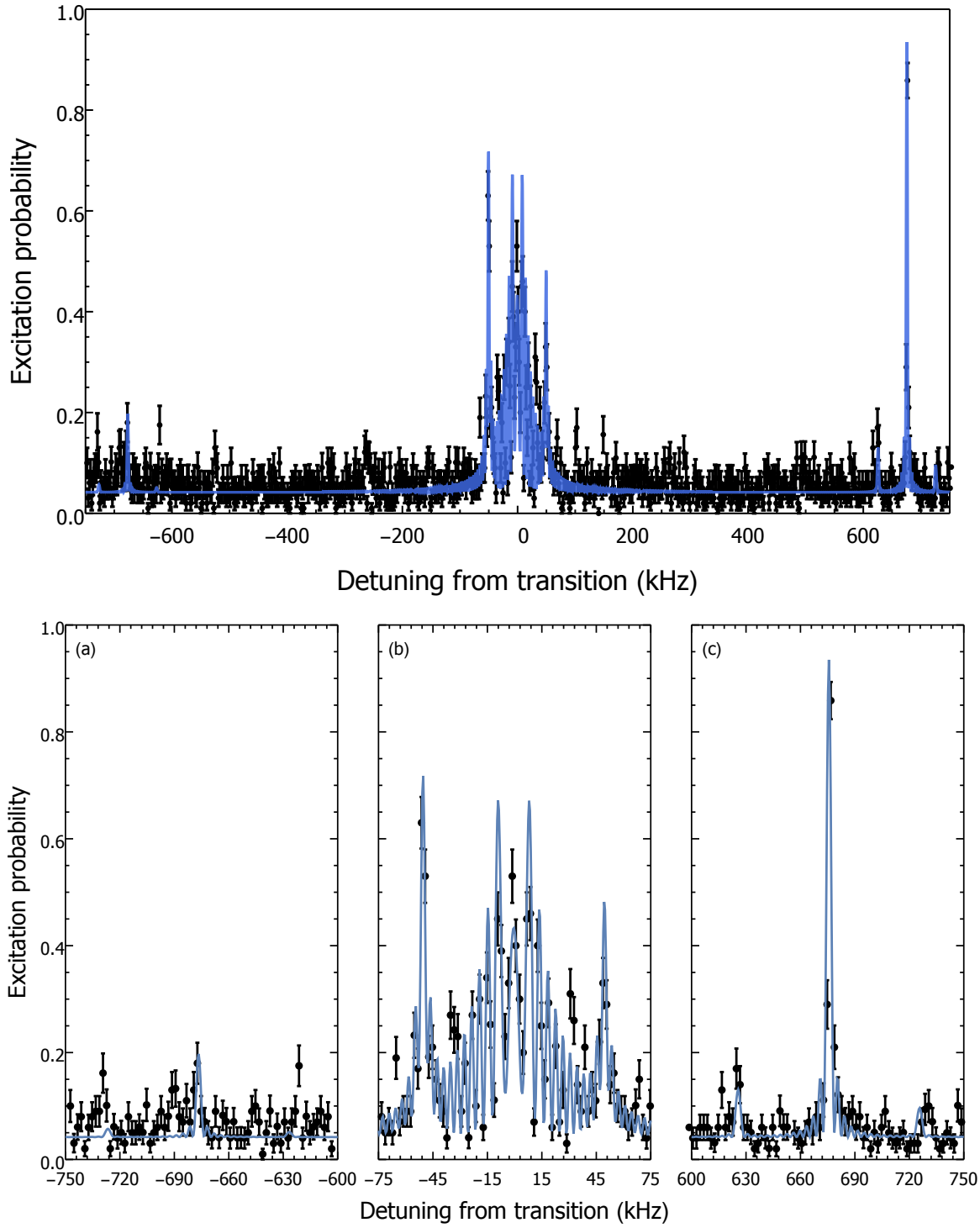

Figure 8.12: *Top* – Continuous spectrum after 69 ms of sideband cooling (see table8.1) with a probe time of 280 μs. *Bottom* – Zoomed in plots around (a) red cyclotron sideband (b) carrier with magnetron sidebands and (c) blue cyclotron sideband. Fit parameters using a two mode thermal model: $\bar{n}_+ = 0.30(5)$, $\bar{n}_- = 1.7(2)$, $\Omega_0/2\pi = 14.13(3)$ kHz.

the voltage offsets on each segment are produced independently. To perform an accurate heating rate measurement we cool the radial motion of an ion at 100 V endcap potential using the same cooling sequence as in table 8.1 and afterwards we add a delay period with all lasers off for a given period of time before probing the first order modified cyclotron and magnetron sidebands of the carrier. We fit all the sidebands at different wait times simultaneously with the same

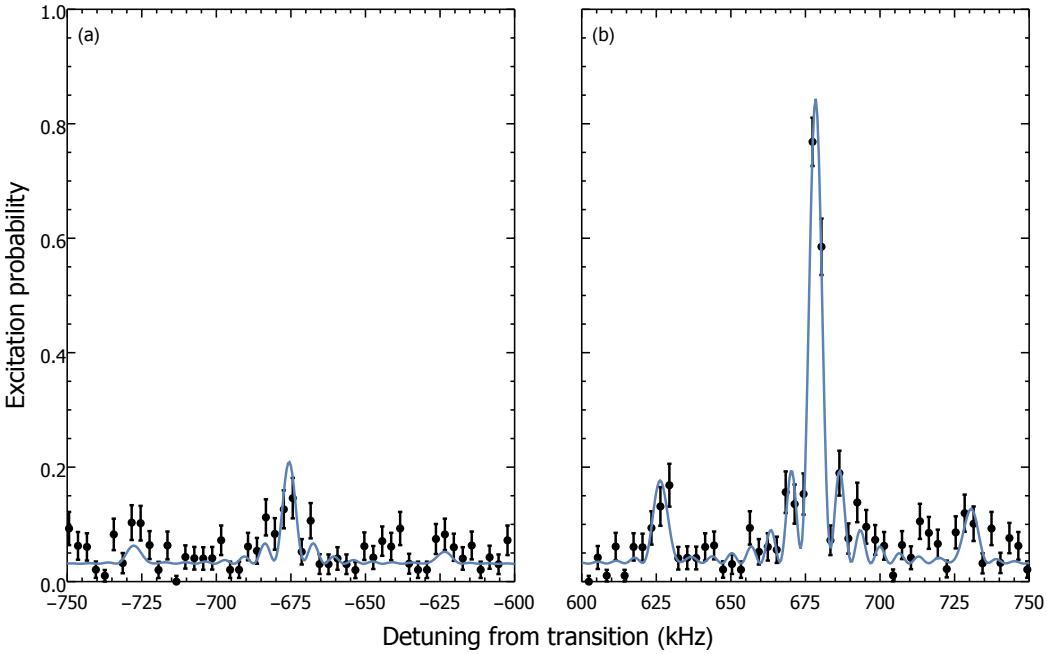

Figure 8.13: Spectrum after 66 ms of sideband cooling (see 8.2) probed for 280 μs. Fit parameters to the two mode thermal model: $\Omega_0/2\pi = 29.5(11)$ kHz, $\bar{n}_+ = 0.28(6)$, $\bar{n}_- = 1.9(4)$.

Sideband	Pulse length (ms)	AOM RF Power(%)
2^{nd} Cyc.	10	100
1^{st} Cyc.	10	100
3^{rd} Mag.	10	100
2^{nd} Mag.	10	100
1^{st} Mag.	10	100
1^{st} Cyc.	10	100
1^{st} Mag.	5	100
1^{st} Cyc.	1	100

Table 8.2: 66 ms sideband cooling sequence for both radial modes.

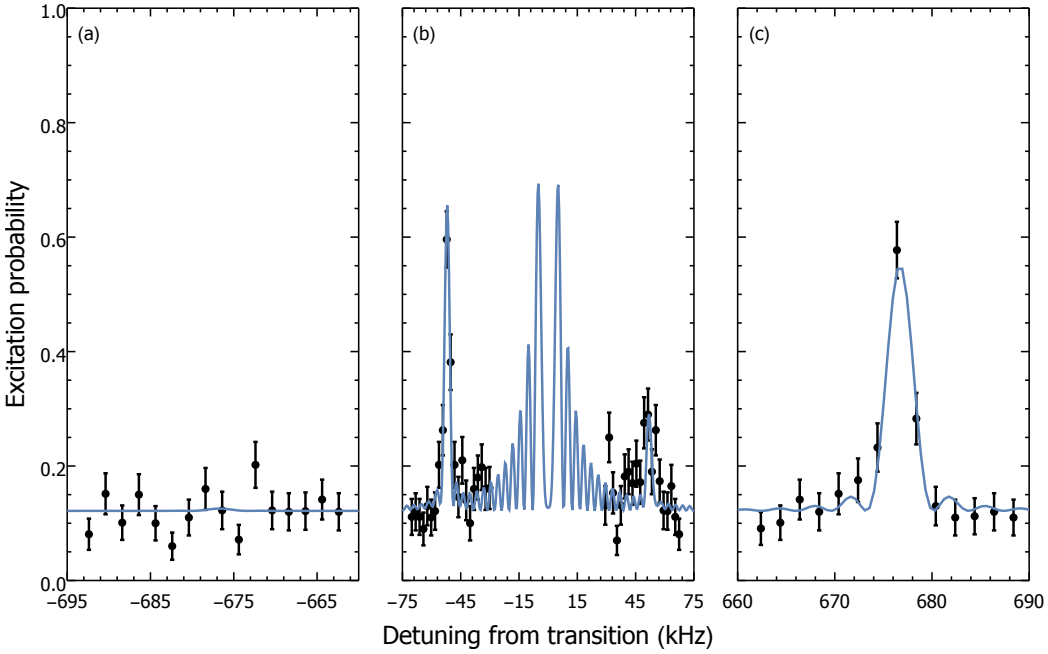

Figure 8.14: Spectrum after 69 ms of sideband cooling probed for 280 μs. Fit parameters to the two mode thermal model: $\Omega_0/2\pi = 7.3(4)$ kHz, $\bar{n}_+ = 0.01(7)$, $\bar{n}_- = 0.4(1)$. This spectrum was taken with only 100 repeats per data point.

fixed offset and Rabi frequency parameters only allowing the relevant mean phonon numbers to vary. The resulting fits are presented in figure 8.15a. Immediately we see that for much shorter waiting times than for the axial mode the red modified cyclotron and blue magnetron sidebands begin rising. The linear fit to the extracted mean phonon numbers in 8.15b indicates a large heating rate of $\dot{\bar{n}}_+ = 240(30)$ s^{-1} and $\dot{\bar{n}}_- = 250(50)$ s^{-1}. Both the heating rates are a radical departure from the axial result and suggest a noise on the radial ring electrodes that is orders of magnitude larger and appears flat in frequency since the magnetron and modified cyclotron are separated by 625 kHz.

One immediate factor to rule out was the leakage of RF from the axialization drive. Since the axialization is required to achieve ground state cooling at 100 V we could not simply repeat the experiment without it. Instead, we Doppler cooled an ion at 10 V with all axialization circuitry disconnected and then sideband cooled just the modified cyclotron motion to near the ground state with 20 ms of cooling on its first red sideband. Using the relative asymmetry of the sideband heights to estimate the mean phonon number, we noticed no improvement in the modified cyclotron heating rate.

The most likely culprits are thus the DC offsets on the ring electrode segments. The offsets are produced by 4 voltage references with 40 ppm/V line regulation powered from the same regulated 12 V power supply and then pass through individual potentiometers before connecting to the trap electrodes. Each of these references can introduce differential noise relative to the others unlike the endcap electrodes which have no further active components after the high voltage power supply[1]. A combination of multiple electrode segments with additional Johnson noise in the potentiometers could point a way to a potential explanation for the observed heating rates, though other factors cannot be ruled out without quantitative measurements of the noise spectrum at the electrodes.

[1]Only when the transistor circuit to adiabatically drop the voltage is not connected.

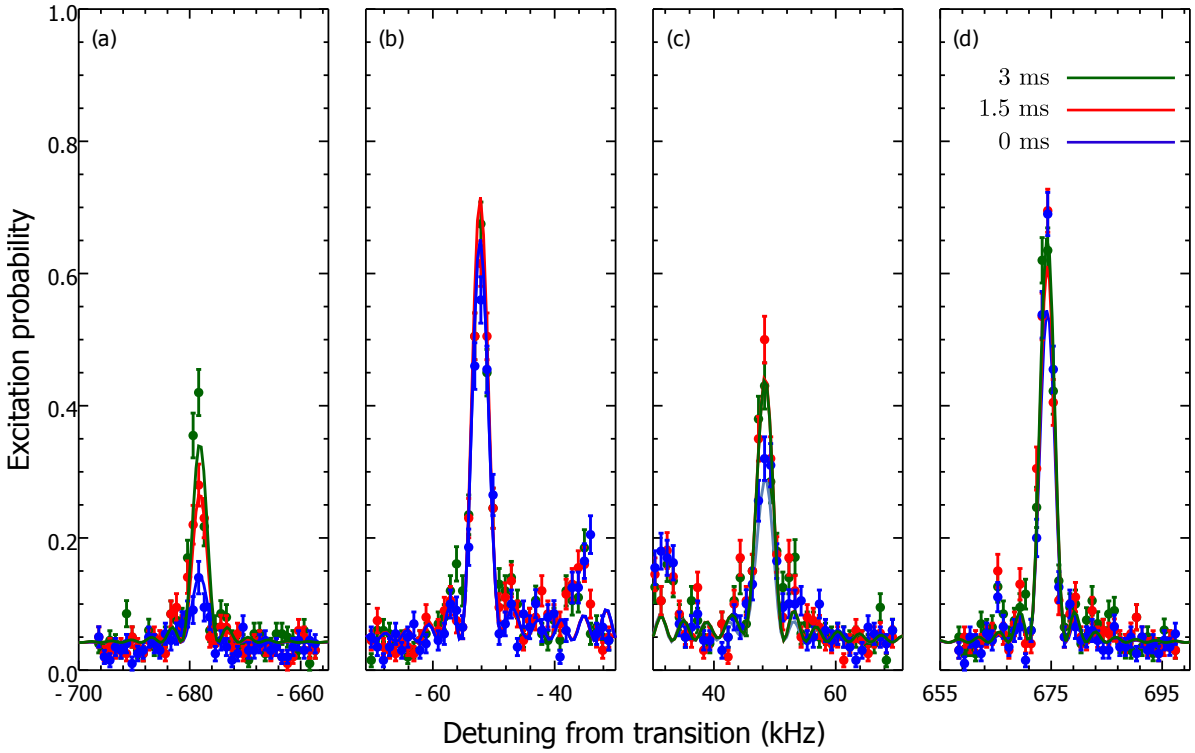

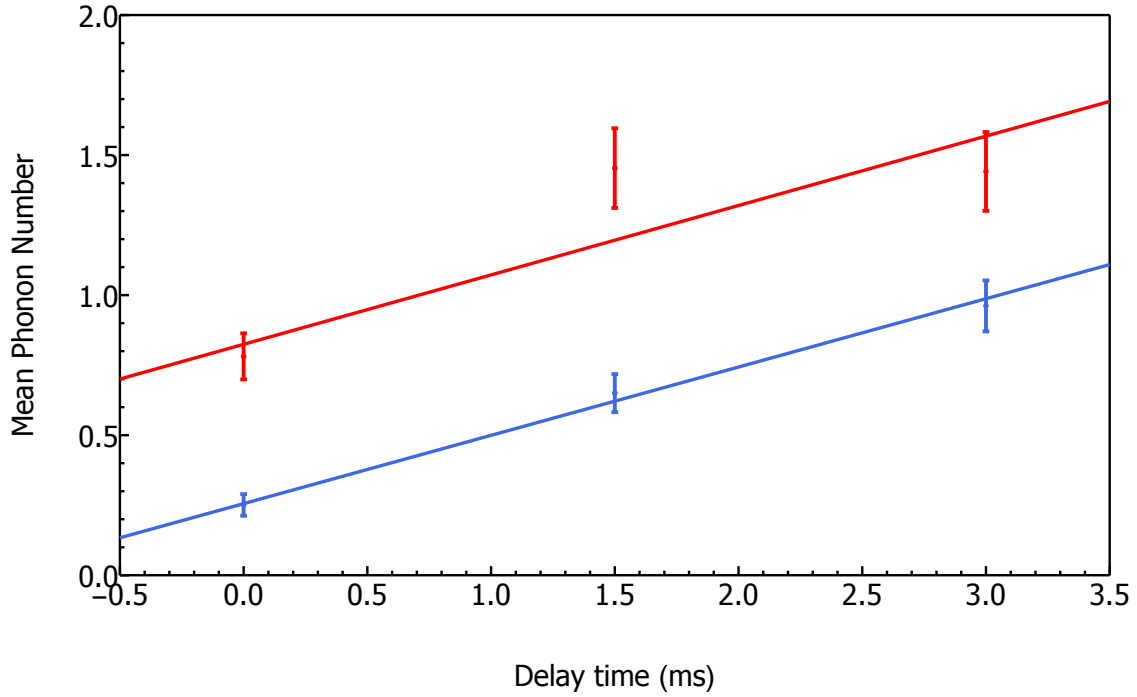

Figure 8.15: *Top* – Heating rate spectra with 0, 1.5 and 3 ms wait time inserted between sideband cooling (see table 8.1) and a 280 μs probe centred around (a) $-\nu_+$, (b) $-\nu_-$, (c) ν_- and (d) ν_+. *Bottom* – The fitted mean phonon numbers of the magnetron (red) and cyclotron (blue) display linear heating rates of $\dot{\bar{n}}_+ = 240(30)\ \mathrm{s}^{-1}$ and $\dot{\bar{n}}_- = 250(50)\ \mathrm{s}^{-1}$.

8.2.4 Rabi Oscillations

We first look at Rabi oscillations of the carrier recorded just after the spectrum of figure 8.13 using the same cooling sequence. The carrier Rabi frequency is only sensitive to n_+, n_- to second order in η_r near the ground state, which means that it won't give us a very accurate measure

of either mode's average phonon number, nor can it distinguish their individual contributions. Nonetheless, we can ascertain that we are far from a thermal regime where the coherence would die out much faster. The data for this experiment, shown in figure 8.16, exhibits coherent Rabi flopping with an exponential decay of the visibility. The following model is used to fit the data:

$$P_e(t) = \sum_{n_+,n_-}^{10} \frac{\bar{n}_+^{n_+}}{(\bar{n}_+ + 1)^{n_+ + 1}} \frac{\bar{n}_-^{n_-}}{(\bar{n}_- + 1)^{n_- + 1}} \left(\frac{1}{2} - \frac{1}{2} e^{-t/\tau_e} \cos \Omega_{n_+,n_+}^{n_-,n_-} t \right) \tag{8.14}$$

yielding a coherence time of $\tau_e = 166(14)$ ms and mean phonon numbers $\bar{n}_+ = \bar{n}_- = 0.0(7)$. As expected, the error on the last two parameter is rather large, but despite this the values are consistent with the low mean phonon numbers we obtain from the spectral measurements. It is also worth noting that despite the noise eater being turned on the coherence time implies a Rabi frequency fractional error of $d\Omega/\Omega = 0.031$, which is almost the same as for the case of an axial spectrum without the noise eater. One possible explanation for this is that there is an excess of polarisation noise in the radial fibre compared to the axial, since we did not perform the same level of careful optimisation to enhance the suppression of the orthogonal polarisation mode. Since the spectrum is short enough, heating effects are expected to be too small to be detectable. If we were not constrained by time, it would have been beneficial to conduct a more thorough study of the Rabi oscillation coherence in the same manner as we had performed for the axial addressing in section 6.2.2

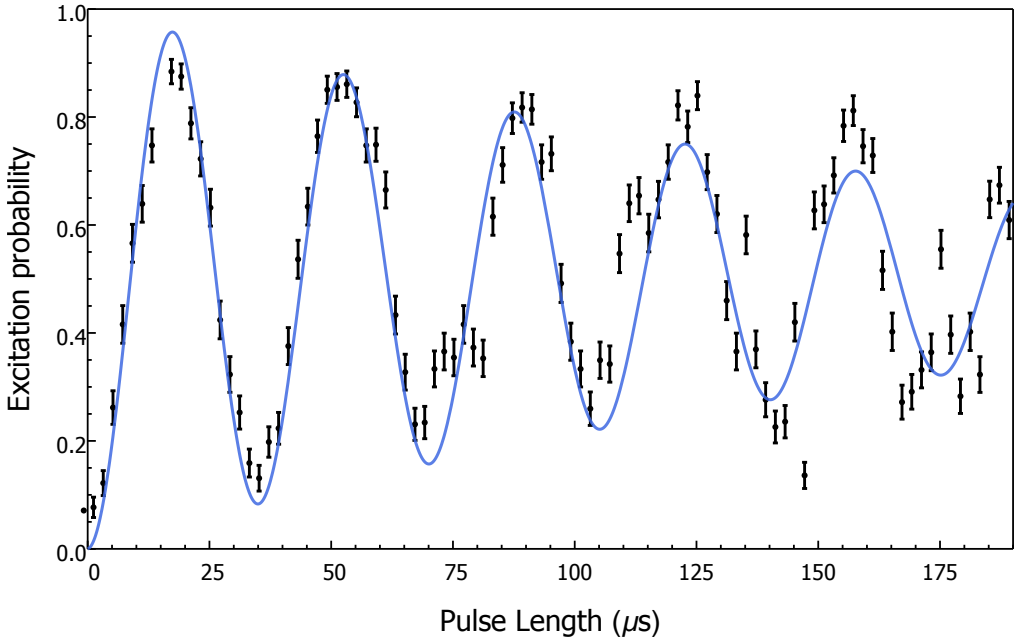

Figure 8.16: Rabi oscillation on the carrier at endcap voltage 100 V, $\nu_+ = 677$ kHz. Fitted parameters: $\Omega_0/2\pi = 28.9(5)$ kHz, $\bar{n}_+ = \bar{n}_- = 0.0(7)$, $\tau_e = 166(14)$ ms corresponding to $d\Omega/\Omega = 0.031$

To gain more precise information about the coherence of each mode, we need to drive their motional sidebands, which have a much stronger dependence on n. Figure 8.17 shows a Rabi oscillation on the first blue sideband of the modified cyclotron after sideband cooling with the sequence of table 8.1 with an additional 500 μs on the first magnetron BSB and 200 μs on the first modified cyclotron RSB at 50% RF power. One immediate feature is the shape of

the oscillations which follows an almost purely sinusoidal form with an exponential visibility decay. Unlike for the carrier, even for values of $\bar{n}_+ \approx 1$, we would see clear visual evidence of interference between different Rabi frequencies. To extract a value using equation 8.14 we fix $\bar{n}_- = 1.3$ (unweighted mean of the three measurements in previous section) and allow all other parameters to float. The fitted mean phonon occupation of the modified cyclotron $\bar{n}_+ = 0.15(3)$ once again confirms that we have cooled a significant part of the population to the ground state. The measured coherence time implies a fractional error $d\Omega/\Omega = 0.096$ which is inconsistent with that measured on the carrier and potentially reveals another decoherence mechanism. A possible source of this additional noise could be due to the heating rate of ≈ 250 phonons s^{-1} . Since the modified cyclotron spectrum has a much lower Rabi frequency, its laser noise induced decoherence timescale becomes comparable to the time for the absorption probability of at least one phonon to approach 0.5. If we include a very crude linear time dependence to $\bar{n}_+$ with a rate given by $\dot{\bar{n}}_+$ then the estimated fractional error due to the laser would drop down to $d\Omega/\Omega = 0.052$. However, at the moment, the data cannot distinguish with a high degree of confidence between these two models. If our laser/qubit stability was an order of magnitude higher, we would be able to more precisely measure the heating rate using the sideband Rabi oscillations.

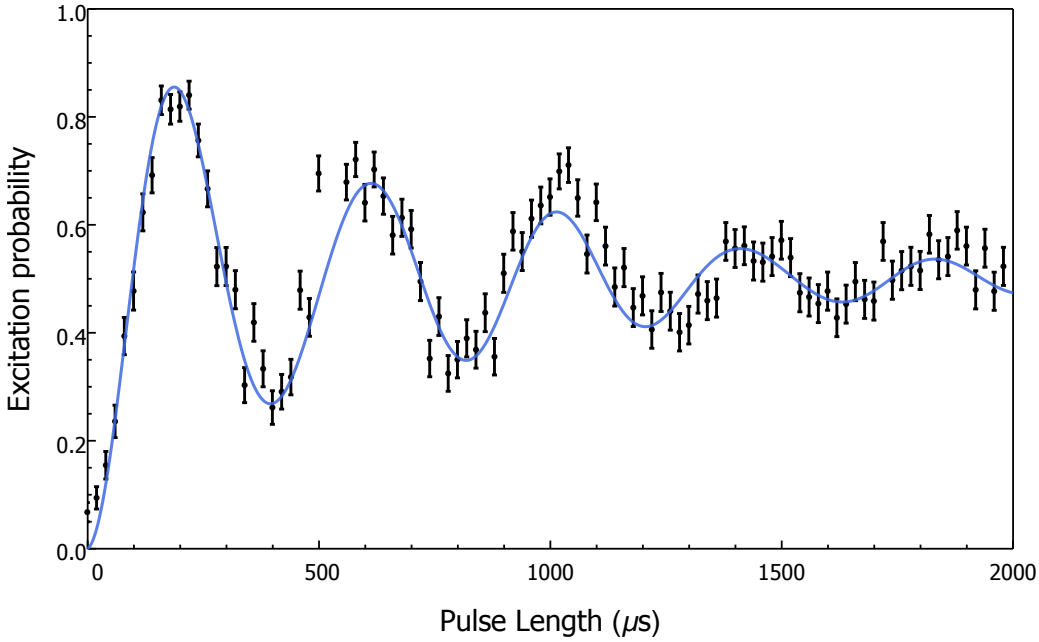

Figure 8.17: Rabi oscillation on the modified cyclotron blue sideband at endcap voltage 100 V, $\nu_+ = 677$ kHz. Fitted parameters for a fixed $\bar{n}_- = 1$: $\Omega_0/2\pi = 20.70(7)$ kHz, $\tau_e = 780(40)\mu$s, $\bar{n}_+ = 0.15(3)$, $d\Omega/\Omega = 0.096$.

Ultimately, these data sets provide additional evidence that we have indeed cooled most of the population to near the ground state of motion for both modes, however they also highlight the current limitations of our system to perform coherent operations. The decoherence rate compares unfavourably to the axial modes due to the influence of the increased Rabi frequency noise from due to the laser polarisation and the effects of the heating can become appreciable at low Rabi frequencies and long pulse lengths. There is still more work to be done characterising the behaviour of the radial motion, including Rabi oscillations on the magnetron which still suffer from off-resonant carrier excitation at $\nu_- = 52$ kHz. Based on the results of section 8.1.2

we still have some room to go higher in trapping voltage before the temperature after Doppler cooling begins to climb quickly. Increasing the frequency of the magnetron mode will reduce this off-resonant excitation and allow us to perform high contrast Rabi oscillations of the magnetron mode.

CHAPTER 9

CONCLUSION AND OUTLOOK

Since beginning work on this experiment, we have made large strides to bring the coherent control of small numbers of ions in a Penning trap to a mature level comparable to early RF trap experiments. Two distinct themes emerge in this thesis. First, a significant effort went into performing ground state cooling of a single ion and all its motional modes as well as the axial modes of Coulomb crystals. This is a fundamental part of the ion trapping toolkit and is often a pre-requisite for experiments in the field of quantum information processing, simulation or thermodynamics. Second, the ability to coherently manipulate the ions was developed and characterised in the context of our particular experimental setup. Here we shall summarize the most important achievements while simultaneously discussing their implications and suggesting future applications or improvements.

9.1 Cooling Outside the Lamb-Dicke Regime

9.1.1 Single Ion Axial Mode

Prior to this thesis, sideband cooling to the ground state in a Penning trap had been demonstrated only on the axial mode of a single ion over a frequency range where addressing the first two orders of red sidebands was sufficient to prevent population trapping. By developing sideband cooling sequences that address higher order sidebands in turn, we have opened up a much larger range of trapping frequencies for which the axial mode can be directly cooled to the ground state. This direct sideband cooling outside of the Lamb-Dicke regime allowed us to reach a trapping frequency of 187 kHz with a mean phonon number of $n_z = 0.02(1)$. Using the technique of adiabatic potential relaxation, we were able to prepare an ion with $n_z = 0.07(1)$ all the way down at 67 kHz.

An immediate benefit of these techniques was to exploit the strong coupling to the second order sideband when the trapping frequency is low and the Lamb-Dicke parameter is large to effectively prepare the motional superposition state $|0\rangle + |1\rangle + |2\rangle$, which would be difficult to do at large trap frequencies. Similarly, any experiment that requires strong sideband coupling in the ground state will benefit from these cooling schemes. Importantly for us, the experience with cooling on higher order sidebands prepared us for the more challenging task of cooling two modes outside the Lamb-Dicke regime – required for the axial modes of a two ion chain and the radial modes of a single ion.

9.1.2 Single Ion Radial Modes

The work on sideband cooling the radial modes of motion built on the results of G. Stutter who demonstrated cooling of the modified cyclotron mode to near the ground state, but did not achieve any significant cooling of the magnetron motion ($\bar{n}_- \approx 6000$) [144]. The first key result was improving the Doppler cooling such that we could consistently prepare both modes with $\bar{n}_+, \bar{n}_- \sim 100$ phonons. To do this, we optimised the radial cooling beam focus and intensity to achieve lower Doppler temperature. The most crucial improvement was the integration of the axialization drive into the experimental sequence to effectively couple the two modes of motion allowing us to trap at higher frequencies of ν_- such that we could resolve the sidebands with the spectroscopy laser at higher Rabi frequency. At $\nu_- = 52$ kHz, we managed to achieve average motional occupation numbers of $\bar{n}_+ = 96(5)$ and $\bar{n}_- = 136(8)$. Starting from this distribution, a 68 ms long cooling sequence addressing sidebands up to the third order was used to achieve occupation numbers $\bar{n}_+ < 1, \bar{n}_- < 2$ assuming a thermal model. While we have clearly demonstrated that there is a significant occupation of the ground state of both modes, a continuous data set had some indication of a potential non-thermal population of the magnetron mode. Without further investigation it is difficult to confirm or rule it out.

Future work in this direction with fine measurements of all higher order magnetron sidebands should shed light on this potential issue. In general, radial sideband cooling is ripe for exploring the parameter space of the laser settings and trapping voltage to determine where the ground state can be effectively reached. The simulations in this work show that higher frequencies of ν_- should be achievable without significant heating allowing for less off resonant excitation of the carrier when cooling on the magnetron sidebands. In terms of the pulse sequence, incorporating sidebands that reduce the quantum numbers of both modes in the early stages of cooling might allow for faster cooling. If it is confirmed that some population trapping does indeed occur with the sequence used in this thesis, these sidebands may hold the key to effectively pump out of these trapping states. Another issue to be explored is the source of the large heating rate which is two orders greater than for the axial mode. One could try additional aggressive filtering of voltage noise before the electrodes to see if there is a significant Johnson noise component to the heating.

A potential upgrade to this system is to use a single 4 channel DDS to provide the axialization RF to the segments of the radial electrode. This would allow a much finer control of the phase and amplitude of the signal, removing any residual driven motion at higher voltages and give a more efficient coupling and hence faster cooling.

The first demonstration of ground state cooling of the magnetron motion is a fascinating achievement in itself because it shows that by adding energy we can effectively confine a particle to the minimum of its radial oscillation amplitude. The ability to cool the radial motion of an ion can be very useful in experiments where one wishes to sympathetically cool the radial motion of another particle that cannot be laser cooled. An experiment aiming to sympathetically cool protons or antiprotons using beryllium ions is already under preparation. Ultimately, the technique of quantum logic spectroscopy will be used to map the state of the (anti-)proton onto the beryllium ion to provide very high precision measurements of its g-factor and charge to mass ratio [193].

9.1.3 Cooling Two ions in a 1D Chain

The final test of our ability to cool far outside the Lamb-Dicke regime involved sideband cooling of the axial modes of a two ion Coulomb crystal in a 1D chain at $\nu_z = 162$ kHz, achieving motional occupation numbers of $\bar{n}_{COM} = 0.30(4)$ and $\bar{n}_B = 0.07(3)$. The vast majority of quantum information experiments have been performed on crystals in this configuration, but typically at much higher axial frequencies ≈ 1 MHz or on even higher frequency radial modes. One of the reasons for this is that one of the main limiting factors of entangling gate fidelity is off-resonant excitation of the carrier. When the sidebands are far away in frequency, the fidelity is improved, but larger laser intensities are required to maintain the same gate length as the Lamb-Dicke parameter and hence coupling strength scales as $\eta \propto 1/\sqrt{\nu_z}$. However, new theoretical proposals suggest that using polychromatic laser fields (i.e. multiple modulating frequencies applied to the AOM of the gate laser) to perform the Mølmer-Sørensen gate can strongly suppress off resonant excitations of the carrier [64]. Thus preparing ground state cooled ions at low trapping frequencies will form an essential part of the experimental effort to demonstrate these new types of fast and robust polychromatic gates. The Imperial College ion trapping ground has recently secured a grant to pursue this work further in a new RF trap that is currently being designed.

As for the Penning trap, the Mølmer-Sørensen interaction is not suitable as its performance is severely compromised by the fact the two ions have a frequency difference of 2.1 kHz on the spectroscopy transition due to the large magnetic field gradient. It is highly unlikely that this splitting can be reduced any further due to the inherent field inhomogeneity of the superconducting magnet without the addition of compensation coils. Furthermore, the ion chain is not very robust against collisions with background particles that can induce a transition to a planar configuration. Nevertheless, even if chains are not scalable in the Penning traps our experience with their cooling can guide any future trapping experiment that requires large Lamb-Dicke parameters in RF traps or as discussed in 9.1.2 sympathetic cooling in Penning traps.

9.2 Cooling of 2D Planar Coulomb Crystals

The 2D planar Coulomb crystal geometry is much more natural for a Penning trap. At sufficiently high applied axial potential, the ions are guaranteed to stay in a regular lattice structures that rotates around the magnetic field axis with no micromotion. The results in this thesis present the first ever ground state cooling of these rotating crystal. Using 20-30 ms of sideband cooling around the first centre of mass red sideband we were able to cool a significant population of the axial modes of up 10 ions to near the ground state. We showed coherent Rabi oscillations on 3 and 6 ion crystals confirming these results. This opens up the possibility of using these crystals for further quantum information or quantum simulation studies.

The simplest experiment to first consider would be the entanglement of a two ion crystal using the Mølmer-Sørensen scheme. One of the problem is that the two modes are separated by only a few kHz in frequency and interfere with each other at high Rabi frequency. If the Rabi frequency is significantly reduced to suppress this effect, the gate length hits the limits of our system's coherence time. To separate the modes further apart the crystal rotation would need to be significantly increased. However, one of the current limitations is precisely the inability to set the rotation frequency of the crystals as it depends on the torque provided by the radial

cooling beam. Increasing the torque to raise the rotation frequency has requirements for the beam parameters that are in conflict with efficient Doppler cooling. The most pressing upgrade to the Penning trap would be to further segment the radial ring electrodes such that a rotating wall RF drive can be applied to fix the crystal rotation frequency.

There are also other entangling schemes that could be applied to these planar crystals such as pushing gates, that use a strongly focused, flat top beam detuned from the $S_{1/2} \leftarrow P_{1/2}$ transition to induce AC Stark shifts [52]. In this scheme the qubit would be formed by the Zeeman sublevels of the $S_{1/2}$ state and would also require us to be able to deliver microwave frequencies near 60 GHz to the ion to perform single qubit rotations. The 397 nm laser powers would also have to be significantly increased to deliver a few mW of power to the ions.

9.3 Coherent Manipulation in a Penning Trap

A significant part of the work in this thesis was focussed on improving and and characterising our ability to coherently manipulate ions in our trap. We can further divide this into the addressing and coherence of the optical qubit and the coherence of the ion's motional states.

9.3.1 Optical Addressing and Coherence

One of the first improvements of the experimental setup was the introduction of a continuous 729 nm laser intensity stabilisation feedback system that reduced the Rabi frequency noise by a factor of 4 to 0.9% as measured through single ion axial Rabi oscillations. The remaining noise will have contributions due to both polarisation change induced by the final fibre leading to the breadboard and beam pointing instability. Since the final fibre is located after the double pass AOM used to shutter the laser, a continuous analogue stabilisation system like the one currently implemented can't be simply moved closer to the ion because of the constant on/off cycling of the laser during the experiment. The double pass AOM also cannot be set up after the final fibre due to space constraints of the breadboard underneath the superconducting magnet. Instead, a method that samples the light when the laser is on and holds the required feedback signal when the laser is off is required. One possibility is to use hardware such as a Red Pitaya board that features fast 125 MS/s ADC/DAC modules to digitise the intensity signal and to output the analog control voltage, RAM to hold the feedback value and a CPU/FPGA to implement the PID algorithm. Other FPGA based schemes with the same principle can also be used [194]. When the signal is picked off after a polarising beam splitter on the output of the final fibre, the polarisation noise is thus also strongly suppressed.

To correct for beam pointing instability, we would need to install a quadrant photodiode/camera in the path of the laser exiting the trap and feed back to piezo actuators that control the orientation of a mirror mount. Once again, this can be performed digitally by sampling when the laser is on and holding the beam position when it is off.

Ramsey interferometry was used to measure the qubit coherence time of 1.78(4) ms, which is respectable, but not sufficient if high fidelity operations that last hundreds of microseconds are required. We also show that through dynamical decoupling this coherence time can be extended, adding 3.9(3) ms per additional π pulse. There is ample scope to investigate which are the limiting factors between the laser linewidth, stray magnetic field noise or trap vibrations. Furthermore, the ion is also sensitive to any phase noise that is acquired as the laser beam travels

from source through two fibres and AOMs to the ion. A phase stabilisation system can be built around a beat note derived from light that is reflected at the output face of the fibre making a round trip and the incoming light. With an appropriate PID loop, the phase noise can be corrected by feeding back to an AOM. Such control units are now also available commercially from Stable Laser Systems.

We also demonstrated that we can synthesize bichromatic light fields that were used to create coherent and squeezed states of a single ion. The bichromatic beam is essential to performing the Mølmer-Sørensen gate and thus it forms an essential part of the quantum manipulation toolbox.

9.3.2 Motional Coherence

To characterise motional coherence we used sideband spectroscopy to measure the parametric heating rate of the axial mode and Ramsey type superposition experiments to measure the stability of the trapping frequency. We confirmed that the heating rate at 184 kHz is 1.1(3) phonons s^{-1} consistent with previous measurements in our trap and one of the best in the world in terms of scaled spectral noise density $S_E(\omega_z) = 1.4(4)$ V^2 m^{-2}. The trap frequency stability was measured to be $\pm 0.40(1)$ Hz with a model that assumes slow Gaussian noise. We also performed the same experiments using an ion prepared in the ground state using adiabatic cooling. In these data sets, the heating rate was an order of magnitude larger and we could clearly distinguish a different decay curve consistent with motional coherence time limited by heating. We were then able to verify that the same noise models could accurately reproduce the coherence decay of superpositions that were prepared in high lying Fock states distributed around $n = 145$ and $n = 291$. To prepare these states, we developed a technique of sideband heating whereby we could incoherently pump the ion to form a narrow distribution ($\sigma_n \approx 10$) around the first coupling minimum of the n^{th} sideband. This was a success in its own right and showed that these mixed, yet highly non-thermal states can exhibit a great degree of coherence as evidenced by both the Ramsey type experiments as well as Rabi oscillations on higher order sidebands. To improve the scheme and narrow the spread around the desired Fock state, heating sequences that adjust the pulse power and use a combination of red and blue sidebands could be investigated.

In general, the very low heating rates and long motional coherence time make the Penning trap system ideal for studying effects of noise sources and decoherence models. To clearly discriminate between the contribution from heating and trap frequency stability, engineered noise with a known power spectrum could be placed on the electrodes, while resistors connected between the endcaps can also be used to introduce additional Johnson noise. We can then study whether the response remains the same for superpositions of high lying states compared to those near the ground state.

Finally, the triple state superposition experiment explores interference between three quantum paths. As such, it probes any validity of Born's rule, which implies that interference only ever occurs between pairs of quantum states i.e. there is no third order interference term. Experiments with photons and a physical triple slit have recently been used to place upper bounds on any violation [195, 196]. If we were to make improvements in our state preparation and detection then we could place an upper bound using the same interference scheme that we used.

APPENDIX A

HENE LOCK SIGNALS

The record of these signals only exists in paper form and is thus included here for future reference.

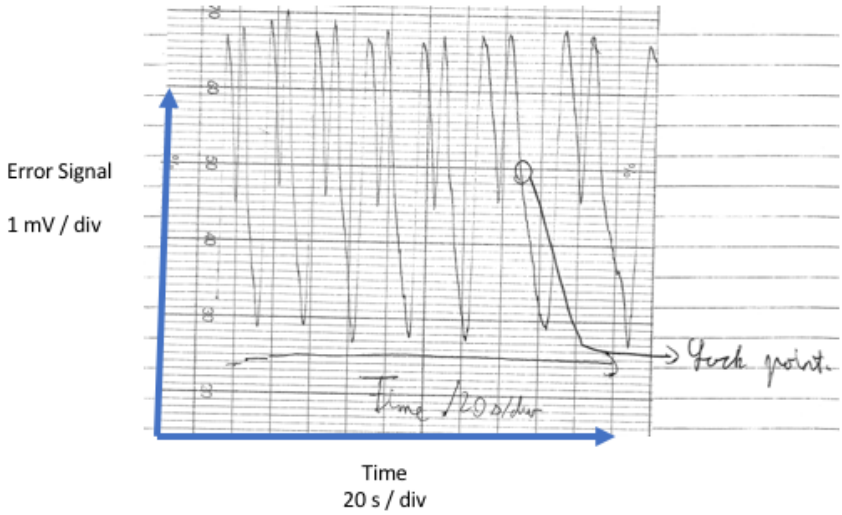

Figure A.1: A time trace of the error signal from comparing the intensity of two orthogonal polarisation modes of the HeNe laser under constant heating. Note the discontinuous behaviour corresponding to a 'flip'in polarisation

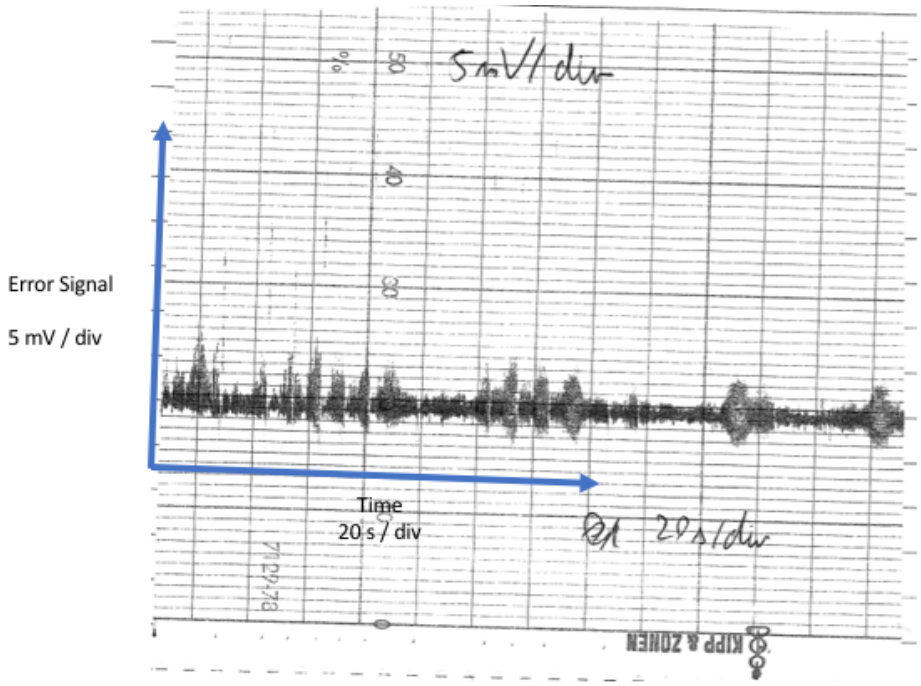

Figure A.2: A time trace of the error signal from comparing the intensity of two orthogonal polarisation modes of the HeNe laser after the lock is engaged. Note the aperiodic noise induced due to the flipping behaviour of the laser.

APPENDIX B

OPTICAL RAMSEY DATA

B.1 Dynamical Decoupling - 1 Pulse

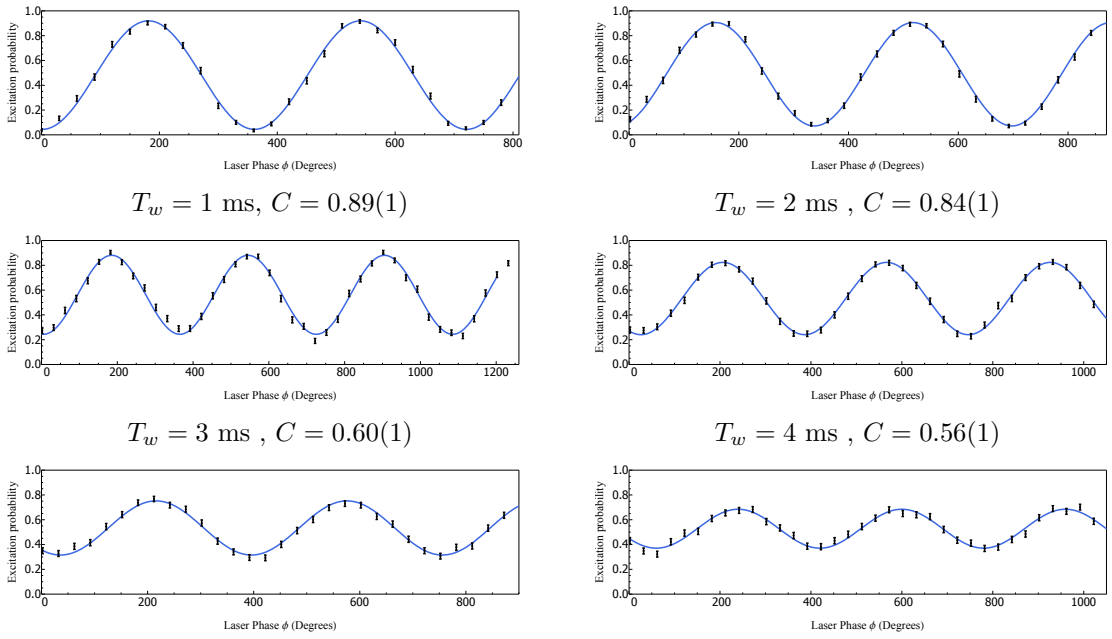

$T_w = 1$ ms, $C = 0.89(1)$ | $T_w = 2$ ms , $C = 0.84(1)$

$T_w = 3$ ms , $C = 0.60(1)$ | $T_w = 4$ ms , $C = 0.56(1)$

$T_w = 5$ ms, $C = 0.42(2)$ | $T_w = 6$ ms, $C = 0.31(2)$

Figure B.1: A set of Spin-Echo measurements taken at ν_z= 418 kHz with the phase of the second $\pi/2$ pulse scanned.

B.2 Dynamical Decoupling - 2 Pulse

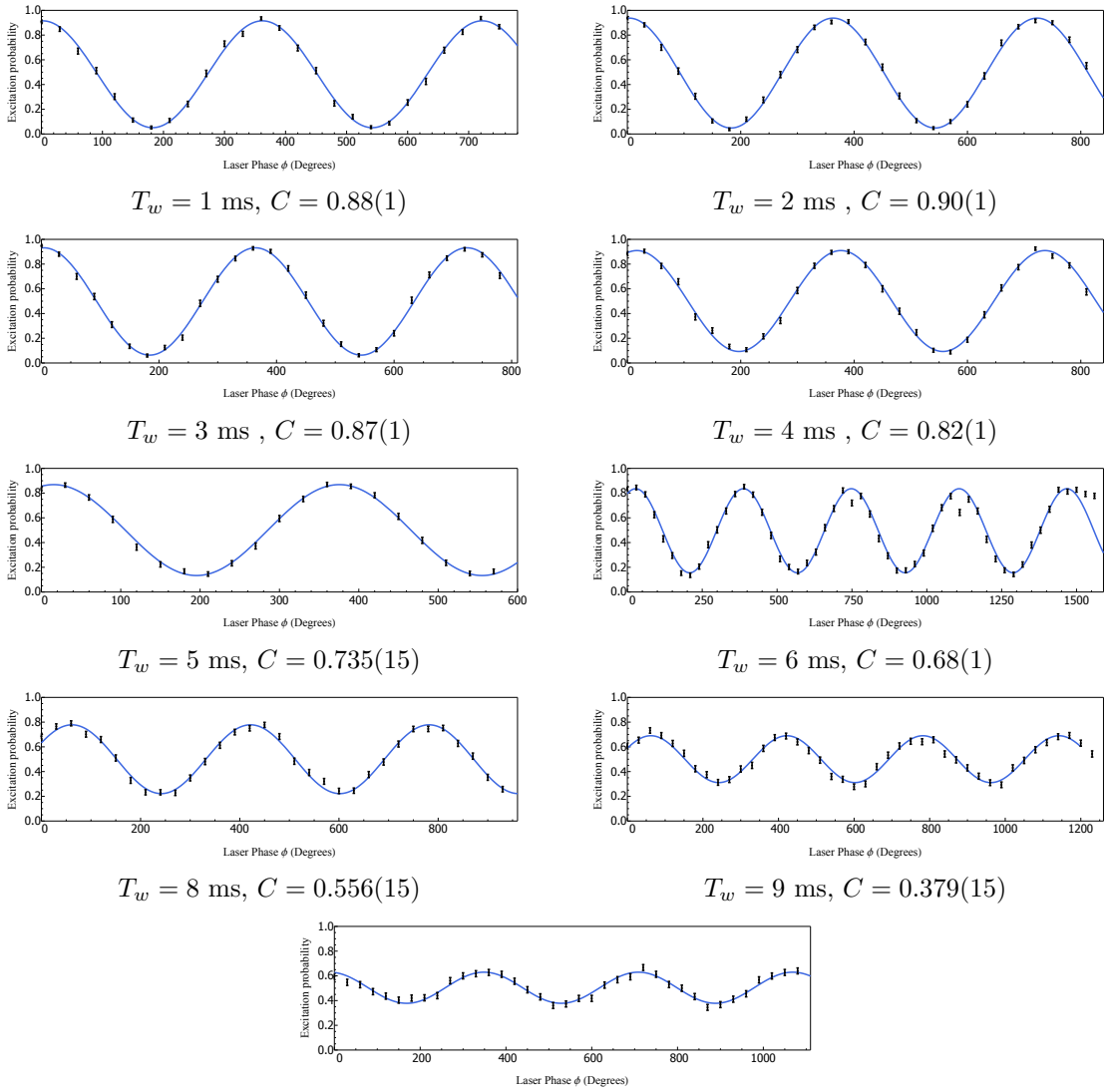

$T_w = 1$ ms, $C = 0.88(1)$ $T_w = 2$ ms , $C = 0.90(1)$

$T_w = 3$ ms , $C = 0.87(1)$ $T_w = 4$ ms , $C = 0.82(1)$

$T_w = 5$ ms, $C = 0.735(15)$ $T_w = 6$ ms, $C = 0.68(1)$

$T_w = 8$ ms, $C = 0.556(15)$ $T_w = 9$ ms, $C = 0.379(15)$

$T_w = 10$ ms, $C = 0.250(16)$

Figure B.2: A set of two pulse UDD measurements taken at ν_z= 418 kHz with the phase of the second $\pi/2$ pulse scanned.

B.3 Dynamical Decoupling - 3 Pulse

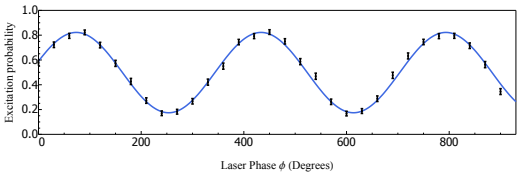

$T_w = 10$ ms, $C = 0.650(15)$

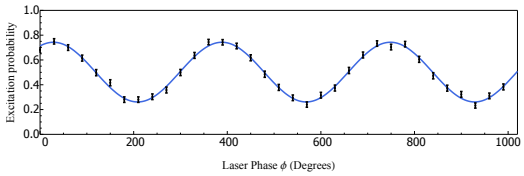

$T_w = 12$ ms , $C = 0.480(15)$

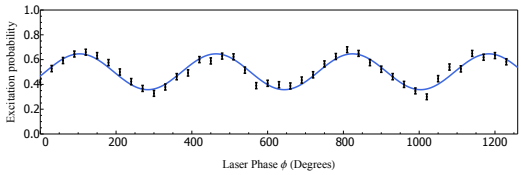

$T_w = 14$ ms , $C = 0.288(15)$

Figure B.3: A set of thee pulse UDD measurements taken at ν_z= 418 kHz with the phase of the second $\pi/2$ pulse scanned.

APPENDIX C

MOTIONAL COHERENCE DATA

C.1 $|0\rangle + |1\rangle$ Ramsey Data

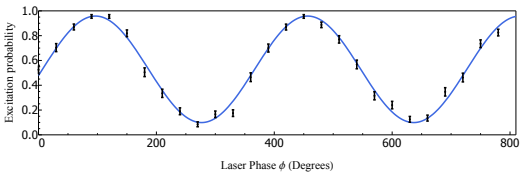

$T_w = 0.2$ ms, $C = 0.859(12)$

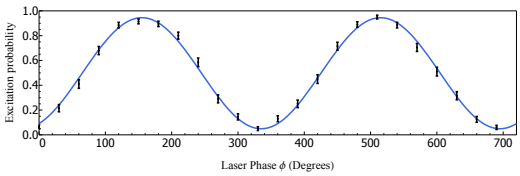

$T_w = 0.5$ ms , $C = 0.896(12)$

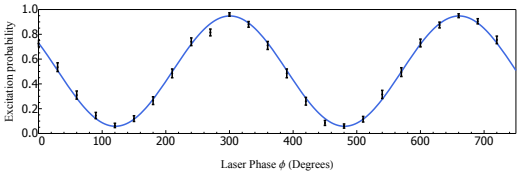

$T_w = 1$ ms , $C = 0.890(11)$

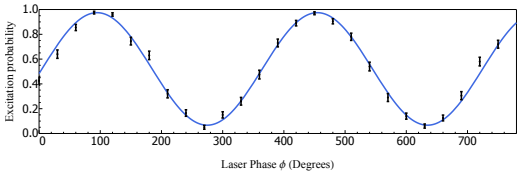

$T_w = 1.5$ ms , $C = 0.91(1)$

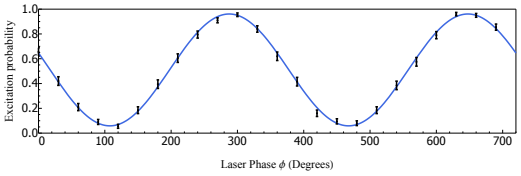

$T_w = 3$ ms, $C = 0.90(1)$

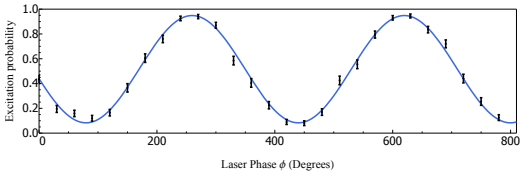

$T_w = 4$ ms, $C = 0.865(12)$

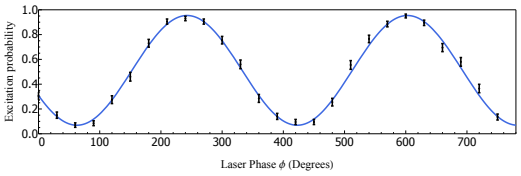

$T_w = 10$ ms, $C = 0.885(12)$

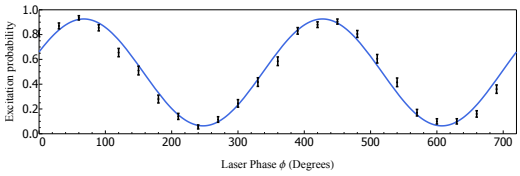

$T_w = 50$ ms, $C = 0.862(13)$

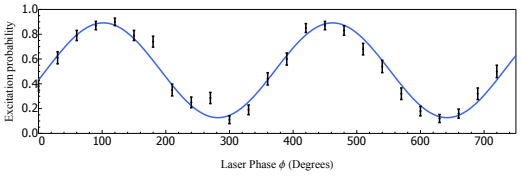

$T_w = 100$ ms, $C = 0.76(2)$

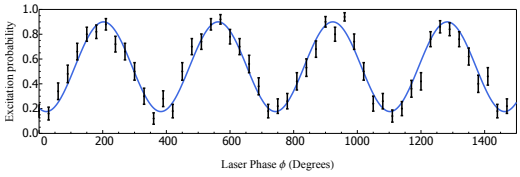

$T_w = 100$ ms, $C = 0.72(2)$

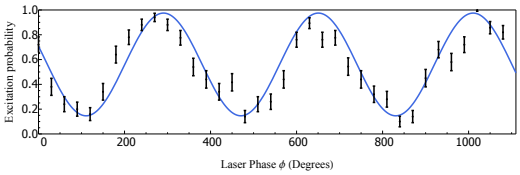

$T_w = 200$ ms, $C = 0.83(2)$

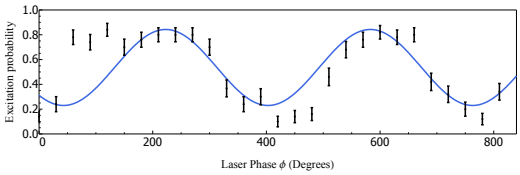

$T_w = 333$ ms, $C = 0.61(3)$

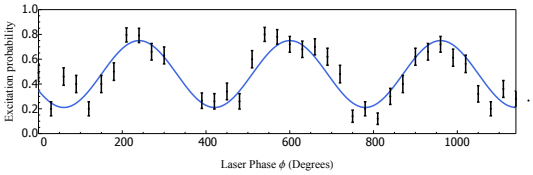

$T_w = 400$ ms, $C = 0.54(3)$

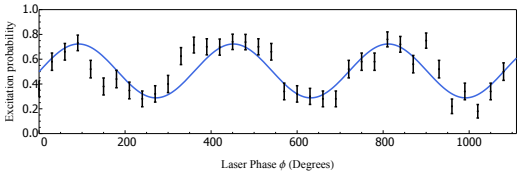

$T_w = 500$ ms, $C = 0.43(3)$

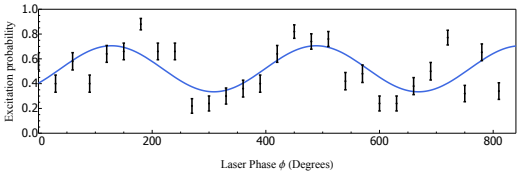

$T_w = 666$ ms, $C = 0.37(3)$

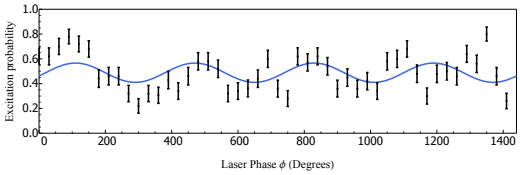

$T_w = 700$ ms, $C = 0.16(3)$

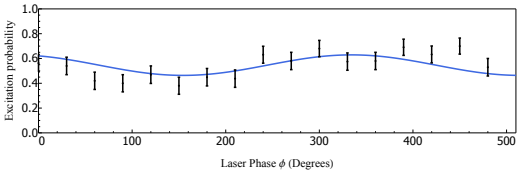

$T_w = 700$ ms, $C = 0.17(5)$

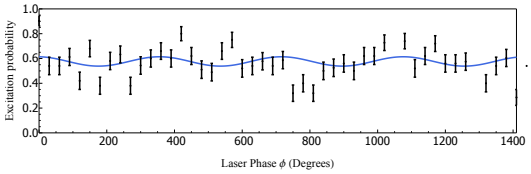

$T_w = 1000$ ms, $C = 0.08(3)$

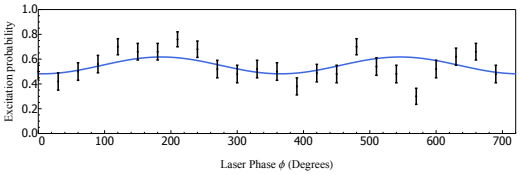

$T_w = 1000$ ms, $C = 0.13(4)$

Figure C.1: A set of motional Ramsey measurements taken at ν_z= 418 kHz with the phase of the second $\pi/2$ pulse scanned.

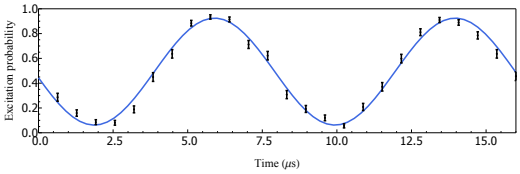

$T_w = 0$ ms, $C = 0.863(12)$

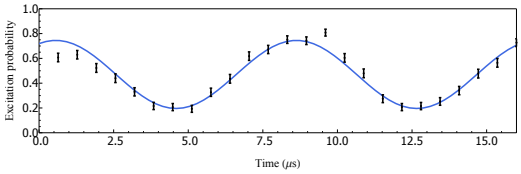

$T_w = 25$ ms , $C = 0.55(2)$

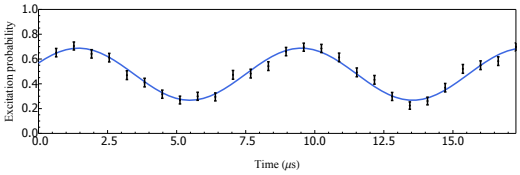

$T_w = 50$ ms , $C = 0.42(2)$

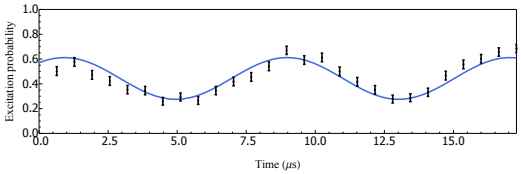

$T_w = 75$ ms , $C = 0.34(2)$

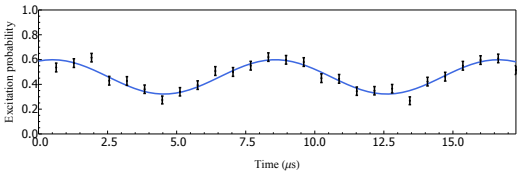

$T_w = 100$ ms, $C = 0.28(2)$

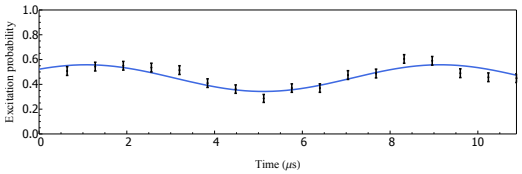

$T_w = 150$ ms, $C = 0.22(2)$

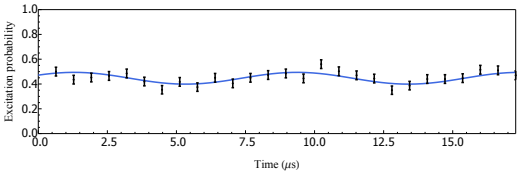

$T_w = 200$ ms, $C = 0.01(2)$

Figure C.2: A set of motional Ramsey measurements taken at ν_z= 124 kHz with the wait time of the final $\pi/2$ pulse incremented.

C.2 $|0\rangle + |2\rangle$ Ramsey Data

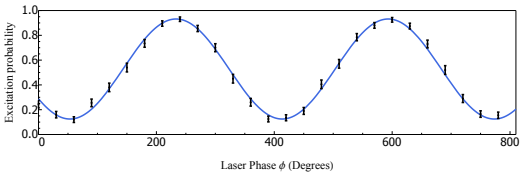

$T_w = 2$ ms, $C = 0.763(12)$

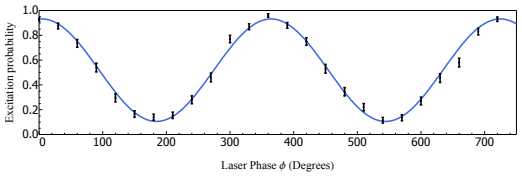

$T_w = 10$ ms , $C = 0.800(13)$

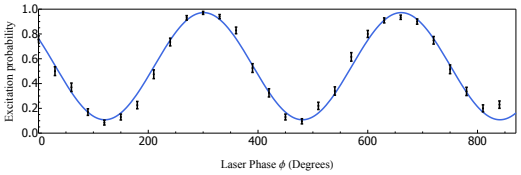

$T_w = 10$ ms , $C = 0.800(11)$

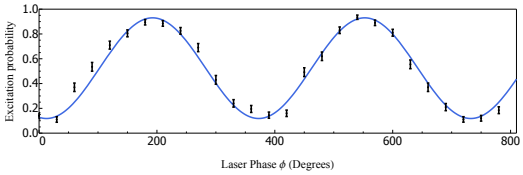

$T_w = 50$ ms , $C = 0.77(13)$

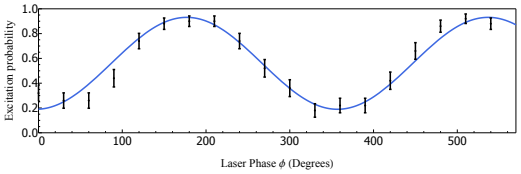

$T_w = 100$ ms , $C = 0.66(3)$

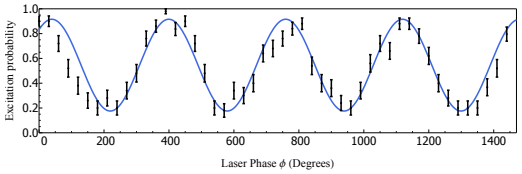

$T_w = 100$ ms , $C = 0.68(2)$

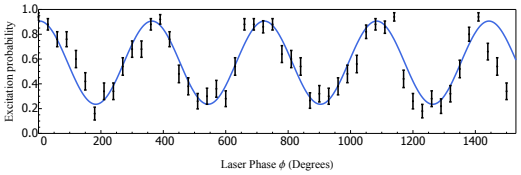

$T_w = 200$ ms, $C = 0.59(2)$

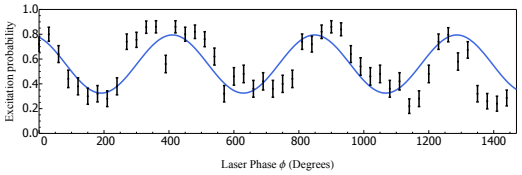

$T_w = 300$ ms, $C = 0.42(3)$

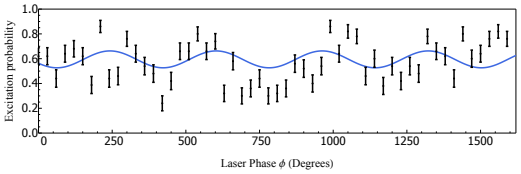

$T_w = 500$ ms, $C = 0.11(3)$

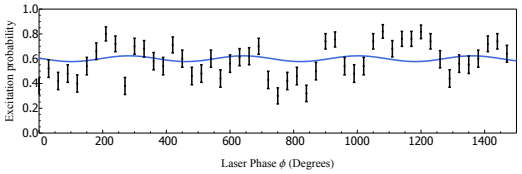

$T_w = 600$ ms , $C = 0.04(3)$

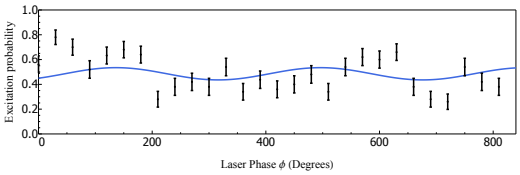

$T_w = 666$ ms, $C = 0.11(4)$

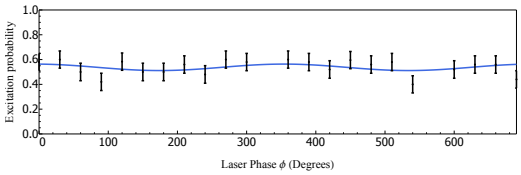

$T_w = 1000$ ms, $C = 0.05(4)$

Figure C.3: A set of motional Ramsey measurements taken at ν_z= 418 kHz with the phase of the final $\pi/2$ pulse scanned.

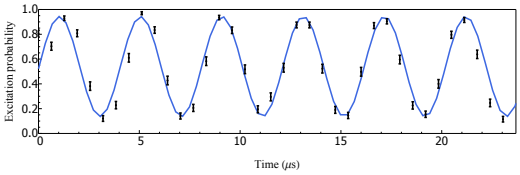

$T_w = 1$ ms, $C = 0.806(10)$

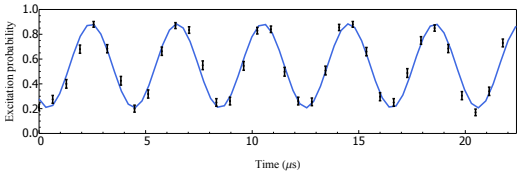

$T_w = 10$ ms , $C = 0.678(13)$

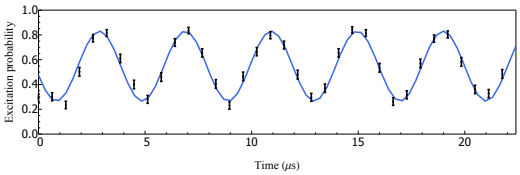

$T_w = 20$ ms , $C = 0.564(15)$

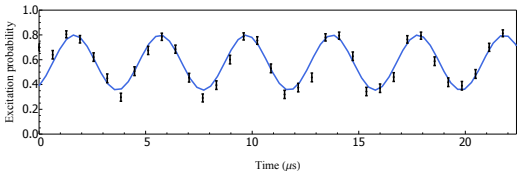

$T_w = 30$ ms , $C = 0.444(15)$

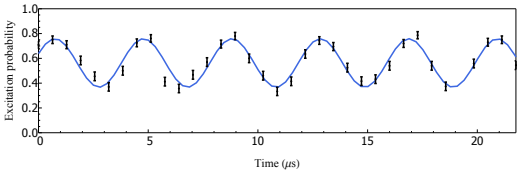

$T_w = 40$ ms , $C = 0.40(2)$

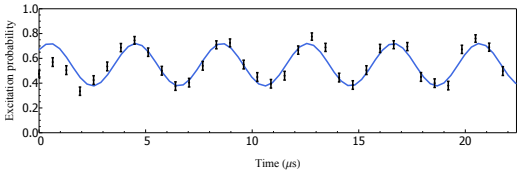

$T_w = 50$ ms , $C = 0.34(2)$

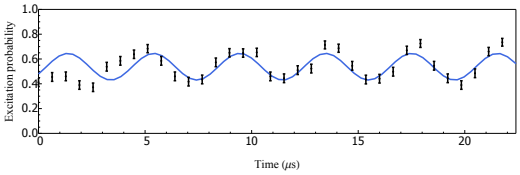

$T_w = 70$ ms, $C = 0.22(2)$

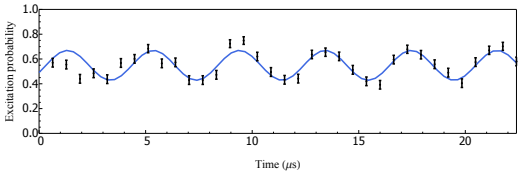

$T_w = 90$ ms, $C = 0.24(2)$

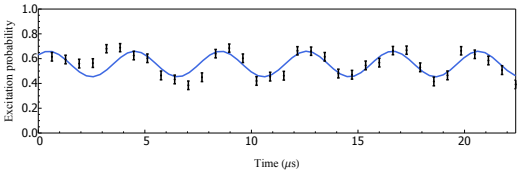

$T_w = 90$ ms, $C = 0.21(2)$

Figure C.4: A set of motional Ramsey measurements taken at ν_z= 124 kHz with the wait time of the final $\pi/2$ pulse incremented.

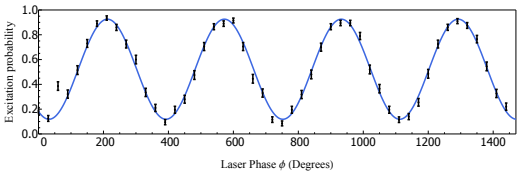

$T_w = 2$ ms, $C = 0.801(10)$

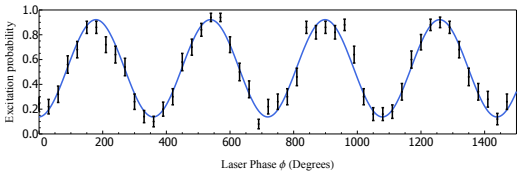

$T_w = 100$ ms , $C = 0.78(2)$

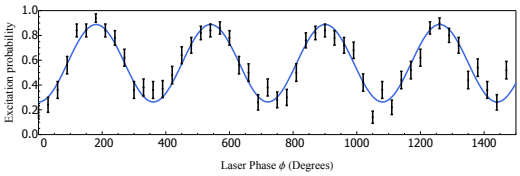

$T_w = 200$ ms , $C = 0.62(2)$

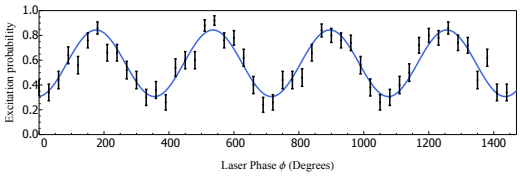

$T_w = 300$ ms , $C = 0.54(2)$

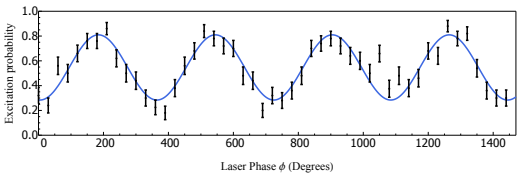

$T_w = 400$ ms , $C = 0.53(2)$

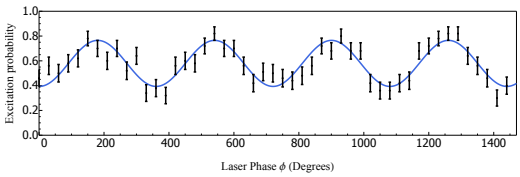

$T_w = 500$ ms , $C = 0.37(3)$

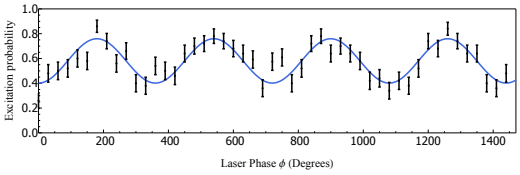

$T_w = 600$ ms, $C = 0.36(3)$

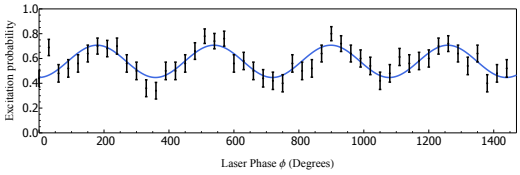

$T_w = 700$ ms, $C = 0.26(3)$

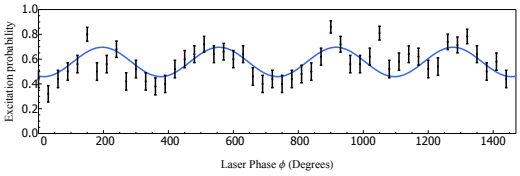

$T_w = 800$ ms, $C = 0.24(3)$

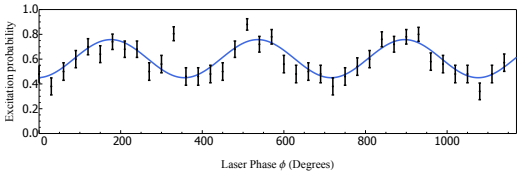

$T_w = 800$ ms, $C = 0.31(3)$

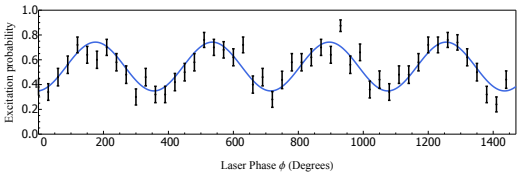

$T_w = 900$ ms, $C = 0.39(3)$

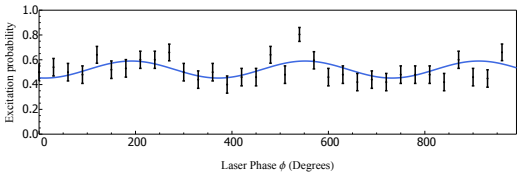

$T_w = 2000$ ms, $C = 0.13(3)$

Figure C.5: A set of motional Spin Echo measurements taken at ν_z= 418 kHz with the phase of the final $\pi/2$ pulse scanned.

C.3 $(|gn\rangle + |gn+3\rangle + |en\rangle + |en-3\rangle)/2$ Ramsey Data

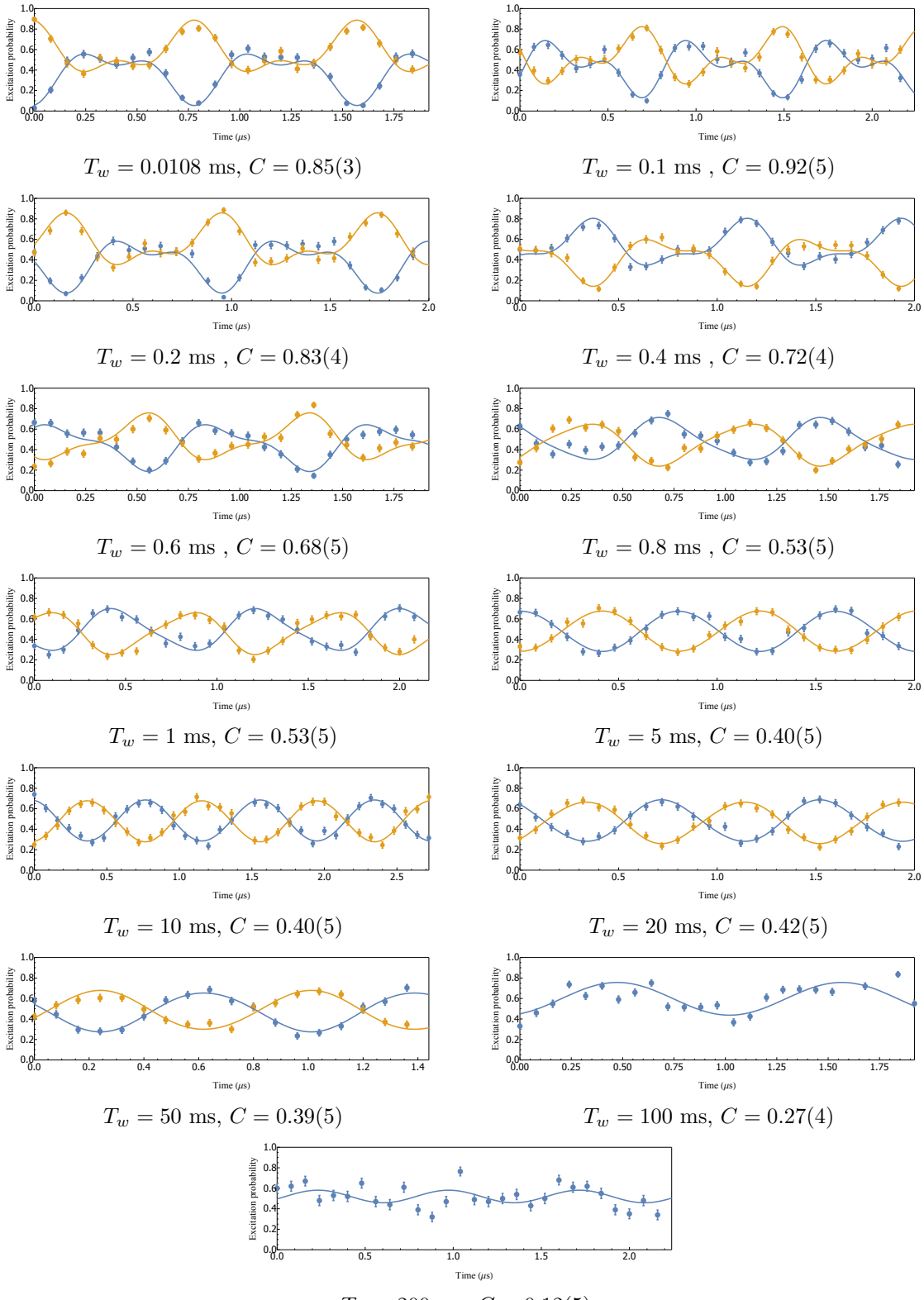

$T_w = 0.0108$ ms, $C = 0.85(3)$ | $T_w = 0.1$ ms , $C = 0.92(5)$

$T_w = 0.2$ ms , $C = 0.83(4)$ | $T_w = 0.4$ ms , $C = 0.72(4)$

$T_w = 0.6$ ms , $C = 0.68(5)$ | $T_w = 0.8$ ms , $C = 0.53(5)$

$T_w = 1$ ms, $C = 0.53(5)$ | $T_w = 5$ ms, $C = 0.40(5)$

$T_w = 10$ ms, $C = 0.40(5)$ | $T_w = 20$ ms, $C = 0.42(5)$

$T_w = 50$ ms, $C = 0.39(5)$ | $T_w = 100$ ms, $C = 0.27(4)$

$T_w = 200$ ms, $C = 0.12(5)$

Figure C.6: An interferometry measurements on the $(|gn\rangle + |gn+3\rangle + |en\rangle + |en-3\rangle)/2$ state taken at ν_z= 418 kHz with the wait time before the retrieval pulses scanned. The two curves are phase shifted by π on the final pulse. The C coefficient is the average visibility over both frequency components.

C.4 $(|gn\rangle + |gn+2\rangle + |en-1\rangle + |en-3\rangle)/2$ Ramsey Data

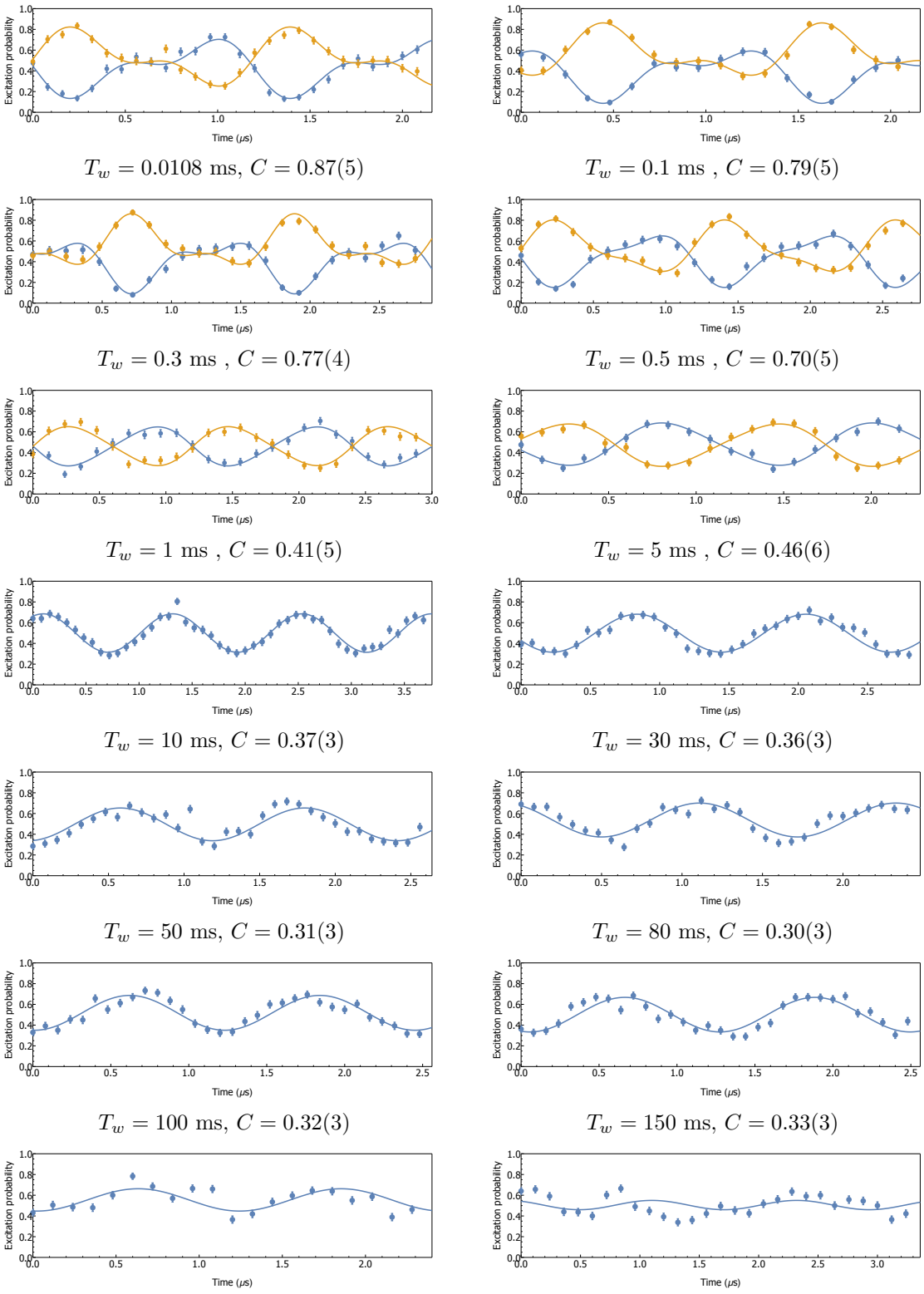

$T_w = 0.0108$ ms, $C = 0.87(5)$ | $T_w = 0.1$ ms , $C = 0.79(5)$

$T_w = 0.3$ ms , $C = 0.77(4)$ | $T_w = 0.5$ ms , $C = 0.70(5)$

$T_w = 1$ ms , $C = 0.41(5)$ | $T_w = 5$ ms , $C = 0.46(6)$

$T_w = 10$ ms, $C = 0.37(3)$ | $T_w = 30$ ms, $C = 0.36(3)$

$T_w = 50$ ms, $C = 0.31(3)$ | $T_w = 80$ ms, $C = 0.30(3)$

$T_w = 100$ ms, $C = 0.32(3)$ | $T_w = 150$ ms, $C = 0.33(3)$

$T_w = 200$ ms, $C = 0.19(4)$ | $T_w = 300$ ms, $C = 0.09(4)$

Figure C.7: An interferometry measurements on the $(|gn\rangle + |gn+2\rangle + |en-1\rangle + |en-3\rangle)/2$ state taken at ν_z= 418 kHz with the wait time before the retrieval pulses scanned. The two curves are phase shifted by π on the final pulse. The C coefficient is the average visibility over both frequency components.

BIBLIOGRAPHY

[1] P. W. Shor, SIAM Journal on Computing **26**, 1484 (1997), URL http://dx.doi.org/10.1137/S0097539795293172.

[2] R. P. Feynman, International Journal of Theoretical Physics **21**, 467 (1982), URL http://dx.doi.org/10.1007/BF02650179.

[3] D. P. DiVincenzo, Fortschritte der Physik **48**, 771 (2000), URL https://onlinelibrary.wiley.com/doi/pdf/10.1002/1521-3978%28200009%2948%3A9/11%3C771%3A%3AAID-PROP771%3E3.0.CO%3B2-E.

[4] W. Paul and H. Steinwedel, Zeitschrift für Naturforschung A **8**, 448 (1953), URL https://www.degruyter.com/view/j/zna.1953.8.issue-7/zna-1953-0710/zna-1953-0710.xml.

[5] W. Paul, Rev. Mod. Phys. **62**, 531 (1990), URL http://link.aps.org/doi/10.1103/RevModPhys.62.531.

[6] H. G. Dehmelt, Advances in Atomic, Molecular and Optical Physics **3**, 53 (1968), URL http://dx.doi.org/10.1016/S0065-2199(08)60170-0.

[7] D. Wineland, P. Ekstrom, and H. Dehmelt, Phys. Rev. Lett. **31**, 1279 (1973), URL http://dx.doi.org/10.1103/PhysRevLett.31.1279.

[8] A. G. Marshall, C. L. Hendrickson, and G. S. Jackson, Mass spectrometry reviews **17**, 1 (1998), URL https://doi.org/10.1002/(SICI)1098-2787(1998)17:1<1::AID-MAS1>3.0.CO;2-K.

[9] D. J. Douglas, A. J. Frank, and D. Mao, Mass Spectrometry Reviews **24**, 1 (2005), URL http://dx.doi.org/10.1002/mas.20004.

[10] J. Van Schelt, D. Lascar, G. Savard, J. A. Clark, S. Caldwell, A. Chaudhuri, J. Fallis, J. P. Greene, A. F. Levand, G. Li, et al., Phys. Rev. C **85**, 1 (2012), URL http://dx.doi.org/10.1103/PhysRevC.85.045805.

[11] D. Hanneke, S. Fogwell, and G. Gabrielse, Phys. Rev. Lett. **100**, 120801 (2008), URL https://link.aps.org/doi/10.1103/PhysRevLett.100.120801.

[12] J. Disciacca and G. Gabrielse, Phys. Rev. Lett. **108**, 153001 (2012), URL http://dx.doi.org/10.1103/PhysRevLett.108.153001.

[13] H. Nagahama, C. Smorra, S. Sellner, J. Harrington, T. Higuchi, M. J. Borchert, T. Tanaka, M. Besirli, A. Mooser, G. Schneider, et al., Nat. Comms **8**, 1 (2017), URL http://dx.doi.org/10.1038/ncomms14084.

[14] S. Ulmer, C. Smorra, A. Mooser, K. Franke, H. Nagahama, G. Schneider, T. Higuchi, S. Van Gorp, K. Blaum, Y. Matsuda, et al., Nature **524**, 196 (2015), URL http://dx.doi.org/10.1038/nature14861.

[15] K. Blaum, H. Kracke, S. Kreim, A. Mooser, C. Mrozik, W. Quint, C. C. Rodegheri, B. Schabinger, S. Sturm, S. Ulmer, et al., J. Phys. B **42**, 154021 (2009), URL http://dx.doi.org/10.1088/0953-4075/42/15/154021.

[16] K. Blaum, Y. N. Novikov, and G. Werth, Contemporary Physics **51**, 149 (2010), URL http://dx.doi.org/10.1080/00107510903387652.

[17] M. Ahmadi, B. X. Alves, C. J. Baker, W. Bertsche, E. Butler, A. Capra, C. Carruth, C. L. Cesar, M. Charlton, S. Cohen, et al., Nature **541**, 506 (2017), URL http://dx.doi.org/10.1038/nature21040.

[18] M. Ahmadi, B. X. Alves, C. J. Baker, W. Bertsche, E. Butler, A. Capra, C. Carruth, C. L. Cesar, M. Charlton, S. Cohen, et al., Nature **548**, 66 (2017), URL http://dx.doi.org/10.1038/nature23446.

[19] D. J. Wineland, R. E. Drullinger, and F. L. Walls, Phys. Rev. Lett. **40**, 1639 (1978), URL http://dx.doi.org/10.1103/PhysRevLett.40.1639.

[20] W. Neuhauser, M. Hohenstatt, P. Toschek, and H. Dehmelt, Phys. Rev. Lett. **41**, 233 (1978), URL http://dx.doi.org/10.1103/PhysRevLett.41.233.

[21] F. Diedrich, J. C. Bergquist, W. M. Itano, and D. J. Wineland, Phys. Rev. Lett. **62**, 403 (1989), URL https://link.aps.org/doi/10.1103/PhysRevLett.62.403.

[22] J. I. Cirac and P. Zoller, Phys. Rev. Lett. **74**, 4091 (1995), URL https://link.aps.org/doi/10.1103/PhysRevLett.74.4091.

[23] Q. A. Turchette, C. S. Wood, B. E. King, C. J. Myatt, D. Leibfried, W. M. Itano, C. Monroe, and D. J. Wineland, Phys. Rev. Lett. **81**, 3631 (1998), URL https://link.aps.org/doi/10.1103/PhysRevLett.81.3631.

[24] K. Mølmer and A. Sørensen, Phys. Rev. Lett. **82**, 1835 (1999), URL http://link.aps.org/doi/10.1103/PhysRevLett.82.1835.

[25] G. Milburn, S. Schneider, and D. James, Fortschritte der Physik **48**, 801 (2000), URL https://onlinelibrary.wiley.com/doi/abs/10.1002/1521-3978%28200009%2948%3A9/11%3C801%3A%3AAID-PROP801%3E3.0.CO%3B2-1.

[26] C. A. Sackett, D. Kielpinski, B. E. King, C. Langer, V. Meyer, C. J. Myatt, M. Rowe, Q. A. Turchette, W. M. Itano, D. J. Wineland, et al., Nature **404**, 256 (2000), URL http://www.nature.com/articles/35005011.

[27] D. Leibfried, B. DeMarco, V. Meyer, D. Lucas, M. Barrett, J. Britton, W. M. Itano, B. Jelenković, C. Langer, T. Rosenband, et al., Nature **422**, 412 (2003), URL http://dx.doi.org/10.1038/nature01492.

[28] F. Schmidt-Kaler, S. Gulde, M. Riebe, T. Deuschle, A. Kreuter, G. Lancaster, C. Becher, J. Eschner, H. H ffner, and R. Blatt, J. Phys. B **36**, 623 (2003), URL http://dx.doi.org/10.1088/0953-4075/36/3/319.

[29] D. Leibfried, E. Knill, S. Seidelin, J. Britton, R. B. Blakestad, J. Chiaverini, D. B. Hume, W. M. Itano, J. D. Jost, C. Langer, et al., Nature **438**, 639 (2005), URL http://dx.doi.org/10.1038/nature04251.

[30] T. Monz, P. Schindler, J. T. Barreiro, M. Chwalla, D. Nigg, W. A. Coish, M. Harlander, W. Hänsel, M. Hennrich, and R. Blatt, Phys. Rev. Lett. **106**, 130506 (2011), URL http://dx.doi.org/10.1103/PhysRevLett.106.130506.

[31] C. J. Ballance, T. P. Harty, N. M. Linke, M. A. Sepiol, and D. M. Lucas, Phys. Rev. Lett. **117**, 060504 (2016), URL http://dx.doi.org/10.1103/PhysRevLett.117.060504.

[32] P. H. Leung, K. A. Landsman, C. Figgatt, N. M. Linke, C. Monroe, and K. R. Brown, Phys. Rev. Lett. **120**, 020501 (2018), URL https://doi.org/10.1103/PhysRevLett.120.020501.

[33] J. D. Wong-Campos, S. A. Moses, K. G. Johnson, and C. Monroe, Phys. Rev. Lett. **119**, 230501 (2017), URL http://dx.doi.org/10.1103/PhysRevLett.119.230501.

[34] V. M. Schäfer, C. J. Ballance, K. Thirumalai, L. J. Stephenson, T. G. Ballance, A. M. Steane, and D. M. Lucas, Nature **555**, 75 (2018), URL http://nature.com/doifinder/10.1038/nature25737.

[35] S. Gulde, M. Riebe, G. P. T. Lancaster, C. Becher, J. Eschner, H. Häffner, F. Schmidt-Kaler, I. L. Chuang, and R. Blatt, Nature **421**, 48 (2003), URL http://www.nature.com/articles/nature01336.

[36] S. Debnath, N. M. Linke, C. Figgatt, K. A. Landsman, K. Wright, and C. Monroe, Nature **536**, 63 (2016), URL http://dx.doi.org/10.1038/nature18648.

[37] K.-A. Brickman, P. C. Haljan, P. J. Lee, M. Acton, L. Deslauriers, and C. Monroe, Phys. Rev. A **72**, 050306 (2005), URL https://link.aps.org/doi/10.1103/PhysRevA.72.050306.

[38] C. Figgatt, D. Maslov, K. A. Landsman, N. M. Linke, S. Debnath, and C. Monroe, Nat. Comms **8**, 1918 (2017), URL http://dx.doi.org/10.1038/s41467-017-01904-7.

[39] T. Monz, D. Nigg, E. A. Martinez, M. F. Brandl, P. Schindler, R. Rines, S. X. Wang, I. L. Chuang, and R. Blatt, Science **351**, 1068 (2016), URL http://www.sciencemag.org/cgi/doi/10.1126/science.aad9480.

[40] B. P. Lanyon, P. Jurcevic, M. Zwerger, C. Hempel, E. A. Martinez, W. Dür, H. J. Briegel, R. Blatt, and C. F. Roos, Phys. Rev. Lett. **111**, 210501 (2013), URL https://link.aps.org/doi/10.1103/PhysRevLett.111.210501.

[41] J. Chiaverini, D. Leibfried, T. Schaetz, M. D. Barrett, R. B. Blakestad, J. Britton, W. M. Itano, J. D. Jost, E. Knill, C. Langer, et al., Nature **432**, 602 (2004), URL http://www.nature.com/articles/nature03074.

[42] P. Schindler, J. T. Barreiro, T. Monz, V. Nebendahl, D. Nigg, M. Chwalla, M. Hennrich, and R. Blatt, Science **332**, 1059 (2011), URL http://www.sciencemag.org/cgi/doi/10.1126/science.1203329.

[43] C. Monroe and J. Kim, Science **339**, 1164 (2013), URL http://dx.doi.org/10.1126/science.1231298.

[44] D. Kielpinski, C. Monroe, and D. J. Wineland, Nature **417**, 709 (2002), URL http://www.nature.com/articles/nature00784.

[45] A. Walther, F. Ziesel, T. Ruster, S. T. Dawkins, K. Ott, M. Hettrich, K. Singer, F. Schmidt-Kaler, and U. Poschinger, Phys. Rev. Lett. **109**, 080501 (2012), URL http://dx.doi.org/10.1103/PhysRevLett.109.080501.

[46] R. Bowler, J. Gaebler, Y. Lin, T. R. Tan, D. Hanneke, J. D. Jost, J. P. Home, D. Leibfried, and D. J. Wineland, Phys. Rev. Lett. **109**, 080502 (2012), URL http://dx.doi.org/10.1103/PhysRevLett.109.080502.

[47] H. Kaufmann, T. Ruster, C. T. Schmiegelow, M. A. Luda, V. Kaushal, J. Schulz, D. Von Lindenfels, F. Schmidt-Kaler, and U. G. Poschinger, Phys. Rev. A **95**, 052319 (2017), URL http://dx.doi.org/10.1103/PhysRevA.95.052319.

[48] B. Vogell, B. Vermersch, T. E. Northup, B. P. Lanyon, and C. A. Muschik, Quantum Science and Technology **2**, 045003 (2017), URL http://dx.doi.org/10.1088/2058-9565/aa868b.

[49] B. Lekitsch, S. Weidt, A. G. Fowler, K. Mølmer, S. J. Devitt, C. Wunderlich, and W. K. Hensinger, Science Advances **3**, 1601540 (2017), URL http://advances.sciencemag.org/lookup/doi/10.1126/sciadv.1601540.

[50] J. F. Goodwin, G. Stutter, R. C. Thompson, and D. M. Segal, Phys. Rev. Lett. **116**, 143002 (2016), URL http://dx.doi.org/10.1103/PhysRevLett.116.143002.

[51] D. Porras and J. I. Cirac, Phys. Rev. Lett. **96**, 1 (2006), URL http://dx.doi.org/10.1103/PhysRevLett.96.250501.

[52] M. Kitaoka, I. M. Buluta, and S. Hasegawa, Phys. Lett. A **373**, 2911 (2009), URL http://dx.doi.org/10.1016/j.physleta.2009.06.019.

[53] J. D. Baltrusch, A. Negretti, J. M. Taylor, and T. Calarco, Phys. Rev. A **83**, 042319 (2011), URL http://dx.doi.org/10.1103/PhysRevA.83.042319.

[54] J. F. Goodwin, B. J. Brown, G. Stutter, H. Dale, R. C. Thompson, and T. Rudolph, Phys. Rev. A **92**, 032314 (2015), URL http://link.aps.org/doi/10.1103/PhysRevA.92.032314.

[55] B. C. Sawyer, J. W. Britton, A. C. Keith, C.-C. J. Wang, J. K. Freericks, H. Uys, M. J. Biercuk, and J. J. Bollinger, Phys. Rev. Lett. **108**, 213003 (2012), URL http://link.aps.org/doi/10.1103/PhysRevLett.108.213003.

[56] J. W. Britton, B. C. Sawyer, A. C. Keith, C.-C. J. Wang, J. K. Freericks, H. Uys, M. J. Biercuk, and J. J. Bollinger, **484**, 489 (2012), URL http://dx.doi.org/10.1038/nature10981.

[57] J. G. Bohnet, B. C. Sawyer, J. W. Britton, M. L. Wall, A. M. Rey, M. Foss-Feig, and J. J. Bollinger, Science **352**, 1297 (2016), URL http://www.sciencemag.org/cgi/doi/10.1126/science.aad9958.

[58] P. Jurcevic, B. P. Lanyon, P. Hauke, C. Hempel, P. Zoller, R. Blatt, and C. F. Roos, Nature **511**, 202 (2014), URL http://dx.doi.org/10.1038/nature13461.

[59] P. Richerme, Z.-X. Gong, A. Lee, C. Senko, J. Smith, M. Foss-Feig, S. Michalakis, A. V. Gorshkov, and C. Monroe, Nature **511**, 198 (2014), URL http://dx.doi.org/10.1038/nature13450.

[60] S. Korenblit, D. Kafri, W. C. Campbell, R. Islam, E. E. Edwards, Z.-X. Gong, G.-D. Lin, L.-M. Duan, J. Kim, K. Kim, et al., New Journal of Physics **14**, 095024 (2012), URL http://stacks.iop.org/1367-2630/14/i=9/a=095024?key=crossref.07cfc106733d1383a9775b85b9b3d1bb.

[61] K. Kim, M.-S. Chang, S. Korenblit, R. Islam, E. E. Edwards, J. K. Freericks, G.-D. Lin, L.-M. Duan, and C. Monroe, Nature **465**, 590 (2010), URL http://dx.doi.org/10.1038/nature09071.

[62] J. L. Rosales and V. Martin, Phys. Rev. A **97**, 032325 (2018), URL https://link.aps.org/doi/10.1103/PhysRevA.97.032325.

[63] F. Haddadfarshi and F. Mintert, New Journal of Physics **18**, 123007 (2016), URL http://dx.doi.org/10.1088/1367-2630/18/12/123007.

[64] M. Cheung and F. Mintert, arXiv p. 1711.06142v1 (2017), URL https://arxiv.org/abs/1711.06142.

[65] Y. Nakamura, Y. A. Pashkin, and J. S. Tsai, Nature **398**, 786 (1999), URL http://www.nature.com/articles/19718.

[66] I. Chiorescu, Science **299**, 1869 (2003), URL http://dx.doi.org/10.1126/science.1081045.

[67] J. M. Martinis, Quantum Information Processing **8**, 81 (2009), URL http://link.springer.com/10.1007/s11128-009-0105-1.

[68] A. A. Houck, J. A. Schreier, B. R. Johnson, J. M. Chow, J. Koch, J. M. Gambetta, D. I. Schuster, L. Frunzio, M. H. Devoret, S. M. Girvin, et al., Phys. Rev. Lett. **101**, 080502 (2008), URL https://link.aps.org/doi/10.1103/PhysRevLett.101.080502.

[69] M. H. Devoret and R. J. Schoelkopf, Science **339**, 1169 (2013), URL http://www.sciencemag.org/cgi/doi/10.1126/science.1231930.

[70] J. M. Gambetta, J. M. Chow, and M. Steffen, npj Quantum Information **3**, 2 (2017), URL http://www.nature.com/articles/s41534-016-0004-0.

[71] *Google ai blog: A preview of bristlecone, googles new quantum processor*, https://ai.googleblog.com/2018/03/a-preview-of-bristlecone-googles-new.html, acessed: 2018-06-27.

[72] *Ibm blog: The future is quantum*, https://www.ibm.com/blogs/research/2017/11/the-future-is-quantum/, acessed: 2018-06-27.

[73] *Intel newsroom: quantum computing*, https://newsroom.intel.com/press-kits/quantum-computing/, acessed: 2018-06-27.

[74] N. M. Linke, D. Maslov, M. Roetteler, S. Debnath, C. Figgatt, K. A. Landsman, K. Wright, and C. Monroe, PNAS **114**, 3305 (2017), URL http://www.pnas.org/lookup/doi/10.1073/pnas.1618020114.

[75] R. Barends, L. Lamata, J. Kelly, L. García-Álvarez, A. G. Fowler, A. Megrant, E. Jeffrey, T. C. White, D. Sank, J. Y. Mutus, et al., Nature Communications **6**, 7654 (2015), URL http://www.nature.com/articles/ncomms8654.

[76] A. Kandala, A. Mezzacapo, K. Temme, M. Takita, M. Brink, J. M. Chow, and J. M. Gambetta, Nature **549**, 242 (2017), URL http://dx.doi.org/10.1038/nature23879.

[77] D. J. Brod and J. Combes, Phys. Rev. Lett. **117**, 080502 (2016), URL https://link.aps.org/doi/10.1103/PhysRevLett.117.080502.

[78] E. Knill, R. Laflamme, and G. J. Milburn, Nature **409**, 46 (2001), URL http://www.nature.com/articles/35051009.

[79] J. Carolan, C. Harrold, C. Sparrow, E. Martin-Lopez, N. J. Russell, J. W. Silverstone, P. J. Shadbolt, N. Matsuda, M. Oguma, M. Itoh, et al., Science **349**, 711 (2015), URL http://www.sciencemag.org/cgi/doi/10.1126/science.aab3642.

[80] E. Martín-López, A. Laing, T. Lawson, R. Alvarez, X.-Q. Zhou, and J. L. O'Brien, Nature Photonics **6**, 773 (2012), URL http://www.nature.com/doifinder/10.1038/nphoton.2012.259.

[81] J. Wang, S. Paesani, Y. Ding, R. Santagati, P. Skrzypczyk, A. Salavrakos, J. Tura, R. Augusiak, L. Mančinska, D. Bacco, et al., Science **360**, 285 (2018), URL http://www.sciencemag.org/lookup/doi/10.1126/science.aar7053.

[82] D. Su, K. K. Sabapathy, C. R. Myers, H. Qi, C. Weedbrook, and K. Brádler, arXiv p. 1805.02645 (2018), URL http://arxiv.org/abs/1805.02645.

[83] T. Rudolph, APL Photonics **2**, 030901 (2017), URL http://aip.scitation.org/doi/10.1063/1.4976737.

[84] F. Flamini, N. Spagnolo, and F. Sciarrino, arXiv p. 1803.02790v2 (2018), URL http://arxiv.org/abs/1803.02790.

[85] G. Tosi, F. A. Mohiyaddin, V. Schmitt, S. Tenberg, R. Rahman, G. Klimeck, and A. Morello, Nature Communications **8**, 1 (2017), URL http://dx.doi.org/10.1038/s41467-017-00378-x.

[86] T. F. Watson, B. Weber, Y.-L. Hsueh, L. C. L. Hollenberg, R. Rahman, and M. Y. Simmons, Science Advances **3**, e1602811 (2017), URL http://advances.sciencemag.org/lookup/doi/10.1126/sciadv.1602811.

[87] M. A. Broome, S. K. Gorman, M. G. House, S. J. Hile, J. G. Keizer, D. Keith, C. D. Hill, T. F. Watson, W. J. Baker, L. C. L. Hollenberg, et al., Nature Communications **9**, 980 (2018), URL http://www.nature.com/articles/s41467-018-02982-x.

[88] T. van der Sar, Z. H. Wang, M. S. Blok, H. Bernien, T. H. Taminiau, D. M. Toyli, D. A. Lidar, D. D. Awschalom, R. Hanson, and V. V. Dobrovitski, Nature **484**, 82 (2012), URL http://dx.doi.org/10.1038/nature10900.

[89] K. Nemoto, M. Trupke, S. J. Devitt, A. M. Stephens, B. Scharfenberger, K. Buczak, T. Nöbauer, M. S. Everitt, J. Schmiedmayer, and W. J. Munro, Phys. Rev. X **4**, 031022 (2014), URL https://link.aps.org/doi/10.1103/PhysRevX.4.031022.

[90] A. Sipahigil, R. E. Evans, D. D. Sukachev, M. J. Burek, J. Borregaard, M. K. Bhaskar, C. T. Nguyen, J. L. Pacheco, H. A. Atikian, C. Meuwly, et al., Science **354**, 847 (2016), URL http://www.sciencemag.org/lookup/doi/10.1126/science.aah6875.

[91] K. M. Maller, M. T. Lichtman, T. Xia, Y. Sun, M. J. Piotrowicz, A. W. Carr, L. Isenhower, and M. Saffman, Phys. Rev. A **92**, 022336 (2015), URL http://dx.doi.org/10.1103/PhysRevA.92.022336.

[92] M. Saffman, Journal of Physics B: Atomic, Molecular and Optical Physics **49** (2016).

[93] S. Earnshaw, Trans. Camb. Phil. Soc **7**, 97 (1842).

[94] P. Ghosh, *Ion Traps*, International Series of Monograms (Clarendon Press, 1995), ISBN 9780198539957.

[95] L. S. Brown and G. Gabrielse, Phys. Rev. A **25**, 2423 (1982), URL https://link.aps.org/doi/10.1103/PhysRevA.25.2423.

[96] T. M. O'Neil and C. F. Driscoll, Physics of Fluids **22**, 266 (1979), URL http://scitation.aip.org/content/aip/journal/pof1/22/2/10.1063/1.862577.

[97] S. A. Prasad and T. M. O'Neil, Physics of Fluids **22**, 278 (1979), URL http://scitation.aip.org/content/aip/journal/pof1/22/2/10.1063/1.862578.

[98] J. H. Malmberg and C. F. Driscoll, Phys. Rev. Lett. **44**, 654 (1980), URL https://link.aps.org/doi/10.1103/PhysRevLett.44.654.

[99] C. F. Driscoll, J. H. Malmberg, and K. S. Fine, Phys. Rev. Lett. **60**, 1290 (1988), URL http://dx.doi.org/10.1103/PhysRevLett.60.1290.

[100] J. J. Bollinger and D. J. Wineland, Phys. Rev. Lett. **53**, 348 (1984), URL https://link.aps.org/doi/10.1103/PhysRevLett.53.348.

[101] S. L. Gilbert, J. J. Bollinger, and D. J. Wineland, Phys. Rev. Lett. **60**, 2022 (1988), URL http://dx.doi.org/10.1103/PhysRevLett.60.2022.

[102] J. N. Tan, J. J. Bollinger, B. Jelenkovic, and D. J. Wineland, Phys. Rev. Lett. **75**, 4198 (1995), URL https://link.aps.org/doi/10.1103/PhysRevLett.75.4198.

[103] T. B. Mitchell, J. J. Bollinger, D. H. E. Dubin, X.-P. Huang, W. M. Itano, and R. H. Baughman, Science **282**, 1290 (1998), URL http://dx.doi.org/10.1126/science.282.5392.1290.

[104] S. Mavadia, J. F. Goodwin, G. Stutter, S. Bharadia, D. R. Crick, D. M. Segal, and R. C. Thompson, Nat. Comms **4**, 2571 (2013), URL http://dx.doi.org/10.1038/ncomms3571.

[105] M. G. Raizen, J. M. Gilligan, J. C. Bergquist, W. M. Itano, and D. J. Wineland, Phys. Rev. A **45**, 6493 (1992), URL https://link.aps.org/doi/10.1103/PhysRevA.45.6493.

[106] S. Gulde, Ph.D. thesis, University of Innsbruck (2003).

[107] D. F. V. James, Applied Physics B: Lasers and Optics **66**, 20 (1997), URL http://dx.doi.org/10.1007/s003400050373.

[108] C. C. J. Wang, A. C. Keith, and J. K. Freericks, Phys. Rev. A **87**, 013422 (2013), URL http://dx.doi.org/10.1103/PhysRevA.87.013422.

[109] D. H. E. Dubin, Phys. Rev. Lett. **71**, 2753 (1993), URL https://link.aps.org/doi/10.1103/PhysRevLett.71.2753.

[110] F. G. Major, V. N. Gheorghe, and G. Werth, *Charged particle traps: physics and techniques of charged particle field confinement*, vol. 37 (Springer Science & Business Media, 2006).

[111] H. Ball, M. W. Lee, S. D. Gensemer, and M. J. Biercuk, Review of Scientific Instruments **84**, 063107 (2013), URL http://dx.doi.org/10.1063/1.4811093.

[112] G. Hua, H. Yao, P. L. Liu, B. Wu, S. Hu, and K. L. Gao, Chinese Physics B **24**, 14 (2015), URL http://dx.doi.org/10.1088/1674-1056/4/5054213.

[113] Y. Wan, F. Gebert, J. B. Wübbena, N. Scharnhorst, S. Amairi, I. D. Leroux, B. Hemmerling, N. Lörch, K. Hammerer, and P. O. Schmidt, Nat. Comms **5**, 3096 (2014), URL http://dx.doi.org/10.1038/ncomms4096.

[114] F. Gebert, Y. Wan, F. Wolf, C. N. Angstmann, J. C. Berengut, and P. O. Schmidt, Phys. Rev. Lett. **115**, 053003 (2015), URL http://dx.doi.org/10.1103/PhysRevLett.115.053003.

[115] M. Hettrich, Ph.D. thesis, Universitat Ulm (2017).

[116] M. S. Safronova and U. I. Safronova, Phys. Rev. A **83**, 012503 (2011), URL https://link.aps.org/doi/10.1103/PhysRevA.83.012503.

[117] S. Mavadia, Ph.D. thesis, Imperial College London (2013).

[118] D. R. Crick, S. Donnellan, D. M. Segal, and R. C. Thompson, Phys. Rev. A **81**, 052503 (2010).

[119] J. D. Jackson, *Classical Electrodynamics* (John Wiley & Sons, 1999), 3rd ed.

[120] D. Leibfried, R. Blatt, C. Monroe, and D. Wineland, Review of Modern Physics **75**, 281 (2003), URL http://dx.doi.org/10.1103/RevModPhys.75.281.

[121] K. E. Cahill and R. J. Glauber, Physical Review **177**, 1857 (1969), URL https://link.aps.org/doi/10.1103/PhysRev.177.1857.

[122] D. Wineland, C. Monroe, W. Itano, D. Leibfried, B. King, and D. Meekhof, Journal of Research of the National Institute of Standards and Technology **103**, 259 (1998), URL http://dx.doi.org/10.6028/jres.103.019.

[123] W. M. Itano, J. C. Bergquist, J. J. Bollinger, and D. J. Wineland, Physica Scripta **T59**, 106 (1995), URL http://dx.doi.org/10.1088/0031-8949/1995/T59/013.

[124] H. G. Dehmelt and F. L. Walls, Phys. Rev. Lett. **21**, 127 (1968), URL https://link.aps.org/doi/10.1103/PhysRevLett.21.127.

[125] D. J. Wineland and H. G. Dehmelt, Journal of Applied Physics **46**, 919 (1975), URL http://dx.doi.org/10.1063/1.321602.

[126] W. D. White, J. H. Malmberg, and C. F. Driscoll, Phys. Rev. Lett. **49**, 1822 (1982), URL https://link.aps.org/doi/10.1103/PhysRevLett.49.1822.

[127] D. Wineland and H. Dehmelt, International Journal of Mass Spectrometry and Ion Physics **16**, 338 (1975), URL http://dx.doi.org/10.1016/0020-7381(75)87031-8.

[128] R. S. Van Dyck, P. B. Schwinberg, and H. G. Dehmelt, Phys. Rev. Lett. **38**, 310 (1977), URL https://link.aps.org/doi/10.1103/PhysRevLett.38.310.

[129] G. Bollen, R. B. Moore, G. Savard, and H. Stolzenberg, Journal of Applied Physics **68**, 4355 (1990), URL http://dx.doi.org/10.1063/1.346185.

[130] G. Savard, S. Becker, G. Bollen, H. J. Kluge, R. B. Moore, T. Otto, L. Schweikhard, H. Stolzenberg, and U. Wiess, Phys. Lett. A **158**, 247 (1991), URL http://dx.doi.org/10.1016/0375-9601(91)91008-2.

[131] D. Wineland and H. Dehmelt, in *Bulletin of the American Physical Society* (1975), vol. 20, pp. 637–637.

[132] T. W. Hänsch and A. L. Schawlow, Optics Communications **13**, 68 (1975), URL http://linkinghub.elsevier.com/retrieve/pii/0030401875901595.

[133] W. Neuhauser, M. Hohenstatt, P. E. Toschek, and H. Dehmelt, Phys. Rev. A **22**, 1137 (1980), URL http://dx.doi.org/10.1103/PhysRevA.22.1137.

[134] R. J. Hendricks, J. L. Sørensen, C. Champenois, M. Knoop, and M. Drewsen, Phys. Rev. A **77**, 1 (2008), URL http://dx.doi.org/10.1103/PhysRevA.77.021401.

[135] C. Monroe, D. Meekhof, B. King, S. Jefferts, W. Itano, D. Wineland, and P. Gould, Phys. Rev. Lett. **75**, 4011 (1995), URL http://dx.doi.org/10.1103/PhysRevLett.75.4011.

[136] H. Che, K. Deng, Z. T. Xu, W. H. Yuan, J. Zhang, and Z. H. Lu, Phys. Rev. A **96**, 013417 (2017), URL http://link.aps.org/doi/10.1103/PhysRevA.96.013417.

[137] C. F. Roos, D. Leibfried, A. Mundt, F. Schmidt-Kaler, J. Eschner, and R. Blatt, Phys. Rev. Lett. **85**, 5547 (2000), URL http://dx.doi.org/10.1103/PhysRevLett.85.5547.

[138] Y. Lin, J. P. Gaebler, T. R. Tan, R. Bowler, J. D. Jost, D. Leibfried, and D. J. Wineland, Phys. Rev. Lett. **110**, 153002 (2013), URL http://dx.doi.org/10.1103/PhysRevLett.110.153002.

[139] R. Lechner, C. Maier, C. Hempel, P. Jurcevic, B. P. Lanyon, T. Monz, M. Brownnutt, R. Blatt, and C. F. Roos, Phys. Rev. A **93**, 053401 (2016), URL http://dx.doi.org/10.1103/PhysRevA.93.053401.

[140] W. M. Itano and D. J. Wineland, Phys. Rev. A **25**, 35 (1982), URL http://dx.doi.org/10.1103/PhysRevA.25.35.

[141] L. Schweikhard and A. G. Marshall, Journal of the American Society for Mass Spectrometry **4**, 433 (1993), URL http://link.springer.com/10.1016/1044-0305(93)80001-F.

[142] R. J. Hendricks, E. S. Phillips, D. M. Segal, and R. C. Thompson, J. Phys. B **41**, 035301 (2008), URL http://stacks.iop.org/0953-4075/41/i=3/a=035301.

[143] I. Marzoli, J. I. Cirac, R. Blatt, and P. Zoller, Phys. Rev. A **49**, 2771 (1994), URL http://link.aps.org/doi/10.1103/PhysRevA.49.2771.

[144] G. Stutter, Ph.D. thesis, Imperial College London (2015).

[145] J. F. Goodwin, Ph.D. thesis, Imperial College London (2015).

[146] D. Crick, Ph.D. thesis, Imperial College London (2009).

[147] *Hamamatsu photomultiplier tubes catalog*, http://www.hamamatsu.com/resources/pdf/etd/PMT_TPMZ0002E.pdf, online; accessed 15 December 2017.

[148] A. Burrell, Ph.D. thesis, University of Oxford (2010).

[149] *iXon Ultra Hardware User Guide*, Andor Technology (2014), version 1.2.

[150] G. Z. Li, R. Poggiani, G. Testera, and G. Werth, Zeitschrift für Physik D Atoms, Molecules and Clusters **22**, 375 (1991), URL http://dx.doi.org/10.1007/BF01438559.

[151] G. Poulsen and M. Drewsen, arXiv p. 1210.4309 (2012), URL http://arxiv.org/abs/1210.4309.

[152] J. Huwer, Ph.D. thesis, Universitat Politècnica de Catalunya (2013).

[153] E. L. Hahn, Physical Review **80**, 580 (1950), URL https://link.aps.org/doi/10.1103/PhysRev.80.580.

[154] H. Y. Carr and E. M. Purcell, Phys. Rev. **94**, 630 (1954), URL http://link.aps.org/doi/10.1103/PhysRev.94.630.

[155] S. Meiboom and D. Gill, Review of Scientific Instruments **29**, 688 (1958), URL http://dx.doi.org/10.1063/1.1716296.

[156] G. S. Uhrig, Phys. Rev. Lett. **98**, 100504 (2007), URL http://link.aps.org/doi/10.1103/PhysRevLett.98.100504.

[157] G. S. Uhrig, New Journal of Physics **10**, 083024 (2008), URL http://stacks.iop.org/1367-2630/10/i=8/a=083024.

[158] D. J. Szwer, S. C. Webster, A. M. Steane, and D. M. Lucas, J. Phys. B **44**, 025501 (2011), URL http://stacks.iop.org/0953-4075/44/i=2/a=025501.

[159] M. J. Biercuk, H. Uys, A. P. VanDevender, N. Shiga, W. M. Itano, and J. J. Bollinger, Nature **458**, 996 (2009), URL http://dx.doi.org/10.1038/nature07951.

[160] B. Lee, W. M. Witzel, and S. Das Sarma, Phys. Rev. Lett. **100**, 160505 (2008), URL http://link.aps.org/doi/10.1103/PhysRevLett.100.160505.

[161] *Breadboard stabilized laser system*, http://www.stablelasers.com/products/breadboard-stabilized-laser-systems/, online; accessed 12 January 2018.

[162] J. W. Britton, J. G. Bohnet, B. C. Sawyer, H. Uys, M. J. Biercuk, and J. J. Bollinger, Phys. Rev. A **93**, 062511 (2016), URL http://dx.doi.org/10.1103/PhysRevA.93.062511.

[163] D. Wineland, C. Monroe, W. Itano, B. King, D. Leibfried, D. Meekhof, C. Myatt, and C. Wood, Fortschritte der Physik **46**, 363 (1998), URL https:dx.doi.org/10.1002/(SICI)1521-3978(199806)46:4/5<363::AID-PROP363>3.0.CO;2-4.

[164] M. Brownnutt, M. Kumph, P. Rabl, and R. Blatt, Reviews of Modern Physics **87**, 1419 (2015), URL https://link.aps.org/doi/10.1103/RevModPhys.87.1419.

[165] Q. A. Turchette, Kielpinski, B. E. King, D. Leibfried, D. M. Meekhof, C. J. Myatt, M. A. Rowe, C. A. Sackett, C. S. Wood, W. M. Itano, et al., Phys. Rev. A **61**, 063418 (2000), URL https://link.aps.org/doi/10.1103/PhysRevA.61.063418.

[166] I. A. Boldin, A. Kraft, and C. Wunderlich, Phys. Rev. Lett. **120**, 23201 (2017), URL http://dx.doi.org/10.1103/PhysRevLett.120.023201.

[167] Q. A. Turchette, C. J. Myatt, B. E. King, C. A. Sackett, D. Kielpinski, W. M. Itano, C. Monroe, and D. J. Wineland, Phys. Rev. A **62**, 053807 (2000), URL https://link.aps.org/doi/10.1103/PhysRevA.62.053807.

[168] J. Home, Ph.D. thesis, University of Oxford (2006).

[169] C. K. Law and J. H. Eberly, Phys. Rev. Lett. **76**, 1055 (1996), URL http://dx.doi.org/10.1103/PhysRevLett.76.1055.

[170] A. Ben-Kish, B. DeMarco, V. Meyer, M. Rowe, J. Britton, W. M. Itano, B. M. Jelenković, C. Langer, D. Leibfried, T. Rosenband, et al., Phys. Rev. Lett. **90**, 037902 (2003), URL http://dx.doi.org/10.1103/PhysRevLett.90.037902.

[171] B. Kneer and C. K. Law, Phys. Rev. A **57**, 2096 (1998), URL http://dx.doi.org/10.1103/PhysRevA.57.2096.

[172] R. Blatt, J. I. Cirac, and P. Zoller, Phys. Rev. A **52**, 518 (1995), URL http://dx.doi.org/10.1103/PhysRevA.52.518.

[173] D. Leibfried, D. M. Meekhof, B. E. King, C. Monroe, W. M. Itano, and D. J. Wineland, Phys. Rev. Lett. **77**, 4281 (1996), URL http://dx.doi.org/10.1103/PhysRevLett.77.4281.

[174] J. Alonso, F. M. Leupold, Z. U. Solèr, M. Fadel, M. Marinelli, B. C. Keitch, V. Negnevitsky, and J. P. Home, Nat. Comms **7**, 11243 (2016), URL http://www.nature.com/doifinder/10.1038/ncomms11243.

[175] P. L. Knight and P. M. Radmore, Phys. Rev. A **26**, 676 (1982), URL http://dx.doi.org/10.1103/PhysRevA.26.676.

[176] G. Rempe, H. Walther, and N. Klein, Phys. Rev. Lett. **58**, 353 (1987), URL http://dx.doi.org/10.1103/PhysRevLett.58.353.

[177] M. Greiner, O. Mandel, T. W. Hänsch, and I. Bloch, Nature **419**, 51 (2002), URL http://www.nature.com/articles/nature00968.

[178] M. Hofheinz, E. M. Weig, M. Ansmann, R. C. Bialczak, E. Lucero, M. Neeley, A. D. O'Connell, H. Wang, J. M. Martinis, and A. N. Cleland, Nature **454**, 310 (2008), URL http://dx.doi.org/10.1038/nature07136.

[179] B. Vlastakis, G. Kirchmair, Z. Leghtas, S. E. Nigg, L. Frunzio, S. M. Girvin, M. Mirrahimi, M. H. Devoret, and R. J. Schoelkopf, Science **342**, 607 (2013), URL http://www.sciencemag.org/cgi/doi/10.1126/science.1243289.

[180] W. B. Gao, C. Y. Lu, X. C. Yao, P. Xu, O. Gühne, A. Goebel, Y. A. Chen, C. Z. Peng, Z. B. Chen, and J. W. Pan, Nature Physics **6**, 331 (2010), URL http://dx.doi.org/10.1038/nphys1603.

[181] C. Monroe, D. M. Meekhof, B. E. King, and D. J. Wineland, Science **272**, 1131 (1996), URL http://www.sciencemag.org/cgi/doi/10.1126/science.272.5265.1131.

[182] G. Breitenbach, S. Schiller, and J. Mlynek, Nature **387**, 471 (1997), URL http://www.nature.com/articles/387471a0.

[183] C. Orzel, A. K. Tuchman, M. L. Fenselau, M. Yasuda, and M. A. Kasevich, Science **291**, 2386 (2001), URL http://www.sciencemag.org/cgi/doi/10.1126/science.1058149.

[184] G. Kirchmair, Ph.D. thesis, Unnivesity of Innsbruck (2010).

[185] C. F. Roos, New Journal of Physics **10**, 013002 (2008), URL http://dx.doi.org/10.1088/1367-2630/10/1/013002.

[186] C. Flühmann, V. Negnevitsky, M. Marinelli, and J. P. Home, Physical Review X **8**, 021001 (2018), URL https://dx.doi.org/10.1103/PhysRevX.8.021001.

[187] M. Šašura and V. Bužek, J. Mod. Opt. **49**, 1593 (2002), URL http://dx.doi.org/10.1088/1367-2630/15/12/123012.

[188] D. Nigg, M. Müller, E. A. Martinez, P. Schindler, M. Hennrich, T. Monz, M. A. Martin-Delgado, and R. Blatt, Science **345**, 302 (2014), URL http://www.sciencemag.org/content/345/6194/302.abstract.

[189] P. Schindler, D. Nigg, T. Monz, J. T. Barreiro, E. Martinez, S. X. Wang, S. Quint, M. F. Brandl, V. Nebendahl, C. F. Roos, et al., New Journal of Physics **15**, 123012 (2013), URL http://dx.doi.org/10.1088/1367-2630/15/12/123012.

[190] G. Kirchmair, J. Benhelm, F. Zähringer, R. Gerritsma, C. F. Roos, and R. Blatt, New Journal of Physics **11**, 023002 (2009), URL http://dx.doi.org/10.1088/1367-2630/11/2/023002.

[191] D. R. Crick, H. Ohadi, I. Bhatti, R. C. Thompson, and D. M. Segal, Optics Express **16**, 2351 (2008), URL http://dx.doi.org/10.1364/OE.16.002351.

[192] G. Stutter, P. Hrmo, V. Jarlaud, M. K. Joshi, J. F. Goodwin, and R. C. Thompson, J. Mod. Opt. **65**, 549 (2018), URL https://doi.org/10.1080/09500340.2017.1376719.

[193] T. Meiners, M. Niemann, A.-G. Paschke, J. Mielke, A. Idel, M. Borchert, K. Voges, A. Bautista-Salvador, S. Ulmer, and C. Ospelkaus, in *Proceedings of the 12th International Conference on Low Energy Antiproton Physics (LEAP2016)* (Journal of the Physical Society of Japan, 2017), vol. 011006, pp. 18–22, ISBN 4-89027-125-2, URL http://journals.jps.jp/doi/10.7566/JPSCP.18.011006.

[194] E. Mount, D. Gaultney, G. Vrijsen, M. Adams, S.-Y. Baek, K. Hudek, L. Isabella, S. Crain, A. van Rynbach, P. Maunz, et al., Quantum Information Processing **15**, 5281 (2016), URL http://link.springer.com/10.1007/s11128-015-1120-z.

[195] U. Sinha, C. Couteau, T. Jennewein, R. Laflamme, and G. Weihs, Science **329**, 418 (2010), URL http://www.sciencemag.org/cgi/doi/10.1126/science.1190545.

[196] O. S. Magaña-Loaiza, I. De Leon, M. Mirhosseini, R. Fickler, A. Safari, U. Mick, B. McIntyre, P. Banzer, B. Rodenburg, G. Leuchs, et al., Nat. Comms **7**, 13987 (2016), URL http://dx.doi.org/10.1038/ncomms13987.